Universidade Estadual Paulista “Júlio de Mesquita Filho” – UNESP

Universiteit Antwerpen - UAntwerpen

Programa de Pós-Graduação em Ciência e Tecnologia de Materiais – POSMAT – Campus de Bauru

Nicolas Porto Vizarim

Dynamic behavior of Skyrmions under the influence of periodic pinning in chiral magnetic infinite thin films

Bauru

2023

Nicolas Porto Vizarim

Dynamic behavior of Skyrmions under the influence of periodic pinning in chiral magnetic infinite thin films

Thesis presented to the Universidade Estadual Paulista “Júlio de Mesquita Filho” – Programa de Pós-Graduação em Ciência e Tecnologia de Materiais and Universiteit Antwerpen – Doctoral Study Program as a partial requirement to award a joint degree of Doctor in Science and Materials Technology and Physics, under the supervision of Prof. Dr. Pablo A. Venegas and Prof. Dr. Milorad V. Milošević.

Bauru

2023

Agradecimentos / Acknowledgements

I would like to acknowledge my family, Neuma, Pedro and Rafaela for always supporting me on my decisions and trajectory.

To my advisor Dr. Pablo Antonio Venegas Urenda for his patience and guidance through all my academic and scientific career. Thanks for the opportunity to let me work with you and your research group.

To my colleagues in the laboratory, Maicon, José and Felipe for helping on the discussions and analysis of my work.

To Dr. Charles Reichhardt and Dr. Cynthia J. O. Reichhardt for their attention and guidance while I was at the USA, and also for the important insights on our recent works together.

To my advisor Dr. Milorad V. Milošević and Dr. Raí M. Menezes for their support and guidance during my time at Antwerp.

To GridUNESP for the computational resources that made this thesis possible.

At last, I would also like to acknowledge the Fundação de Amparo à Pesquisa do Estado de São Paulo – FAPESP, for the financial support on my PhD (Grant:2017/20976-3) and my internship at the Los Alamos National Laboratory (Grant: 2018/13198-7). I would also like to acknowledge the Special Research Funds of the University of Antwerp (BOF) for the joint PhD scholarship during my stay in Antwerp. Also to CAPES and CNPq.

Resumo

Atualmente um dos maiores desafios na área de materiais é a miniaturização dos transistores para aplicação em novos processadores e dispositivos lógicos. Uma das altenativas viáveis é a utilização da spintrônica, baseada no movimento controlado de nanoestruturas magnéticas. Entre os potenciais candidatos, a descoberta de texturas magnéticas conhecidas como *skyrmions*, tem atraído considerável interesse. *Skyrmions* magnéticos são estruturas de spins quirais, topologicamente protegidas, e devido a serem muito estáveis, quando comparados com vórtices ou bolhas magnéticas, tem sido objeto de estudo nesses últimos anos. Com o objetivo de controlar o movimento dos *skyrmions*, essencial para aplicações, estudamos o comportamento dinâmico de *skyrmions* em um magneto quiral bidimensional a temperatura nula, sob influência de redes periódicas de centros de aprisionamento. As simulações são feitas na aproximação onde os *skyrmions* podem ser tratados como partículas pontuais. Neste modelo, o *skyrmion* está sujeito à interação com os demais *skyrmions*, com os centros de aprisionamento dispostos no material, a uma corrente de spins polarizados e à força de Magnus. Os cálculos foram feitos para diversos casos onde há a presença de um único *skyrmion* e também para diversos valores de densidade de *skyrmions* no material, procurando por possibilidades de controle de movimento, diversos regimes dinâmicos e efeitos coletivos. Os resultados mostram que ajustando o tamanho, força e densidade dos centros de aprisionamento é possível controlar o movimento de *skyrmons* individuais, e também controlar o fluxo de múltiplos *skyrmions*. Além disso, mostramos que caso haja espécies diferentes de *skyrmions* com diferentes componentes de Magnus, é possível fazer uma seleção topológica utilizando redes periódicas de centros de aprisionamento. Utilizando correntes alternadas, mostramos que o efeito *ratchet* tem um papel importante na dinâmica de *skyrmions*, fazendo com que ocorra movimento direto e controlado de *skyrmions* em determinadas direções apenas ajustando as amplitudes das correntes alternadas. A expectativa é que estes resultados possam ser úteis à comunidade científica para um melhor entendimento sobre a dinâmica de *skyrmions* e que resultem em futuras aplicações tecnológicas destas quase-partículas.

Palavras chave: Magnetismo. Skyrmions Magnéticos. Redes de Aprisionamento. Arranjos periódicos. Controle de Movimento.

Abstract

The miniaturization of transistors for application in new processors and logic devices poses a significant challenge in the field of materials. Spintronics, which relies on controlled movement of magnetic nanostructures, offers a promising solution. Among the candidates, magnetic skyrmions are considered one of the most promising. These chiral spin structures, characterized by topological protection and enhanced stability compared to vortices or magnetic bubbles, have been extensively studied. To advance in the control of skyrmion motion, essential for practical applications, we investigated their dynamic behavior in a two-dimensional chiral magnet at zero temperature. Our study focused on the influence of periodic arrays of pinning centers. The simulations considered skyrmions as point-like particles considering the following interactions: skyrmion-skyrmion interactions, interactions with pinning center arrays, a current of polarized spins, and the Magnus force. We conducted calculations for scenarios involving a single skyrmion as well as different skyrmion density values in the material. The aim was to explore possibilities for controlled skyrmion motion, investigate different dynamic regimes, and examine collective effects. The results demonstrate that by adjusting the size, strength, and density of the pinning centers, we can effectively control the motion of individual skyrmions and manage the flow of multiple skyrmions. Furthermore, we discovered that periodic arrays of pinning centers can facilitate topological selection when different species of skyrmions with distinct Magnus components are present. Employing alternating currents, we observed the significant role of the ratchet effect in the skyrmion dynamics. By fine-tuning the amplitudes of the alternating currents, we achieved direct and controlled motion of skyrmions in specific directions. These findings hold potential for advancing our understanding of skyrmion dynamics and can inspire future technological applications involving these quasi-particles. Overall, we anticipate that our results will be valuable to the scientific community, contributing to a deeper comprehension of skyrmion dynamics and paving the way for future technological applications.

Keywords: Magnetism. Magnetic Skyrmions. Pinning arrays. Periodic Pinning. Motion Control

Abstract

Op dit moment is een van de grootste uitdagingen op het gebied van materialen de miniaturisatie van transistors voor toepassingen in nieuwe processoren en logische apparaten. Een van de haalbare alternatieven is het gebruik van spintronica, gebaseerd op gecontroleerde beweging van magnetische nanostructuren. Onder potentiële kandidaten heeft de ontdekking van magnetische structuren, bekend als skyrmions, aanzienlijke belangstelling gekregen. Magnetische skyrmions zijn structuren met chirale spins, topologisch beschermd en vanwege hun grote stabiliteit in vergelijking met vortexen of magnetische bubbels, zijn ze de afgelopen jaren intensief bestudeerd. Om de beweging van skyrmions te kunnen controleren, wat essentieel is voor toepassingen, hebben we het dynamisch gedrag van skyrmions bestudeerd in een tweedimensionaal chiraal magnetisch materiaal bij nul temperatuur, onder invloed van periodieke netwerken van vangcentra. De simulaties zijn uitgevoerd in de benadering waarbij de skyrmions als puntdeeltjes kunnen worden behandeld. In dit model ondergaat de skyrmion interactie met andere skyrmions, met de vangcentra gerangschikt in het materiaal, een stroom van gepolariseerde spins en de Magnuskracht. De berekeningen zijn uitgevoerd voor verschillende gevallen waarbij er een enkele skyrmion aanwezig is, evenals voor verschillende waarden van de skyrmiondichtheid in het materiaal. We hebben gezocht naar mogelijkheden om de beweging te controleren, verschillende dynamische regimes en collectieve effecten te onderzoeken. De resultaten tonen aan dat het mogelijk is om de beweging van individuele skyrmions te controleren door de grootte, sterkte en dichtheid van de vangcentra aan te passen. Ook is het mogelijk om de stroming van meerdere skyrmions te beheersen. Bovendien hebben we aangetoond dat als er verschillende soorten skyrmions met verschillende Magnus-componenten zijn, het mogelijk is om topologische selectie uit te voeren met behulp van periodieke netwerken van vangcentra. Met behulp van wisselstromen hebben we aangetoond dat het ratchet-effect een belangrijke rol speelt in de dynamica van skyrmions. Door de amplitudes van de wisselstromen aan te passen, kan de beweging van skyrmions direct en gecontroleerd in bepaalde richtingen plaatsvinden. De verwachting is dat deze resultaten nuttig kunnen zijn voor de wetenschappelijke gemeenschap om een beter begrip van de dynamica van skyrmions te krijgen en dat ze kunnen leiden tot toekomstige technologische toepassingen van deze quasi-deeltjes.

Trefwoorden: Magnetisme. Magnetische Skyrmionen. Arrays vastzetten. Periodiek vastzetten. Beweging controle.

Contents

II - SKYRMIONS AND LINEAR DEFECTS

III - INTERACTION AMONG SKYRMIONS: MICROMAGNETIC APPROACH

1. Introduction

1.1 Motivation

There is a very famous projection that relates how dense can transistors be in an integrated circuit, which is known as the Moore's law [1]. Moore's law refers to Moore's perception that the number of transistors in a microchip double about every two years, tough the cost of computer is halved. This leads to an exponential growth of speed and capability of computers through time. However, the miniaturization of transistors using the traditional complementary-oxide-metal-semiconductor (CMOS) technology appears to be reaching a limitation. The increased dissipation of power due to the leakage currents caused by the quantum effect [2] has become one of most important issues, which results in the failure of Moore's prediction [3]. Thus, a lot of efforts have been made in order to search for alternatives or complementary technologies for further downscaling the transistor's dimensions. One of the possible alternatives is using spintronics, which considers electron spin property rather than electron charge to store and process information [4,5]. Using the singular properties of electron spin, the storage and manipulation of information can now exhibit low power and nonvolatility [6]. As a consequence, spintronics has a great prospect to be one of the most promising candidates in the next era of computers, especially for the emerging topological particle-like spin configurations known as magnetic skyrmions.

Magnetic skyrmions were first observed in 2009 [7], and since then there is a great interest for skyrmion technological applications due to their stability and reduced size compared to other magnetic structures, such as bubbles, vortices or domain walls [8,9]. Besides that, skyrmions may be driven by the application of a spin-polarized current with a much-reduced energy cost, when compared to domain walls, for example [10]. Both of these features make skyrmions an excellent choice as information carriers. On the other hand, skyrmions exhibit a strong and non-dissipative Magnus component caused by topology [11]. This affects both on how the skyrmion flow due to the applied transport current and how they interact with defects present in the sample, which may behave as a pinning (attractive) or an obstacle (repulsive) potential. Therefore, a theoretical approach to study and understand the skyrmion dynamics, and most importantly, control the skyrmion motion is crucial for future technological applications.

One of the alternatives that scientists are considering to control the skyrmion motion is using an array of obstacles, or pinning centers that may guide the motion through the sample. This idea is inspired in the experience obtained before in other systems, such as, superconducting vortices, colloids, electrons and active matter. It is shown that periodic structures of defects may stabilize the flow of particles for a range of applied transport forces [12–16], or even using alternating currents induce a ratchet effect to move particles in a given direction [17–25]. All of these past experiences are being applied to the skyrmion case to see how it behaves, considering its unique properties.

Most of works investigating skyrmion dynamics are very recent due to the novelty of the subject. Most works were made considering a random distribution of pinning centers [26–30], periodic substrate with a washboard potential [31–34], 1D wells [35] or nanotracks [36–38]. However, only few works have considered periodic pinning prior to the start of this thesis [39,40], therefore this is the main motivation for this thesis. In this chapter 1, we introduce the physics of skyrmions in magnetic materials and its fundamentals. In chapter 2 we describe the fundamental theoretical background to support this thesis, discussing the skyrmion formation and its most important interactions: the exchange and Dzyaloshinskii-Moriya interactions, and also address the skyrmion dynamics; explaining the two main models used to simulate the dynamics, the Landau-Lifshitz-Gilbert (LLG) equation and the particle model. In chapter 3 we review some of the most important observations concerning skyrmions interacting with pinning centers and substrates. In chapter 4 we present the model and simulation details used in this thesis. Chapters 5 – 13 show the results of our work during the thesis, concerning skyrmions interacting with different pinning landscapes and possibilities for controlled skyrmion motion. In chapter 14 the general conclusions are presented and in chapter 15 the scientific production during this work.

1.2 Skyrmion Discovery and Fundamentals

The name skyrmion was given due to its mastermind Tony Skyrme which developed the theory of skyrmions in the 1960s. Skyrmions were proposed to account for the stability of hadrons as quantized topological defects in the three-dimensional non-linear sigma model [41,42]. Recently, skyrmions has proven to be highly relevant in spin textures in condensed matter systems. Skyrmion structures were found in quantum Hall ferromagnets [43,44], ferromagnetic monolayers [45], liquid crystals [46,47] and Bose-Einstein condensates [48,49]. The realization of skyrmion in chiral magnets was theoretically

predicted [50–52] and then observed recently [7,53]. Magnetic skyrmions compromise spins pointing in all directions wrapping a sphere, in a similar way to hedgehog, shown in Fig. 1.1 (a).

Figure 1.1 – In (a) the Skyrmion illustration as proposed by Tony Skyrme in the 60s. In (b) an illustration of the helical state present in chiral magnets as a consequence of the competition between the Dzyaloshinskii-Moriya and the ferromagnetic exchange interactions. In (c) the skyrmion representation recently discovered in chiral magnets. In (d) an illustration of a skyrmion array in chiral magnets under the influence of a applied magnetic field. Note that they arrange themselves in a regular triangular lattice (adapted from S. Seki and M. Mochizuki, 2016, page 2).

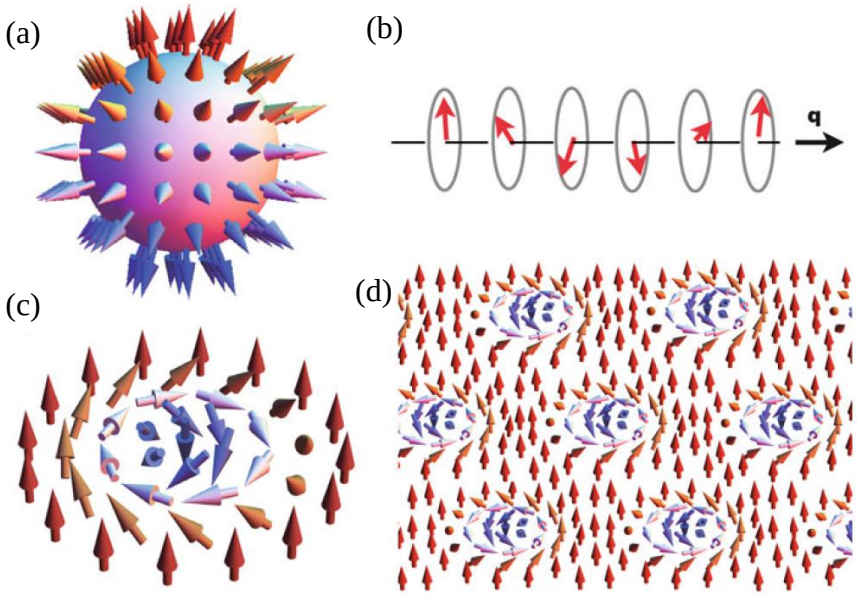

One of the major mechanisms for the formation of skyrmions is the competition between two spin interactions: the ferromagnetic exchange and the Dzyaloshinkii-Moryia (DM) interaction [50–52]. In chiral magnets without spatial inversion symmetry, such as B20 compounds (MnSi, FeGe, $Fe_{1-x}Co_xSi$), the DM interaction becomes finite, which makes possible the formation of skyrmions. In a continuum spin model, the DM interaction hamiltonian may be expressed as [54],

$$\mathcal{H}_{DM} \propto \int d\mathbf{r}\mathbf{M} \cdot (\nabla \times \mathbf{M}), \tag{1.1}$$

where **M** is the classical magnetization vector. As can be seen, this interaction alone favors the rotating magnetization alignment and competes with the ferromagnetic exchange interaction, that favors a colinear spin alignment. Due to this competition between the DM and the ferromagnetic exchange interaction, in the absence of an applied magnetic field, the spins tend to form a helical spin order with uniform turn angle [55–57], as illustrated in Fig. 1.1 (b). If a magnetic field is applied, the helical phase is destroyed and skyrmions begin to appear as a vortex-like topological spin textures, as illustrated in Fig. 1.1 (c). In the skyrmion, the

magnetization changes from parallel to the applied field in the periphery to antiparallel to the applied field in its center. Once the helical phase is being destroyed and skyrmions are forming, they normally organize themselves in a regular triangular lattice called skyrmion crystal, as illustrated in Figure 1.1 (d). This ordering occurs due to the repulsive interaction between the topologically protected spin textures. In chiral magnets, skyrmions range from $3-100$ nm in size, which is determined by the ration between the DM and the exchange interactions, that is, D/J. For example, if D is high, it favors a higher rotation of spins, therefore reducing the skyrmion size [9].

Since the discovery of skyrmions, a variety of new topological magnetic textures have been observed experimentally [58–60]. Some of them are shown in Fig 1.2. Usually, the classification of these spin textures is based on their topology. Two dimensional textures described by a local magnetization direction, **m**, can be classified by the skyrmion winding number [61]:

$$\mathcal{W} = \frac{1}{4\pi}\int dxdy\ \mathbf{m}\cdot\left(\partial_x\mathbf{m}\times\partial_y\mathbf{m}\right), \tag{1.2}$$

Note that topology is a mathematical concept for continuous systems, where a continuous mapping from one structure to the other exists, however in real physical systems it is usually discrete, for example, due to the underlying atomic lattice.

Figure 1.2 – Different types of topological spin textures with distinct winding numbers. In (a) Néel-type skyrmion, (b) Bloch-type skyrmion, (c) antiskyrmion, (d) skyrmionium, (e) biskyrmion, (f) example of in-plane skyrmion and (g) skyrmion in helical background. The winding numbers for (a)-(c), (f), and (g) is $|\mathcal{W}| = 1$ and for (e) is $|\mathcal{W}| = 2$. (adapted from Everschor-Sitte *et. al*. [61], 2018, page 240901-2).

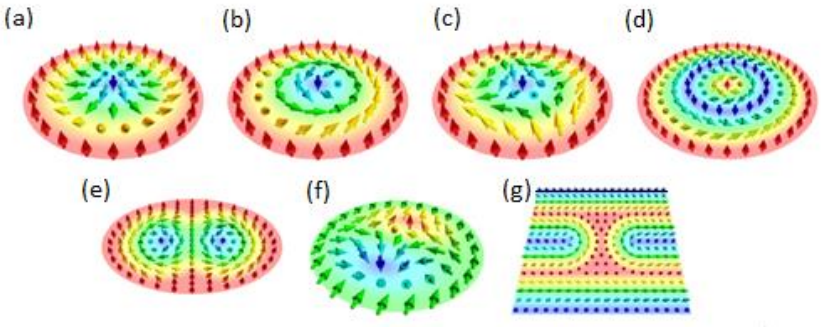

Concerning to skyrmions in chiral magnetic materials, in Fig. 1.3 there is an experimental phase-diagram of applied magnetic field, $B(\mathrm{mT})$, versus temperature, $T(\mathrm{K})$ based on real-space observation for $Fe_{0.5}Co_{0.5}Si$ [53]. In these figures the changing of the spin texture is represented by a contour mapping of skyrmion density [See Fig. 1.3 (d)]. In figures 1.3 (a) –

(c) it is possible to observe for a fixed value of $T = 25\text{K}$ how the skyrmion density changes as a function of the applied magnetic field, B. From Fig. 1.3 (a) it is possible to see the experimental observation of the helical phase (H) being destroyed and the skyrmion crystal (SkX) formation. In Fig. 1.3 (b) the stabilized skyrmion crystal phase, and in Fig. 1.3 (c) the destruction of the skyrmion crystal phase and beginning of the ferromagnetic phase (FM). After further increase of the applied magnetic field, the skyrmion crystal is completely destroyed and all spins align with the magnetic field.

Figure 1.3 – In (a) observation of the phase H + SkX, which represents the transition between helicoidal (H) to the skyrmion crystal phase (SkX). In (b) the stabilized skyrmion crystal phase (SkX). In (c) the transition between the skyrmion crystal (SkX) to the ferromagnetic phase (FM). In (d) the phase diagram for $Fe_{0.5}Co_{0.5}Si$ (adapted from X. Z. Yu *et. al*. [53], 2010, page 903).

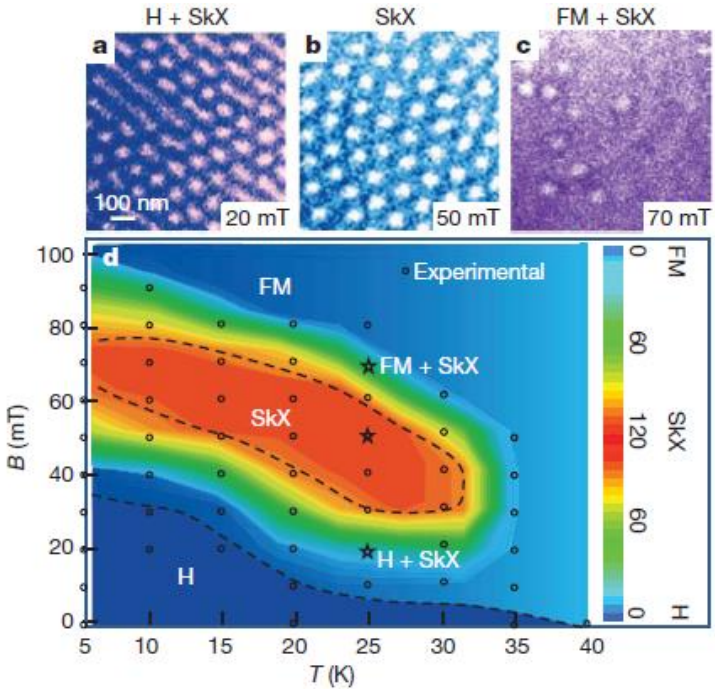

One of the proposed technological applications for skyrmions is to use them as an information storage in future logical and memory devices [62,63], where a bit may be associated to the skyrmion existence. Moreover, simulations indicate that skyrmion positions in a magnetic film may be created [64,65] and manipulated with application of spin polarized currents [9], or spin waves [66]. The necessary current for the skyrmion to depin is much lower than the necessary current to induce motion of magnetic domain walls, which are the other alternative for applications in spintronics [10,67,68]. That is, skyrmions may be set into motion with much less energy cost. Then, it is crucial a theoretical approach for a better understanding of the skyrmion behavior and future applications in technological devices. Nowadays, there are two most common theoretical approaches to simulate skyrmions. One is based on micromagnetism, where

it is calculated the time derivative for each local magnetic moment (treated as classic vectors) inside the material [29,69–71], the other is a particle model which uses the Thiele's approximation for solitons [72,73], both methods will be discussed in section 2.

1.3 Skyrmions and Defects

Most of interesting skyrmion behaviors occur in the presence of defects, which we also call pinning centers or obstacles. In experiments conducted by Schultz *et. al*. [67], the motion of skyrmions was inferred from observations of changes in the topological Hall effect. This technique provided evidence of a finite depinning threshold for the skyrmion motion, and in many subsequent imaging experiments, a wide range of depinning thresholds has been observed ranging from 10^6 to 10^{11} A/m^2. Pinning effects for skyrmions can be attributed to various factors, including modifications in the DMI (Dzyaloshinskii-Moriya interaction), vacancies in the lattice structure, presence of holes in thin films, localized alterations in anisotropy, variations in sample thickness, impurity atoms within the material, or adatoms attached to the surface of the sample [74]. Examples of such defects can be observed in Fig. 1.4. Surface modulations can be implemented by fabricating holes or antidots as in Fig. 1.4 (a), place dots in the form of magnetic nanoparticles on the surface, as shown in Fig. 1.4 (b), take advantage of naturally occurring atomic defects in the bulk such as missing atoms or substitutions, as shown in Fig. 1.4 (c), or place adatoms on the surface as shown in Fig. 1.4 (d).

Figure 1.4 – Schematic illustrations of pinning possibilities in magnetic samples. (a) Surface thickness modulations. (b) Implementation of nanodots to the surface. (c) Naturally occurring atomic defects or substitutions in the bulk system. (d) Adatoms adhered in the sample surface. (adapted from C. Reichhardt *et. al*. [74], 2022, page 11).

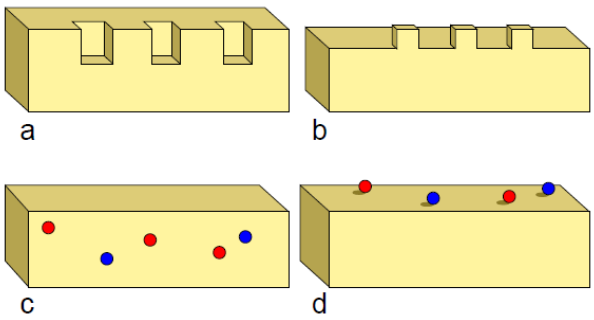

In 2013, Lin *et al*. [75] conducted micromagnetic simulations on uniform samples without defects and demonstrated that there is no threshold current for the skyrmion motion, that is, skyrmions flow for even very small applied transport currents. Iwasaki *et al*. [29] performed one of the earliest theoretical studies on skyrmion pinning, using micromagnetic simulations with parameters suitable for MnSi. They modeled the pinning as small regions with varying

local anisotropy A. In these systems, the current depinning threshold is $j_c \approx 10^{10} - 10^{11}$ A/m^2, and the skyrmion depins elastically. Liu and Li [76] investigated a local exchange mechanism for skyrmion pinning by varying the local density of itinerant electrons. Through micromagnetic simulations and a Thiele equation approach, they observed that the skyrmion is pinned due to the reduction in the skyrmion core energy. They also demonstrated that when subjected to a small drive, the skyrmion follows a spiraling trajectory as it returns to the pinning site, in contrast to the linear movement of an overdamped particle back to its equilibrium position. The spiraling motion is driven by the Magnus force. At higher currents, the skyrmion escapes the trap, leading to depinning. For the case of skyrmions interacting with holes, Müller and Rosch [77] analyzed the interaction between a skyrmion and a hole or locally damaged region using continuum methods and the Thiele equation approach. They discovered that the potential generated by the hole exhibits an intriguing combination of long-range repulsion and short-range attraction. The competition resulting from applied drive produces an unusual effect: the skyrmion moves around the pinning site at low drives due to repulsion, but jumps over the longer-range repulsive barrier and gets captured by the short-range attraction at high drives.

Figure 1.5 – Schematic illustrations of a (a) skyrmion and a (b) superconducting vortex interacting with an attractive point-like pinning site. The velocity component induced by the dissipation is indicated by black arrows, and that produce by the Magnus force is red. The Magnus force is always perpendicular to the attractive force of the pinning center, resulting in a deflection. (adapted from C. Reichhardt *et. al*. [74], 2022, page 14).

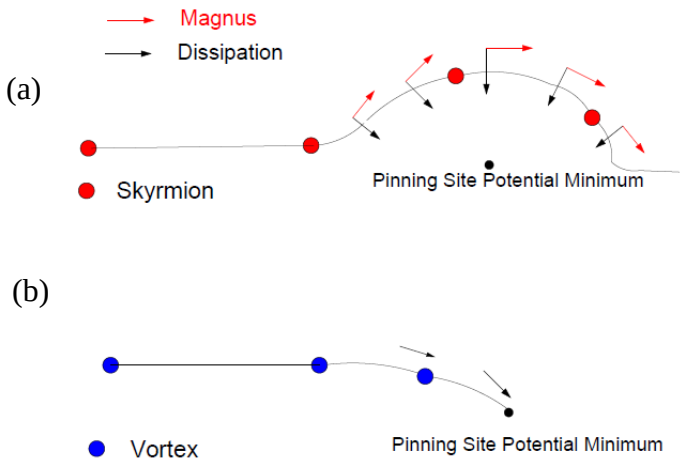

It was initially argued that a skyrmion can move around a point pinning site due to the Magnus effect [11]. Micromagnetic simulations by Iwasaki *et al*. [29] showed that pinning was reduced not only by the Magnus effect, but also by the ability of the skyrmions to modify their shape. Figure 1.5 provides a schematic illustration of how the Magnus force reduces the effectiveness of pinning for a skyrmion interacting with a point pinning site. The black arrows indicate the direction of the attractive force from the pinning site, always pointing towards the

pin. The red arrows represent the Magnus force component, always perpendicular to the force from the pinning site. As a result, while the dissipative term favors the motion of the skyrmion towards the pinning site, the Magnus force causes the skyrmion to deflect around it. In contrast, a purely overdamped particle like a type II superconducting vortex moves directly towards the center of the pinning site and is more likely to be trapped. This is why skyrmions usually exhibit lower depinning thresholds. The deflection of the skyrmion around the pinning site strongly depends on the relative size and extent of the skyrmion compared to that of the pinning site. In section 5 we compile some of the most important works regarding skyrmions interacting with pinning centers in more detail, which is useful for understanding the insights and analysis used in this thesis.

2 Theoretical Background

2.1 Skyrmion formation

As mentioned before, there are several mechanisms responsible for the skyrmion formation inside magnets. The main mechanism is the competition between exchange and Dzyaloshinskii-Moriya interaction [50,51]. As these are the most important ones, we will introduce both spin interactions.

2.1.1 The exchange interaction

The exchange interaction concerns the interaction between two electrons, mainly between neighbor atoms, associated with the Pauli exclusion principle [78]. There is an energy difference between spin configurations $\uparrow_i\uparrow_j$ and $\uparrow_i\downarrow_j$ of two electrons i,j. In this section we demonstrate this interaction.

The Pauli principle [78,79] forbids more than one electron to occupy the same state. As electrons are identical and indistinguishable particles, the exchange between two electrons shall result in the same electron density, that is,

$$|\Psi(1,2)|^2 = |\Psi(2,1)|^2 \tag{2.1}$$

Electrons are fermions, so the only possible solution is that the total wave function of two electrons is asymmetric, that is,

$$\Psi(1,2) = -\Psi(2,1) \tag{2.2}$$

The total wave function Ψ is the product of the space coordinate function, $\phi(r_1, r_2)$, and spin, $\chi(s_1, s_2)$.

The example of a H_2 molecule, with two atoms where each one has an electron in orbital $1s$, gives us a good idea of how the exchange interaction behaves. In this case, the Schrödinger equation for two electrons, neglecting the interaction between them, only considering the interactions between the electrons and the ion, is given by [78,80]:

$$\left[-\frac{\hbar}{2m}\left(\frac{\partial^2}{\partial r_1^2}+\frac{\partial^2}{\partial r_2^2}\right)-\frac{e^2}{4\pi\varepsilon_0}\left(\frac{1}{r_1}+\frac{1}{r_2}\right)\right]\Psi(r_1,r_2)=E\Psi(r_1,r_2) \qquad (2.3)$$

For this particular case, there are two molecular orbitals (See Fig. 2.1). One orbital is a spatially symmetric bonding orbital ϕ_s, with electronic charge piled up between atoms, and a spatially antisymmetric antibonding orbital ϕ_a having a nodal plane with no charge between them. The chemical bonds that describe hybridized wave functions of electrons are given by:

$$\phi_s=\left(\frac{1}{\sqrt{2}}\right)(\psi_1+\psi_2) \qquad \phi_a=\left(\frac{1}{\sqrt{2}}\right)(\psi_1-\psi_2) \qquad (2.4)$$

Where ψ_1 e ψ_2 are spatial components of the individual wave function of electrons 1 and 2, respectively. The wave functions $\psi_1(r_1)$ and $\psi_2(r_2)$ are solution of the Schrödinger equation for each atom.

Figure 2.1 – Representation of molecular orbitals of the H_2 molecule (adapted from https://www.sparknotes.com/chemistry/bonding/molecularorbital/section1/ accessed on 09/20/2021).

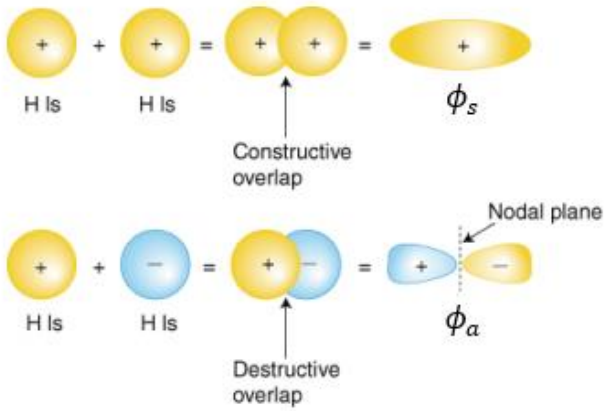

The symmetric and antisymmetric spin functions are known as the singlet and triplet states, respectively. In the singlet state:

$$S=0; \qquad M_S=0$$

$$\chi_a = \left(\frac{1}{\sqrt{2}}\right)(|\uparrow_1\downarrow_2\rangle - |\downarrow_1\uparrow_2\rangle) \tag{2.5}$$

In the triplet state:

$$S = 1; \quad M_S = 1, 0, -1$$

$$\chi_s = |\uparrow_1\uparrow_2\rangle\,; \quad \left(\frac{1}{\sqrt{2}}\right)(|\uparrow_1\downarrow_2\rangle + |\downarrow_1\uparrow_2\rangle); \quad |\downarrow_1\downarrow_2\rangle; \tag{2.6}$$

According to Eq. (2.2), the symmetric spatial function multiplies the antisymmetric spin function, and vice-versa. Thus, the wave functions shall be:

$$\Psi_I = \phi_s(1,2)\chi_a(1,2) \tag{2.7a}$$

$$\Psi_{II} = \phi_a(1,2)\chi_s(1,2) \tag{2.7b}$$

When both electrons are in the spin triplet state, there is no possibility to find them in the same point in space. That is, electrons with parallel spins repel each other. However, if the electrons are in the spin singlet state, with antiparallel spins, there is a non-zero possibility to find them in the same point in space. This phenomena occurs because the spatial part of the wave function is symmetric under exchange of electrons [78].

The energy between these two states may be calculated through the Hamiltonian $\mathcal{H}(\mathbf{r}_1, \mathbf{r}_2)$ of Eq. (2.3):

$$E_{I,II} = \int \phi^*_{s,a}(\mathbf{r}_1, \mathbf{r}_2)\mathcal{H}(\mathbf{r}_1, \mathbf{r}_2)\phi_{s,a}(\mathbf{r}_1, \mathbf{r}_2)dr_1^3 dr_2^3 \tag{2.8}$$

For the hydrogen molecule, $E_I < E_{II}$, due to the spatial restriction of the triplet spin state. If we define the exchange integral as $\mathcal{J} = (E_I - E_{II})/2$, it is possible to write the energy in the form:

$$E = -2\left(\frac{\mathcal{J}}{\hbar^2}\right)\mathbf{s}_1 \cdot \mathbf{s}_2, \tag{2.9}$$

Where the product $\mathbf{s}_1 \cdot \mathbf{s}_2 = \frac{1}{2}[(\mathbf{s}_1 + \mathbf{s}_2)^2 - \mathbf{s}_1^2 - \mathbf{s}_2^2]$. If the spin quantum number $S = s_1 + s_2$ is 0 or 1, the eigenvalues are $-\frac{3}{4}\hbar^2$ or $\frac{1}{4}\hbar^2$, respectively. Therefore, the energy difference between the singlet state, ψ_I, and the triplet state, ψ_{II}, is $2\mathcal{J}$. Thus, $\mathcal{J}$ is the exchange integral:

$$\mathcal{J} = \int \psi_1^*(\mathbf{r}')\psi_2^*(\mathbf{r})\mathcal{H}(\mathbf{r},\mathbf{r}')\psi_1(\mathbf{r})\psi_2(\mathbf{r}')\, dr^3 d^3r' \tag{2.10}$$

In the H_2 molecule, the singlet state has lower energy, therefore the integral is negative. However, in one of the atoms, the orbitals are orthogonal and the exchange integral becomes positive.

Heisenberg generalized the energy expression of Eq. (2.9) for atoms with many electrons through his famous Hamiltonian:

$$\mathcal{H} = -2\mathcal{J}\hat{\mathbf{S}}_1 \cdot \hat{\mathbf{S}}_2, \tag{2.11}$$

where $\hat{\mathbf{S}}_1$ and $\hat{\mathbf{S}}_2$ are dimensionless spin operators. The constant $\hbar^2$ was absorbed by the exchange constant $\mathcal{J}$, which has unities of energy. Hence, the exchange integral has now dimensions of energy. When $\mathcal{J} > 0$ it is said that the interaction is ferromagnetic, so both spins tend to align parallelly. However, when $\mathcal{J} < 0$ it is said that the interaction is antiferromagnetic and both spins tend to align antiparallelly.

In the presence of a lattice, the Hamiltonian is generalized to a sum over all atom pairs on lattice sites i, j:

$$\mathcal{H} = -2\sum_{i>j} \mathcal{J}_{ij}\, \hat{\mathbf{S}}_1 \cdot \hat{\mathbf{S}}_2, \tag{2.12}$$

This is simplified to a sum with a single exchange constant $\mathcal{J}$ with the condition that only first neighbor interactions are considered. The interatomic exchange interaction described by the Heisenberg's Hamiltonian can only be ferromagnetic or antiferromagnetic.

2.1.2 Dzyaloshinkii-Moriya (DM) interaction

In 1958, Dzyaloshinskii made a model to describe weak ferromagnetism [81]. Based on symmetry concepts, he introduced an asymmetric term which was later known as Dzyaloshinkii-Moriya interaction. Moriya was able to insert his name on this term because he discovered later that the mechanism responsible for this effect is the spin orbit coupling [82]. In a few words, the Dzyaloshinskii-Moriya (DM) interaction is induced by the lack of inversion symmetry of the compound, and also by a strong spin orbit coupling.

As an example of such material, one may cite the MnSi. In Fig. 2.2 it is possible to see that the inversion symmetry is broken inside the unity cell. Moreover, MnSi exhibits a very strong spin orbit coupling [83–86].

The DM interaction may be represented by the following Hamiltonian [78]:

$$\mathcal{H}_{DM} = -\mathbf{D} \cdot \left(\mathbf{S}_i \times \mathbf{S}_j\right), \tag{2.13}$$

where **D** is a vector along a high symmetry axis (See Fig. 2.3), therefore the tendency is to couple both spins perpendicularly. Then, as this expression shows, the DM interaction only occurs when there is a misalignment of spins, otherwise $\mathcal{H}_{DM}$ becomes null.

Figure 2.2 –Crystal structure of MnSi with B20 cubic symmetry, which is noncentrosymmetric, as revealed by the fact that inversion operation (r → − r) does not produce identical unit (adapted from T. Y. Ou-Yang *et. al*., J. Phys. Condens. Matter 28, 026004 (2015) [87]).

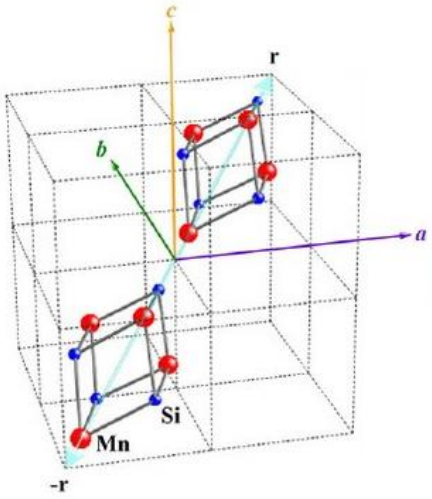

Figure 2.3 – Vector representation of the Dzyaloshinskii-Moriya interaction. Here, **D** is always perpendicular to the plane formed by $\mathbf{S}_1$ and $\mathbf{S}_2$ (Adapted from Coey, 2009, page 139).

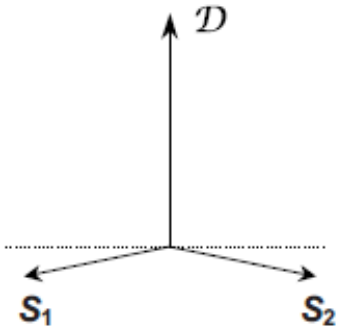

For the particular case of skyrmions, its formation occurs due to the DM interaction being induced by the broken inversion symmetry, or by the interface in magnetic films. For ultrathin films, the interfacial DM interaction was predicted [88,89] to occur due to the interaction of two atomic spins ($\mathbf{S}_1$ and $\mathbf{S}_2$) interacting with a neighbor atom with high spin orbit coupling [See Fig. 2.4 (a)]. The resulting vector, $\mathbf{D}_{1,2}$, of this interaction is perpendicular to the triangle plane, as illustrated in Fig. 2.4 (a). Meanwhile, the interfacial DM interaction occurs on the interface between a ferromagnetic material (grey) and another material with high spin orbit coupling (light blue) as can be seen in Fig. 2.4 (b).

Figure 2.4 – In (a) a schematic representation of the DM interaction generated by a triangle with two atomic spins interacting with an atom with high spin orbit coupling. In (b) a schematic representation of a interfacial DM interaction between a ferromagnetic material (grey) and a metal with high spin orbit coupling (SOC) (light blue). The DM interaction vector, $\mathbf{D}_{1,2}$, is always perpendicular to the triangle plane (Adapted from Fert *et. al*. [9], 2013, pg. 153).

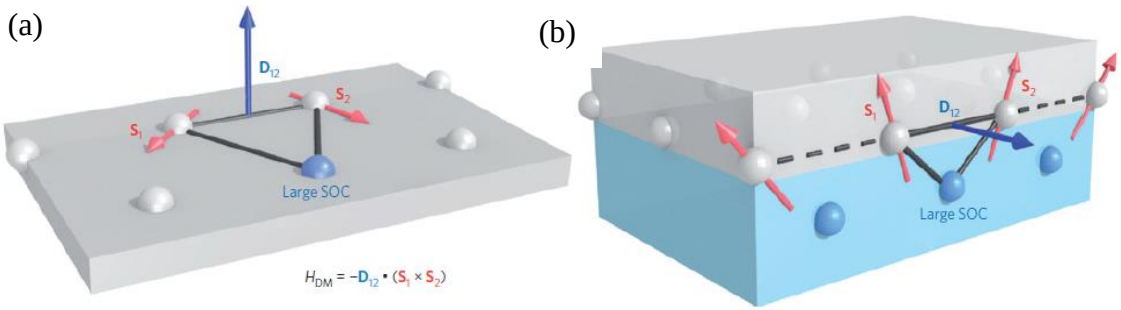

Considering a ferromagnetic state, with $\mathbf{S}_1$ parallel to $\mathbf{S}_2$, the DM interaction tilts $\mathbf{S}_1$ with respect to $\mathbf{S}_2$ by a rotation around $\mathbf{D}_{1,2}$. In a bidimensional ferromagnet, with uniaxial anisotropy and a significant DM interaction, the energy is minimized by a skyrmion structure similar to what is shown in Fig 2.5 (a), when $\mathbf{D}_{1,2}$ is perpendicular to $\mathbf{R}_{1,2}$, or similar to Fig. 2.5 (b), when $\mathbf{D}_{1,2}$ is parallel to $\mathbf{R}_{1,2}$. The skyrmion of Fig. 2.5 (a) is known as Néel, and in Fig. 2.5 (b) known as Bloch [8,9]. $\mathbf{R}_{1,2}$ is defined as a vector connecting $\mathbf{S}_1$ to $\mathbf{S}_2$ site. The extension of this principle to the three dimensional case is analogous, the skyrmion structure is obtained by the translation along the anisotropy axis, forming tubes [9]. In most of this work, we consider the case of ultrathin chiral magnets where the skyrmions are present in the Neél configuration, however, we also simulate the interaction between Bloch skyrmions in bulk samples in section 15.

Figure 2.5 – Representation of the spin orientation in skyrmions. In (a) the Néel skyrmion and in (b) the Bloch skyrmion (Adapted from Fert *et. al*., 2013, pg. 153).

(a)  (b) 

2.2 Landau-Lifshitz-Gilbert (LLG) Equation

The first theoretical approach to study the magnetism inside materials was elaborated by Landau and Lifshitz in 1935 [90], where an equation that described the time evolution of magnetic moments was deduced for the first time. Later, Gilbert added a damping term to the equation in order to consider the spin alignment to the external magnetic field. In this section we aim to explain the foundations of the Landau-Lifshitz-Gilbert (LLG) equation for proper use and simplification in the particle model section ahead.

2.2.1 Foundations of Magnetization Precession

First, we consider the case of magnetization precession, where in quantum mechanics [79,91] it states that the time evolution of the mean value of the spin operator derives from the Schrödinger's equation using the Ehrenfest theorem [92]:

$$i\hbar\frac{d}{dt}\langle\mathbf{S}\rangle(t) = \langle[\mathbf{S}, \mathcal{H}(t)]\rangle \tag{2.14}$$

If the spin is under the influence of the solo action of a time-dependent external magnetic field, the Hamiltonian simply becomes the Zeeman term,

$$\mathcal{H}(t) = -\frac{g\mu_B}{\hbar}\mathbf{S}\cdot\mathbf{B}(t), \qquad \mathbf{B}(t) = \mu_0\mathbf{H}(t) \tag{2.15}$$

Now, looking just at the x component for instance, we can combine (2.14) and (2.15) as:

$$[S_x, \mathcal{H}(t)] = -\frac{g\mu_B}{\hbar}\left[S_x, S_xB_x(t) + S_yB_y(t) + S_zB_z(t)\right]$$

$$= -\frac{g\mu_B}{\hbar}\left(B_y(t)\left[S_x, S_y\right] + B_z(t)[S_x, S_z]\right). \tag{2.16}$$

By applying the usual commutation rules for spin:

$$[S_x, S_y] = i\hbar S_z,$$

$$[S_y, S_z] = i\hbar S_x,$$

$$[S_z, S_x] = i\hbar S_y, \tag{2.17}$$

It is possible to apply (2.17) into (2.16) to obtain

$$[S_x, \mathcal{H}(t)] = -\frac{g\mu_B}{\hbar} i\hbar\big(B_y(t)S_z - B_z(t)S_y\big). \tag{2.18}$$

Thus, rewriting (2.14) using (2.18) we came to a conclusion that the expectation value of the spin operator is as follows:

$$\frac{d}{dt}\langle \mathbf{S}\rangle(t) = \frac{g\mu_B}{\hbar}(\langle \mathbf{S}\rangle(t) \times \mathbf{B}(t)). \tag{2.19}$$

2.2.2 Relation Between Classical Mechanics and Electromagnetism

The Equation (2.19) calculates the time variation of the expected value of the spin operator, however, for the LLG equation it is necessary to calculate how the magnetization behaves as a function of time. Thus, to relate the spin and the magnetization it is necessary to consider the magnetic dipole moment, **m**. In classical mechanics the angular momentum of a moving electron can be written as:

$$\boldsymbol{\mathcal{L}} = m_e(\mathbf{r} \times \mathbf{v}), \tag{2.20}$$

where m_e is the electron mass, **v** is the velocity and **r** the distance between the electron and the center of the circular motion, as illustrated in Fig. 2.6 (a). The force exerted on a current element (intensity i and length $d\mathbf{l}$) by the applied magnetic field is given by

$$d\mathbf{F} = id\mathbf{l} \times \mathbf{B}. \tag{2.21}$$

Integrating the Eq. (2.21), the torque exerted by **B** on the current loop, with area A, is given by

$$\boldsymbol{\tau} = i\mathbf{A} \times \mathbf{B}, \qquad \mathbf{A} = A\hat{\mathbf{n}}. \tag{2.22}$$

In analogy to the torque acting upon a magnetic dipole due to **B**, the current loop dipole moment is classically defined as

$$\mathbf{M} = i\mathbf{A} \tag{2.23}$$

Figure 2.6 – The relation between the classic angular momentum (a) and the magnetic dipole moment (b) (Adapted from B. Hillebrands and K. Ounadjela 2002, pg. 1283).

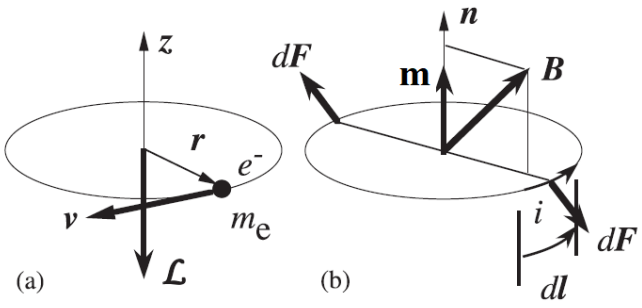

The current intensity in the magnetic dipole of a current loop can be written as

$$i = \frac{q_e v}{2\pi r} \tag{2.24}$$

Substituting Eq. (2.24) into Eq. (2.23) we find that the magnetic moment reads

$$\mathbf{M} = \frac{q_e}{2m_e}\boldsymbol{\mathcal{L}}. \tag{2.25}$$

Note that **m** is antiparallel to $\boldsymbol{\mathcal{L}}$ due to negative charge of the electron, q_e, as illustrated in Fig. 2.6.

There is a geometric relation between the spin and the magnetization, which is given by

$$\mathbf{M} = \gamma\langle\mathbf{S}\rangle, \tag{2.26}$$

where $\gamma = g\mu_B/\hbar$ is known as the gyromagnetic ratio. In the gyromagnetic ratio, $g \cong 2$ for a free electron and μ_B is the Bohr magneton.

The previous Eq. (2.19) for the expected mean value of spin can now be rewritten as the time variation of the magnetization

$$\frac{d}{dt}\mathbf{M}(t) = \gamma[\mathbf{M}(t) \times \mathbf{B}(t)] \tag{2.27}$$

As the magnetization is defined as the sum over all individual dipole moments in the material, that is,

$$\mathbf{M} = \frac{\sum_i \mathbf{m}_i}{V}, \tag{2.28}$$

Then, using $\gamma_0 = \mu_0 \frac{g|\mu_B|}{\hbar} = -\mu_0\gamma$, Eq. (2.27) becomes

$$\frac{d}{dt}\mathbf{m}(t) = -\gamma_0[\mathbf{m}(t) \times \mathbf{H}(t)], \tag{2.29}$$

From Eq. (2.29) it is clear that $\mathbf{m} \cdot \mathbf{m} = \text{const.}$ and $\mathbf{m} \cdot \mathbf{H} = \text{const.}$ As a consequence, the modulus of the magnetization remains unchanged during motion and the angle between the field and the magnetization also remains constant as a function of time [93]. This equation describes a precessional motion of the magnetization around the applied magnetic field, as illustrated in Fig. 2.7 (a).

2.2.3 Introducing the Gilbert Damping Term

In ferromagnetic samples it is well known that above certain critical values of applied magnetic field the sample is considered saturated, that is, the magnetization is uniform and align with the field. Precession alone does not allow us to reach this limit observed experimentally. Therefore, the precession equation must include a damping term that makes the magnetization align with the field, this is also known as the Gilbert damping parameter [94]. The simplest way to introduce this damping term in Eq. (2.29) is to replace the magnetic field, **H**, by an effective magnetic field including the dissipation term:

$$\mathbf{H}_{\text{eff}} = \mathbf{H} - \alpha \frac{1}{\gamma_0 m_s} \frac{d\mathbf{m}}{dt}, \tag{2.30}$$

where m_s is the saturation magnetization and α is the phenomenological damping parameter. Substituting Eq. (2.30) into (2.29) we find that

$$\frac{d\mathbf{m}(t)}{dt} = -\gamma_0[\mathbf{m}(t) \times \mathbf{H}(t)] + \frac{\alpha}{m_s}\left[\mathbf{m}(t) \times \frac{d\mathbf{m}(t)}{dt}\right]. \tag{2.31}$$

The Eq. (2.31) is known as the Landau-Lifshitz-Gilbert (LLG) equation. The damping effect on the magnetization is illustrated in Fig. 2.7 (b). As time evolves, the magnetization

spirals around the applied magnetic field until it becomes completely align with the external field. All torques acting on **m** vanishes.

Figure 2.7 – Sketch of the time evolution of the magnetic dipole moment (a) in the presence of an applied magnetic field and (b) when the damping term is included (Adapted from M. Lashmanam 2011, pg. 1283).

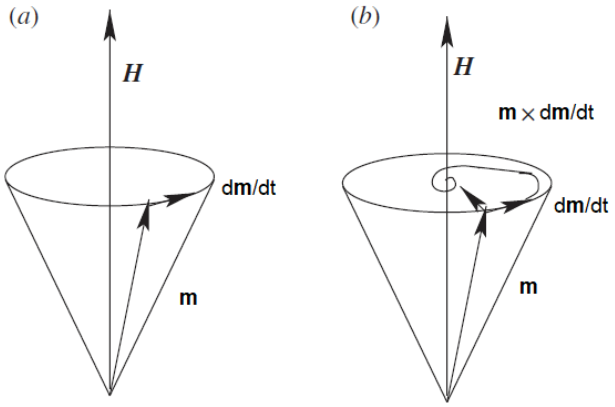

Using dimensionless variables $\tau = \gamma_0 m_s t$, $\mathbf{n} = \mathbf{m}/m_s$, $\mathbf{h} = \mathbf{H}/m_s$ and rearranging terms, the LLG can also be written as:

$$(1+\alpha^2)\frac{d\mathbf{n}(t)}{d\tau} = -[\mathbf{n}(t)\times\mathbf{h}(t)] - \alpha\{\mathbf{n}(t)\times[\mathbf{n}(t)\times\mathbf{h}(t)]\}. \qquad (2.32)$$

This LLG equation is capable to simulate several spin structures inside ferromagnets, like bubbles, domain walls, skyrmions, and others. However, when we are interested to simulate the dynamic and collective behavior of many skyrmions in large samples, a simulation using the LLG equation requires a high computational demand, since it calculates the time evolution of each individual local magnetic moment. So, if you are interested in simulating systems with multiple skyrmions in large samples, where each skyrmion has several numbers of local magnetic moments, a different approach using some approximations may be useful.

2.3 The Particle Model

2.3.1 Equation of Motion

Recently, a new method was developed to calculate the skyrmion dynamics in chiral magnets [73]. The model considers skyrmions as rigid point-like objects, which simplifies significantly the dynamics and also reduces the computational cost for these simulations. The particle model considers the Thiele approximation [72], used to describe the dynamics of magnetic solitons. In order to obtain a simplified expression of the equation of motion, the model considers a thin film of a chiral magnet with Dzyaloshinskii-Moriya (DM) interaction

that supports skyrmions. Magnetic moments are described by the vector $\mathbf{n}(\mathbf{r})$. Thus, starting from an action functional for magnetic moments, which can be written as [73,95],

$$S = S_B - \frac{d\alpha_g}{\gamma}\int dtdt'd^2r\left[\frac{\mathbf{n}(t)-\mathbf{n}(t')}{t-t'}\right]^2 - \int dt\mathcal{H} \tag{2.33}$$

$$S_B = d\int d^2rdtz^\dagger\, i\left(\frac{1}{\gamma}\partial_t - \frac{\hbar}{2e}\mathbf{J}\cdot\boldsymbol{\nabla}\right)z \tag{2.34}$$

where $z \equiv |z\rangle$ is the coherent spin state defined as $\mathbf{n}\cdot\sigma|z\rangle = |z\rangle$. The Pauli matrices has the vector represent by σ, d is the thickness of the thin film, α_g is the Gilbert damping term and $\gamma = a^3/\hbar s$, with a being the lattice constant and s the total spin. The first term, S_B, corresponds to the Berry phase [96] for the spin precession in $\mathbf{r} = (x, y)$. In a few words, the Berry phase, also known as geometric phase, is a phase difference acquired over the course of a cycle. In the first term of S_B in Eq. (2.34), the conducting electrons, provided by the external applied current **J**, become polarized by the local magnetic moments **n** (See Fig. 2.8). The second term of S_B is responsible for the Berry phase that the electron acquires when passing through a skyrmion and interacting with the internal local magnetic moments of the skyrmion.

Figure 2.8 – Schematic representation of electrons (yellow spheres with an arrow) passing through a skyrmion (colorful arrows). The spin of the electron follows the spin texture of the skyrmion as it passes through the skyrmion. The black arrows (or dots) are spin projection in the $x-y$ plane, and the spins in the ferromagnetic state are along the z axis (mostly in red). (Adapted from Lin, *et. al*. (2013), page 214419-2).

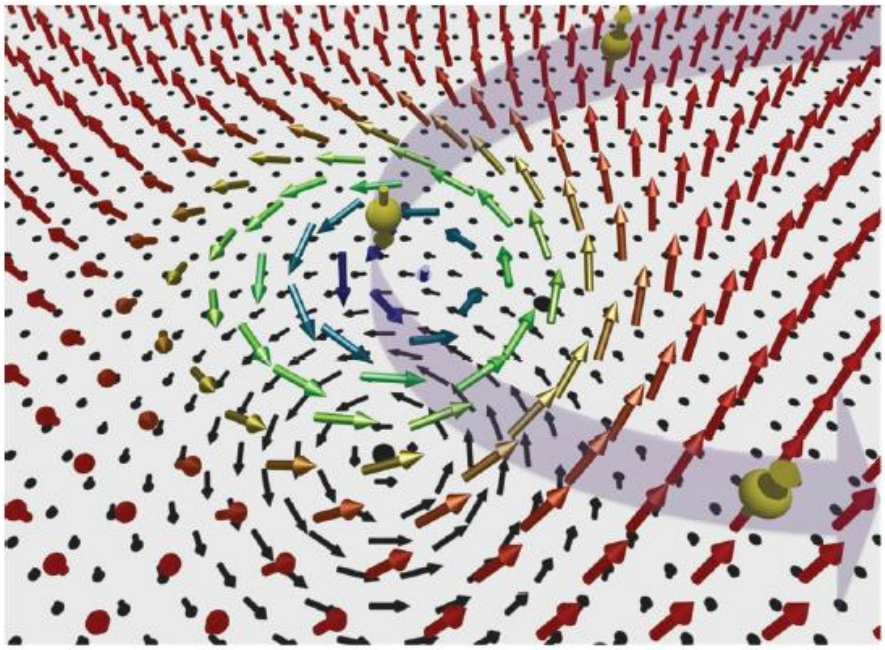

The spin Hamiltonian, $\mathcal{H}$ is given by [73,95]:

$$\mathcal{H} = d\int d\mathbf{r}^2 \left[\frac{J_{ex}}{2}(\nabla\mathbf{n})^2 + D\mathbf{n}\cdot\nabla\times\mathbf{n} - \mathbf{H}_a\cdot\mathbf{n}\right]. \tag{2.35}$$

In this Hamiltonian the first term is the Heisenberg exchange interaction, the second term is DM and the third is the Zeeman energy, where $\mathbf{H}_a$ is the external magnetic field, which is normal to the film surface. Skyrmions are present in systems that follow Eq. (2.35) when the magnetic field has values $0.2D^2/J < H_a < 0.8D^2/J$ [62].

According to expressions in Eq. (2.34) and (2.35), the spin dynamics is governed by the Landau-Lifshitz-Gilbert (LLG) equation as [29,97]:

$$\partial_t\mathbf{n} = \frac{\hbar\gamma}{2e}(\mathbf{J}\cdot\nabla)\mathbf{n} - \gamma\mathbf{n}\times\mathbf{H}_{eff} + \alpha_g\partial_t\mathbf{n}\times\mathbf{n} \tag{2.36}$$

Note that Eq. (2.36) is similar to Eq. (2.32) from previous section where we describe the LLG equation, however, in the present case the interaction with the conducting electrons from the applied transport current, **J**, is added. The effective field is given by $\mathbf{H}_{eff} \equiv \delta\mathcal{H}/\delta\mathbf{n}$. In metallic chiral magnets, skyrmion motion gives rise to electric fields, therefore inducing a dissipating current $\mathbf{J}_{diss} = \sigma\hbar[\mathbf{n}\cdot(\nabla\mathbf{n}\times\partial_t\mathbf{n})]/2e$, where σ is the conductivity [98]. In insulating materials, the dissipating current is null, because $\sigma = 0$. Thus, the current density in Eq. (2.36) is given by $\mathbf{J} = \mathbf{J}_B + \mathbf{J}_{diss}$, where $\mathbf{J}_B$ is the external applied current.

2.3.2 Considerations for the Particle Model

The expressions shown in Eq. (2.33) to (2.36) are sufficient to describe the skyrmion motion in chiral magnets, including their internal deformations due to the application of the external current, interaction with other skyrmions or possible obstacles. On the other hand, it is also possible to derive a particle model in which the internal deformations are small enough, that is, it is assumed a rigid internal structure. Furthermore, it is also necessary to consider that the skyrmion density is sufficiently low so that there is no superposition of skyrmion spin textures. In this case, spins precess collectively when a rigid skyrmion moves with velocity **v**. The internal structure of the skyrmion becomes irrelevant under these circumstances, which are satisfied in the low velocity regime for certain magnetic fields [75,98]. Hence, the spin magnetic moments can be described as $\mathbf{n}_s(\mathbf{r} - \mathbf{v}t)$, and its evolution is governed by the LLG equation

$$\partial_t\mathbf{n}_s = \frac{\hbar\gamma}{2e}(\mathbf{J}\cdot\nabla)\mathbf{n}_s - \gamma\mathbf{n}_s\times\mathbf{H}_i + \alpha_g\partial_t\mathbf{n}_s\times\mathbf{n}_s. \tag{2.37}$$

Here, $\mathbf{H}_i = \mathbf{H}_s + \mathbf{H}_d$, with $\mathbf{H}_s$ as the magnetic field produced by other skyrmions, and $\mathbf{H}_d$ the magnetic field produced by the defects in the sample. The effective field $\mathbf{H}_{eff} = \delta\mathcal{H}/\delta\mathbf{n}_s$ due to the skyrmion $\mathbf{n}_s$ does not contribute to $\mathbf{H}_i$, because $\mathbf{H}_{eff} \times \mathbf{n}_s = 0$ for a rigid skyrmion. If both sides of Eq. (2.37) are multiplied by $\times\, \mathbf{n}_s$, then by $\cdot\, \partial_\mu \mathbf{n}_s$ and integrate over the skyrmion area, we find that

$$\alpha \mathbf{v} = \frac{\gamma}{4\pi}\left[\mathbf{F}_M + \mathbf{F}_D + \int dr^2 \mathbf{H}_\perp(\mathbf{r}-\mathbf{r}') \cdot \nabla_r \mathbf{n}_s(\mathbf{r})\right], \tag{2.38}$$

where $\mathbf{H}_\perp$ is the component of the magnetic field which is perpendicular to $\mathbf{n}_s$ and using $\int dr^2 \partial_x \mathbf{n}_s \cdot \partial_y \mathbf{n}_s = 0$ for a rigid skyrmion. The potential of the interaction between a skyrmion in $\mathbf{r}$ and another skyrmion in $\mathbf{r}'$ is

$$U_{ss}(\mathbf{r}-\mathbf{r}') = -\int dr''^2 \mathbf{n}_s(\mathbf{r}-\mathbf{r}'') \cdot \mathbf{H}_s(\mathbf{r}'-\mathbf{r}''), \tag{2.39}$$

and the corresponding force is

$$\mathbf{F}_{ss} = -\nabla U_{ss} = \int dr''^2 \nabla_r \mathbf{n}_s(\mathbf{r}-\mathbf{r}'') \cdot \mathbf{H}_{s,\perp}(\mathbf{r}'-\mathbf{r}''). \tag{2.40}$$

The self-energy of the skyrmion in the presence of defects is given by

$$E_s(\mathbf{r}-\mathbf{r}') = -\int dr''^2 \mathbf{n}_s(\mathbf{r}-\mathbf{r}'') \cdot \mathbf{H}_d(\mathbf{r}'-\mathbf{r}''), \tag{2.41}$$

where $\mathbf{H}_d(\mathbf{r}) = J_{ex}(\mathbf{r})\nabla^2 \mathbf{n}_s/2 - D(\mathbf{r})\nabla \times \mathbf{n}_s + \mathbf{B}$. Thus, the corresponding pinning force is

$$\mathbf{F}_d = -\nabla \mathrm{E}_s = \int dr''^2 \nabla \mathbf{n}_s(\mathbf{r}-\mathbf{r}'') \cdot \mathbf{H}_{d,\perp}(\mathbf{r}'-\mathbf{r}''). \tag{2.42}$$

Hence Eq. (2.38) can be reduced if we substitute the integral by the corresponding forces shown in Eq. (2.41) and (2.42), as shown in Eq. (2.43).

$$\frac{4\pi\alpha}{\gamma}\, \mathbf{v}_i = \mathbf{F}_M + \mathbf{F}_D + \sum_j \mathbf{F}_{ss}(\mathbf{r}_j - \mathbf{r}_i) + \sum_j \mathbf{F}_d(\mathbf{r}_j - \mathbf{r}_i) \tag{2.43}$$

where $\mathbf{v}_i$ is the velocity of the ith skyrmion, the term on the left is related to the damping due to the precession of the spin and due to the conducting electrons present in the skyrmion core. The driving force $\mathbf{F}_D = 2\pi\hbar e^{-1}\hat{\mathbf{z}} \times \mathbf{J}$ that acts on the skyrmion due to the presence of the spin polarized current. $\mathbf{F}_M = 4\pi\gamma^{-1}\hat{\mathbf{z}} \times \mathbf{v}_\mathrm{i}$ is the Magnus force per unit length, and it is perpendicular

to $\mathbf{F}_D$. $\mathbf{F}_d$ is the force between skyrmions and the defects present in the sample. $\mathbf{F}_{ss}$ is the force between a pair of skyrmions. In the case of thin films, skyrmions are always straight in the direction normal to film surface and all forces are defined by unit of length.

Throughout this work we consider the adiabatic spin transfer torque described in the form of $\hbar\gamma(\mathbf{J}\cdot\nabla)\mathbf{n}/(2e)$ in Eq. (2.37). In some cases it may also exist a nonadiabatic spin transfer torque given by the expression $-\zeta\hbar\gamma\mathbf{n}\times(\mathbf{J}\cdot\nabla)\mathbf{n}/(2e)$ [99]. If this is the case, the expression Eq. (2.43) may be adjusted by introducing the nonadiabatic term $\mathbf{F}_{non} = 2\pi\hbar\zeta\eta e^{-1}\mathbf{J}_B$, where $\mathbf{J}_B$ is the applied external current. Thus, the particle-model with nonadiabatic spins transfor torque becomes:

$$\frac{4\pi\alpha}{\gamma}\mathbf{v}_i = \mathbf{F}_M + \mathbf{F}_D + \mathbf{F}_{non} + \sum_j \mathbf{F}_{ss}(\mathbf{r}_j - \mathbf{r}_i) + \sum_j \mathbf{F}_d(\mathbf{r}_j - \mathbf{r}_i) \tag{2.44}$$

2.3.3 Interaction between Skyrmions and interaction with Defects

In order to calculate the interaction between skyrmions and defects, first it is necessary to comprehend the skyrmion structure. An isolated skyrmion is described as $\mathbf{n}_s(r,\phi) = \sin\theta\,\hat{\phi} + \cos\theta\,\hat{z}$ in polar coordinates, with $\hat{\phi}$ and $\hat{z}$ as the unit vectors [73,100]. The function $\theta(r)$ below [Eq. (2.45)] is determined minimizing the Hamiltonian $\mathcal{H}$ from Eq. (2.35), using the boundary conditions $\theta(r=0)=\pi$ and $\theta(r\to\infty)=0$. The distances r are renormalized to $r\to r/(J_{ex}/D)$, and $\beta = 2H_aJ_{ex}/D^2$. The profile of $\theta(r)$ is illustrated in Fig. 2.9.

$$-r\partial_r^2\theta - \partial_r\theta + \cos(2\theta) + \frac{\sin(2\theta)}{2r} + \frac{\beta}{2}r\sin\theta - 1 = 0 \tag{2.45}$$

Figure 2.9 – Profile of $\theta(r)$ obtained through a numerical solution of Eq. (2.45) for different values of applied magnetic field. (From Lin, *et. al.* (2013), page 214419-4)

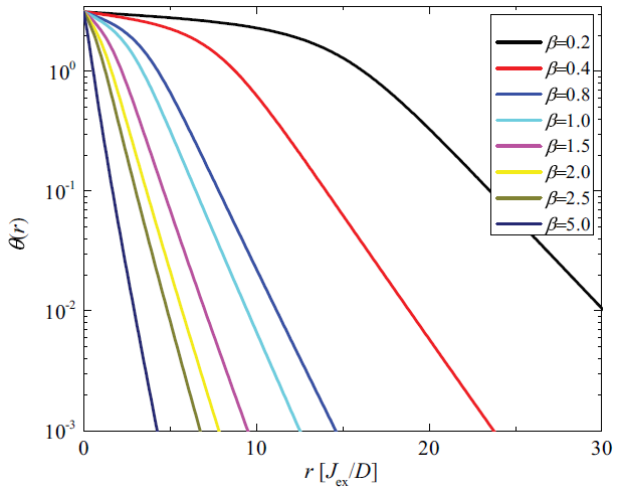

There are two scales related to the skyrmion, θ decreases exponentially with r for values in which $r \ll 1$, meanwhile the asymptotic solution far from the skyrmion center, $r \to \infty$ is $\theta \sim K_0(r/\xi)$, where ξ is the skyrmion core radius.

The interaction between skyrmions is the result of the overlapping of spins textures. When skyrmions are far apart, the interaction is mediated by and exchange of massive magnons. In this linear region the skyrmion interaction is pairwise. As can be seen in Fig. 2.10, the interaction decays exponentially with r_d and can be well described by $F_{ss} \sim K_1(r_d/\xi)$. When the separation between skyrmions is reduced so that the distance is comparable to the size of the skyrmion itself, the interaction is induced by the overlapping of the nonlinear cores. In this situation, the interaction is nonlinear, and in principle, there is many-body interaction between skyrmions. To calculate the interaction among skyrmions at an arbitrary distance, it was calculated the energy of the system by fixing two skyrmions at a separation r_d by freezing the spins within radius $r_d \leq J_{ex}/D$. As can be seen in Fig. 2.10, the interaction among skyrmions is repulsive.

Figure 2.10 – Force between two skyrmions as a function of the distance between them, r_d, using two different applied magnetic fields. The dots of both curves, represented as black triangles and red circles, are obtained through a numerical solution of Eq. (2.37) and the lines are the fit using $K_1(r_d/\xi)$. In the inset there is a static skyrmion configuration at a distance of $r_d = 3.6 J_{ex}/D$. The vectors show n_x and n_y and the color scale shows n_z. (From Lin, *et. al*. (2013), page 214419-4)

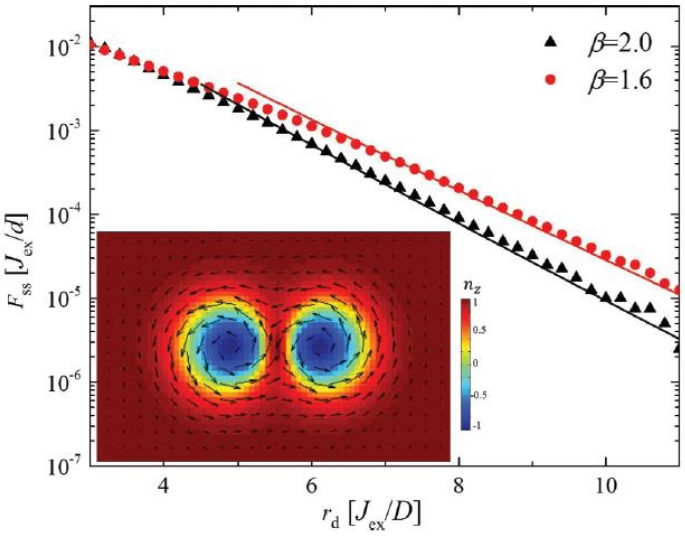

Next, we consider the case where skyrmions interact with defects present in inhomogeneous samples. Thus, we assume an inhomogeneous electron density, which gives rise to an inhomogeneous exchange interaction J_{ex} produced by the double-exchange mechanism. The defect is modeled following the profile of J_{ex} [73,100]:

$$J_{ex}(r) = J_0\left(1 + \sum_i J_d \exp\left[-\frac{|\mathbf{r} - \mathbf{r}_{d,i}|}{\xi_d}\right]\right), \tag{2.46}$$

where ξ_d is the size of the defect and it is comparable to the interatomic separation. The distance between the skyrmion and the center of the pinning potential is given by $|\mathbf{r} - \mathbf{r}_{d,i}|$, and J_d represents the strength of the defects. Normally, skyrmion in the presence of pinning may deform to adapt to the pinning potential. For weak pinning case, this deformation is very small and we can still use the approximation of a rigid-body skyrmion. Thus, the pinning energy is the self-energy of skyrmion [See Eq. (2.41)] using $J_{ex}(r)$ described in (2.46). It was used two methods to calculate the pinning energy of a skyrmion. First, it was obtained a stationary skyrmion structure from Eq. (2.46) by using a uniform distribution of $J_{ex}(r)$, that is, $J_d = 0$. Then, calculated the self-energy of a skyrmion using $J_{ex}(r)$ by holding the spin at the center of the skyrmion fixed in order to pin the skyrmion at a desired location. Both results are in a good agreement with each other (see Fig. 2.11). The pinning for large separation can be fitted by $F_d \sim J_d \exp(-r_d/\xi_d)$. The results show that the force is repulsive for $J_d > 0$ and attractive for $J_d < 0$. The pinning force decreases exponentially with the decay length determined by ξ_d. The nonuniformity of the electron density in real solids is of the order of interatomic length, $\xi_d \sim 0.1$ nm, that is much smaller than the size of a typical skyrmion. Thus, the interaction of pinning centers and skyrmions is very weak.

Figure 2.11 – The force between a skyrmion and a defect for different size and strength of the defect. Lines are results obtained by numerical solutions of Eq. (2.35) and (2.36). The symbols are results assuming the skyrmion to have a rigid internal structure. (From Lin, *et. al.* (2013), page 214419-4)

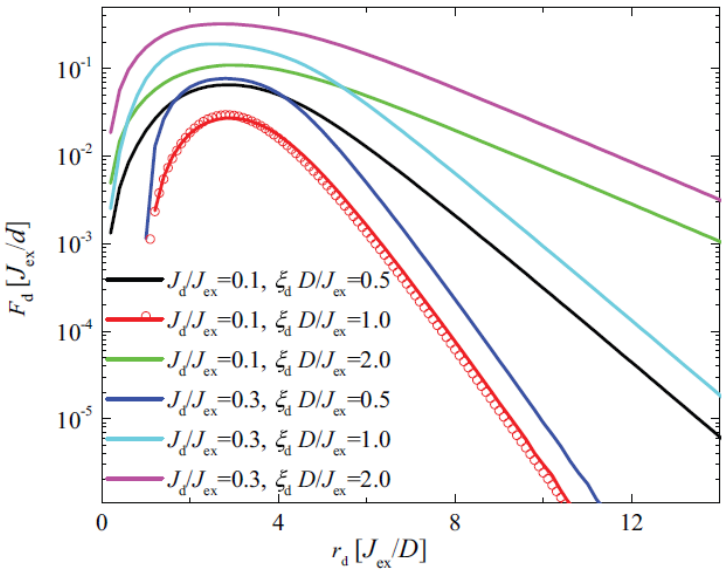

In most of this work we consider the particle model of Eq. (2.44) to simulate the skyrmion dynamical behavior in chiral magnets thin films. We focus on cases where there is a single, or multiple skyrmions in a sample with periodic arrays of obstacles. Further details will be discussed in the Model section.

2.4 Skyrmion Dynamics

One of the most interesting aspects of skyrmions is that they can be moved through the application of an external transport current, moreover, this process has low energy cost comparable to magnetic domain walls, for example. The skyrmion lattice motion was observed in very early experiments. In 2010, Jonietz et. al. [10] detected a current-induced rotation of the skyrmion lattice in MnSi, and in 2012 it was observed a current-induced flow regime of skyrmions in FeGe [68]. A general feature that can be observed in the skyrmion motion is the coexistence of a longitudinal motion (which follows the direction of the applied drive) and a transverse motion due to gyroscopic forces induced by the skyrmion topology. As shown in Fig. 2.12 (a), in the transient regime (where $T < 0.1\text{ns}$) the skyrmion exhibits both components, the longitudinal and tranversal motion [8,101]. However, as this sample is a nanotrack, the transversal motion [also known skyrmion Hall effect (SHE)] is counterposed by the skyrmion-edge interaction, which is repulsive. As a result, the skyrmion keeps on track and has only longitudinal motion and the velocity depends on the applied current density. The direction of the longitudinal motion depends both on the chirality of the skyrmion and on the sign of the spin Hall angle in the metal. The deflection of the skyrmion in the transverse direction depends on the polarization in the skyrmion center (up or down). In the nanotracks as shown in Fig. 2.12 (a) the skyrmion can only be on track if the applied current densities are sufficiently low. If higher currents are applied, the skyrmion can reach the edge, slide along it and be expelled [8,101].

The current-induced motion of skyrmions can be well described using the Thiele equation for magnetic solitons [72]:

$$\mathbf{F} + \mathbf{G} \times \mathbf{v} + \alpha D \mathbf{v} = 0, \tag{2.47}$$

where **F** is the force exerted by the spin Hall effect, **G** is the gyrovector oriented along the out-of-plane direction and proportional to the skyrmion number, **v** is the velocity of the soliton, α is the damping parameter, and D is the dissipative tensor that can be calculated following the skyrmion parameters [71,72,101,102]. Following the Thiele's approach, the skyrmion Hall effect (SHE) induced longitudinal (v_x) and transversal (v_y) can be expressed as:

$$v_x = \frac{\delta}{1+\delta^2}\frac{\mathbf{F}}{G_z}, \tag{2.48}$$

$$v_y = \frac{1}{1+\delta^2}\frac{\mathbf{F}}{G_z}, \tag{2.49}$$

$$\theta_{SHE} = \operatorname{atan}\left(\left|\frac{v_y}{v_x}\right|\right) = \operatorname{atan}\left(\frac{1}{\delta}\right). \tag{2.50}$$

Where $\delta = \alpha D_{xx}/G_z$. The most important features of the skyrmion motion can be derived using the Thiele's approach. Another interesting feature is the skyrmion dynamics as a function of the skyrmion size. The skyrmion radius ξ is defined as the radius of the circle with zero out-of-plane magnetization. If ξ is considerably larger than Δ, where $\Delta = \sqrt{A/K}$, A is the exchange stiffness and K is the out-of-plane anisotropy, the resulting dependence of the skyrmion Hall angle and the longitudinal and transverse velocities on ξ and α can be seen in Fig. 2.12 (b). Note that in the present thesis, we use the particle-model for skyrmion, in which skyrmions are considered point-like objects, thus in our case here it is considered low values of ξ/Δ.

Figure 2.12 – (a) The skyrmion motion in a nanotrack. Initially in the transient regime the skyrmion moves with both transverse and longitudinal velocities, then the trajectory is bended due to the repulsion of the sample edge. (From Sampaio *et. al*. (2013), page 842). (b) The skyrmion Hall angle, θ_{SH}, versus the skyrmion size ξ/Δ. (Adapted from Fert *et. al.* (2017), pg. 8).

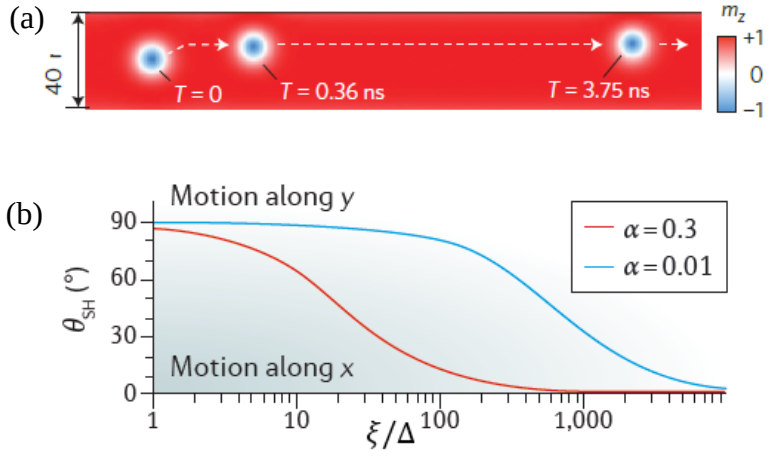

One of the first and more important works concerning skyrmion dynamics and interaction with randomly placed defects in the sample was done by Iwasaki *et. al.* in 2013 [29]. One of the main results in this work was the discovery of a universal current-velocity relation and understanding the details of skyrmion deformation and shape adjustment as it moves through the sample. Using the LLG equation, Iwasaki *et. al.* calculated the current-velocity curves for both spins textures phases, the helical phase (HL) and also the skyrmion crystal phase

(SkX). In Fig. 2.13 it is shown the average velocities, $v_{\parallel}$, parallel to the applied current density, **j**, as function of the current density magnitude j for both HL and SkX phases with different values of β. The average velocities of the skyrmion lattice and the helical domains are calculated using emergent electric fields. β is a parameter in the LLG equation that describes the coupling between spin-polarized current and local magnetic moments due to non-adiabatic effects. As can be seen clearly, the SkX phase has a universal current-velocity curve. Meanwhile, the helical phase exhibit very different behaviors according to the parameters used, which is similar to the case ferromagnetic domain walls [103].

Figure 2.13 – Current-velocity curves, $v_{\parallel}$ vs. j, for the helical (HL) and skyrmion crystal (SkX) phases. The clean case is when $x = 0$, where x is the impurity concentration. The dirty case when $x = 0.1\%$. Lines for the SkX phase are all the same, while for HL phase it greatly depends on the parameters (From Iwasaki *et. al.* (2013), pg 3).

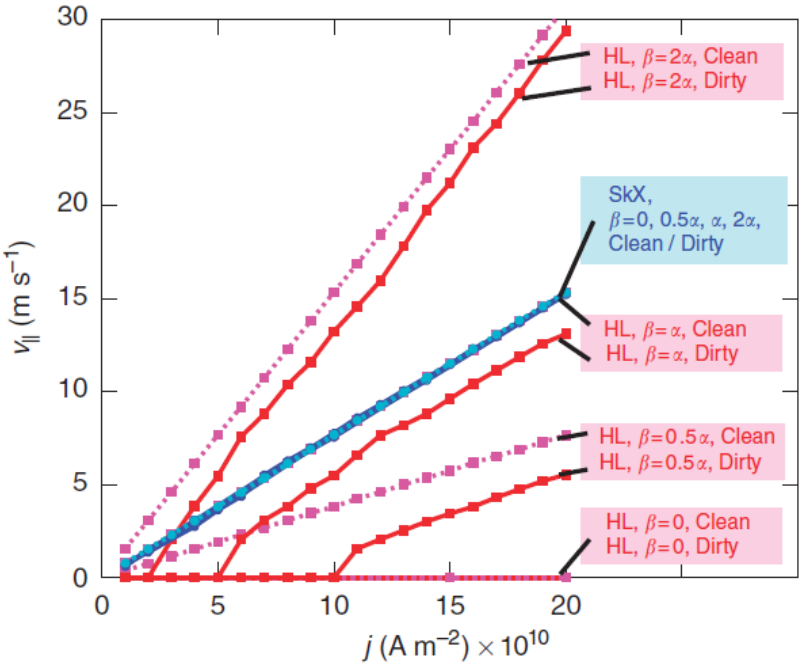

The effects of impurities in the system are also considered and can also be seen in Fig. 2.13. In Fig. 2.14 the effects of the impurities can be clearly seen in the spin textures of the sample, where snapshots of magnetizations in the moving HL (a,b) and SkX (c,d,e) phases can be seen. The impurity positions are marked as green dots. In the HL case, due to the line-shaped spin arrangements the impurities can never be avoided, so the impurities always act on the HL dynamics, distorting its shape. The motion of the skyrmion crystal phase is completely different. Skyrmions can avoid being trapped by the impurities. Skyrmions can distort their triangular arrangement and also modify individually their shape for smoother motion. This may allow small fluctuations in the collective skyrmion velocity, but it is much reduced when compared to the helical phase bumping in all impurities.

Figure 2.14 – Snapshots of magnetizations profile for select cases. (a) Helical phase (HL) with $t = 4.55 \times 10^{-8}$s. (b) HL with $t = 4.87 \times 10^{-8}$s. (c) Skyrmion crystal (SkX) with $t = 1.30 \times 10^{-8}$s. (d) SkX with $t = 2.60 \times 10^{-8}$s. (e) SkX with $t = 4.87 \times 10^{-8}$s. In (f) a magnified view of (d) where the skyrmion distortion passing through the impurities can be seen. (From Iwasaki *et. al.* (2013), pg 3).

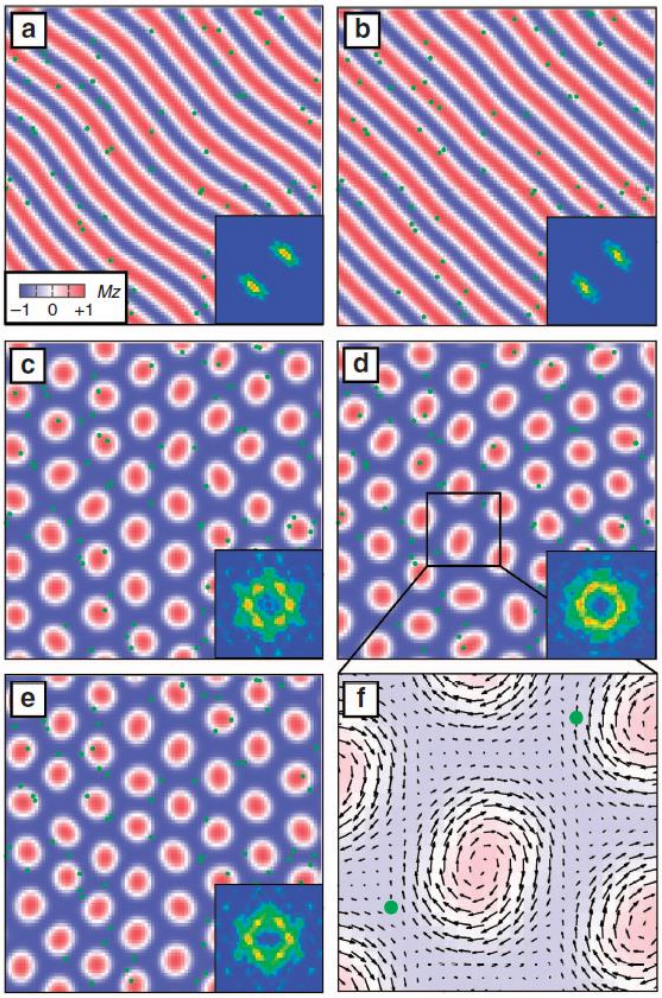

Since then, many researches have been conducted trying to further understand the skyrmion dynamics and also searching for possible ways to control the skyrmion motion in the sample. There are many different ideas on how to address skyrmion motion, some of them try to control using magnons or temperature gradients [104–106], strain gradients [107], magnetic field gradients [108,109], ferromagnetic-superconductor heterostructure [110], but most of them focus on the sample interface [71,101,111], using pinning center arrays [39,40,64,77,112–114] or periodic substrates [32–34]. This thesis aims to collaborate on the understanding of skyrmion dynamics and control using periodic pinning, hence, in the next section we review some important results of skyrmion dynamics using pinning centers.

3 Skyrmions Interacting with Substrates: A Review

In this section we aim to review some important results concerning skyrmions interacting with pinning centers. The idea to use pinning centers as an effective way to control skyrmions has its origins on previous works that investigated particles interacting with pinning centers, like colloids [13,115] and superconducting vortices [116–120]. The main difference is that in the case of skyrmions there is a strong Magnus component that modifies significantly the dynamics, thus new dynamic studies were necessary.

3.1 Skyrmions with Random Disorder

One of the first works to address skyrmions interacting with random disorder was made to examine the static and driven phases of skyrmions [26]. It was shown that the depinning threshold is reduced due to the Magnus term. Moreover, the skyrmion hall angle is dependent to the external drive.

Using the particle model described in section 2.3 it was calculated the force curves for this system. In the particle-model, the force curves are analogous to the current-velocity curves found with LLG model and in experiments [29,102,121]. As an illustration of the skyrmion motion in random disorder, Fig. 3.1 shows the skyrmion trajectory while moving through the disorder using a pinning force of $F_P = 0.03$ and driving force $F_D = 0.0125$ [26]. Note that due to the strong Magnus component, the skyrmion exhibit a series of spiral and curvy motion. In systems where the Magnus force is negligible, the particle moves almost directly to the center of the pin and remains trapped, however, for skyrmions with strong Magnus components they may circle around the inner edge of the pin.

Figure 3.1 –Illustration of skyrmion (red circles) and the pinning centers randomly placed (blue circles). The black line is a selected skyrmion trajectory as it moves through the sample and interact with pinning centers. (From Reichhardt *et. al*. (2015), pg 217202-2 [26]).

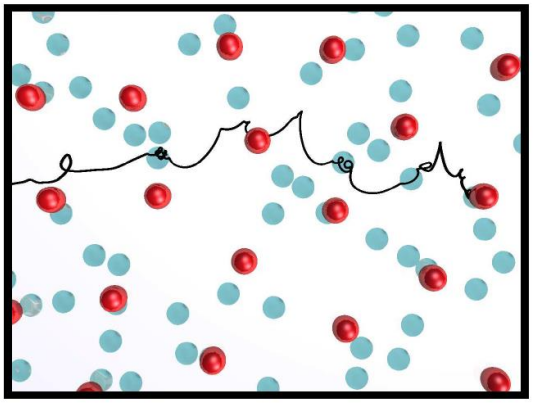

In Fig. 3.2 it is shown how the skyrmion hall angle is affected by the random pinning. In Fig. 3.2 (a) it is plotted the skyrmion average velocity along the drive direction, $\langle V_{drive} \rangle$, and the transversal velocity component, $\langle V_{\perp} \rangle$ as a function of the applied drive, F_D. For very low drives, $F_D < 0.00625$ the skyrmions are disordered and trapped in the pinning sites. Just above the depinning, $\langle V_{drive} \rangle \approx \langle V_{\perp} \rangle$, so that the skyrmion Hall angle is about $\theta_{sk} = 45°$, which is much less than the clean-limit value. The clean-limit value is the intrinsic skyrmion Hall angle $\left(\theta_{sk}^{int}\right)$, that is, the angle that the skyrmion would move respective to the applied drive if there were no impurities in the sample. For this particular system, $\theta_{sk}^{int} = 84.25°$ in the clean-limit.

Figure 3.2 – (a) $\langle V_{drive} \rangle$ and $\langle V_{\perp} \rangle$ as a function of the external drive F_D. Inset: Skyrmion Hall angle, θ_{sk} vs. F_D. (b) Corresponding $\langle V_{drive} \rangle$ and the fraction of sixfold coordinate particles P_6 vs. F_D. (From Reichhardt *et. al.* (2015), pg 217202-3 [26]).

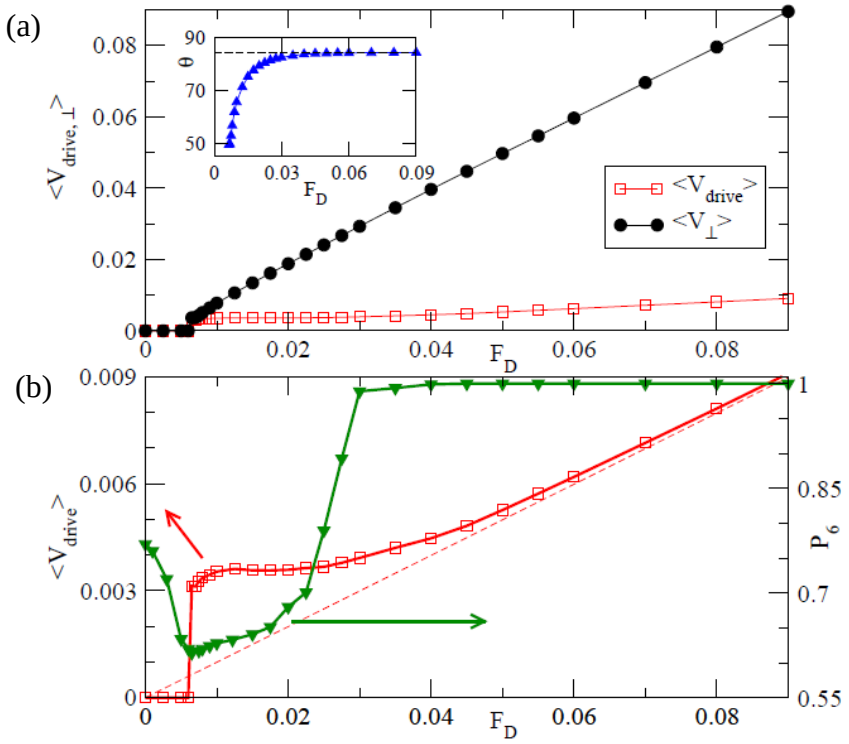

As the applied drive is increased, $\langle V_{drive} \rangle$ decreases and $\langle V_{\perp} \rangle$ increases, so that the skyrmion Hall angle approaches the clean-limit value, as can be seen in the inset of Fig. 3.2 (a). In this high drive regime, skyrmions reorder into a moving crystal phase. In Fig. 3.2 (b) it is plotted the fraction of sixfold coordinate particles, P_6, as a function of the drive F_D. The P_6 is a measurement that helps looking for order in an arrangement of particles, if $P_6 = 1$ the particles are perfectly ordered in a hexagonal lattice. As can be seen in Fig. 3.2 (b), P_6 reaches its lowest level near the depinning of skyrmions, when they are most disordered. However, it reaches $P_6 = 1$ very quickly around $F_D \cong 0.03$, indicating the dynamical reordering.

Concerning the skyrmion dynamic phases in random disorder, in Fig. 3.3 it is plotted a dynamical phase diagram highlighting static and dynamic phases as F_D and F_P is varied. The pinning force is very important for this system. In the weak pinning regime, skyrmions form a pinned triangular crystal (PC) which depins elastically to a moving crystal phase (MC) for increasing F_D. However, if the pinning force is increased skyrmion may form an amorphous pinned skyrmion glass (PG) which depins plastically into a fluctuating moving skyrmion liquid (ML). The lower inset of Fig. 3.3 shows the structure factor $S(\mathbf{k}) = N_s^{-1}\left|\sum_{i=1}^{N_s} e^{-i\mathbf{k}\cdot\mathbf{r}_i}\right|^2$ for the ML phase, where N_s is the number of skyrmions. As the external drive, F_D, increases the skyrmion dynamically reorder into the moving crystal with sixfold ordering, as illustrated by the superior inset of Fig. 3.3. The phase diagram is very similar to the superconducting vortex case in random disorder [122], however skyrmions rearrange themselves into a moving crystal phase, and vortices rearrange into a smectic phase. In the skyrmion case, additional fluctuations terms due to the Magnus term reduces the transverse pinning, allowing the skyrmions to form a more isotropic moving structure [26].

Figure 3.3 – The dynamical phase diagram of F_D vs. F_P highlighting the different static and moving phases. PC is pinned crystal, PG is pinned amorphous glass, ML is moving liquid and MC is moving crystal. Circles represent elastic depinning from PC to MC; squares represent plastic depinning from PG to ML; triangles are dynamical ordering from ML to MC. Upper inset is structure factor for skyrmion positions in the MC phase and lower inset is the structure factor for the ML phase. (From Reichhardt *et. al.* (2015), pg 217202-3 [26]).

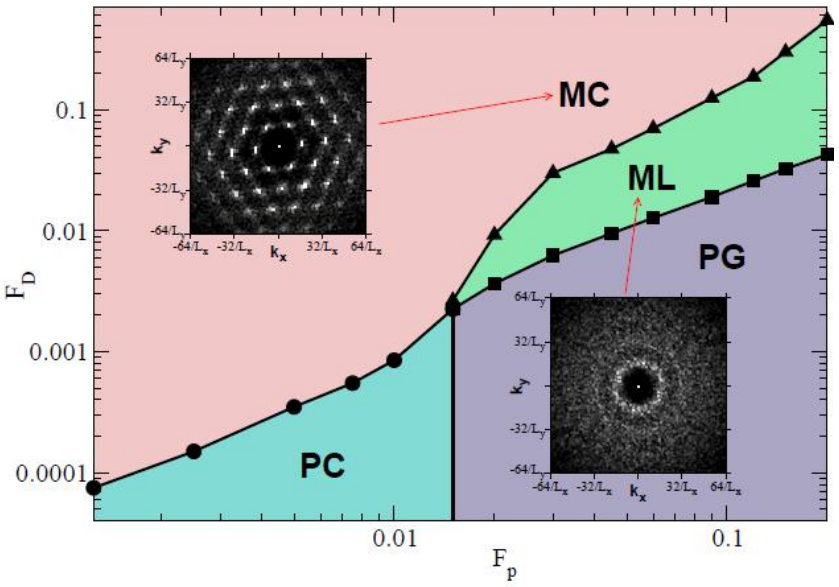

Experimental observations of plastic flow as a function of the external drive have been made recently with direct imaging for room temperature skyrmion in thin films [123]. The skyrmion trajectories show a mix of moving skyrmions and some pinned skyrmions along with

some channels or rivers in which skyrmions flow nicely. In Fig. 3.4 it is shown the real image and some processed images of the skyrmion motion. Interestingly the skyrmion motion in these images are slightly similar to what was observed experimentally in superconducting vortices near the depinning transition in random substrates [124]. As the tracking of individual skyrmion is difficult using static images of before and after a pulse of current, the authors decided to process the image for a better visualization. In Fig. 3.4 (b) is the processed image of 3.4 (a), where the white regions are skyrmions. Figs. 3.4 (c) – (f) show the main motion that results after 4 pulses of current, where the pinned skyrmions are white regions, and the purple regions the channels of motion.

Figure 3.4 – Current induced motion of dipole skyrmions in room temperature experiments with Ta (5 nm)/[Fe (0.34 nm)/Gd (0.4 nm)] × 100/Pt (3 nm). (a) Raw image of x-ray microscopy of a closed-pack skyrmion lattice. (b) Processed image where the white regions represent the skyrmions. (c,d,e,f) processed images of the skyrmion lattice after 4 pulses of applied current, the white regions represent the pinned skyrmions and the purple are the riverlike motion of skyrmions. (From Montoya *et. al.* (2018), pg 104432-5 [123]).

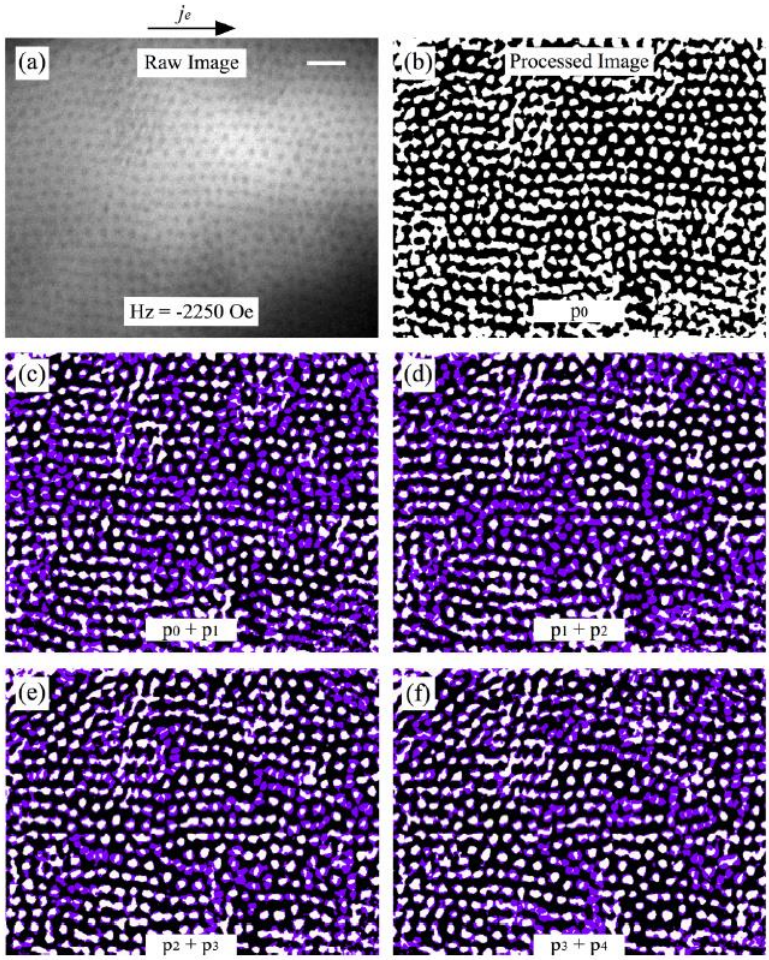

Both experimental and theoretical results show very clearly that skyrmion motion in random disorder may exhibit plastic flow. Moreover, in theoretical results, for higher applied

drives it can reorder into a moving crystal phase. Another interesting feature is that in the presence of random pinning skyrmion may have different skyrmion Hall angles depending on the applied drive. This opened the first insights on how the skyrmion behaves under the influence of pinning.

3.2 Skyrmions in Periodic Substrates

When a periodic array of pinning centers is used, new type of phenomena emerges from the skyrmion dynamics. In this section we are going to discuss some previous important results concerning skyrmions with periodic pinning. One of the first works was made by Reichhardt *et. al*. [39] that considered a single skyrmion interacting with a square array of obstacles. Obstacles are repulsive potentials to skyrmions. Due to the periodic array of defects, the skyrmion Hall angle exhibit quantized values as a function of the applied external drive. Moreover, for a square array the quantized angles follow the rule $\theta_{sk} = \operatorname{atan}\left(\frac{n}{m}\right)$, where m and n are integers. For example, a skyrmion moving with $\theta_{sk} = 45°$ corresponds to the skyrmion moving one lattice constant in the y direction ($n = 1$) and one lattice constant in the x direction ($m = 1$). In Fig. 3.5 we show the velocity curves and the R curve as a function of the applied drive, F_D. In this plot, R is analogous to the skyrmion Hall angle curve, where $\theta_{sk} = \operatorname{atan} R$ and the applied drive is always in the x direction. In this system it is used a rate of α_m/α_d as a free parameter, where α_m is the Magnus and α_d is the damping constant. The intrinsic Hall angle can be found using $\theta_{sk}^{int} = \operatorname{atan}(\alpha_m/\alpha_d) = \operatorname{atan} 0.45 = 24.23°$.

Figure 3.5 – (a) The average velocity curves, $\langle V_\parallel \rangle$ and $\langle V_\perp \rangle$, as a function of the applied driving force F_D for a system using $\alpha_m/\alpha_d = 0.45$. $\langle V_\parallel \rangle$ is the velocity parallel to the applied drive and $\langle V_\perp \rangle$ is perpendicular. (b) The R curve as a function of the applied drive F_D. The velocity dips are related to a change in the skyrmion direction of motion. The dashed line in (a) represents null velocities and in (b) it represents the intrinsic skyrmion Hall angle. (From Reichhardt *et. al.* (2015), pg 104426-4 [39]).

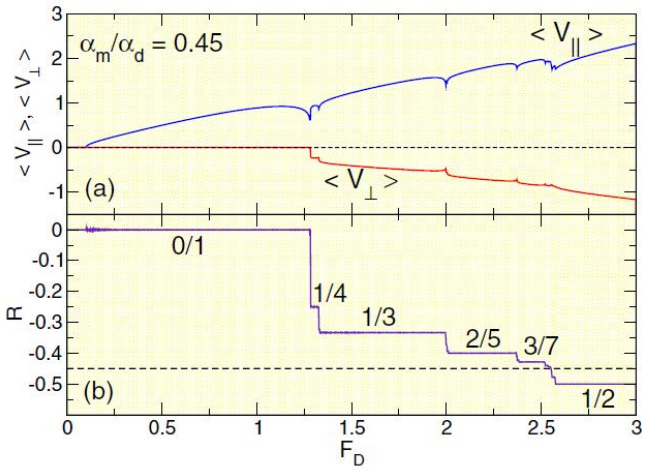

From Fig. 3.5 the velocity dips are related to changes in the skyrmion direction of motion. These transitions are characterized by a decreasing in the velocity, giving rise to a negative differential mobility. Hence, these steps of stabilized motion enable a controlled motion for skyrmions, since for a certain range of applied transport force the skyrmion is locked in a certain direction. This phenomenon is known as *directional locking* and has been extensively studied for overdamped particles [13–15,115]. However, in overdamped particle systems the angle of the external drive must change with respect to the symmetry direction of the substrate in order to produce these locking steps, but for the skyrmion just an increase in the external drive is sufficient enough, due to the Magnus term. Note that for $F_D > 2.5$, the skyrmion moves with a skyrmion Hall angle *higher* than the intrinsic Hall angle. This is another interesting feature that periodic arrays of obstacles can induce in the system. Due to the ordering of obstacles, skyrmions are forced to move with higher angles, as can be seen in Fig. 3.5 (b).

In Fig. 3.6 it is shown some selected skyrmion trajectories for the system of Fig. 3.5. In Fig. 3.6 (a), for low drives, the skyrmion is moving with $\theta_{sk} = 0°$ and as F_D increases more possible types of motion occur, including a higher angle than the intrinsic angle, as shown in Fig. 3.6 (d).

Figure 3.6 – Illustrations of skyrmion trajectories for the system of Fig. 3.5. The skyrmion is represented as a red dot, its trajectories as lines and the obstacles maxima as black dots. In (a) $R = 0/1$, (b) $R = 1/4$, (c) $R = 2/5$ and (d) $R = 1/2$. (From Reichhardt *et. al.* (2015), pg 104426-4 [39]).

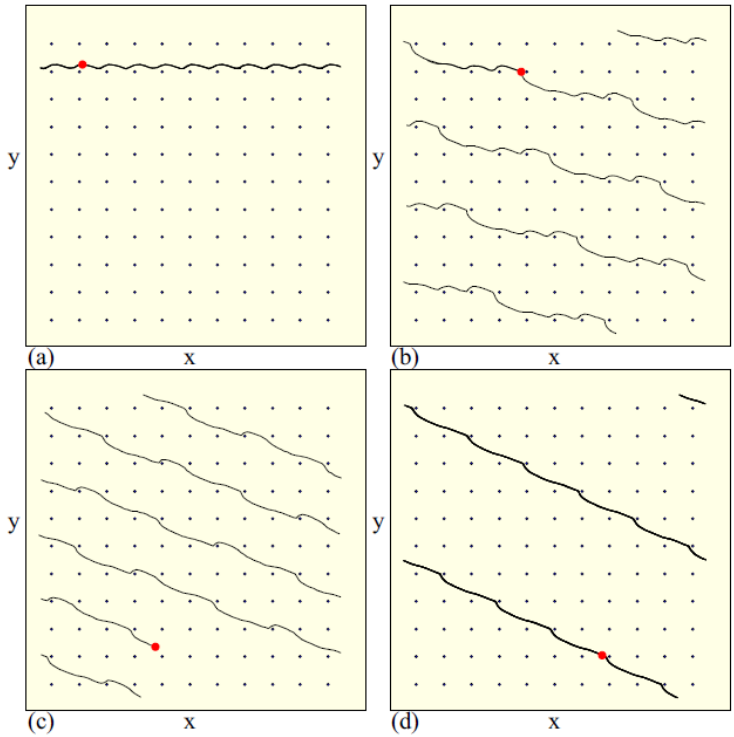

Figure 3.7 – (a) The average velocity curves, $\langle V_{\parallel} \rangle$ and $\langle V_{\perp} \rangle$ and R curve, as a function of the applied driving force F_D for a system (a,c) using $\alpha_m/\alpha_d = 4.925$ and (b,d) using $\alpha_m/\alpha_d = 9.962$. $\langle V_{\parallel} \rangle$ is the velocity parallel to the applied drive and $\langle V_{\perp} \rangle$ is perpendicular. (From Reichhardt *et. al.* (2015), pg 104426-6 [39]).

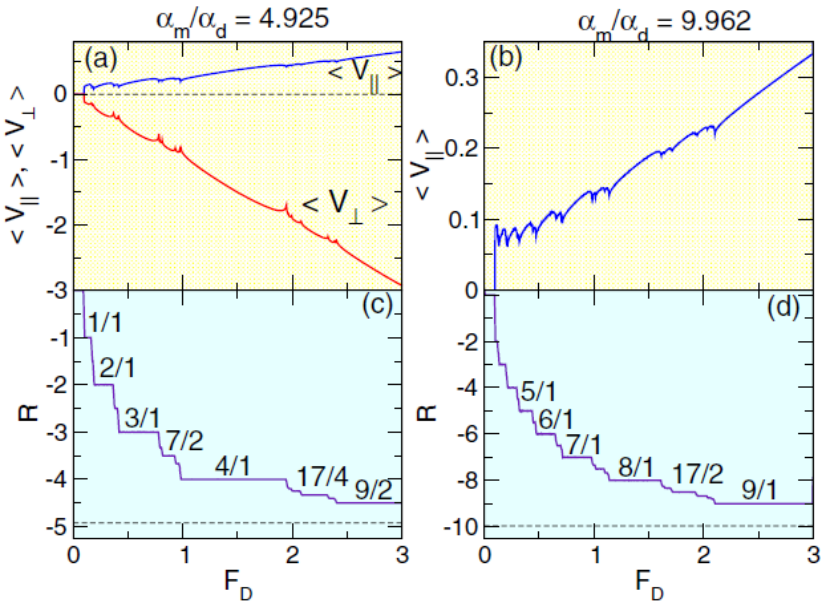

The force-velocity curves also depend strongly on the rate α_m/α_d. In Fig. 3.7 it is illustrated some velocity curves for systems with $\alpha_m/\alpha_d = 4.925$ and $\alpha_m/\alpha_d = 9.962$. As can be seen, these systems exhibit several new skyrmion directions of motion due to the stronger Magnus term that induces a higher intrinsic skyrmion Hall angle. The rate α_m/α_d can be understood as skyrmions in different samples, where the samples have distinct values of D/J. For different Dzyaloshinskii-Moriya strengths, the skyrmion can exhibit different sizes and, therefore, different dynamics.

Recently, Feilhauer *et. al.* [125] studied the effects of damping in the skyrmion motion under the influence of a magnetic antidot array. Using micromagnetic simulations and Thiele's approach, it was found that directional locking effects can also emerge for varied damping values in the system. Also, skyrmions can be guided to move into plaquettes, that is, regions between the magnetic antidots by simply adjusting current pulses intensity and intervals of pulse, Δt. In Fig. 3.8 it is shown the results of the skyrmion behavior in a damping free scenario under the influence of the current pulses. In Fig. 3.8 (a) the pulse is not strong enough, so the skyrmion just follows a closed isoenergy counter loop. In Fig. 3.8 (b) the pulse is stronger and the skyrmion is trapped in a closed orbit around the obstacle. For stronger pulses the skyrmion move from a valley to the other, as illustrated in Fig. 3.8 (c), or also move even further between valleys, as illustrated in Fig. 3.8 (e). A phase diagram of pulse interval Δt versus the current intensity j_{FM} is shown in 3.8 (f), where the different regions can be related to the skyrmion

trajectories of Fig. 3.8 (a) – (e) through color. These insights on how to control the skyrmion positions using current pulses may be very useful for future devices.

Figure 3.8 – (a) – (e) Skyrmion trajectories for a magnetic antidot array and in absence of damping. The phase diagram of current pulses interval vs. intensity are illustrated in (f) and for each red dot in (f) represents a trajectory in (a) – (e). The skyrmion trajectories follow the corresponding color of the regions in (f). (From Feilhauer *et. al.* (2020), pg 184425-6 [125]).

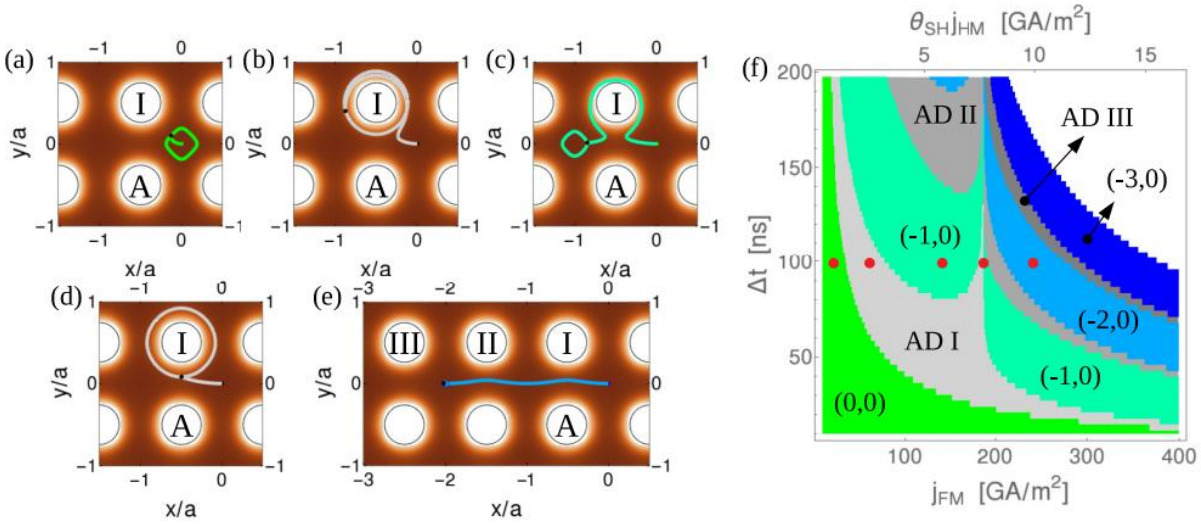

When the damping constant is finite, that is $\alpha \neq 0$, the skyrmion exhibits again the skyrmion Hall effect, which makes it flow with an angle respective to the drive. Now, using a fixed uniform current density, in Fig. 3.9 it is shown some skyrmion trajectories for different values of damping. In the case of undamped $(\alpha = 0)$ the skyrmion moves along the x direction. This is the result of the applied current and the corresponding force $\mathbf{F}_j$ acting on the skyrmion being parallel to symmetry axes of the magnetic antidot lattice. For finite damping, the skyrmion direction of motion is tilted due to the skyrmion Hall effect. Both Reichhardt *et. al.* [39] and Feilhauer *et. al.* [125] works corroborate to the idea of a topological separator, that could sort skyrmions of different species, with slightly different values of θ_{sk} just by using a periodic array of repulsive potentials.

Figure 3.9 – Skyrmion trajectories starting from a valley coordinate (0,0) for various values of damping. The skyrmion motion is driven by a uniform fixed current of $j_{FM} = 90\ \mathrm{GA/m^2}$ (or $j_{HM} = 3.7\ \mathrm{GA/m^2}$) applied along the x (or y) direction. (From Feilhauer *et. al*. (2020), pg 184425-6 [125]).

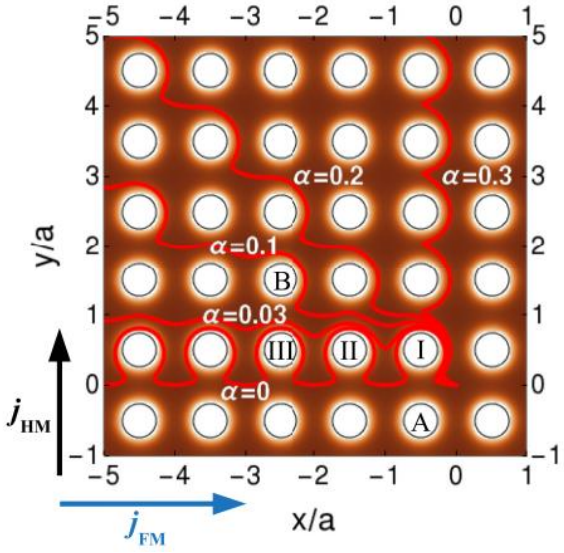

So far, the works described here considered the dynamics of a single skyrmion in the sample, however, when multiple skyrmions are added, the collective behavior emerges and the dynamics can be very different from the single skyrmion case. Reichhardt *et. al.* [40] studied the collective behavior of skyrmions in a square pinning array using particle-based simulations. The main focus of this work was to understand the Magnus contribution on the sliding phases. One of the most interesting results is that skyrmions may exhibit a moving *clustered* or *segregated* state, where skyrmions clump into a dense stripe. This clustered state is in agreement with Koshibae *et. al*. [126] findings studying skyrmions under strong quenched disorder in continuum-based simulations. However, the mechanism for the clustered state here is different. The creation of segregated states in continuum-based simulations was attributed to the emission of spin waves that produces an effective attraction among skyrmions and make they clump together [126]. Here, in the particle-bases simulations the segregated state occurs due to the velocity dependence of the skyrmion Hall angle in the presence of pinning, since no spin waves are present in Reichhardt's simulation. Basically, the regions in the sample are moving with different relative velocities, causing each region to move with a different skyrmion Hall angle and clumping them into the dense stripe observed [40]. In Fig. 3.10 (a) it is plotted the velocity curve $\langle V_{\parallel} \rangle$ vs. F_D for a system with strong Magnus component, $\alpha_m/\alpha_d = 9.96$ and filling factor $f = 1.0117$. The filling factor is number of skyrmions divided by number of pinning centers. In Fig 3.10 (b) it is shown the mean-square deviations in the instantaneous velocities for both parallel ($\delta V_{\parallel}$) and perpendicular ($\delta V_{\perp}$), and in Fig. 5.10 (c) shows the corresponding fraction of

sixfold-coordinate skyrmions, P_6. The vertical dashed lines are separating the different dynamic phases found.

Figure 3.10 – (a) The velocity curve $\langle V_\parallel \rangle$ vs. F_D for skyrmion interaction with a square array of pinning centers with filling factor $f = 1.0117$ and $\alpha_m/\alpha_d = 9.96$.The corresponding velocity deviations parallel and perpendicular to the drive, $\delta V_\parallel$ and $\delta V_\perp$ respectively. (c) The corresponding fraction of sixfold-coordinate of skyrmions, P_6. The dashed vertical lines are separating the dynamic phases found. (From Reichhardt *et. al*. (2018), pg 134418-3 [40]).

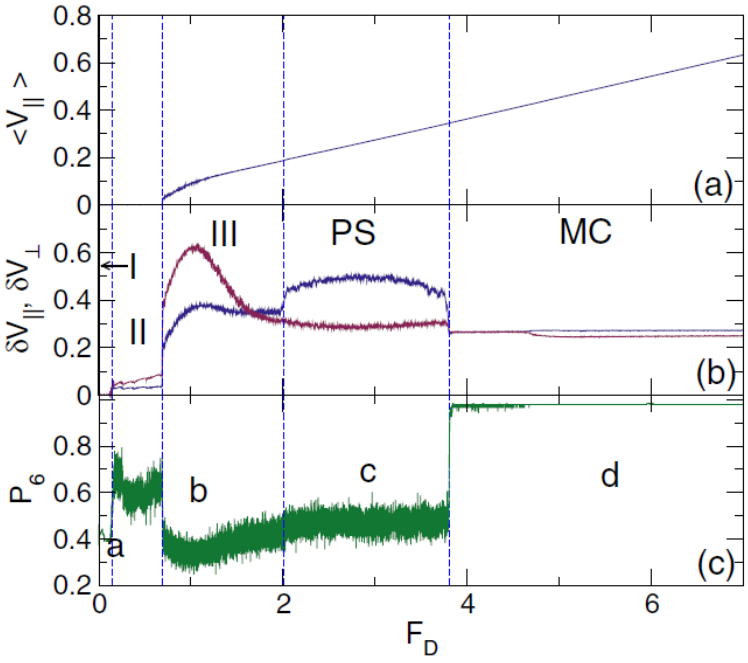

Phase I is the pinned phase, where the velocities are null, as illustrated in Fig. 3.11 (a). For $F_D = 0$, skyrmions form a commensurate state with few skyrmions in interstitial positions between pinning sites. Phase II is the phase where interstitial skyrmion flows between the pinned ones. This phase exhibits a series of quantized direction of motion as results of directional locking. As can be seen there are jumps in $\delta V_\parallel$ and $\delta V_\perp$, and P_6 exhibits strong oscillations. Phase III consists of chaotic disordered flow of skyrmions, as illustrated in Fig. 3.11 (b). Skyrmions flow through the sample and other remain pinned. After further increase of the external drive, the skyrmion begin the clustered or segregated phase, illustrated in Fig. 3.11 (c). This phase is called PS in the Fig. 3.10. Then, for higher drives the skyrmions reorganize their motion into the moving crystal phase, called MC, as illustrated in Fig. 3.11 (d). The transition to from PS to MC phase is characterized by drops in $\delta V_\parallel$ and $\delta V_\perp$, which become nearly isotropic, along with an upward jump in P_6 to a value very close to $P_6 = 1$.

Figure 3.11 – Skyrmion positions (blue dots) and pinning center positions (red circles) for the system of Fig. 3.10. (a) The pinned Phase I, (b) the disordered flow os skyrmions Phase III, (c) the segregated skyrmion phase PS, and (d) the moving crystal MC phase. (From Reichhardt *et. al*. (2018), pg 134418-4 [40]).

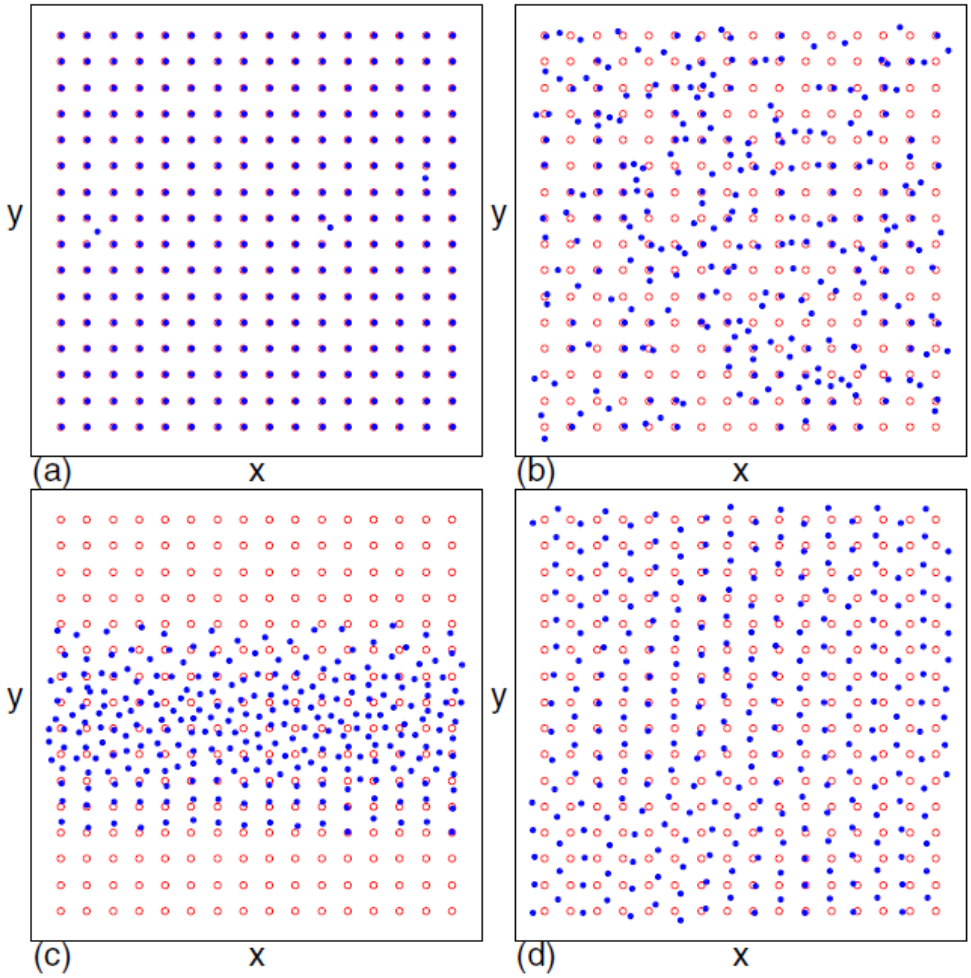

After a series of simulations it was possible to make the plot illustrated in Fig. 3.12, where it shows a phase diagram of F_D vs. F_P, where F_P is the strength of pinning interaction. This plot enables a better understanding on how the pinning affects the skyrmion dynamics. The system considered has $f = 1.0117$, $\alpha_m/\alpha_d = 9.96$ and has a pinning density of $n_p = 0.1975$. As can be seen, the PS phase only happens for a certain range of pinning strength and it is in agreement with continuum-based simulations [126]. Interestingly it was also found a reentrant pinning phase, where after the first depinning the skyrmion system can become pinned again. These results are very important to understand some features of skyrmions interacting with periodic pinning.

Figure 3.12 – Phase diagram of F_D vs. F_P, where F_D is the external driving force and F_P is the strength of the pinning centers. I is the pinned phase, II, is the interstitial skyrmion flow, III is the disordered flow phase, I_{re} is the reentrant pinned phase, PS is the phase separated phase, DPS is diagonal separated phase, and MC is the moving crystal phase. (From Reichhardt *et. al.* (2018), pg 134418-8 [40]).

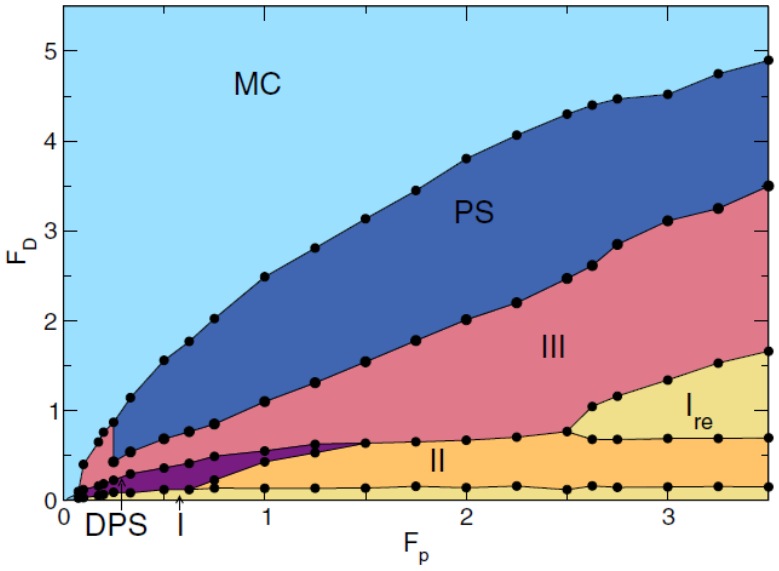

Concerning experimental observations of skyrmions in periodic patterned samples, Saha *et. al*. [64] were one of the first to address how skyrmions could nucleate and stabilize in such periodic arrays of antidots. The sample consists of multilayer films of [Pt (3 nm)/Co (1.1 nm)/ Ta (4 nm)]$_{12}$ deposited on 200-nm-thick x-ray transparent Si_3N_4 membranes supported by 200-μm-thick Si frames. The antidot lattice was made with focused Ga^+ ion beam that is able to produce complete holes in the multilayer film. In Fig. 3.13 there is a representation of the multilayer film and also a scanning electron microscope image of the sample with the antidots.

Considering two samples with different lattice constants, LC, the authors were able to understand the influence of the lattice constant on the skyrmion formation in these samples. For the sample with $LC = 550$ nm it was found that skyrmions did not form due to the proximity of the defects. The labyrinth domains form connections between the antidots as the magnetic field increases, as indicated by the red dashed ellipses. These connections prevent the formation and stabilization of skyrmions. On the other hand, when the lattice constant is larger, $LC = 1000$ nm, there is enough gap between the antidots to allow the skyrmion formation. As the magnetic field increases, the magnetic domain connections are disconnected from one of the antidots creating an open domain end. These open domains shrink and form magnetic skyrmions in the sample, as clearly illustrated in Fig. 3.14 (h). This demonstration of the skyrmion formation in antidot lattices is a significant advance towards generation, confinement and stabilization of magnetic skyrmions at room temperature.

Figure 3.13 – (a) The multilayer film schematic illustration and the Ga^+ ion beam producing the antidots. (b) Scanning electron microscope image of the antidot lattice with lattice constant of LC = 550 nm patterned in the film. (From Saha *et. al*. (2019), pg 144435-2 [64]).

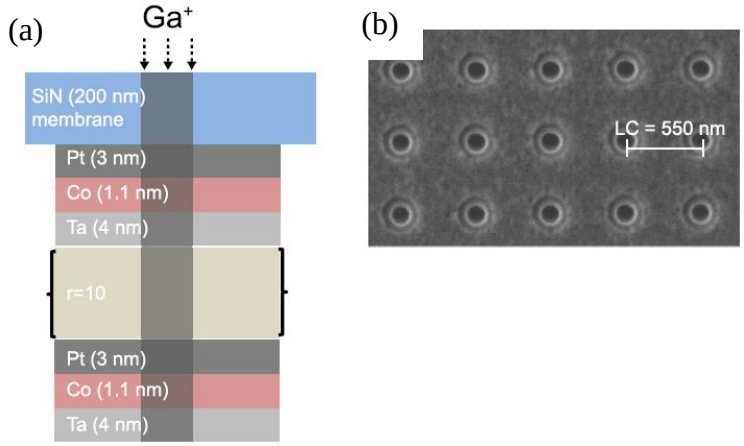

Figure 3.14 – XMCD-STXM images of the magnetic evolution as the applied magnetic field is varied in the antidot array. From (a) – (d) using LC = 550 nm and from (e) – (h) using LC = 1000 nm. Dark and bright contrasts represents the magnetization domains point up or down, respectively. Skyrmion are highlighted with solid circles and magnetic domains with red dashed circles and ellipses. (From Saha *et. al*. (2019), pg 144435-6 [64]).

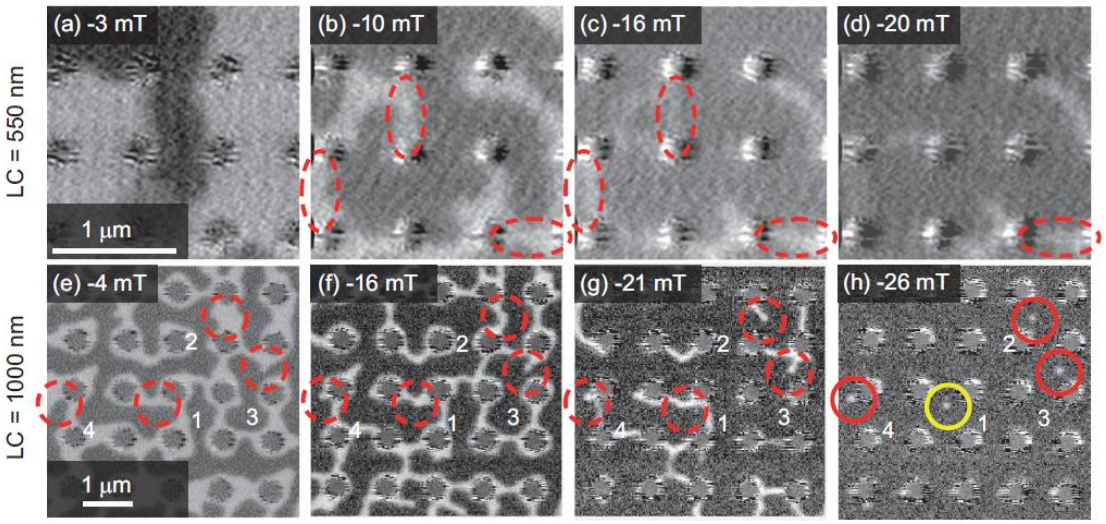

3.3 Skyrmions in Asymmetric Potentials with Alternating Currents

In general, when particles interact with an asymmetric potential their motion can be controlled by means of the *ratchet effect*. The ratchet effect is a net dc motion of particles that emerges from the combination of a broken spatial symmetry and an oscillating drive. It sometimes can also be referred as the diode effect, where the asymmetry produces different depinning forces in different directions, yielding a preferential or "easy" direction of motion [127]. The ratchet effect has been investigated extensively in several particle systems,

such as, protein motors [128], molecular motors [17,18], colloids [129], type II superconducting vortices [20,23,130], electrons [25], active matter [22] and also recently in skyrmions [32,111,112,131].

The first proposal for skyrmion ratchet was studied by Reichhardt *et. al*. [32] in a type of quasi-one-dimensional (1D) asymmetric substrate that was known to induce ratcheting motion in superconducting vortices. Using a particle-based approach, the skyrmions were submitted to a potential in the form of

$$U(x) = U_0[\sin(2\pi x/a) + 0.25\cos(4\pi x/a)], \tag{3.1}$$

where a is the substrate periodicity. For the case of overdamped particles, like colloids and vortices, when an ac drive is applied in the x direction, a ratchet motion is induced in the easy $(+x)$ axis, and the particle may move one or more substrates periods under each ac drive cycle. As the depinning threshold in $+x$ is lower than in the $-x$, in the dc current limit the system acts like a diode, easy to flow in $+x$ and very hard to flow in $-x$. If the oscillating drive is applied in the y direction, the skyrmion does not exhibit a ratchet motion due to the lack of asymmetry in the y direction of this system. Considering now the skyrmion case, which exhibits the skyrmion Hall effect, a ratchet effect can occur even when the ac drive is applied only in the y direction. Due to the skyrmion hall angle, this applied ac drive in y will induce a skyrmion motion in the transversal component, which has a broken symmetry, thus inducing a ratchet effect. This transversal ratchet effect was named Magnus-induced transverse ratchet effect. In Fig. 3.16 shows the velocity component in both parallel and perpendicular directions for the system of Fig. 3.15 under an ac driving $F_{\perp}^{ac}$. In Fig. 3.16 (a) shows the velocity curves for a system with $\alpha_m/\alpha_d = 0.855$, in (b) for $\alpha_m/\alpha_d = 4.0$ and in (c) $\alpha_m/\alpha_d = 7.018$. The inset in Fig. 3.16 (a) illustrates the case of overdamped particles without the Magnus component, which has no net motion at all. The profile of the average velocities exhibits well defined quantized values for the skyrmion motion, and there are regions of ac drive amplitude where the skyrmion ratchet is absent.

In Fig. 3.17 it shows some selected cases for the skyrmion trajectories. The trajectories show that despite the ac drive is applied perpendicular to the asymmetry direction, the skyrmion has motion parallel to the asymmetry due to the Magnus term, and therefore inducing the ratchet motion.

Figure 3.15 – Schematic of sample geometry where the skyrmion is the red ball and the asymmetric potential is the yellow terrain. An ac driving, F^{ac} may be applied parallel, $F_{\parallel}^{ac}$, or perpendicular, $F_{\perp}^{ac}$, to the asymmetry of the substrate. (From Reichhardt *et. al*. (2015), pg 2 [32]).

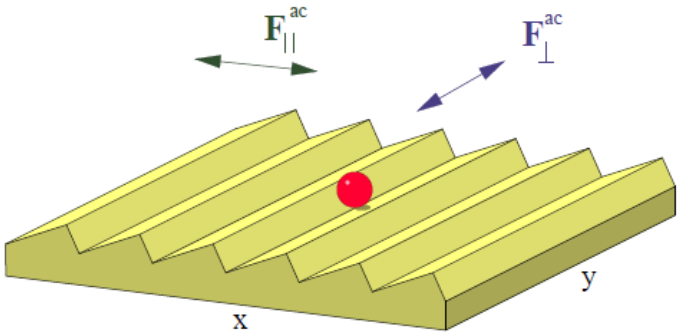

Figure 3.16 – The skyrmion average velocity parallel, $\langle V_{\parallel} \rangle$ and perpendicular $\langle V_{\perp} \rangle$ to the substrate asymmetry versus $F_{\perp}^{ac}$. (a) for $\alpha_m/\alpha_d = 0.855$, in the inset is shown the overdamped case where the ratchet is absent, (b) $\alpha_m/\alpha_d = 4.0$ and (c) $\alpha_m/\alpha_d = 7.018$, the inset shows a blowup of $\langle V_{\parallel} \rangle$. (From Reichhardt *et. al*. (2015), pg 5 [32]).

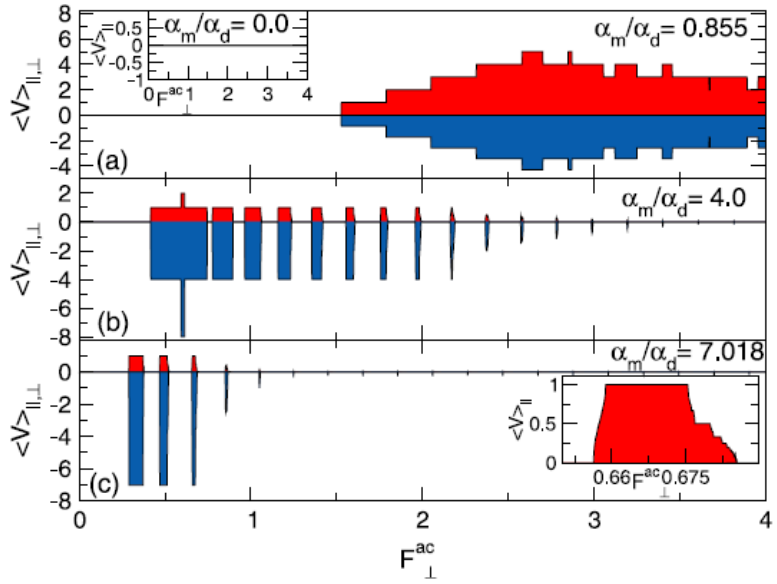

The direction of the ratchet motion can also be controlled, as Ma *et. al*. [112] showed recently in his work. Using particle-based simulations, they showed that ac driven skyrmions with different densities and ac drive amplitudes can ratchet in any direction, up to 360° rotation. They call this direction of motion as *vector ratchet*. This opens a new method to control the skyrmion motion in the sample with asymmetric substrates, not just parallel or perpendicular to the asymmetry direction.

Figure 3.17 – The skyrmion trajectories for the system of Fig. 3.16. The black lines represent the skyrmion trajectory, the red ball is the skyrmion position at the snapshot, and the green (white) regions are the high (low) areas of the substrate potential. In (a) for $\alpha_m/\alpha_d = 0.855$ and $F_\perp^{ac} = 2.0$, (b) for $\alpha_m/\alpha_d = 4.0$ and $F_\perp^{ac} = 0.7$, (c) a non-ratcheting orbit for $\alpha_m/\alpha_d = 4.0$ and $F_\perp^{ac} = 0.76$ and (d) for $\alpha_m/\alpha_d = 4.0$ and $F_\perp^{ac} = 1.97$. (From Reichhardt *et. al*. (2015), pg 5 [32]).

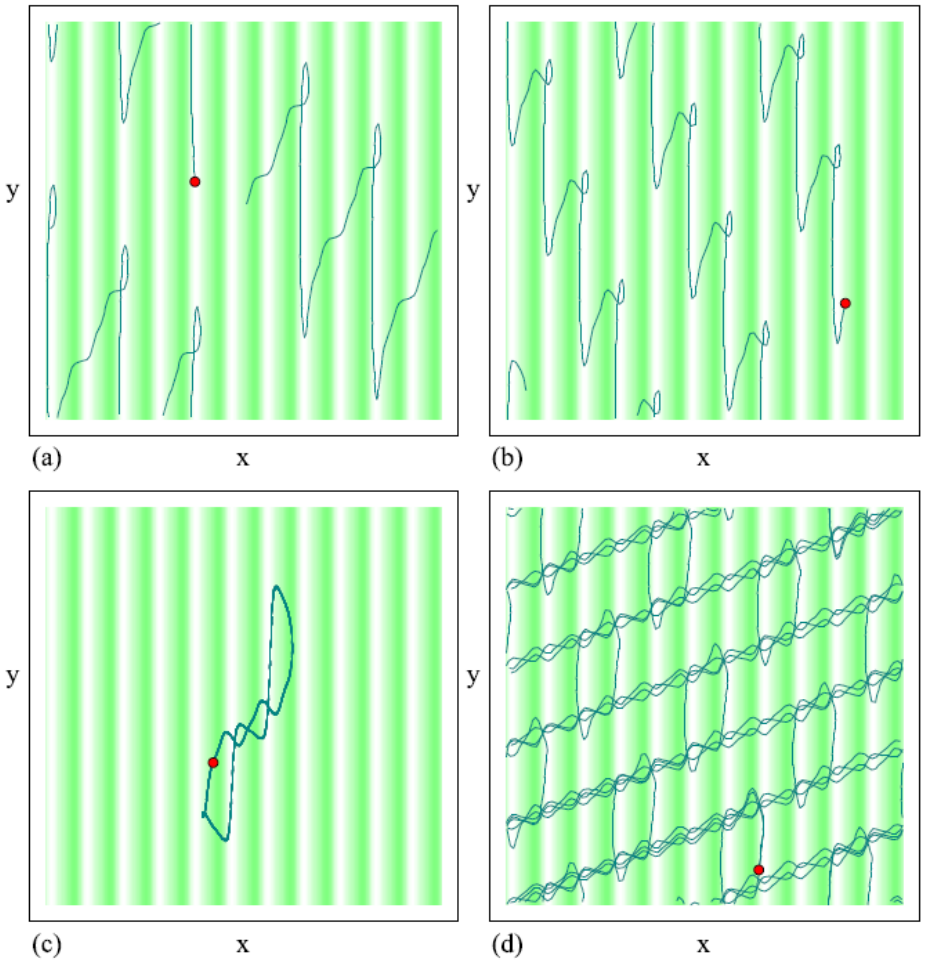

The skyrmion ratchet can also be applied in racetrack devices to guide the skyrmion motion along the racetrack, as shown by Göbel and Mertig in 2021 using continuum-based simulations [111]. It is widely known that the skyrmion Hall effect is problematic in racetrack devices, since the skyrmion Hall angle can push the skyrmions towards the edge of the sample and then can be destroyed. However, Göbel and Mertig proposed a racetrack edge with a broken inversion symmetry, so the skyrmion can translate through the sample due to the ratchet effect. In Fig. 3.18 it is illustrated the proposed racetrack with asymmetric edge.

When a skyrmion is introduced in the sample of Fig. 3.18 and the ac drive is applied, a dc net skyrmion motion appears, as presented in Fig. 3.19. After a transient period of $T = 80$ ns of ac drive (cyan and orange trajectories) the skyrmion moves a length of $L = 240$ nm per

current period [See Fig. 3.19 (a)] and oscillates in the valleys of the edge asymmetry (blue and red trajectories). The skyrmion average velocity can be seen as the slope of the Fig. 3.19 (b).

Figure 3.18 – Illustration of the racetrack and the ac propulsion of skyrmions. A Co layer (light gray) is interfaced with an Pt layer (dark gray). The applied current $j(t)$ is applied along the $\pm x$ direction, thus the skyrmion may move along $\pm v$ directions. Due to the interaction with the edges, the skyrmion experiences a net propulsion along the $+x$ direction. Note that only of the edges has asymmetry while the other is straight. (From Göbel and Mertig (2021), pg 2 [111]).

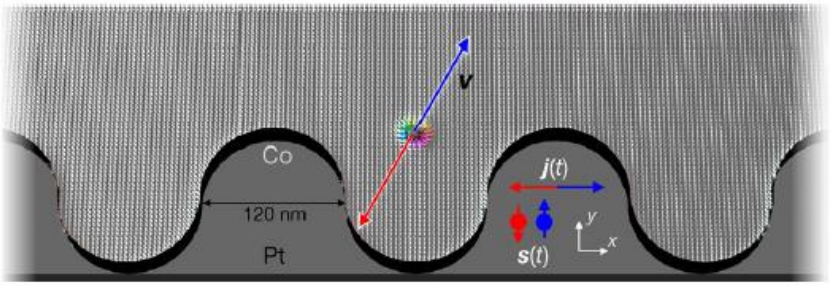

Figure 3.19 – (a) The skyrmion trajectory along the racetrack with asymmetric edge under the influence of applied ac drive. (b) Plot of skyrmion position as a function of time, where the average velocity is the slope of the curve. (c) The shape of the skyrmion orbit as a function of the velocity in the x component, v_x versus the relative displacement in the x from the average position. (From Göbel and Mertig (2021), pg 4 [111]).

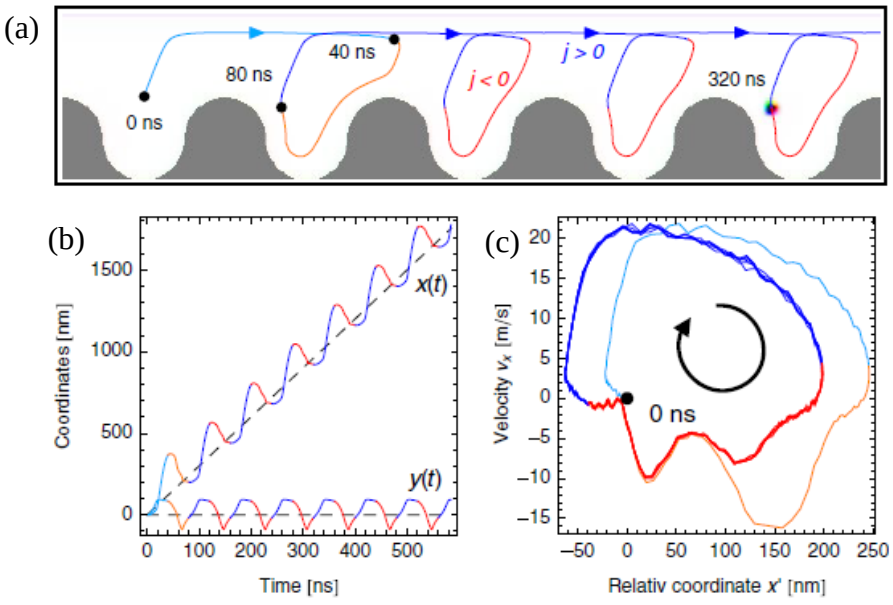

The quasi-periodic motion of the skyrmion can be characterized by x'-v_x diagram, where $x' = x - \overline{v_x}t$. The curve shows that almost all the curves are identical after the transient behavior. Thus, the skyrmion moves with a periodic trajectory, as can also be seen in Fig. 3.19 (a).

These results show clearly that skyrmion ratchet is a very promising concept to control the skyrmion motion in different samples, even in racetrack devices. There are also several other

types of skyrmion ratchet that take into account internal excitations of skyrmion nodes and its deformations to induce a ratchet motion [131–133]. However, the focus here is on skyrmion ratchet induced by pinning or substrates.

4 Model and Simulation

4.1 Model

In most of this thesis, we consider the case of a chiral thin film magnet placed in the *x*-*y* plane in the presence of an applied magnetic field normal to the sample surface. The model used in this work is the same developed by Lin *et. al.* [73], which is well described in section 2.3 of this thesis. The equations of motion for skyrmions are obtained using the Thiele's approximation [72], which rules the motion of magnetic solitons. As a result, the equation that describes the skyrmion motion used throughout this thesis is:

$$\alpha_d \mathbf{v}_i = \mathbf{F}_i^{ss} + \mathbf{F}_i^{P} + \alpha_m \times \hat{\boldsymbol{z}} + \mathbf{F}_i^{D} + \mathbf{F}_i^{ac} + \mathbf{F}_i^{T} \tag{4.1}$$

Where $\mathbf{v}_i$ is the velocity of the skyrmion i and α is the damping constant that is related both to the spin precession and to the conduction electrons localized in the skyrmion core. The $\mathbf{F}_i^D = 2\pi\hbar e^{-1}\hat{\mathbf{z}} \times \mathbf{J}$ is the driving force that rises due to the application of a direct spin polarized current. The external drive $\mathbf{F}_i^D = F^D\hat{\mathbf{d}}$, where is $\hat{\mathbf{d}} = \hat{\mathbf{x}}$, unless otherwise noted. The $\mathbf{F}_i^M = 4\pi\gamma^{-1}\hat{\mathbf{z}} \times \mathbf{v}_\mathrm{I}$ is the Magnus term. $\mathbf{F}_i^{ac}$ is analogous to $\mathbf{F}_i^D$, but $\mathbf{F}_i^{ac}$ is an ac drive that provokes an oscillation of the skyrmion in the sample. The ac drive follows the expression $\mathbf{F}_i^{ac} = A\,\mathrm{sen}(2\pi\omega_1 t)\,\hat{\mathbf{x}} + B\cos(2\pi\omega_2 t)\,\hat{\mathbf{y}}$, where A and B are the ac drive amplitudes and $\omega_{1,2}$ are the ac drive frequencies. $\mathbf{F}_i^T$ is responsable for the thermal kicks that finite temperatures adds to the system, $\mathbf{F}_i^T$ is modeled as a thermal white noise obeying $\langle \mathbf{F}(t)^T \rangle = 0$ and $\langle \mathbf{F}(t)_i^T \mathbf{F}(t)_j^T \rangle = 2\eta k_B T \delta_{ij}$ [134–136]. The interaction between skyrmions can be modeled as $\mathbf{F}_i^{ss} = K_1\left(\frac{r_{ij}}{\xi}\right)\hat{\boldsymbol{r}}_{ij}$ [73]. Here ξ is the screening length, $r_{ij} = \left|\mathbf{r}_i - \mathbf{r}_j\right|$ is the distance between skyrmions i and j, and $\hat{\boldsymbol{r}}_{ij} = \left(\mathbf{r}_i - \mathbf{r}_j\right)/r_{ij}$. In order to enhance computational efficiency, we used a cutoff in the skyrmion-skyrmion interaction beyond $r_{ij} = 6.0\xi$, where the magnitude of the interaction becomes negligible. The $\mathbf{F}_i^P$ is the force between skyrmions and the artificial pinning centers in the sample, which may be attractive or repulsive to skyrmion. However, the general shape of the pinning force $\mathbf{F}_i^P$ was modeled following a Gaussian potential in the form

$U_P = C_0 e^{-(r_{io}/a_o)^2}$, where C_0 is the potential strength, a_o is the pinning radius and r_{io} is the distance between the pinning o and the skyrmion i. For $C_0 > 0$ the interaction is repulsive and for $C_0 < 0$ it is attractive. Hence, the force is $\mathbf{F}_i^P = -\nabla U_P = -F_o r_{io} e^{-(r_{io}/a_o)^2} \hat{\mathbf{r}}_{io}$, where $F_o = 2C_0/a_o^2$. For values of $r_{io} > 2.0\xi$ a cutoff is used since the interaction becomes negligible. We measure the skyrmion velocity parallel, $\langle V_\parallel \rangle$, and perpendicular, $\langle V_\perp \rangle$, to the drive, so that $\langle V \rangle = \sqrt{\langle V_\parallel \rangle^2 + \langle V_\perp \rangle^2}$. When the skyrmion is flowing without obstacles, it moves with a Hall angle respective to the drive direction, $\theta_{sk} = \arctan(\langle V_\perp \rangle / \langle V_\parallel \rangle) = \arctan(\alpha_m/\alpha_d)$. The damping and the Magnus term are normalized by $\alpha_m^2 + \alpha_d^2 = 1$, unless otherwise noted. The Eq. (6.1) is integrated numerically following the second order Runge-Kutta method. In Fig. 1 there is an illustration of the skyrmion flowing in an obstacle array, that is, pinning centers that have repulsive interaction with skyrmions. The terrain maxima peaks are the center of the obstacles, the skyrmion is the dark blue sphere and its trajectory is the light blue line.

Figure 4.1 – Illustration of skyrmion dynamics in a periodic obstacle array with applied external drive. The landscape maxima peaks represent the obstacle positions, the dark blue sphere is the skyrmion and the light blue line is the skyrmion trajectory. (From Vizarim *et. al*. (2020), pg 4 [137]).

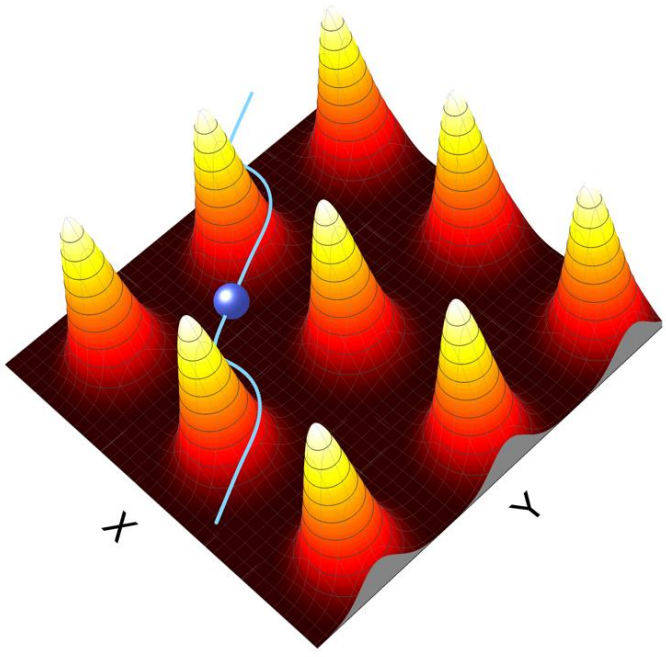

The different results that are described in this thesis use the general Eq. (4.1), however, depending on the work some interactions may be neglected or slightly modified. For each specific case, before going into details of the results it will be expressed the specific type of Eq. (4.1) that was used to simulate the system and its specificities.

One of the fundamental steps is to search for the skyrmion ground state using simulated annealing technique [138]. Then, this equation of motion will be integrated numerically using

Molecular Dynamics (MD) technique, allowing us to obtain the skyrmions trajectories, and consequently, skyrmion velocities, depinning forces and dynamic behaviors. In the next sections the simulated annealing and molecular dynamics are discussed.

4.2 Simulated Annealing

Simulated annealing is a very common numerical technique used to search for global maxima and minima of n-dimension continuous mathematical functions. This method is based on metallurgy, simulating the annealing process of a solid, where initially the solid is set at an initial temperature T, then the temperature is slowly cooling down, accommodating the atoms to reach the minimal energy state. For the case of systems where there is only one minimum value of energy, any other optimization algorithm based on gradients is sufficient, however, for more complex cases where the system can be trapped in metastable states, a more sophisticated method must be used [138].

In the simulated annealing technique one or more artificial temperatures are added and gradually cooled. These artificial temperatures act like a stochasticity source. This randomness is very convenient avoid being trapped in metastable configurations [138].

The first non-trivial solution was elaborated by Kirkpatrick *et. al.* [139] for classic systems. The algorithm elaborated by Kirkpatrick follows Boltzmann-Gibbs quasi-equilibrium statistics, which is known as the Classical Simulated Annealing (CSA). In 1987, Szu and Hartley [140] propose a simulated annealing that uses the Cauchy-Lorentz distribution instead of the gaussian distribution of Boltzmann. This algorithm developed by Szu and Hartley was known as Fast Simulated Annealing (FSA). A few years later, Tsallis [138] looked at both simulated annealings and developed the Generalized Simulated Annealing (GSA), which generalizes both annealings in a single unified method. As the parameters of the GSA are adjusted, it can behave like a FSA or CSA.

In general words, the simulated annealing technique uses a *visiting function* which determines how the domain of the function is searched. Moreover, there is also an *acceptance function* that determines if a result with higher energy may be accepted or rejected. The algorithm that rules this acceptance of higher energy is known as Metropolis algorithm [141] and is used in all kinds of simulated annealing. The Metropolis algorithm may be described as the following steps:

1. From an initial set of parameters of the cost function, chosen randomly, an initial "energy", E_{ref}, is calculated and an initial artificial temperature $T = T_0$ is chosen.

2. A random perturbation is generated in the system parameters using a *visiting function*, and then a new energy, E_{new}, is calculated.
3. If $\Delta E = E_{new} - E_{ref} \leq 0$, the new set of parameters is better (or at least of the same quality) than the previous one, thus the new set of parameters used to generate E_{new} is chosen to be the reference parameters, that is, $E_{ref} \leftarrow E_{new}$.
4. If $\Delta E > 0$, the new set of parameters is worse than the previous one, but still can be accepted depending on the *acceptance function* defined by the Metropolis criterion.
5. The temperature T is reduced following a function for temperature reduction.
6. The steps from 2 to 5 are repeated during a given number of iterations or any other stop condition is satisfied.

In the classic simulated annealing (CSA), the visiting function was simply a random state. However, for more complex problems the used visiting function is the Boltzmann-Gibbs probability distribution shown in Eq. (4.2). The acceptance function of the CSA algorithm is also the Boltzmann-Gibbs distribution [139],

$$P(\Delta E) = \exp\left(\frac{-\Delta E}{k_B T}\right). \tag{4.2}$$

In CSA the reduction of the temperature is given by the expression [142],

$$T(t) = \frac{T_0}{\log(1+t)}, \tag{4.3}$$

where the time t is the iteration step.

In the fast simulated annealing (FSA), the visiting function is given by Cauchy-Lorentz probability distribution, as shown in Eq. (4.4), where x is the variable of interest [140].

$$G_{T_c} = \frac{T_c(t)}{x^2 + T_c^2(t)} \tag{4.4}$$

The FSA maintain the same acceptance function as the CSA algorithm, which is the Boltzmann-Gibbs distribution illustrated in Eq. (4.2). Szu and Hartley showed that in the FSA the temperature decay should be inversely proportional to the iteration step,

$$T(t) = \frac{T_0}{1+t}, \tag{4.5}$$

because even in low temperatures the algorithm allows big jumps searching for the global minima. This method for reducing the temperature made FSA much faster than the conventional CSA.

In the generalized simulated annealing (GSA), the visiting function depends on the Tsallis probability density, shown in Eq. (4.6), where *D* is the dimension of the cost function and $q_V (1.0 < q_V < 3.0)$ is the visiting parameter,

$$g_{q_V}(x) = \left(\frac{q_V - 1}{\pi}\right)^{\frac{D}{2}} \times \frac{\Gamma\left(\frac{1}{q_V - 1} + \frac{D-1}{2}\right)}{\Gamma\left(\frac{1}{q_V - 1} - \frac{1}{2}\right)} \times \frac{T_{q_V}^{D/(q_v - 3)}}{\left[1 + \frac{(q_v - 1)x^2}{T_{q_V}^{2/(q_v - 3)}}\right]^{\frac{1}{q_V - 1} + \frac{D-1}{2}}} \tag{4.6}$$

In order to obtain the distribution of probabilities it is necessary to integrate Eq. (4.6) as shown in Eq. (4.7).

$$G(\Delta x_1) = \int_{-\infty}^{\Delta x_1} g_{q_v}(x)dx \tag{4.7}$$

The perturbation in Δx_1 is determined at each iteration $x_{t+1} = x_t + \Delta x_t$, where $\Delta x_t = G^{-1}(\Delta x_t)$. The temperature decay is determined by Eq. (4.8).

$$T_{q_v}(t) = \begin{cases} \dfrac{T_{q_v}(1)}{1+t} & \text{, for } q_v = 2 \\ T_{q_v}(t)\dfrac{2^{q_v - 1} - 1}{(1+t)^{q_v - 1} - 1} \end{cases} \tag{4.8}$$

The acceptance function for GSA is given by Eq. (4.9), where q_A $(1.0 < q_A < 3.0)$ is the acceptance parameter.

$$P_{q_A}(\Delta E(x)) = \frac{1}{1 + \left\{1 + \frac{(q_A - 1)[E(x_{t+1}) - E(x_t)]}{T_{q_A}(t)}\right\}} \tag{4.9}$$

The idea of generalized simulated annealing is related to the behavior of the visiting and acceptance parameters, q_V and q_A respectively. When $(q_A, q_V) = (1.0,1.0)$ the GSA acts like the CSA, and when $(q_A, q_V) = (1.0,2.0)$ the GSA acts like the FSA [143]. Thus, it is possible to ajust the GSA parameters so it behaves more likely to CSA or FSA, depending on what parameters minimize the system's energy. The GSA has been used to search for the global maxima or minima in several different systems very successfully [144–146]. It was also shown that GSA is more efficient to search for minima in high complex systems when compared to

FSA and CSA [147]. Our group has also great experience using GSA code to minimize the superconducting vortex lattice under the influence of periodic [148–150] and conformal [151] pinning arrays. In this thesis, the GSA algorithm was used to minimize the energy of multiple skyrmions, where the cost function is the energy interaction between skyrmions and interaction between skyrmions and pinning centers.

4.3 Molecular Dynamics

Molecular Dynamics (MD) is a numerical simulation technique used to calculate the motion of particles, such as atoms, molecules, colloids or any other physical object that has a particle-like behavior and their motion can be described by an equation of motion. As the equation of motion is numerically solved, it is possible to obtain the particles positions and velocities at each time step. In general cases, MD has the following steps:

1. An initial particle configuration is prepared, usually through optimization techniques
2. The forces exerted in each particle are calculated. These forces may be due to its interaction with other particles or interaction with external forces.
3. Time evolves and the forces are calculated again on the new state
4. The particles positions at each time step are saved and can be plotted as trajectories
5. It is possible to calculate the velocities by subtracting the new position by the old one and dividing by the time step of the simulation

For this present thesis, the MD technique is used to describe the motion of skyrmions in chiral magnets, as described in section 2.3. In this case, the chiral magnet is a thin-film placed in the $x-y$ plane and subjected to a magnetic field normal to the surface of the sample. The sample is infinite in both x and y directions, the technique used to simulate such system is to use a central (main) simulation box and image boxes that mirrors the exact features of the main simulation box, as illustrated in Fig. 4.2 (a). The particles in the main simulation box interacts between them and also with the particles in the image boxes. The number of image boxes necessary to represent an infinite system depends on the interaction between particles, in the case of skyrmions that has a Bessel interaction, for separations between skyrmions $r_{ij} > 6.0$ the interaction may be neglected. Besides that, during the motion if a skyrmion reaches the border of the simulation box, a skyrmion from the opposite image box enters the main simulation box, so that the number of skyrmions remain constant. This is called *boundary condition*, and it can be clearly seen in Fig. 4.2 (b), where the particle initially in P_1 is moved by external forces up to

the end of the simulation box, and reenters in the opposite side of the box finalizing its motion in P_2.

Figure 4.2 – (a) Representation of the simulation boxes, where the central box is the main simulation box and the other ones are image boxes. It also shows the main particles 1 and 2, and its images in the other boxes. The model predict that the boxes do not need to be square, it may have an inclination with size ξ, which in our case is zero. (From N. Grønbech-Jensen [152]) (b) Illustration of particle moving from an initial position P_1 and finilizing its motion in P_2. Due to the boundary conditions the particle reenters in the opposite side of the box (Elaborated by the author).

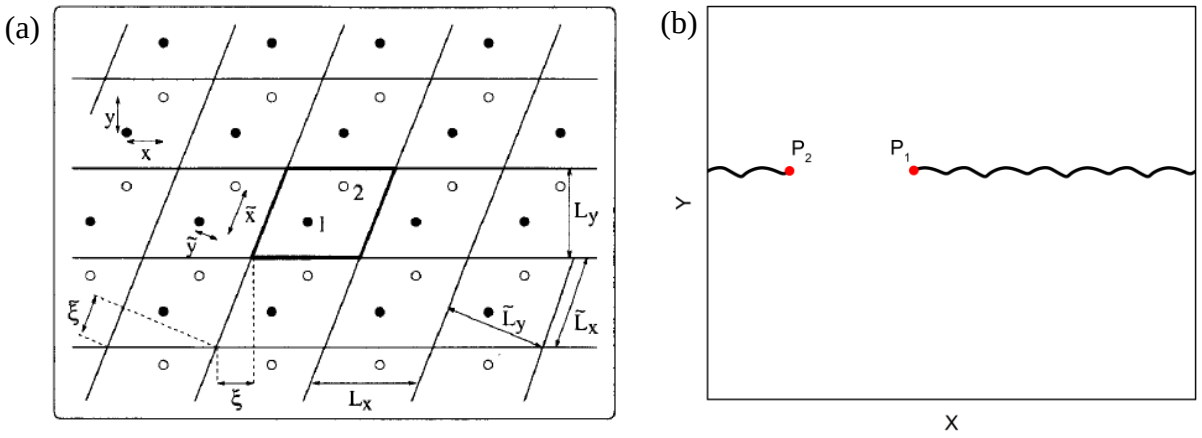

However, if there is a great number of particles inside the main simulation box, the interaction loop of particle *i* interacting with all other particles *j* on main simulation box and image boxes may be too overwhelming. If particles are separated by a distance greater than the potential cutoff, the MD could neglect these distant particles and go directly to the end of the loop, saving time. The method that takes these distances into consideration is called Neighbor Lists [153].

There are two most common Neighbor Lists used: Verlet neighbor lists and Cell structures. In 1967, Verlet suggested a technique to improve the speed of a program by maintaining a list of the neighbors of a given particle that is updated at intervals. Between a certain interval, the program does not check through all the *j* particles, but just those that are inside the list. Thus, the number of interactions is significantly reduced and saves time during the loop. The Verlet method consists of a potential cutoff sphere, of radius r_c, around a particle. This sphere has also a 'skin', to give a larger sphere of radius r_1, as shown in Fig. 4.3. The first step of the simulation is to construct the neighbor list of all particles, for which the pair separation is within r_1.

From time to time the Verlet list should be reconstructed and the cycle repeated. The algorithm is successful because the skin around r_c is chosen to be thick enough so that between

reconstructions a particle, such as particle 7 in Fig. 4.3, which is not on the list of particle 1, cannot penetrate through the skin. Particles 3 and 4 can move in and out of the sphere, but since they are on the list of particle 1, they are always considered in the calculations, until the next update. The interval between updates must be chosen according to the system used, but it is usually recommended to update every 10 to 20 steps. There are also some algorithms that does the updated following some specific rules, but it depends on the system where the Verlet list is being used.

Figure 4.3 – The cutoff and skin spheres around the particle 1. The particles 2, 3, 4, 5 and 6 are on the list of particle 1, but particle 7 is not on the list. Only particles 2, 3 and 4 are within the range of the potential cutoff at the time the list is constructed (From M. P. Allen, D. J. Tildesley, and L. Allen [153]).

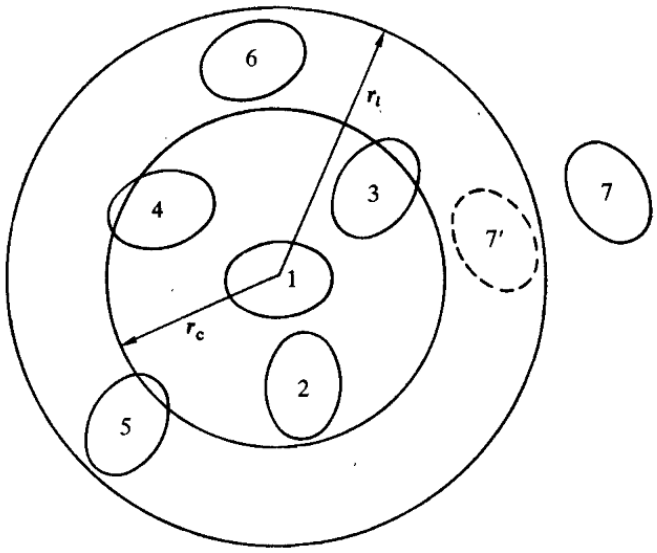

Although the Verlet list is proven to be good method, it is not ideal for system with great number of particles. As the size of the system increases towards 1000 particles, the Verlet list becomes too large to store easily, and the logical testing of every pair is inefficient. Therefore, another method is necessary. The cell structures method is based on cubic cells divided in a regular lattice of $M \times M$, see Fig. 4.4. These cells must be chosen so the side of the cell $l = L/M$ is greater than the cutoff distance of the forces, where L is the side length of the main simulation box. As shown in Fig. 6.4, the particles inside cell 13 have neighbors in cells 7, 8, 9, 14, 19, 18, 17 and 12. In each cell, there is approximately $N_c = N/M^2$ particles. Using this cell structure, we need only to examine $9NN_c$ pairs. This is a great contrast with the case of no neighbor lists, where it is necessary to examine N^2 pairs.

The first step is to sort all particles into the appropriate cells. This sorting process is fast, and may be done in every step. After that, the particle in a given cell must interact with all particles inside its own cell and then with neighbor cells. Note that a cutoff can be associated in this process, as some particles in neighbor cells may surpass the cutoff limit. For example, a particle inside cell 13 must interact with all particles inside 13 and also with particles inside 7, 8, 9, 14, 19, 18, 17 and 12. Some particles inside cell 7, for example, may be over the distance $r_d = 6.0$, so using this method associated with the cutoff is the most efficient. For boxes in the edge of the main simulation box, periodic boundary conditions are necessary. For example, the particles in box 5 should interact with particles in boxes 4, 9 and 10, and also 24, 25, 21, 1 and 6 of the image boxes. Fig. 4.5 shows a visual illustration of these periodic boundary conditions for the cells.

Figure 4.4 – The cell method in two dimensions. The main simulation box is divided into $M \times M$ cells (in this illustration, $M = 5$) (From M. P. Allen, D. J. Tildesley, and L. Allen [153]).

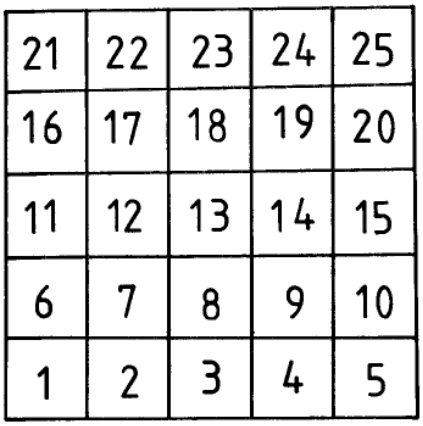

Figure 4.5 – Periodic boundary conditions being applied to a cell on the edge of the main simulation box. Particles inside the cell in red interact with particles from the opposite side of the main simulation box.

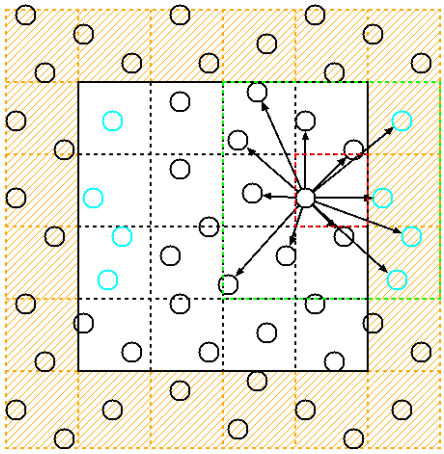

If this method is used with a small quantity of particles inside the simulation box, its speeding effect may not be seen, but for high density of particles the speeding effect is very significant. In the simulations made in this project, most of them were using a single skyrmion interacting with an obstacle array. For a single skyrmion this method is not necessary for skyrmion-skyrmion interaction. However, for the skyrmion-obstacle interaction this method is efficient, reducing the time for force calculations. In this thesis there are calculations made for a high number of skyrmions, as may be explained later. For these particular cases this cell neighbor list method was used and improved a lot the MD program running time.

Part I

Skyrmions Interacting with Periodic Substrates

5 Skyrmion Dynamics and Topological Sorting on Periodic Obstacle Arrays

5.1 Obstacle size and Topological Sorting

In this work we simulate the dynamic behavior of skyrmions under the influence of a square lattice of obstacles. This work was published at New Journal Of Physics [137] and was the first paper from this thesis. Here, it is considered a single skyrmion dynamics under the influence of a square array of obstacle and zero temperature. The effects on varying the size of the obstacles are analyzed. A visual representation of this system can be seen in Fig. 6.1, where a skyrmion flows under the influence of a square obstacle array. The results show that as the obstacle size is changed, several dynamic phases may appear or vanish. For smaller obstacles, the system exhibits fewer dynamic phases due to the reduced size of obstacles that reduce its influence on the system. On the other hand, if the obstacle size is too large, the system may also exhibit fewer dynamic phases due to the reduction in the size of the gaps between the obstacles, which reduces the possibilities for skyrmion motion. Hence, the highest number of dynamic phases appears for intermediate values of obstacle sizes. We also investigate the influence of the damping term, α_d, on the dynamics of the system. For systems with low damping, the skyrmion is locked parallel to the applied current, however for systems with high damping the skyrmion is locked perpendicular to the applied current. Thus, the damping term and the obstacle size can be used to control the skyrmion motion. Motivated by these results, the dynamic behavior of skyrmions of different species is analyzed under the influence of the obstacle array. The results indicate that it is possible to separate the species according to their skyrmion Hall angles when a driving current is applied.

5.2 Model and Simulation details

In this work we consider a two-dimensional skyrmion system with $L \times L$ with periodic boundary conditions on y and x directions. First, a single skyrmion is subjected to this obstacle landscape in order to characterize its movement. Then, we introduce more skyrmions with total number as $N = N_a + N_b$, where N_a are the number of skyrmions of species a and N_b are the number of species b. We also set $N_a = N_b = N/2$. Here, skyrmions of different species represent skyrmions with different sizes, that can coexist with each other in a given sample [8,64,154,155]. The skyrmion density in the sample is $n_s = N/L^2$, using $L = 36\xi$. The

dynamical properties of this skyrmion system interacting with the obstacle array were simulated using the particle model for skyrmions, shown in Eq. (5.1), using Molecular Dynamics technique.

$$\alpha_d^\gamma \mathbf{v_i} + \alpha_m^\gamma \hat{z} \times \mathbf{v_i} = \mathbf{F}_i^{ss} + \mathbf{F}_i^o + \mathbf{F}^D \tag{5.1}$$

In this equation, the first term on the left is the damping term, where α_d^γ is the damping term of the species γ, where γ may be a or b. The second term on the left represents the Magnus force, where α_d^γ is the Magnus term of the species γ. The Magnus force produces a force that is perpendicular to the skyrmion velocity. The first term on the right is the skyrmion repulsive interaction with other skyrmions, where it is described as $\mathbf{F}_i^{ss} = \sum_i^N K_1(r_{ij}/\xi)\hat{\mathbf{r}}_{ij}$ [73], discussed previously in section 2.3. Here, ξ is the screening length which we take to be 1.0 in dimensionless units, $r_{ij} = |\mathbf{r}_i - \mathbf{r}_j|$ is the distance between skyrmions i and j, and $\hat{\mathbf{r}}_{ij} = (\mathbf{r}_i - \mathbf{r}_j)/r_{ij}$. The second term on the right of Eq. (5.1) is the interaction between the skyrmions and the obstacles. We model this potential energy interaction in the repulsive Gaussian form $U_o = C_o e^{-(r_{io}/a_o)^2}$, where C_o is the strength of the obstacle potential, r_{io} is the distance between the skyrmion i and the obstacle o, and a_o is the obstacle radius. Thus, the force between the obstacles and the skyrmions take the form $\mathbf{F}_i^o = -\nabla U_o = -F_o r_{io} e^{-(r_{io}/a_o)^2}\hat{\mathbf{r}}_{io}$, where $F_o = 2C_o/a_o^2$. The obstacle density used in this work is $0.093/\xi^2$. The third term on the right side, $\mathbf{F}^D = F^D\hat{\mathbf{d}}$, where $\hat{\mathbf{d}}$ is the direction of the dc driving force, is the force interaction between the skyrmion and the external current. In this work the applied dc drive is in x direction, so $\hat{\mathbf{d}} = \hat{\mathbf{x}}$. We measure the skyrmion velocity parallel, $\langle V_\parallel \rangle$, and perpendicular, $\langle V_\perp \rangle$, to the drive. When the skyrmion is flowing without obstacles in the overdamped limit $\alpha_m/\alpha_d = 0$, the skyrmion moves only in the direction of the drive. However, if there is a finite value for α_m/α_d, the skyrmion moves with a Hall angle, $\Theta = \arctan(\langle V_\perp \rangle/\langle V_\parallel \rangle) = \arctan(\alpha_m/\alpha_d)$. If one increases the quantity α_m/α_d, the angle Θ is increased respective to the drive. In order to quantify the direction of the skyrmion motion we measure $R = \langle V_\perp \rangle/\langle V_\parallel \rangle$. The external drive is increased in small steps of $\delta F = 0.001$ and wait 10^5 simulation time steps between increments to ensure steady state. Unless otherwise noted, we normalize the damping and magnus coefficients as $\alpha_d^2 + \alpha_m^2 = 1$.

5.3 Results

5.3.1 Obstacle Size Effect

First, we consider the case of a single skyrmion moving under the influence of the square array of obstacles. Our main goal here is to understand how the obstacle size affects the dynamics of the system. Thus, we begin looking to the case where $a_0 = 0.65$ with $\alpha_m/\alpha_d = 0.45$. In Fig. 5.1 (a), it is plotted the average velocity curves, $\langle V_\parallel \rangle$ and $\langle V_\perp \rangle$, as a function of the applied dc drive, F^D. In Fig. 5.1 (b) it is plotted the R curve as a function of F^D.

Figure 5.1 - (a) the average velocity curves $\langle V_\parallel \rangle, \langle V_\perp \rangle$ as a function of the transport force F^D containing a single skyrmion where $a_o = 0.65$ and $\alpha_m/\alpha_d = 0.45$. For $F^D < 1.0$ the motion is strictly in the x direction, parallel to the driving force. (b) the corresponding skyrmion Hall angle $\theta_{sk} = \arctan(R)$ vs F^D curve (From Vizarim *et. al.* [137], pg. 4).

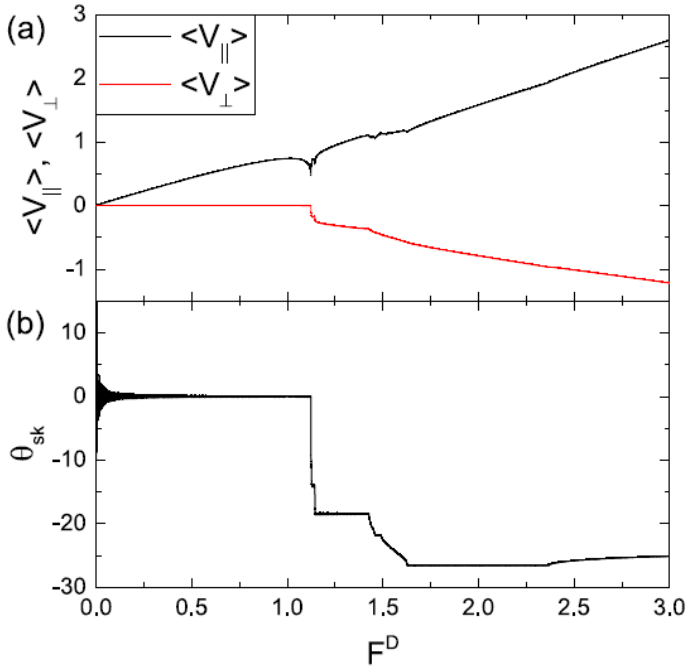

If there are no obstacles, the skyrmion flows at the intrinsic skyrmion Hall angle, $\theta_{sk}^{int} = \arctan(\alpha_m/\alpha_d) = 24.23°$. However, as can be seen from Fig. 5.1, for $F^D < 1.0$ the skyrmion velocities are $\langle V_\perp \rangle = 0$ and $\langle V_\parallel \rangle$ increases with the applied drive, so that the skyrmion Hall angles is $\theta_{sk} = 0°$, that is, moves exclusively in the x direction. As shown in Fig. 5.2 (a), at $F^D = 0.5$, the skyrmion exhibits an oscillatory motion in y but translates only in the x direction. As the applied drive, F^D, increases, the skyrmion starts to move in both $+x$ and $-y$ directions. At the transition to a finite $\langle V_\perp \rangle$, there is a drop in $\langle V_\parallel \rangle$, indicating that the particle is slowing down in the x direction as a function of F^D just before the transition. This indicates the appearance of a negative differential conductivity with $d\langle V_\parallel \rangle/dF^D < 0$. For higher F^D, several

additional dips and cusps appear in both $\langle V_{\parallel} \rangle$ and $\langle V_{\perp} \rangle$ indicating other transitions. As shown in Fig. 5.1 (b), the skyrmion Hall angle in quantized, similar to what has been found in previous work with skyrmions with periodic substrates [39].

In Fig. 5.2 (b), it is illustrated the skyrmion motion for $R = -0.33$ ($\theta_{sk} = -18.43°$) at $F^D = 1.25$. The orbit winds periodically around the system and the skyrmion undergoes multiple collisions with the obstacles during its course. As F^D increases, the magnitudes of both $\langle V_{\parallel} \rangle$ and $\langle V_{\perp} \rangle$ jumps up and the system reaches the $R = -0.5$ ($\theta_{sk} = -26.56°$). The corresponding motion appears in Fig. 5.2 (c) for $F^D = 2.0$, where the skyrmion moves 2 lattice constants in $+x$ for every one lattice in $-y$. Note that this means that the skyrmion is moving with an angle *higher* than its intrinsic Hall angle, $\theta_{sk}^{int} = 24.23°$. The strong locking step in $R = -0.5$ pulls the skyrmion to this higher Hall angle due to the symmetry of the obstacle landscape. It is a clear effect of the obstacle array on the skyrmion dynamics. The skyrmion remains locked in $R = -0.5$ until $F^D > 2.3$, after which the skyrmion motion drops to a lower value of θ_{sk}, which rapidly approaches the intrinsic Hall angle value.

In Fig. 5.3 it is plotted θ_{sk} versus F^D for a system with $\alpha_m/\alpha_d = 0.45$ at varied obstacle sizes $a_0 = 0.15$ to $a_0 = 1.0$. For smaller obstacles, the skyrmion initially moves at an angle close to the intrinsic Hall angle of $\theta_{sk}^{int} = 24.23°$ since it experiences very few collisions and influence of the obstacles in the sample. When $a_0 = 0.2$, the system starts off in the $R = -0.5$ ($\theta_{sk} = 26.56°$) state and jumps to the $R = -0.45$ ($\theta_{sk} = 24.23°$) state at higher drives. For $a_0 \geq 0.65$, the system initially locks with $R = 0$ state. At the largest value of obstacle size, $a_0 = 1.0$, it is possible to a see a series of smaller steps at rational fractions of $R = -n/m$, and at large drives, R gradually approaches the intrinsic value. In Fig. 5.2 (d) it is plotted the skyrmion trajectory for the system in Fig. 5.3 with $a_0 = 0.15$ at $F^D = 0.5$, where the motion is locked at $R = -0.45$ state, while in Fig. 5.2 (e) at $F^D = 0.5$ and $a_0 = 0.2$ the motion is now locked in $R = -0.5$ state. In Fig. 5.2 (f) it is illustrated the skyrmion trajectory for $a_0 = 0.2$ and $F^D = 2.0$, where the trajectory is almost linear due to the reduced size and influence of obstacles.

Figure 5.2 – (a) – (c) The obstacles (open circles) and the skyrmion trajectory (black lines) for the system in Fig. 5.1 with $a_0 = 0.65$ and $\alpha_m/\alpha_d = 0.45$. (a) $F^D = 0.5$, where $R = 0$. (b) $F^D = 1.25$, where $R = -1/3$ and the system is on a locking step. (c) $F^D = 2.0$, where $R = -0.5$. (d) Obstacle and skyrmion trajectories for the system in Fig. 5.3 with $a_0 = 0.15$ and $\alpha_m/\alpha_d = 0.45$ at $F^D = 0.5$ and $R = -0.45$. (e) – (f) The same for the system in Fig. 5.3 with $a_0 = 0.2$ and $\alpha_m/\alpha_d = 0.45$. (e) $F^D = 0.5$, where $R = -0.5$ and (f) $F^D = 2.0$, where $R = -0.45$ (From Vizarim *et. al.* [137], pg. 5).

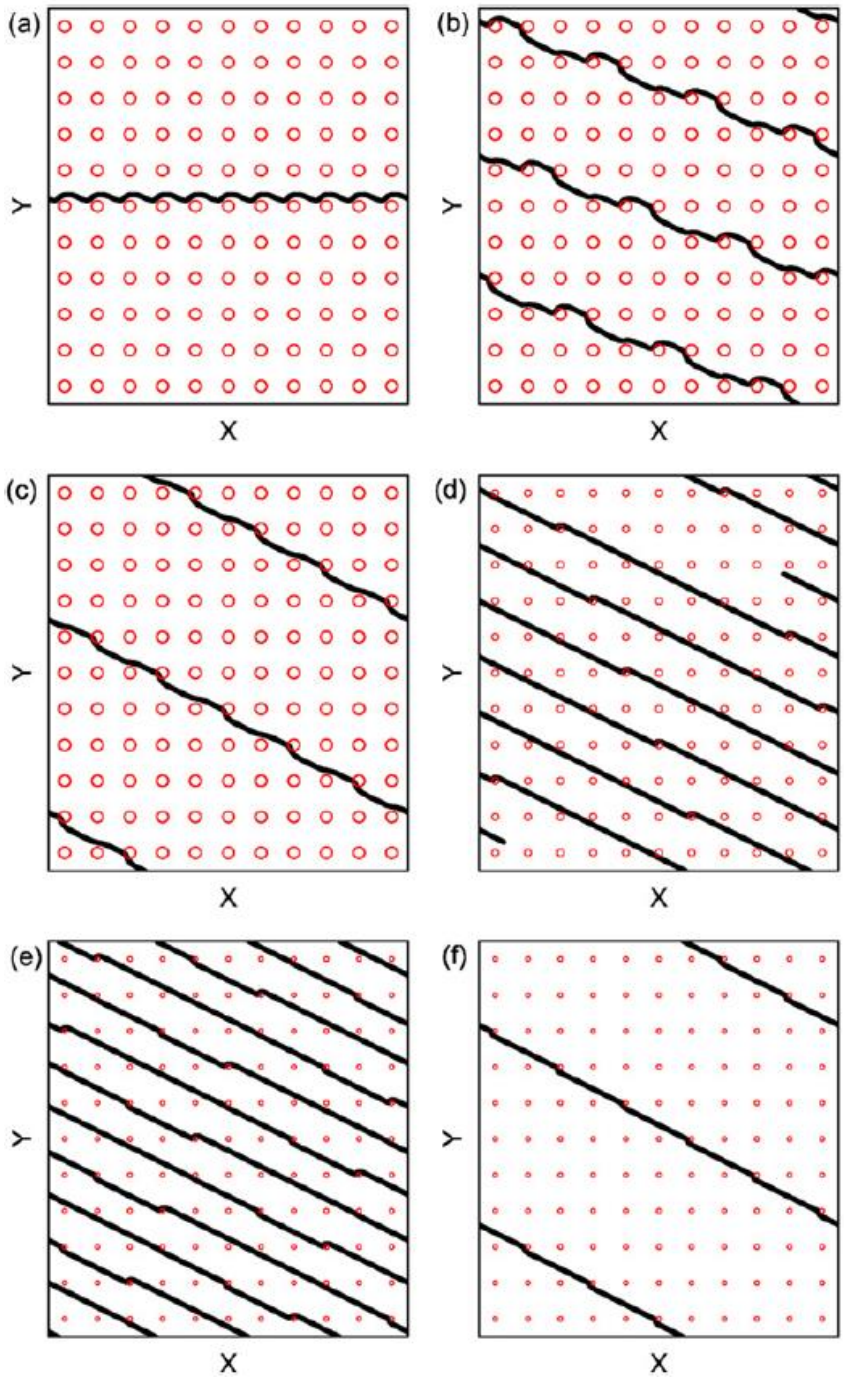

Figure 5.3 – The skyrmion Hall angle, $\theta_{sk} = \arctan R$ vs. F^D, where $R = \langle V_\perp \rangle / \langle V_\parallel \rangle$, in samples with $\alpha_m/\alpha_d = 0.45$ at varied a_0 (From Vizarim *et. al.* [137], pg. 5).

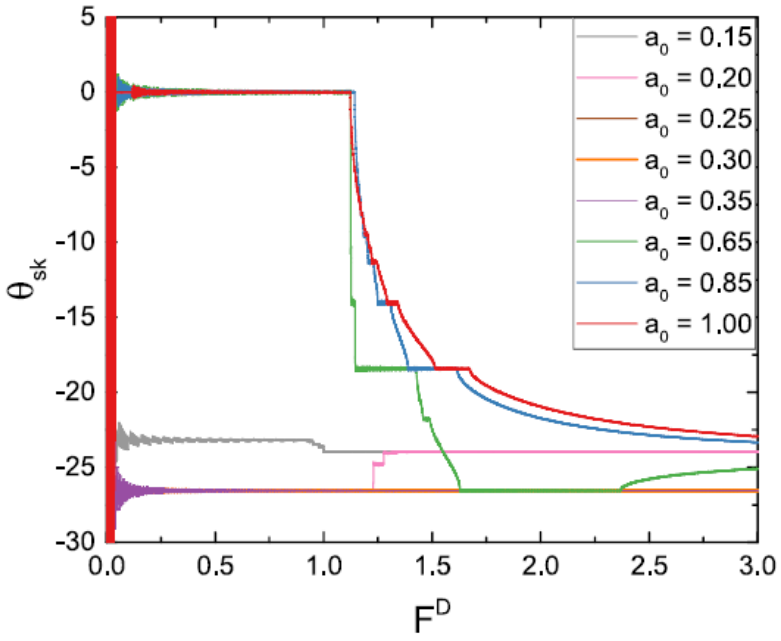

We can also characterize the different locking phases by examining the width of the force interval ΔF^D over which the system remains locked to a given direction of motion for varied values of a_0. This may be helpful in a given device in which it is necessary to move a skyrmion at a given direction, so this may help to choose the appropriate obstacle size and range of transport forces to set the direction of the skyrmion motion. In Fig. 5.4 it is plotted the locking intervals F^D for select cases of $\theta_{sk} = 0°, -14°, -18.3°, -26.6°$ steps using $\alpha_m/\alpha_d = 0.45$. The phase where $\theta_{sk} = 0°$ appears for $a_0 > 0.3$ and saturates to a maximum width near $a_0 = 0.7$. The width of $R = -26.6°$ step is large when $a_0 = 0.25$, decreases for increasing a_0, and drops to zero when $a_0 > 0.7$. The widths of $\theta_{sk} = -14.3°$ and $-18.3°$ steps are smaller but generally increase with increasing a_0. In the presence of random pinning, the skyrmion Hall angle increases roughly linear with the external drive, $\theta_{sk} \propto F^D$, until it saturates near θ_{sk}^{int} [28]. This linear increase in θ_{sk} is preserved when the pinning is periodic, but it is accompanied by locking steps that occur when the Hall angles matches the symmetry angles of the square array, $\theta_{sk} = \arctan(p/q)$ with integer p and q. On the locking steps, the skyrmion translates by an integer number p obstacles in y direction and a q number of obstacles in the x direction. The system remains locked on a step over a window of driving forces before unlocking.

Figure 5.4 - Range of forces ΔF^D as a function of the obstacle radius a_o for a single skyrmion in the square obstacle array using $\alpha_m/\alpha_d = 0.45$ (From Vizarim *et. al.* [137], pg. 6).

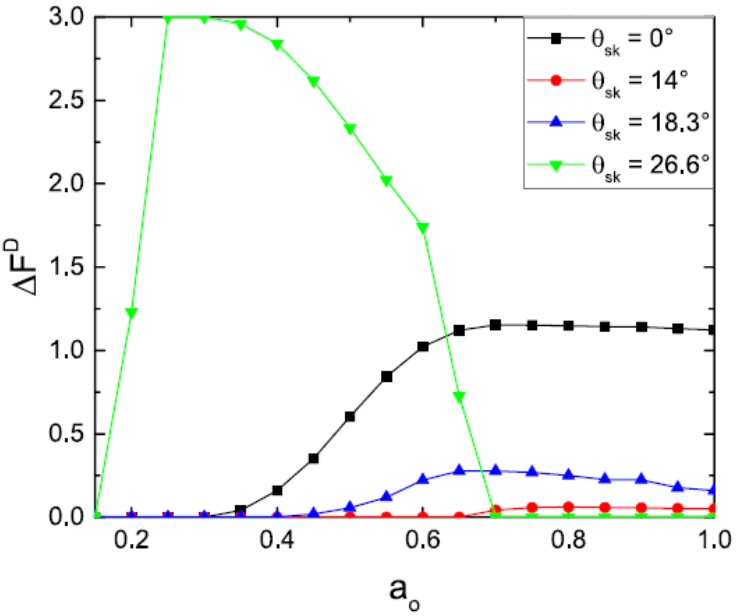

If the ratio α_m/α_d is changed, the skyrmion can move with higher intrinsic Hall angles, making it possible to observe a larger number of locking steps. In Fig. 5.5 (a) it is plotted θ_{sk} vs. F^D for samples with $\alpha_m/\alpha_d = 1.91$ with varied size of obstacles, from $a_o = 0.15$ to $a_0 = 1.0$. It can be seen clearly some pronounced locking steps at $R = 0\ (0°)$, $-1.0\ (-45°)$, $-1.5\ (-56.3°)$, $-2.0\ (-63.4°)$ and $-1.91\ (-62.37°)$ along with some higher order steps. When $a_0 = 0.15$ th skyrmion remains locked at $R = -1.91$, while when $a_0 = 0.25$, the skyrmion is initially locked in $R = -2.0$, corresponding to Hall angle that is *higher* than the intrinsic Hall angle. When $a_o \geq 0.65$, the $R = 0$ state appears at low drives, and for $a_0 = 0.85$, there are additional number of locking steps such as $R = -1.25\ (-51.34°)$, $-1.33\ (-53.06°)$, $-1.67\ (-59.08°)$. In Fig. 5.6 it is plotted the skyrmion trajectories for the system in Fig. 5.5 (a) with $a_0 = 0.65$ at $F^D = 0.04$ in the $R = 0\ (0°)$ state, while in Fig. 5.6 (b) it is shown the trajectories in the same system but with $F^D = 0.5$ and $R = -1.0\ (-45°)$. At $F^D = 1.0$ the skyrmion is in the $R = -1.5\ (-56.3°)$ state, which is illustrated in Fig. 5.6 (c). In this case the skyrmion moves 3 lattice constants in the y direction while moving 2 lattice constants in the x direction. If the obstacle size is reduced to $a_0 = 0.2$, then for $F^D = 1.0$ the skyrmion moves in the $R = -1.85\ (-61.6°)$ state, shown in Fig. 5.6 (d). In Fig. 5.5 (b), it is plotted ΔF^D versus a_0 for the same system highlighting some of the most pronounced states $\theta_{sk} = 0°, -45°, -56.3°$ and $-63.4°$.

Figure 5.5 – (a) The skyrmion Hall angle, $\theta_{sk} = \arctan R$ vs. F^D, where $R = \langle V_\perp \rangle / \langle V_\parallel \rangle$, in samples with $\alpha_m/\alpha_d = 1.91$ at varied a_0. (b) Range of forces ΔF^D as a function of the obstacle radius a_o for a single skyrmion in the square obstacle array using $\alpha_m/\alpha_d = 1.91$ (From Vizarim *et. al.* [137], pg. 6).

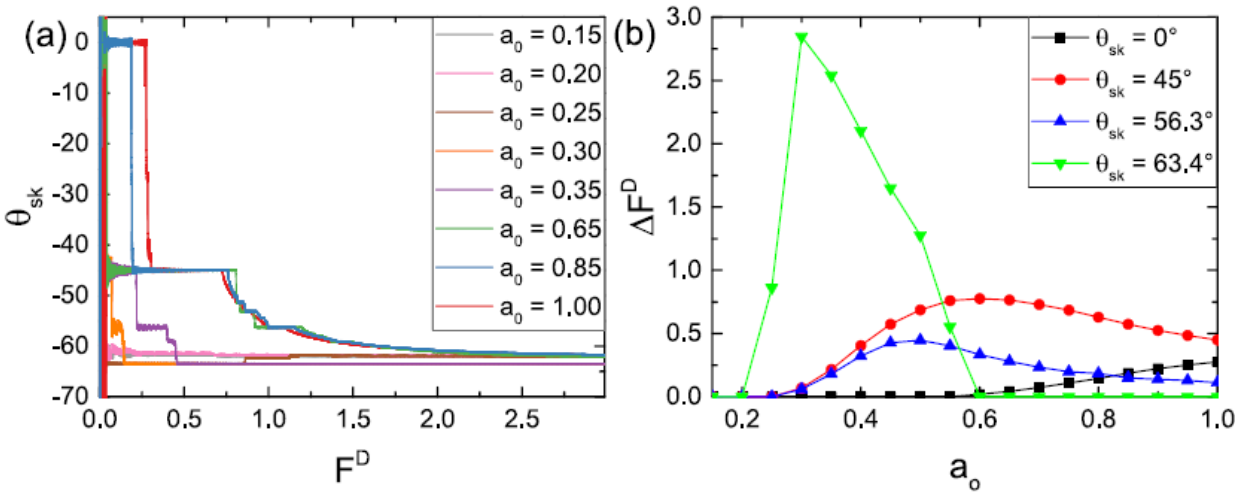

Figure 5.6 – The obstacles (open circles) and the skyrmion trajectory (black lines) for the system in Fig. 5.5 (a) with $\alpha_m/\alpha_d = 1.91$. (a) The $R = 0$ state for $a_0 = 0.65$ and $F^D = 0.04$. (b) The $R = -1.0$ state for $a_0 = 0.65$ and $F^D = 0.5$. (c) The $R = -1.5$ state for $a_0 = 0.65$ and $F^D = 1.0$. (d) The $R = -1.85$ state for $a_0 = 0.2$ and $F^D = 1.0$. (From Vizarim *et. al.* [137], pg. 6).

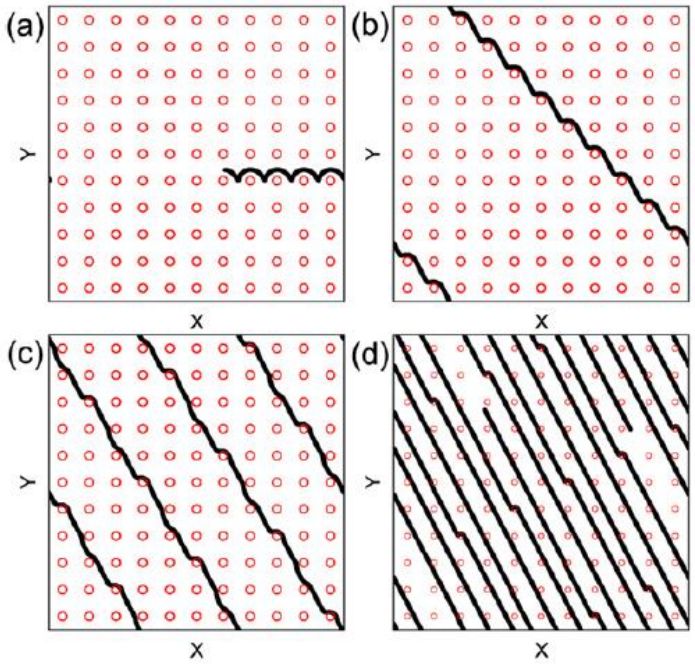

In Fig. 5.7 (a) it is plotted $\theta_{sk} = \arctan R$ versus F^D for samples with $\alpha_m/\alpha_d = 4.925$ where a_0 ranges from $a_0 = 0.15$ to $a_0 = 1.0$. Here, even more steps of direction of motion are found, ranging from $R = 0(0°)$ to $R = -4.8(-78.23°)$, with prominent steps at $R = 0(0°), -1.0\ (-45°), -2(-63.4°), -3(-71.6°), -4(-75.9°)$ as well as many additional steps. In Fig. 5.7 (b) it is shown ΔF^D versus a_0 for $\theta_{sk} = 0°$ to $\theta_{sk} = -78.2°$. As the obstacle size a_0 increases it is possible to observe an increase in the number of different allowed steps. In Fig.

5.8 it is illustrated some select trajectories for the system of Fig. 5.7 (a) using $a_o = 1.0$. In Fig. 5.8 (a) shows the $R = -1.0$ $(-45°)$ state where the skyrmion follows a sinusoidal path between the large obstacles. In Fig. 5.8 (b) the trajectories for the $R = -2.0$ $(-63.4°)$ state, while in Fig. 5.8 (c) the trajectories for $R = -3.0$ $(-71.6°)$ state. At $R = -4.0$ $(-75.9°)$ state the skyrmion trajectory becomes greatly tilted due to the strong Magnus term.

Figure 5.7 – (a) The skyrmion Hall angle, $\theta_{sk} = \arctan R$ vs. F^D, where $R = \langle V_\perp \rangle / \langle V_\parallel \rangle$, in samples with $\alpha_m/\alpha_d = 4.925$ at varied a_0. (b) Range of forces ΔF^D as a function of the obstacle radius a_o for a single skyrmion in the square obstacle array using $\alpha_m/\alpha_d = 4.925$ (From Vizarim *et. al.* [137], pg. 7).

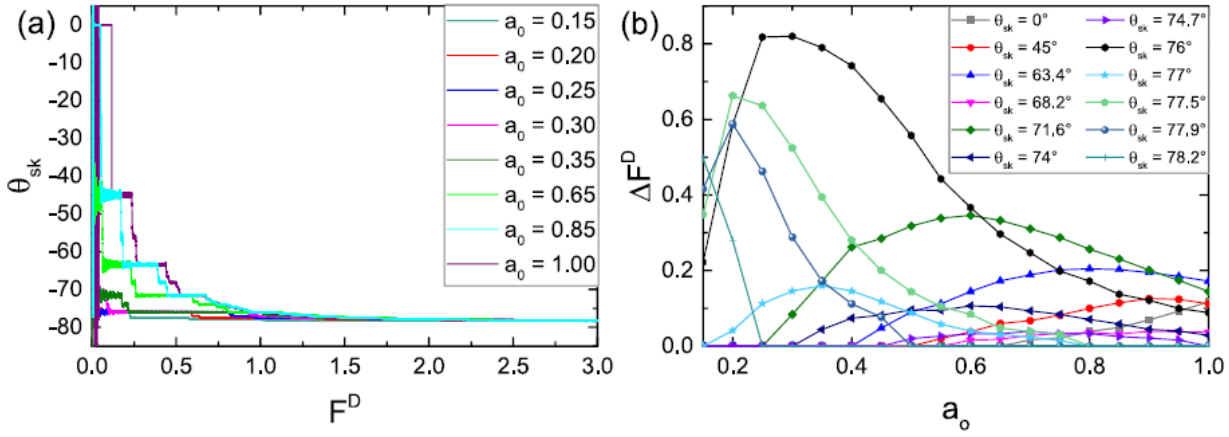

Figure 5.8 – The obstacles (open circles) and the skyrmion trajectory (black lines) for the system in Fig. 5.7 (a) with $\alpha_m/\alpha_d = 4.925$ and $a_0 = 1.0$. (a) The $R = -1.0$ state, (b) the $R = -2.0$, (c) the $R = -3.0$ state and (d) $R = -4.0$ state. (From Vizarim *et. al.* [137], pg. 8).

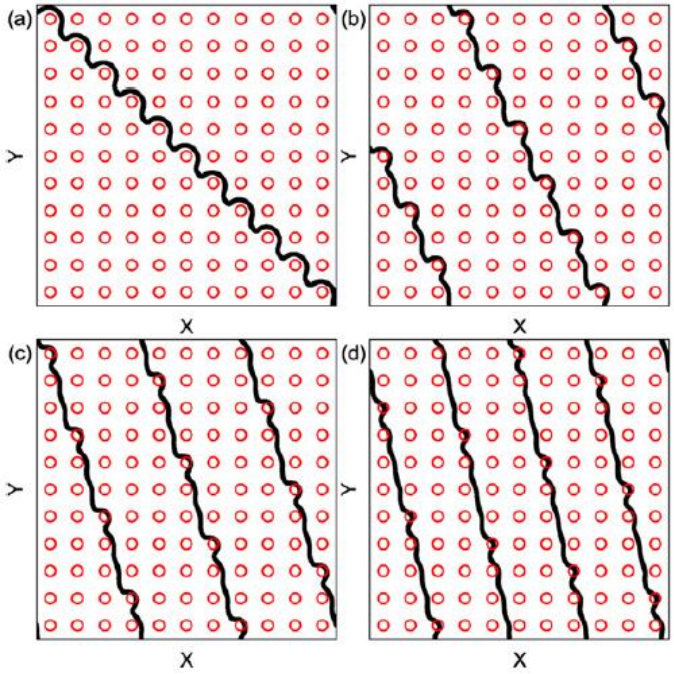

5.3.2 The Damping Effect

Besides the obstacle array and size, a recent work also provided new insights about a controlled motion for skyrmions related to the damping term α_d and to the parameters of an applied current pulse [114]. Here, we investigate the damping effect using a dc drive that is increasing slowly. In this section we no longer use the constraint $\alpha_d^2 + \alpha_m^2 = 1$, we set $\alpha_m = 1$ and vary the term α_d. In Fig. 5.9 (a) it is plotted the perpendicular and parallel velocity components versus F^D for a system with $a_0 = 0.65$ at $\alpha_d = 0.0, 0.2$ and 0.4. It is possible to see that a series of dips in both velocity components that are associated with directional locking effects. In Fig. 5.9 (b), where $\alpha_d = 0.6, 0.8$ and 1.0, the $\alpha_d = 0.6$ exhibits the most prominent steps. The velocity force curves for $\alpha_d = 1.5, 2.0, 5.0$ and 10.0 in Fig. 5.9 (c) indicate that $\langle V_\parallel \rangle$ becomes more prominent for increased values of α_d.

Figure 5.9 - In (a), (b) and (c), the average velocity curves $\langle V_\parallel \rangle, \langle V_\perp \rangle$ as a function of the transport force F^D for a single skyrmion in the square obstacle array for varied values of α_d, fixed $\alpha_m = 1.0$ and $a_0 = 0.65$ (From Vizarim *et. al.* [137], pg. 8).

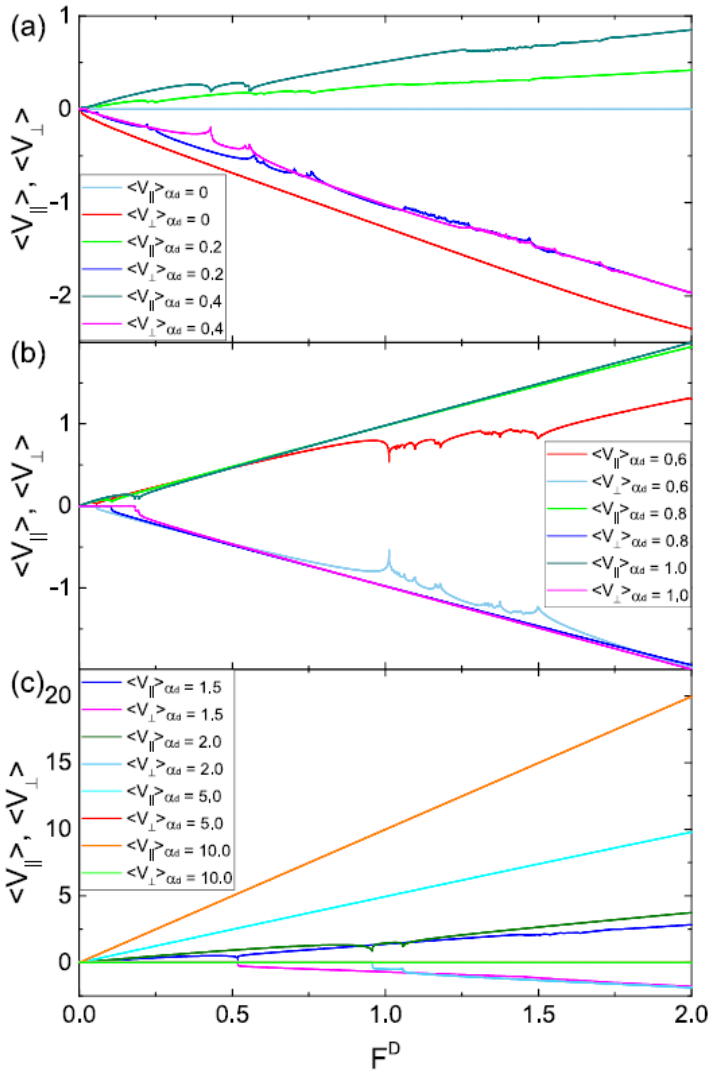

In Fig. 5.10 (a) it is plotted θ_{sk} versus F^D for the system of Fig. 5.9. As α_d increases, fewer steps appear in the Hall angle curve. The largest number of transitions occurs for the lowest value of damping term, $\alpha_d = 0.2$. In Fig. 5.10 (b) shows the θ_{sk} versus F^D for higher values of damping, $\alpha_d = 1.5, 2.0, 5.0$ and 10.0, where steps occur at $\theta_{sk} = 0°, -18.3°, -26.56°$ and $-33.42°$.

Figure 5.10 - In (a) and (b) the θ_{sk} vs F^D curve for the system of Fig. 5.9 with fixed $\alpha_m = 1.0$ and $a_0 = 0.65$ (From Vizarim *et. al.* [137], pg. 9).

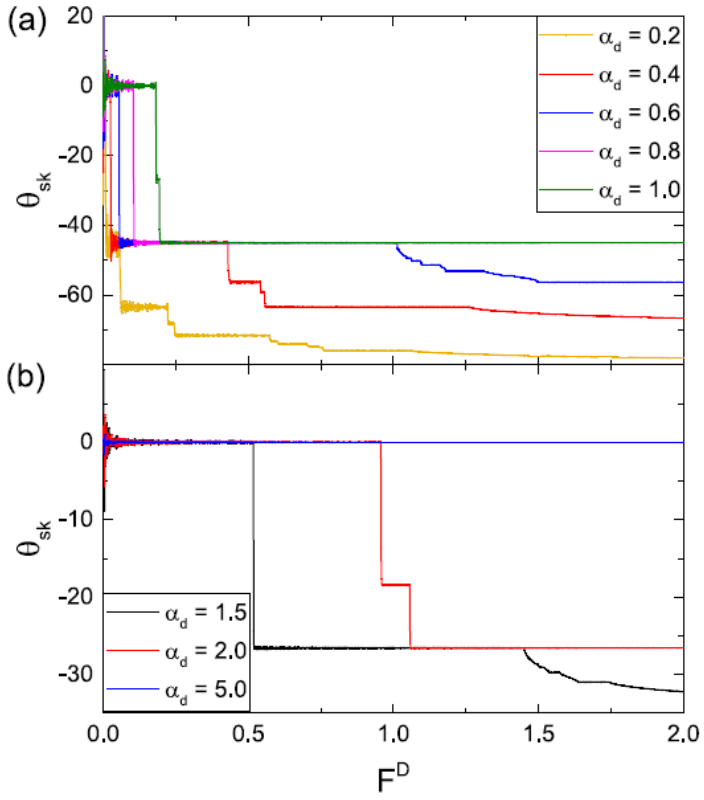

In Fig. 5.11 it is plotted the skyrmion trajectories for the systems of Fig. 5.9 and 5.10 for $\alpha_d = 0$, 2.0 and 5.0 at $F^D = 1.0$. In the limit case of zero damping, $\alpha_d = 0$, the skyrmion moves with $\theta_{sk} = 90°$ with respect to the driving force. For $\alpha_d = 5.0$, the skyrmion is locked at the state $R = 0\ (0°)$, while for $\alpha_d = 2.0$ the skyrmion is locked at the state $R = -0.5\ (-26.56°)$, which indicates that the skyrmion motion is strongly dependent on the damping term.

In Fig. 5.12 it is plotted $\langle V_\perp \rangle$ and $\langle V_\parallel \rangle$ versus F^D for a system with large obstacle $a_0 = 1.3$ for damping value of $\alpha_d = 0$, 0.2 and 0.4. For zero damping, the parallel skyrmion velocity is null, $\langle V_\parallel \rangle = 0$, for all values of external driving force. The depinning threshold occurs for $F^D = 0.255$, where the perpendicular velocity becomes finite. There is also a partial two step

depinning process, where the second depinning threshold occurs at $F^D = 0.976$. In Fig. 5.12 (b) and (c) it is illustrated the skyrmion trajectories for this system. At $F^D = 0.5$, shown in Fig. 5.12 (b), the skyrmion is strongly oscillating between obstacles, while in Fig. 5.12 (c) at $F^D = 1.0$, above the second step, the skyrmion flows more freely through the column of obstacles, with lower oscillation. For the case of $\alpha_d = 0.2$, in Fig. 5.12 (a), there is still a sharp depinning transition along with a series of jumps in both $\langle V_\parallel \rangle$ and $\langle V_\perp \rangle$. It is also possible to observe an extended interval of F^D over which $\langle V_\parallel \rangle$ decreases with increasing F^D, but for $F^D > 1.0$, $\langle V_\parallel \rangle$ increases monotonically with the external driving force.

Figure 5.11 - The obstacles (open circles) and the skyrmion trajectory (lines) for a system with $a_0 = 0.65$ at $\alpha_d = 0$ (black), 2.0 (green) and 5.0 (orange). (From Vizarim *et. al*. [137], pg. 9).

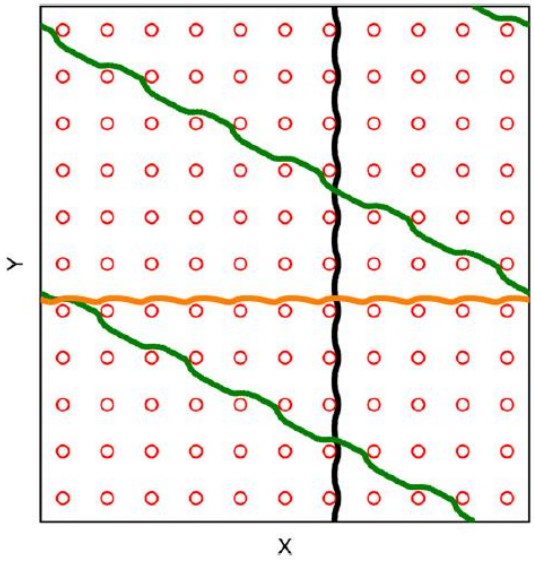

In Fig, 5.13 (a) it is plotted $\langle V_\perp \rangle$ and $\langle V_\parallel \rangle$ versus F^D for a system with fixed $\alpha_m = 1.0$ and $a_0 = 1.3$ using $\alpha_d = 0.6$, 0.8 and 1.0. There is a finite depinning threshold for motion in both parallel and perpendicular directions, and the width of the state $R = 0$ (0°) grows with increasing damping. In Fig. 5.13 (b) it is shown $\langle V_\perp \rangle$ and $\langle V_\parallel \rangle$ versus F^D for $\alpha_d = 1.5$, 2.0, 5.0 and 10.0, where the depinning transition still sharp and the number of steps in the velocity-force curves decreases with increasing damping. In general, for the drive at which $\langle V_\perp \rangle$ becomes finite, the magnitude of $\langle V_\parallel \rangle$ drops. In Fig. 5.13 (c) it is shown the Hall angle curve as a function of the drive for the samples of Fig. 5.13 (a) and (b), where a series of locking steps occur.

These results indicate that the skyrmion Hall angle can be controlled precisely in systems with periodic substrates. This also implies that it may be possible to create new types of transitor-like devices by exploiting the sharp jumps between the different Hall angles. In this case, certain values of R or θ_{sk} could be used to achieve a specific resistance value. It could also

be possible to create periodic arrays with obstacles of different sizes that would allow skyrmions to have one value of θ_{sk} in one part of the sample, and different value of θ_{sk} in another part of the sample.

Figure 5.12 – (a) $\langle V_{\parallel} \rangle$ and $\langle V_{\perp} \rangle$ versus F^D for a system with $\alpha_m = 1.0$ for varied values of α_d. (b) and (c) The obstacles (open circles) and the skyrmion trajectory (black lines) for a system with $a_0 = 1.3$ and $\alpha_d = 0$ for (b) $F^D = 0.5$ and (c) $F^D = 1.0$ (From Vizarim *et. al.* [137], pg. 10).

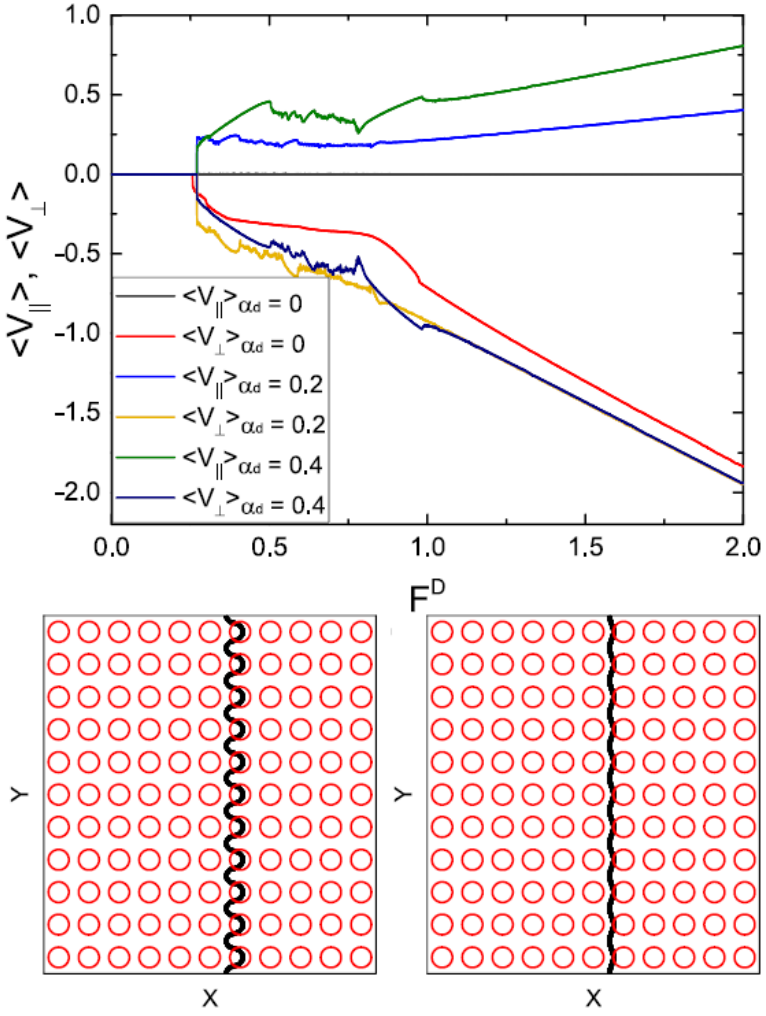

Figure 5.13 - In (a) and (b) the average velocity curves $\langle V_{\parallel}\rangle, \langle V_{\perp}\rangle$ as a function of the transport force F^D for a single skyrmion in the square obstacle array using $\alpha_m = 1.0$ and $a_0 = 1.3$. In (c) the θ_{sk} vs F^D curve for the different damping term values. (Adapted from Vizarim *et. al.* [137], pg. 11).

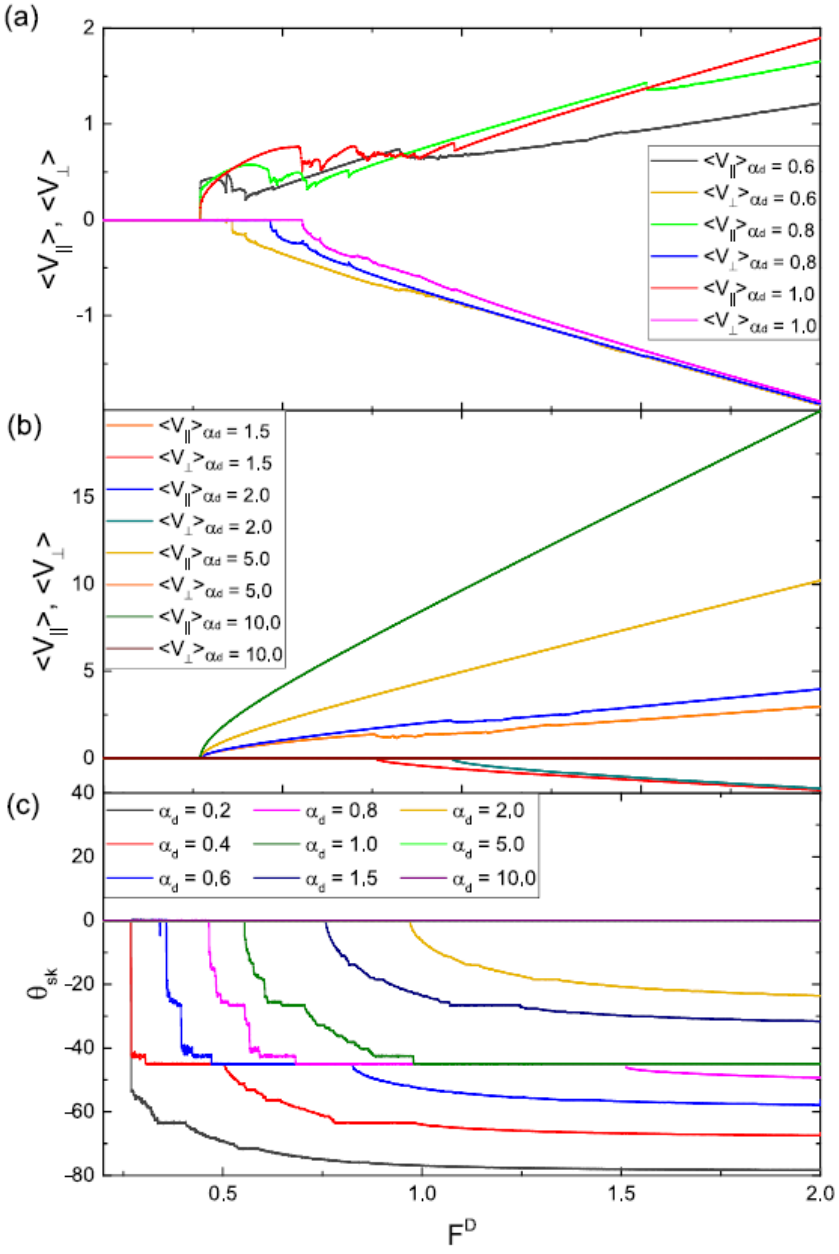

5.3.3 Attractive Pinning Sites

In this section it is considered the case of attractive pinning sites instead of the repulsive obstacles, which can be achieved by just changing the signal of C_0, the strength of the pinning potential. A single skyrmion not subjected to a drive stabilizes inside the pinning center, and there is a finite depinning threshold or driving force necessary to remove the skyrmion from the pinning center and start its motion. In Fig. 5.14 (a) it is plotted $\langle V_{\perp}\rangle$ and $\langle V_{\parallel}\rangle$ versus F^D for the same system of Fig. 5.1 containing a single skyrmion where $a_o = 0.65$ and $\alpha_m/\alpha_d = 0.45$, but using attractive pinning sites. In Fig. 5.14 (c) shows the corresponding skyrmion Hall angle

curve. Unlike the systems with obstacles, where the skyrmion flows along the x direction at low drives, for the attractive pins it is found a pinned phase where the skyrmion has no motion in both x or y directions. On the other hand, it is still possible to see quantized skyrmion Hall angle behavior after the depinning threshold, but they are strongly reduced in size when compared to the systems with obstacles. In Fig. 5.14 (b) it is plotted $\langle V_\perp \rangle$ and $\langle V_\parallel \rangle$ versus F^D for the same system, but using $\alpha_m/\alpha_d = 1.91$ and $a_0 = 1.0$. In this case the depinning threshold is lower, and although steps appear in the velocity and skyrmion Hall angle curves, shown in Fig. 5.14 (d), they are strongly reduced in size. These results indicate that the attractive pinning sites produce much reduced directional locking effects when compared to systems using obstacles.

Figure 5.14 - (a) The average velocity curves $\langle V_\parallel \rangle, \langle V_\perp \rangle$ as a function of the transport force F^D for a single skyrmion in the square attractive pinning array using $a_0 = 0.65$ and $\alpha_m/\alpha_d = 0.45$. (b) The average velocity curves $\langle V_\parallel \rangle, \langle V_\perp \rangle$ as a function of the transport force F^D using $a_0 = 1.0$ and $\alpha_m/\alpha_d = 1.91$ (c) the corresponding skyrmion Hall angle curve for panel (a). (d) The corresponding skyrmion Hall angle curve for system of panel (b). (From Vizarim *et. al.* [137], pg. 12).

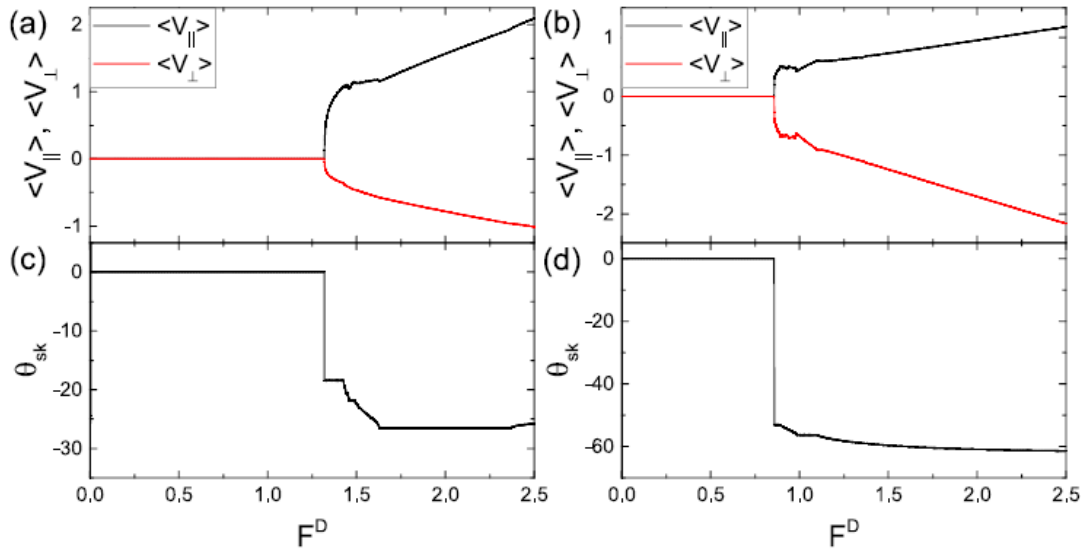

5.3.4 Topological Sorting

In this section it is considered the effects of multiple interacting skyrmions moving in periodic obstacle arrays for varied species of skyrmions. It is well known that in experimental samples skyrmions may form with different sizes that exhibit different Magnus terms [102,155,156]. In Fig. 5.15 (a) it is plotted $\langle V_\perp \rangle$ and $\langle V_\parallel \rangle$ for each species versus F^D for a system containing 44 skyrmions at a density of $n_s = 0.034$ and $a_0 = 0.65$. Half of the skyrmions has $\alpha_m/\alpha_d = 0.45$ (species a) and the other half $\alpha_m/\alpha_d = 1.91$ (species b). In Fig. 5.15 (b) it is illustrated the corresponding θ_{sk} versus F^D curve for both species. In this case, the skyrmions from species a have always different Hall angle curves when compared to species b.

Moreover, the θ_{sk} is always lower than the intrinsic Hall angle value for both species, which means that the skyrmion-skyrmion interactions cause a reduction in the Hall angle for both species. The pronounced steps observed for the single skyrmion case is not present for multiple skyrmions, this occurs due to the disordering effect that occurs when the different skyrmion species move at different angles, causing collisions among the skyrmions and resulting in the disordered trajectories illustrated in Fig. 5.16 for $F^D = 0.5$. In Fig. 5.17, species a is moving with $\theta_{sk} = -18.43°$, but when it collides with species b skyrmions, the trajectories begin to disorder. As F^D is increase, species a eventually jumps out of the phase $\theta_{sk} = -18.43°$ and move with higher angle. For collective effects among monodisperse skyrmions, locking steps similar to those found for single skyrmion case can occur. The fact that different species can be set into motion with different Hall angles opens the possibility to create skyrmion sorting in systems containing skyrmions with different sizes or different winding numbers, similar to the species fractionation that can be achieved for different species of colloidal particles moving over periodic substrates [157–160]. The separation can be more difficult in systems where there are only small differences between the skyrmion species, but it should be possible to adjust the external drive F^D carefully to the edge of a locking step that one species is locked in a given direction and the other species is not.

Figure 5.15 - Results for 44 skyrmions (density of $0.034/\xi^2$) under the influence of the square obstacle array, which half of them are from species a ($\alpha_m/\alpha_d = 0.45$) and the other half b ($\alpha_m/\alpha_d = 1.91$). In (a) the average velocity curves $\langle V_\parallel \rangle, \langle V_\perp \rangle$ as a function of the transport force F^D and in (b) the θ_{sk} vs F^D curve. In both figures $a_o = 0.65$ (From Vizarim *et. al.* [137], pg. 13).

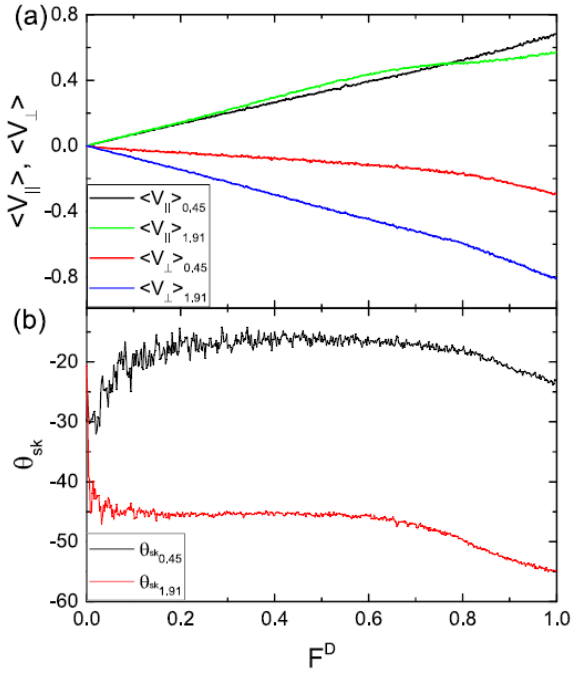

Figure 5.16 - The obstacles (open circles) and the skyrmion trajectory (lines) for system of mixed species, where species a are represented by black lines and species b by blue lines, using $a_o = 0.65$ and $F^D = 0.5$. The skyrmions of species a are moving with $\theta_{sk}^a = -18.43°$ while the skyrmions of species b moves with $\theta_{sk}^b = -45°$ [See Fig. 5.15 (b)] (From Vizarim *et. al*. [137], pg. 14).

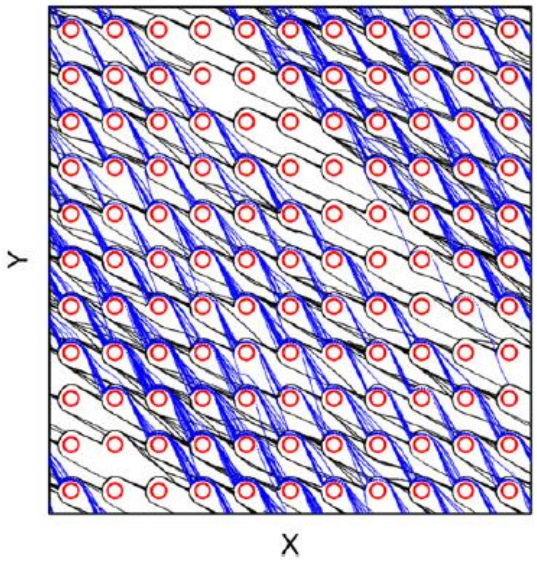

If the density of both species is increased an interesting phenomenon occurs, the skyrmion-skyrmion interaction becomes stronger and at low drives regimes a jammed state emerges, where the two species move while rigidly locked together. In Fig. 5.17 (a) it is shown $\langle V_\perp \rangle$ and $\langle V_\parallel \rangle$ for each species versus F^D in a sample with 110 skyrmions, where $n_s = 0.085$, and in Fig. 5.17 (b) the corresponding Hall angle curve for both species. Species a reaches a step with $\theta_{sk} = -26.56°$, which is *higher* than the intrinsic $\theta_{sk}^{int} = -24.22°$ value for species a, which means that there is a dragging effect from species b on species a. At higher drives, species a settles at $\theta_{sk} = -21.8°$. At the lowest values of F^D, θ_{sk} is close to 0° when the system forms a jammed state where the skyrmions of both species start to form an elastically moving lattice due to the repulsive skyrmion-skyrmion interactions. In Fig. 5.18 (a) it is illustrated the skyrmion trajectories for the system in Fig. 5.17 at $F^D = 0.01$, where skyrmions move mostly in the state where $\theta_{sk} = 0°$ in a jammed state. In Fig. 5.18 (b) it shows the skyrmion trajectories for $F^D = 0.5$, where species b is locked at $\theta_{sk} = -45°$ and species a is locked at $\theta_{sk} = -21.8°$. In this case the system is not jammed anymore due to the higher drives.

Figure 5.17 - Results for 110 skyrmions (density of $0.085/\xi^2$) under the influence of the square obstacle array, which half of them are from species a ($\alpha_m/\alpha_d = 0.45$) and the other half b ($\alpha_m/\alpha_d = 1.91$). In (a) the average velocity curves $\langle V_\parallel \rangle, \langle V_\perp \rangle$ as a function of the transport force F^D and in (b) the θ_{sk} vs F^D curve. In both figures $a_o = 0.65$ (From Vizarim *et. al.* [137], pg. 14).

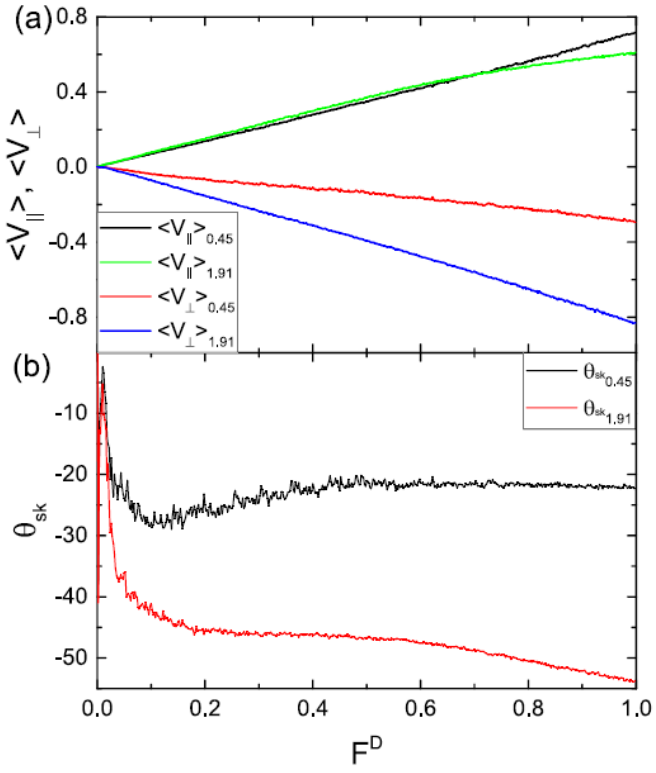

Figure 5.18 - The obstacles (open circles) and the skyrmion trajectory (lines) for system of mixed species, where species a are represented by black lines and species b by blue lines, using $a_o = 0.65$. (a) For $F^D = 0.01$, the skyrmions of both species are locked together in a jammed state moving mostly with $\theta_{sk} = 0°$. (b) For $F^D = 0.5$, the species a are moving with $\theta_{sk}^a = -21.8°$ while the skyrmions of species b moves with $\theta_{sk}^b = -45°$ [See Fig. 5.17 (b)] (From Vizarim *et. al.* [137], pg. 15).

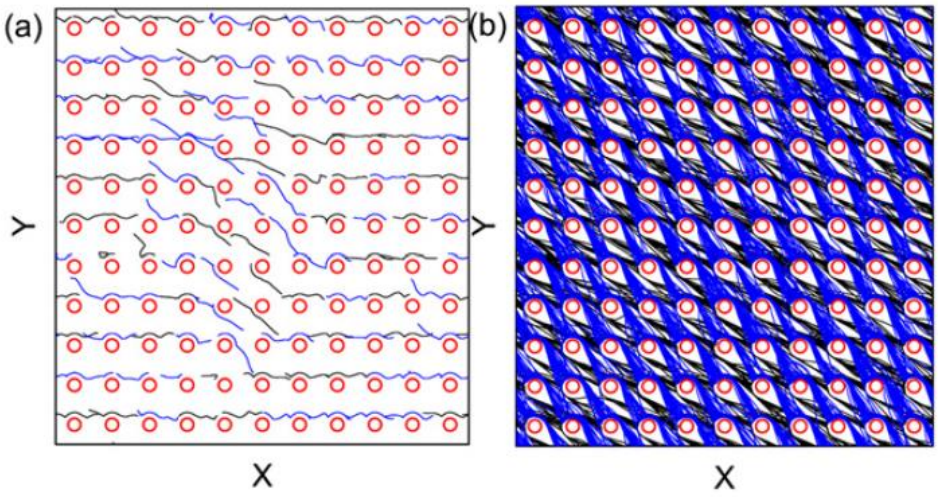

In order to quantify the efficiency of the sorting process, it was measured the difference $A_{ab} = \langle V_a \rangle - \langle V_b \rangle$ between the velocity of the two species in both parallel and perpendicular

directions. In Fig. 5.19 it is shown that the efficiency A_{ab} of the separation drops with increasing skyrmion density for the systems in Fig. 5.16 and 5.17. For the perpendicular direction, there is a monotonic decrease in the efficiency for increasing skyrmion density, n_s, due to the increased drag effect between the two species. Meanwhile, for the parallel direction there is a non-monotonic behavior of the efficiency as a function of n_s due to the partial jamming effect. The jamming effect appears at low drives and can also occur for motion in different directions. In Fig. 5.20 it is plotted the width ΔF_{jam} of the jammed phase as a function of n_s. The jammed state is defined to extend from the depinning threshold to the drive at which the species velocities begin to decouple.

Figure 5.19 - Area between the velocity curves of the different species, A_{ab}, versus the skyrmion density, n_s. In black the area between the velocities parallel to the drive, $A_{ab}\langle V_{\parallel}\rangle$, and in red the area between velocities perpendicular to the applied drive, $A_{ab}\langle V_{\perp}\rangle$. The figure shows the sorting efficiency as a function of the skyrmion density (From Vizarim *et. al.* [137], pg. 15).

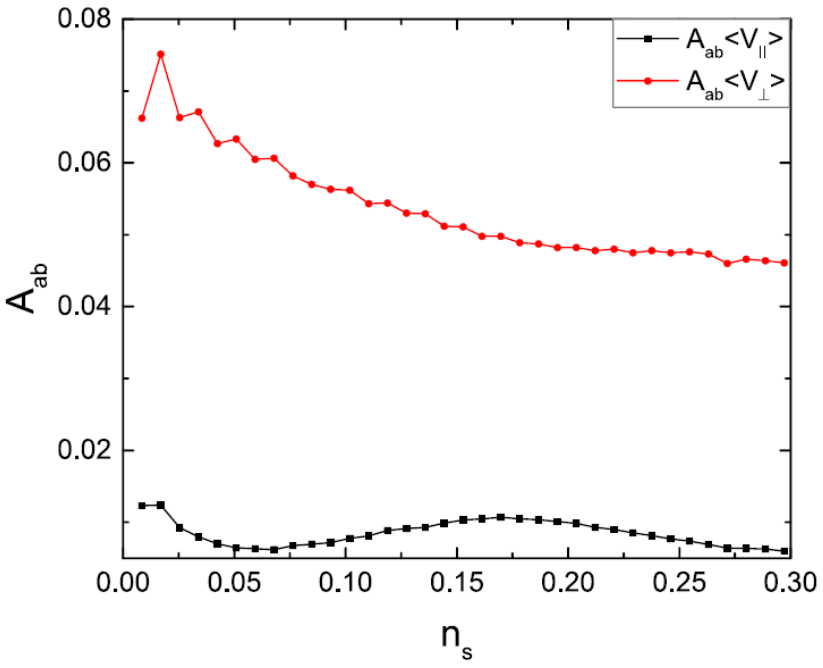

In Fig. 5.20, for $n_s \leq 0.0594$, there is no jamming since the skyrmion density is low enough that skyrmions can easy pass by each other with minimal interactions. For $0.0594 < n_s < 0.0933$, the initial motion occurs in tha jammed state with $\theta_{sk} = 0°$, while for $0.0933 < n_s < 0.1188$, the skyrmions form a jammed state that moves with $\theta_{sk} = -26.56°$. Over the interval $0.1188 < n_s < 0.1867$, the jammed state moves now with $\theta_{sk} = -45°$, while for $n_s > 0.1867$ another jammed state appears with $\theta_{sk} = 0°$. For larger skyrmion densities the jammed state is larger and can be moved with different directions, that is, even in the same jammed state the direction of motion may change due to the dragging effect.

Figure 5.20 - Range of forces where the skyrmions are jammed, ΔF_{jam}^{D}, versus the skyrmion density, n_s. The figure shows that as the skyrmion density increases, the range of forces where the skyrmions are jammed becomes larger and may change the direction of motion (From Vizarim *et. al*. [137], pg. 15).

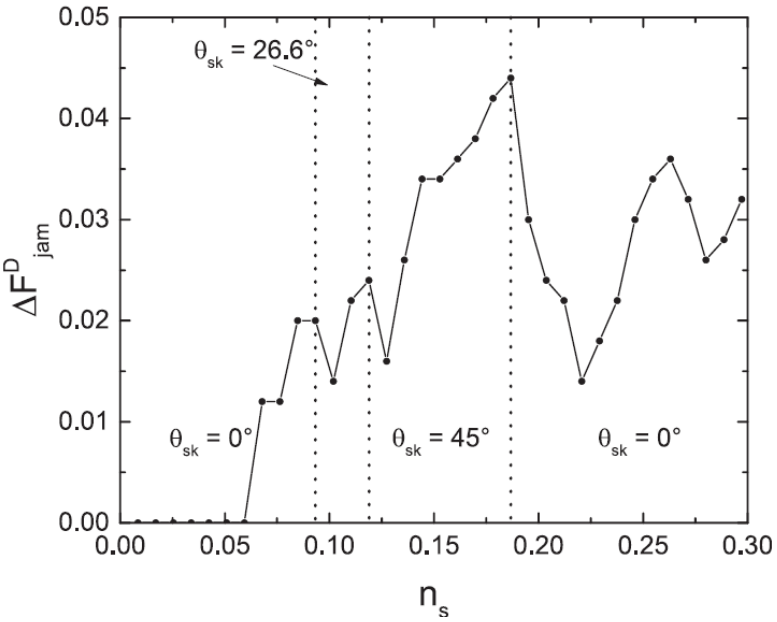

5.3.5 Discussion and Summary

We have examined individual and multiple interacting skyrmions moving through a square array of obstacles. In the single skyrmion case, we observe a series of directional locking effects where the skyrmion Hall angle increases in both a quantized and a continuous manner. The transitions between the different locking steps are associated with dips or cusps in the velocity-force curves as well as with a quantized skyrmion Hall angle. For small obstacles, the skyrmion motion is oriented close to the intrinsic Hall angle, but directional locking to higher or lower Hall angles can occur. For larger obstacles, the number of directional locking steps is increased. The angle of skyrmion motion is 90° with respect to the drive at zero damping, and it decreases with increasing damping until, for high damping, the skyrmion remains locked in the drive direction. When multiple species of interacting skyrmions are present, we show that it is possible to achieve a sorting effect in which one species of skyrmion locks to a symmetry direction of the obstacle lattice while the other species does not. The sharp steps in the velocity force curves disappear when there are multiple skyrmion species due to the disordering of the skyrmion trajectories that occurs when the different species move in different directions and collide. At lower drives, as the skyrmion density increases we observe a jammed state in which two species form a rigid assembly and all move in the same direction, while at higher drives the motion of the two species decouple. For increasing skyrmion density, we observe a series of transitions among jammed phases that move at different angles with respect to the drive.

6 Shapiro Steps and Nonlinear Skyrmion Hall angles

6.1 Skyrmions under ac and dc drives

This works aims to investigate the skyrmion behavior under the influence of dc drives associated with ac drives and it was published in Physical Review B [161]. Overdamped particles moving over a two-dimensional periodic substrate under combined dc and ac drives can exhibit a series of steps that appear in the velocity force curves that are known as Shapiro steps [162]. Here we show that for skyrmions driven over a two-dimensional periodic obstacle array with a dc drive and an ac drive that is either parallel or perpendicular to the dc drive, the system exhibits numerous transverse and longitudinal synchronization dynamics due to the Magnus force. These phenomena originate in interactions between two different types of phase locking effects: Shapiro steps and directional locking. In some cases, the skyrmion Hall angle is constant but longitudinal Shapiro steps appear, while in other regimes the skyrmion Hall angle can either increase or decrease with increasing dc drive during the phase locking as the skyrmion locks to different symmetry directions of the obstacle lattice. For a transverse ac drive we find that strong Hall angle overshoots can occur in certain locked phases where the skyrmion is moving at an angle that is considerably larger than the intrinsic Hall angle. For the strongest Magnus force, the phase locking effects are reduced and there are larger regions of disordered dynamics. It is shown that the skyrmion Hall angle can be controlled by fixing the dc drive and changing the amplitude of the ac drive.

6.2 Model and Simulation details

In this work, a single skyrmion is subjected to a square obstacle landscape while a dc drive is applied in the x direction, and ac drives are applied in both x and y directions. The dynamical properties of the skyrmion system interacting with the obstacle array were simulated using the particle model for skyrmions, shown in Eq. (6.1), using Molecular Dynamics technique.

$$\alpha_d \mathbf{v_i} + \alpha_m \hat{z} \times \mathbf{v_i} = \mathbf{F}_i^o + \mathbf{F}^D + \mathbf{F}^{ac} \tag{6.1}$$

The first term on the left α_d is the damping term, and the second term on the left α_m is the Magnus term that produces a force that is perpendicular to the skyrmion velocity. Unless otherwise noted, we used the normalization $\alpha_d^2 + \alpha_m^2 = 1$.

The first term on the right is the interaction between the skyrmions and the obstacles. The potential energy of this interaction has a Gaussian form $U_o = C_o e^{-(r_{io}/a_o)^2}$, where C_o is the strength of the obstacle potential, r_{io} is the distance between the skyrmion i and the obstacle o, and a_o is the obstacle radius. The obstacle density used in this work is $0.093/\xi^2$, and the obstacle size is fixed in $a_0 = 0.65$. The third term on the right side, $\mathbf{F}^D = F^D\hat{\mathbf{d}}$, where $\hat{\mathbf{d}}$ is the direction of the dc driving force, is the force interaction between the skyrmion and the external current. In this work the applied dc drive is in x direction, so $\hat{\mathbf{d}} = \hat{\mathbf{x}}$. The last term is the ac drive, $\mathbf{F}_x^{ac} = A\sin(2\pi\omega_1 t)\,\hat{\boldsymbol{x}}$ for longitudinal driving and $\mathbf{F}_y^{ac} = B\cos(2\pi\omega_2 t)\,\hat{\boldsymbol{y}}$ for transversal driving, where, unless otherwise noted, we use $\omega_1 = \omega_2 = 2\times10^{-4}$ inverse simulation steps. We measure the skyrmion velocity parallel, $\langle V_\parallel\rangle$, and perpendicular, $\langle V_\perp\rangle$, to the drive. The external dc drive is increased in small steps of $\delta F^D = 0.001$ and wait 10^5 simulation time steps between increments to ensure steady state.

6.3 Results

6.3.1 Dc and Ac Drive In The Same Direction

First it is considered the case where ac drive is applied along the same direction as the dc drive, $\mathbf{F}_x^{ac} = A\sin(2\pi\omega_1 t)\,\hat{\boldsymbol{x}}$**.** For an overdamped particle moving under the influence of a periodic array, this drive configuration produces Shapiro steps in the velocity-force curves, and the motion is strictly in the x direction, giving a Hall angle of zero degrees. As shown in the results of section 5, as F^D is increased under zero ac driving, a series of quantized jumps appear in the velocity-force curves that are associated with different locking directions for the skyrmion motion, and are also accompanied by jumps in the skyrmion Hall angle, θ_{sk}. This is a results of the pinning-induced velocity dependence of the skyrmion Hall angle, as previously studied before [39].

When a finite ac drive of $A = 0.5$ is applied along the x direction in a system just like described in section 5, the behavior changes as illustrated in Fig. 6.1. In Fig. 6.1 (a) it is plotted $\langle V_\parallel\rangle$ and $\langle V_\perp\rangle$ versus F^D, while in Fig. 6.1 (b) it is shown the corresponding θ_{sk} versus F^D curve. The skyrmion motion is initially locked along the x direction for $F^D < 0.65$, and above this drive $\langle V_\perp\rangle$ becomes finite and starts to increase in a series of steps. Above the first step in $\langle V_\perp\rangle$, the Hall angle is close to $\theta_{sk} = -12.5°$, and decreases in magnitude with increasing drive to $\theta_{sk} = -8°$ before increasing in magnitude again. This pattern repeats several times until, at high drives, θ_{sk} saturates to $\theta_{sk} = -24.22°$, which is the intrinsic skyrmion Hall angle value. At high

drives, the steps in the velocity-force curves also become smoother. This type of reducing the skyrmion Hall angle with increasing external driving has not been observed before with skyrmions interacting with random pinning.

Figure 6.1 – (a) The average velocities $\langle V_{\parallel} \rangle$ (black) and $\langle V_{\perp} \rangle$ (red) as a function of the applied dc force F^D under a finite ac driving force with amplitude $A = 0.5$. (b) The corresponding θ_{sk} curve as function of the applied dc drive F^D for a single skyrmion in the square obstacle array using $\alpha_m/\alpha_d = 0.45$ and $a_o = 0.65$ (From Vizarim *et. al.* [161], pg. 104413-3).

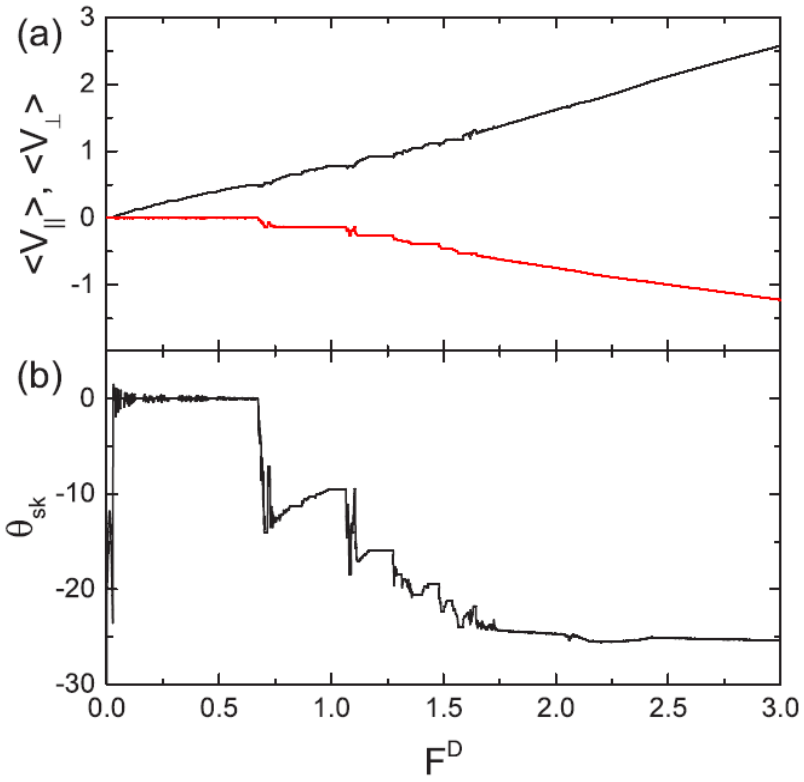

In Fig. 6.2 (a) and (b) it is plotted a zoom of Fig. 6.1 for the range of $0 < F^D < 0.6$. In this case, the skyrmion Hall angle $\theta_{sk} = 0°$ and $\langle V_{\perp} \rangle = 0$, indicating that the motion is only occurring in the x direction. However, a set of phase locking steps still appear in $\langle V_{\parallel} \rangle$. These are Shapiro steps, which also occurs in the overdamped limit [163–166]. The steps correspond to windows of drive over which $\langle V_{\parallel} \rangle$ is locked to a constant value. In contrast, the directional locking found in the absence of an ac drive [See section 5 or [137]] is not associated with constant velocity steps, but instead is accompanied by dips and cusps in the velocity curves.

In Fig. 6.2 (c) and (d) it is shown a zoomed version of Fig. 6.1 for the interval $0.7 < F^D < 1.2$, where two new features can be found. The first is that $\langle V_{\perp} \rangle$ has a finite and constant value, indicating that the particle is moving at an angle to the dc drive. The second is that the series of steps which appear in $\langle V_{\parallel} \rangle$ are correlated with steps in θ_{sk}, which is *decreasing* in

magnitude as F^D increases. This indicates that the velocity is increasing in the x direction but remains constant in y, and the different phase locking steps are associated with decreases in the magnitude of the skyrmion Hall angle. Near $F^D = 1.2$ in Fig. 6.1, there is a substantial jump in θ_{sk} to a larger magnitude which coincides with a jump to a new step of $\langle V_\perp \rangle$.

Figure 6.2 – (a) The zoom in the range of $0 < F^D < 0.6$ from Fig. 6.1, showing the average velocities $\langle V_\parallel \rangle$ (black) and $\langle V_\perp \rangle$ (red) as a function of the applied dc force F^D. (b) The corresponding θ_{sk} curve as function of the applied dc drive F^D . (c) The zoom in the range of $0.7 < F^D < 1.2$ from Fig. 6.1. (d) The corresponding θ_{sk} curve showing the decrease in magnitude of θ_{sk} with increasing F^D for a single skyrmion in the square obstacle array using $\alpha_m/\alpha_d = 0.45$, $a_o = 0.65$ and the ac drive with $A = 0.5$ (From Vizarim *et. al.* [161], pg. 104413-3).

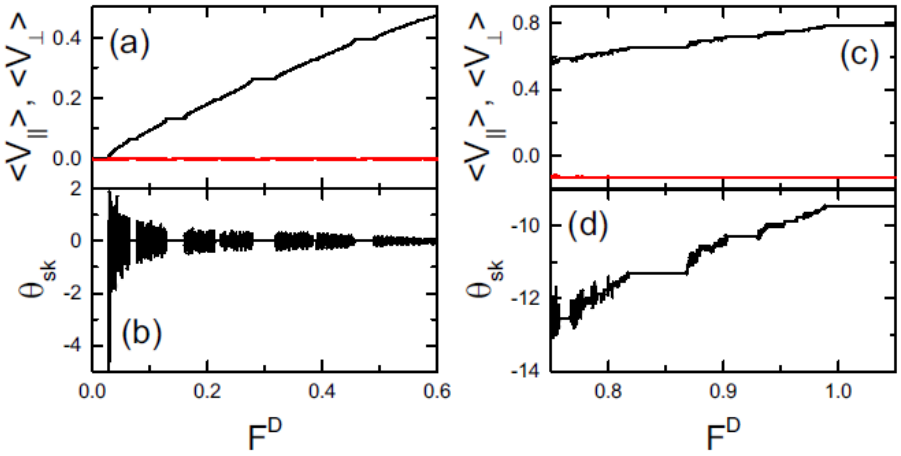

The results in Fig. 6.1 and 6.2 show that the phase-locking behavior found in Fig. 6.1 is actually a *mixture* of two different types of locking. The first one is the Shapiro step phase locking associated with the matching of the ac drive frequency or its higher harmonics to the increasing frequency of the skyrmion velocity oscillations caused by the periodic collisions with the obstacles under an increasing dc drive. This locking is associated with θ_{sk} value that is either constant or increasing in magnitude. The second is the directional locking which occurs even in the absence of an ac drive, as shown in previous works [39,125]. These two locking phenomena can interact with each other to create regions where the magnitude of the skyrmion Hall angle is either constant or decreasing with drive instead of monotonically increasing with F^D. The directional locking effects for a moving particle over a periodic substrate can also occur for overdamped systems, such as vortices in type II superconductors moving over 2D periodic pinning [167,168] and colloids moving over optical traps [157,169] or periodic substrates [170,171]. However, in those systems the direction of the drive with respect to the substrate must be varied, whereas for skyrmions, the velocity dependence of the skyrmion Hall angle changes the direction of motion even when the direction of the driving is fixed [39,137].

In Fig. 6.3 (a) it is plotted the skyrmion trajectories for the system of Fig. 6.1 at $F^D = 0.3$ where the skyrmion motion is locked in the x direction with $\theta_{sk} = 0°$. Note that in the absence of an ac drive, there is still a single locking step at $\theta_{sk} = 0°$ as described in section 5 or Ref. [137], where the skyrmion motion has a similar appearance. However, inclusion of the ac drive provokes multiple phase locking steps even for motion that remains locked along the x direction. At $F^D = 0.85$ in Fig. 6.3 (b), the skyrmion has a finite motion in the $-y$ direction and it moves through five obstacles in the x direction for every obstacle in $-y$, giving a ratio $R = 1/5$ and therefore $\theta_{sk} = \arctan(1/5) = -11.3°$. In Fig. 8.3 (c) at $F^D = 1.0$, the velocity in the y direction is unchanged but the skyrmion Hall angle is smaller in magnitude due to increase $\langle V_{\parallel} \rangle$. In this case, $\theta_{sk} = -8.1°$, and the skyrmion moves seven lattice constants in x and one lattice constant in y during an ac drive cycle. In Fig. 6.3 (d), where $F^D = 2.0$, the skyrmion moves with $\theta_{sk} = -22.24°$. In this case it is not a locking step and the trajectories are more disordered.

Figure 6.3 – The obstacles (open circles) and the skyrmion trajectory (black lines) for the system in Fig. 6.1 with $\alpha_m/\alpha_d = 0.45$, $a_0 = 0.65$ and ac driving in x direction $A = 0.5$. (a) $F^D = 0.3$ where the motion is locked in the x direction. (b) $F^D = 0.85$ where there is a finite motion along y with $\theta_{sk} = -11.3°$. (c) $F^D = 1.0$, where $\theta_{sk} = -8.1°$ and (d) $F^D = 2.0$ where $\theta_{sk} = -22.24°$. (From Vizarim *et. al.* [161], pg. 104413-4).

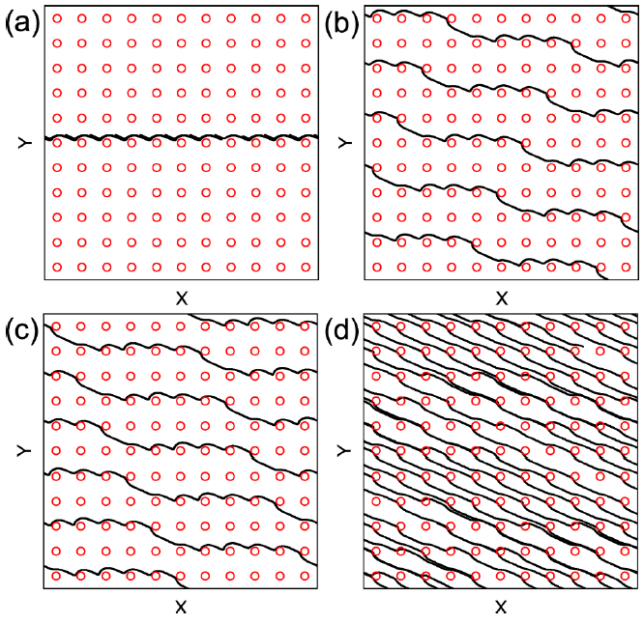

In Fig. 6.4 (a) it is plotted $\langle V_{\parallel} \rangle$ and $\langle V_{\perp} \rangle$ versus F^D for a system with ac drive in the x direction with fixed amplitude $A = 0.5$ as in Fig. 6.1, but now using $\alpha_m/\alpha_d = 1.0$, where the intrinsic Hall angle is $\theta_{sk}^{int} = -45°$. In Fig. 6.4 (b) it is shown the corresponding θ_{sk} curve, which has only two values, with $\theta_{sk} = 0°$ for small drive followed by a jump to the intrinsic skyrmion Hall angle value $\theta_{sk} = -45°$, indicating that there are no intermediate value of θ_{sk}.

Once the system is locked in $\theta_{sk} = -45°$, a series of Shapiro steps still appear in both parallel and perpendicular velocities in Fig. 6.4 (a) that do not correspond to changes in θ_{sk}. This shows that it is possible for Shapiro steps to occur even when the system motion is fixed at a locking angle. In general, if α_m/α_d produces an intrinsic Hall angle that gives a ratio of y to x motion that is close to $1/4$, $1/3$, $1/2$ or 1, which correspond to strong symmetry directions of the square obstacle array, the system locks permanently to this symmetry direction even for very low drives, and steps in the velocity appear that are a signature of Shapiro steps instead of directional locking steps.

Figure 6.4 - (a) The average velocities $\langle V_{\parallel} \rangle$ (black) and $\langle V_{\perp} \rangle$ (red) as a function of the applied dc force F^D under a finite ac driving force with amplitude $A = 0.5$. (b) The corresponding θ_{sk} curve as function of the applied dc drive F^D for a single skyrmion in the square obstacle array using $\alpha_m/\alpha_d = 1.0$ and $a_o = 0.65$ (From Vizarim *et. al.* [161], pg. 104413-5).

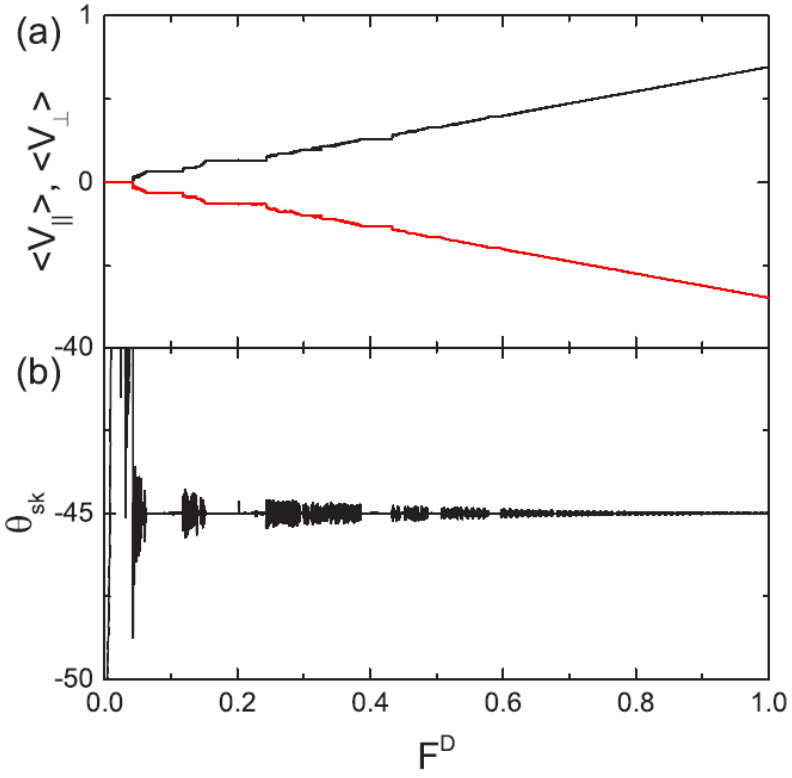

In Fig. 6.5 (a) it is plotted $\langle V_{\parallel} \rangle$ and $\langle V_{\perp} \rangle$ versus F^D for a system using $\alpha_m/\alpha_d = 1.732$ and exact same parameters of Fig. 6.1. In this case the intrinsic Hall angle is $\theta_{sk}^{int} = -60°$. Fig. 6.5 (b) shows the corresponding θ_{sk} versus F^D, where it is possible to see that the system is directionally locked in $\theta_{sk} = -45°$, but there is still a series of steps in the velocities at low F^D despite the fact that the Hall angle is constant in this regime. For $F^D > 0.6$, a series of steps appear in θ_{sk} as the system switches between different locking steps. The larger increases in the magnitude of θ_{sk} are followed by regions in which the magnitude of the skyrmion Hall angle

decreases by a smaller amount. In Fig. 6.6 (a) it is illustrated the skyrmion trajectory for the system in Fig. 6.5 at $F^D = 0.5$ where the skyrmion is in the $\theta_{sk} = -45°$ regime. In Fig. 6.6 (b), for $F^D = 1.0$ the skyrmion is locked to a angle of $\theta_{sk} = -50°$. At $F^D = 1.3$ in Fig. 6.6 (c) the skyrmion is moving in an alternating fashion and for $F^D = 1.75$, in Fig. 6.6 (d), the Hall angle is $\theta_{sk} = -57.5°$.

Figure 6.5 - (a) The average velocities $\langle V_\parallel \rangle$ (black) and $\langle V_\perp \rangle$ (red) as a function of the applied dc force F^D under a finite ac driving force with amplitude $A = 0.5$. (b) The corresponding θ_{sk} curve as function of the applied dc drive F^D for a single skyrmion in the square obstacle array using $\alpha_m/\alpha_d = 1.732$ and $\alpha_o = 0.65$ (From Vizarim *et. al.* [161], pg. 104413-5).

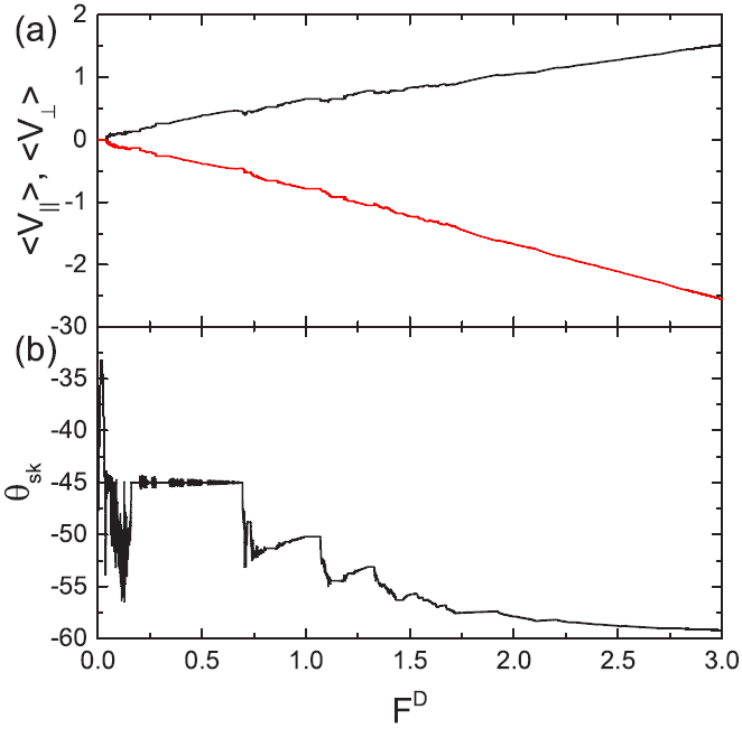

For increasing Magnus force, the skyrmion dynamics becomes increasingly disordered, weakening both the directional locking and the Shapiro steps. Fig. 6.7 (a) shows $\langle V_\parallel \rangle$ and $\langle V_\perp \rangle$ versus F^D for a system with x direction ac driving with $A = 0.5$ but using $\alpha_m/\alpha_d = 9.962$, where the intrinsic skyrmion Hall angle is $\theta_{sk} = -84.3°$. Fig. 6.7 (b) shows the corresponding skyrmion Hall angle curve. In this case there are only small steps in the velocity force curves that are associated with steps in θ_{sk} curve. For these higher Magnus force systems, the skyrmion begin to perform full or partial loops around obstacles, as shown in Fig. 6.7 (c) at $F^D = 0.33$. In Fig. 6.7 (d), at $F^D = 0.5$, the system is in a disordered phase. For $F^D > 1.5$, the locking regimes are lost and θ_{sk} gradually approaches the intrinsic value.

Figure 6.6 – The obstacles (open circles) and the skyrmion trajectory (black lines) for the system in Fig. 6.4 with $\alpha_m/\alpha_d = 1.732$, $a_0 = 0.65$ and ac driving in x direction $A = 0.5$. (a) $F^D = 0.5$ where the motion is locked in $\theta_{sk} = -45°$. (b) $F^D = 1.0$. (c) $F^D = 1.3$. (d) $F^D = 1.75$ where $\theta_{sk} = -57.5°$. (From Vizarim *et. al.* [161], pg. 104413-5).

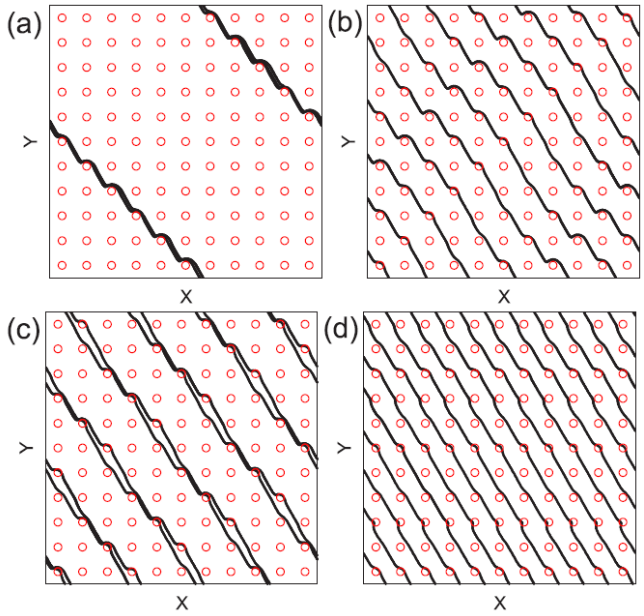

Figure 6.7 – (a) The average velocities $\langle V_\parallel \rangle$ (black) and $\langle V_\perp \rangle$ (red) as a function of the applied dc force F^D under a finite ac driving force with amplitude $A = 0.5$. (b) The corresponding θ_{sk} curve as function of the applied dc drive F^D for a single skyrmion in the square obstacle array using $\alpha_m/\alpha_d = 9.962$ and $a_o = 0.65$. (c) – (d) The obstacles (open circles) and the skyrmion trajectory (black lines) for the system in (a) and (b). (c) $F^D = 0.33$ where loop orbits appear due to high Magnus forces. (d) $F^D = 0.5$, where the motion is disordered (Adapted from Vizarim *et. al.* [161], pg. 104413-6).

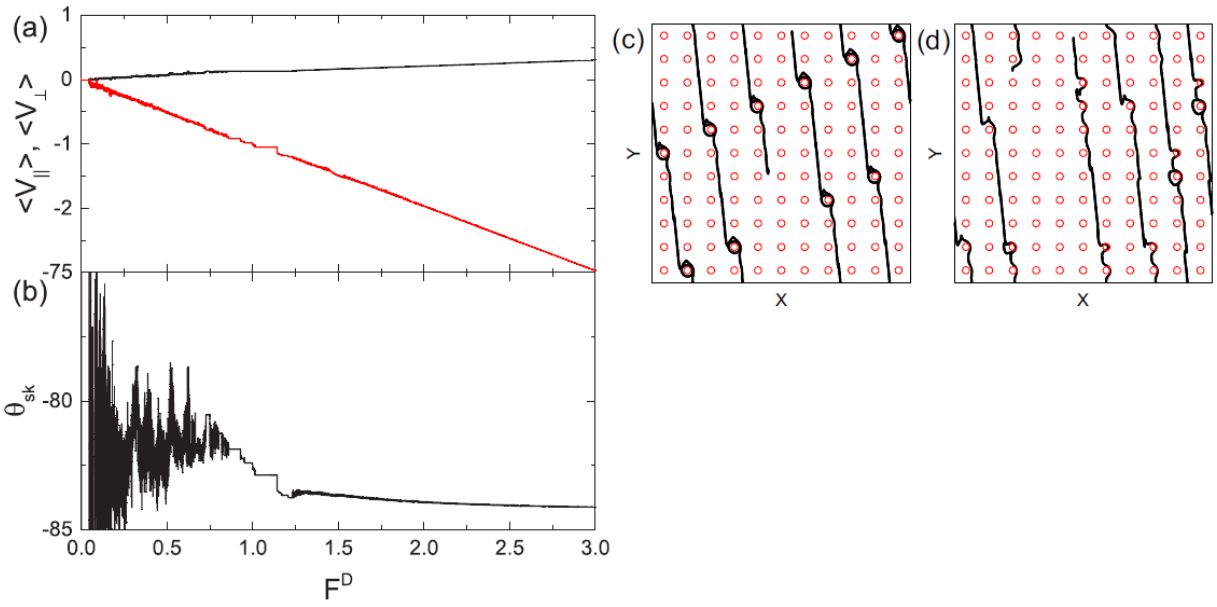

6.3.2 Ac Driving In The Transverse Direction

In this section we consider the case of an ac drive applied along the y direction, transverse to the dc drive. In Fig. 6.8 (a) it is plotted the velocity components as a function of F^D and in Fig. 6.8 (b) it is plotted the corresponding skyrmion Hall angle curve for a system using $\alpha_m/\alpha_d = 0.45$ and $B = 0.5$. The features in the velocity curves exhibit a steplike behavior, rather than cusplike shapes found for the case of ac drive in the x direction shown in Fig. 6.1. In general, it is also possible to observe more locking regions which are associated with both directional locking and the ac phase locking. Another interesting feature is that near $F^D = 0.15$, there is a window of locking to $\theta_{sk} = -45°$, which is considerably larger in magnitude than the intrinsic Hall angle, which in this case is $\theta_{sk}^{int} = -24.22°$. We call this phenomenon a Hall angle overshoot. As F^D increases, θ_{sk} undergoes a number of oscillations until it reaches a saturation near intrinsic Hall angle value at high drives.

Figure 6.8 - (a) The average velocities $\langle V_\parallel \rangle$ (black) and $\langle V_\perp \rangle$ (red) as a function of the applied dc force F^D under a finite ac driving force with amplitude $B = 0.5$. (b) The corresponding θ_{sk} curve as function of the applied dc drive F^D for a single skyrmion in the square obstacle array using $\alpha_m/\alpha_d = 0.45$ and $a_o = 0.65$ (From Vizarim *et. al.* [161], pg. 104413-6).

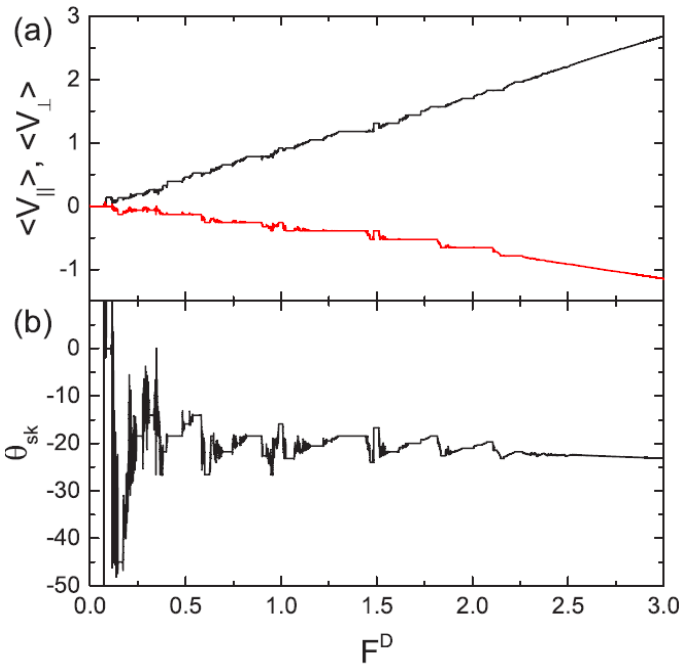

In Figs. 6.9 (a) – (c) it is plotted $\langle V_\parallel \rangle$, $\langle V_\perp \rangle$ and θ_{sk} versus F^D for the system in Fig. 6.8 for the interval $0.4 < F^D < 0.85$. There are sudden jumps both up and down in θ_{sk}. Moreover, there are regions where $\langle V_\perp \rangle$ remains constant but steps appear in $\langle V_\parallel \rangle$ that are associated with jumps in θ_{sk}. In the interval $1.35 < F^D < 1.75$ shown in Figs. 6.9 (d) – (f), there are regions where the velocity can decrease with increasing F^D.

Figure 6.9 - The average velocities (a) $\langle V_{\parallel} \rangle$ (black) and (b) $\langle V_{\perp} \rangle$ (red) and (c) θ_{sk} as a function of the applied dc force F^D under a finite ac driving force with amplitude $B = 0.5$ for the interval $0.4 < F^D < 0.85$. The average velocities (a) $\langle V_{\parallel} \rangle$ (black) and (b) $\langle V_{\perp} \rangle$ (red) and (c) θ_{sk} as a function of the applied dc force F^D under a finite ac driving force with amplitude $B = 0.5$ for the interval $1.35 < F^D < 1.75$ using $\alpha_m/\alpha_d = 0.45$ and $\alpha_o = 0.65$ (From Vizarim *et. al.* [161], pg. 104413-6).

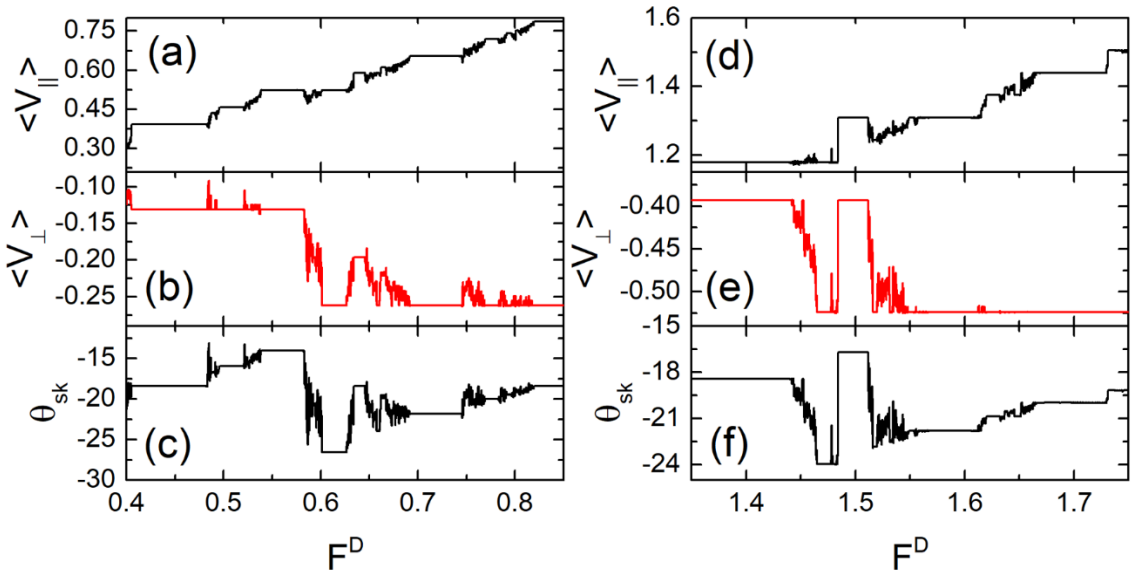

In Fig. 6.10 it is illustrate some representative skyrmion trajectories for the system of Fig. 6.8. At $F^D = 0.1$ in Fig. 6.10 (a) the skyrmion motion is locked in the x direction, and the skyrmion performs a zigzag pattern. In Fig. 6.10 (b), at $F^D = 0.16$, the motion is locked in $\theta_{sk} = -45°$. Fig. 6.10 (c) shows the trajectory for $F^D = 0.26$, where the skyrmion moves with a much smaller angle of $\theta_{sk} = -18.4°$. In Fig. 6.10 (d), at $F^D = 0.44$, the skyrmion still moves with $\theta_{sk} = -18.4°$, but the shape of the trajectory is changed. At $F^D = 0.61$, shown in Fig. 6.10 (e), the motion is along $\theta_{sk} = -26.6°$, and in Fig. 6.10 (f) at $F^D = 1.4$, $\theta_{sk} = -18.4°$, indicating that the system has returned to the previous state. This trajectory is different than the previous ones, indicating that this phase where the skyrmion moves with $\theta_{sk} = -18.4°$ can occur in many different ways.

Figure 6.10 – The obstacles (open circles) and the skyrmion trajectory (black lines) for the system in Fig. 6.8 with $\alpha_m/\alpha_d = 0.45$, $a_0 = 0.65$ and ac driving in y direction $B = 0.5$. (a) $F^D = 0.1$ where the motion is locked in $\theta_{sk} = 0°$. (b) $F^D = 0.16$ the overshoot motion where $\theta_{sk} = -45°$. (c) $F^D = 0.26$ where $\theta_{sk} = -18.4°$. (d) $F^D = 0.44$. (e) $F^D = 0.61$ and (f) $F^D = 1.4$ (From Vizarim *et. al.* [161], pg. 104413-7).

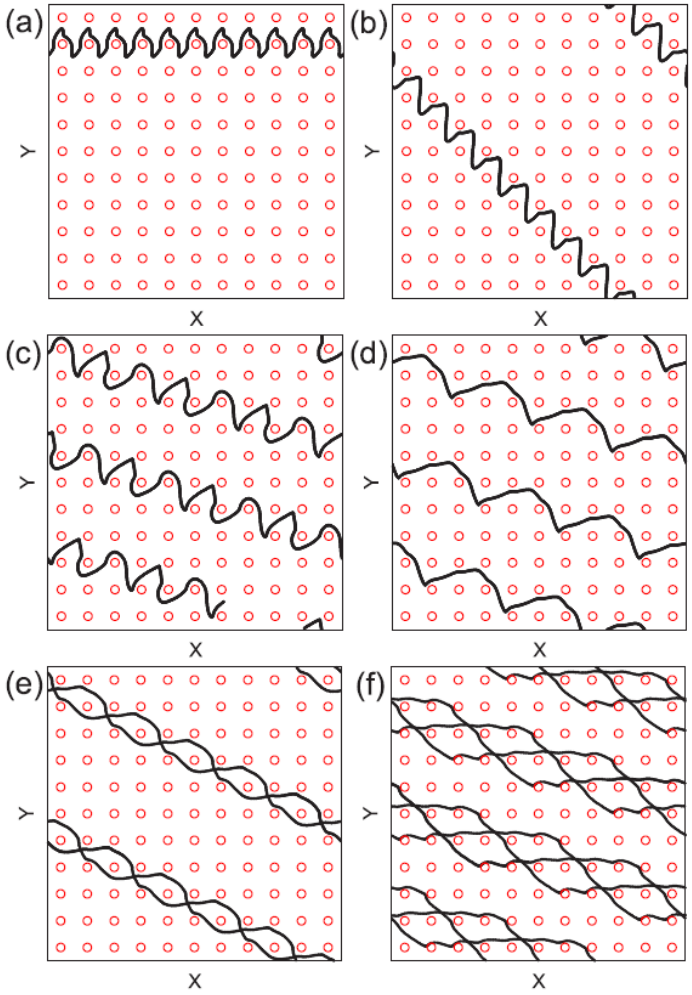

In Fig. 6.11 (a) it is plotted the velocity components versus F^D and in Fig. 6.11 (b) the corresponding skyrmion Hall angle curve for a system using $\alpha_m/\alpha_d = 1.732$, wherethere are again a series of steps at which θ_{sk} increases or decreases. Locking occurs in several regimes and the system jumps in and out of $\theta_{sk} = -45°$ locked state since 45° locking is a particularly strong symmetry direction for the square obstacle lattice. In Fig. 6.12 (a) and (b) it is plotted the trajectories for the system in Fig. 6.11 at $F^D = 0.15$ in the $\theta_{sk} = -45°$ locking regime and at $F^D = 0.175$, where the motion occurs with lower Hall angle magnitude, $\theta_{sk} = -33.7°$. In Fig. 6.12 (c) at $F^D = 0.3$, the system jumps to a new phase where $\theta_{sk} = -45°$ again with a braiding pattern, and in Fig. 6.12 (d) at $F^D = 0.43$, the motion is along $\theta_{sk} = -56.3°$.

Figure 6.11 - (a) The average velocities $\langle V_{\parallel} \rangle$ (black) and $\langle V_{\perp} \rangle$ (red) as a function of the applied dc force F^D under a finite ac driving force with amplitude $B = 0.5$. (b) The corresponding θ_{sk} curve as function of the applied dc drive F^D for a single skyrmion in the square obstacle array using $\alpha_m/\alpha_d = 1.732$ and $\alpha_o = 0.65$ (From Vizarim *et. al.* [161], pg. 104413-7).

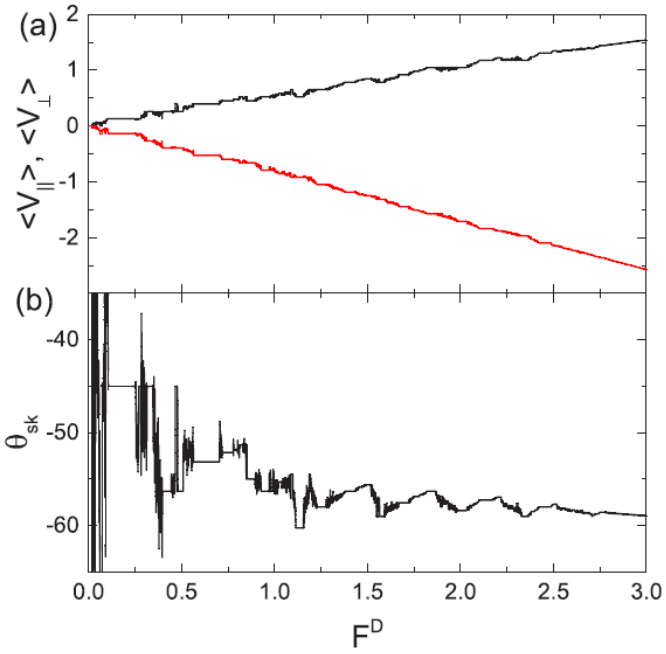

Figure 6.12 – The obstacles (open circles) and the skyrmion trajectory (black lines) for the system in Fig. 6.11 with $\alpha_m/\alpha_d = 1.732$, $\alpha_0 = 0.65$ and ac driving in y direction $B = 0.5$. (a) $F^D = 0.15$ where the motion is locked in $\theta_{sk} = -45°$. (b) $F^D = 0.175$ the motion locks with $\theta_{sk} = -33.7°$. (c) $F^D = 0.3$ the motion returns to $\theta_{sk} = -45°$. (d) $F^D = 0.43$ where $\theta_{sk} = -56.3°$. (From Vizarim *et. al.* [161], pg. 104413-7).

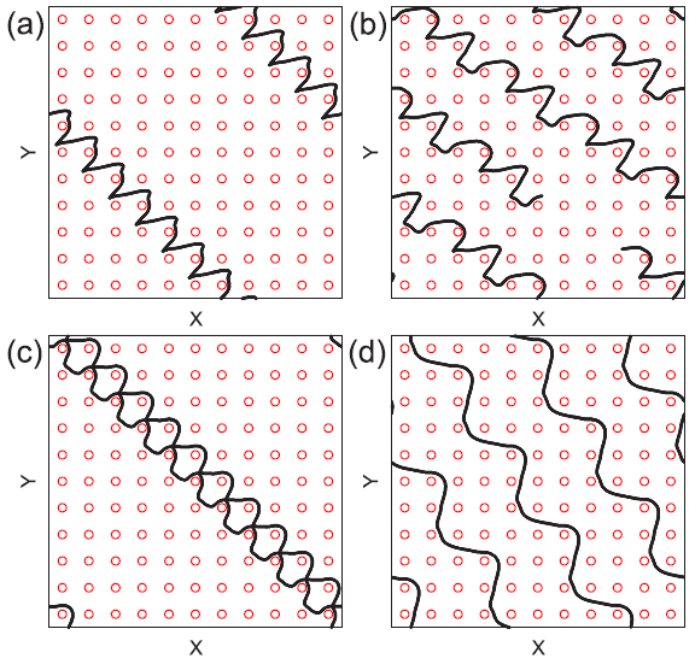

For higher values of α_m/α_d there are extended regions where the trajectories are disordered, and the phase-locking phenomena is generally lost. In Fig. 6.13 it is shown the velocity curves for a system using $\alpha_m/\alpha_d = 9.962$. In this case, there are a number of smaller steps, particularly in the range of $0.35 < F^D < 1.0$, along with one larger step near $F^D = 2.5$. The trajectories become increasingly aligned with the y direction as the external drive is increased.

When the ac drive is in the y direction, there is an interplay between three types of phase locking. These are the Shapiro steps, the directional locking and the transverse phase locking effect. This is the reason why there are a larger number of steps in the velocity and skyrmion Hall angle curves compared to the case of ac driving in the x direction.

Figure 6.13 - (a) The average velocities $\langle V_{\parallel} \rangle$ (black) and $\langle V_{\perp} \rangle$ (red) as a function of the applied dc force F^D under a finite ac driving force with amplitude $B = 0.5$. (b) The corresponding θ_{sk} curve as function of the applied dc drive F^D for a single skyrmion in the square obstacle array using $\alpha_m/\alpha_d = 9.962$ and $a_o = 0.65$ (From Vizarim *et. al.* [161], pg. 104413-8).

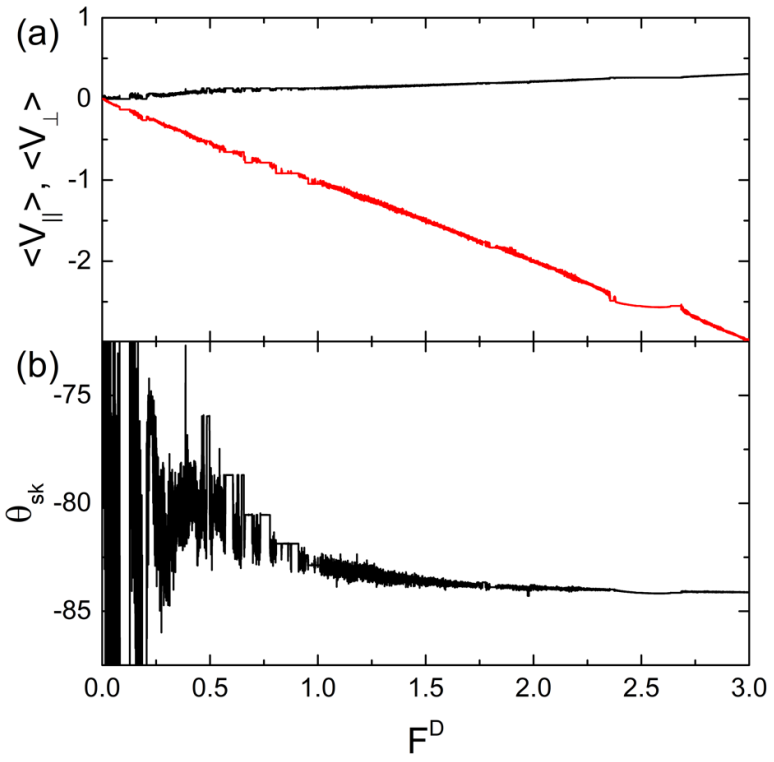

6.3.3 Hall Angle Reversal

In most cases, the results shown so far shows that although the skyrmion Hall angle may increase or decrease with drive, it maintains always the same sign. Under certain circumstances, however, we find regions in which the skyrmion Hall angle changes from negative to positive.

This effect is generally associated with windows of disordered motion at smaller external drive values where the skyrmion is jumping among different paths. In Fig. 6.14, it is plotted $\langle V_{\parallel} \rangle$, $\langle V_{\perp} \rangle$ and θ_{sk} versus F^D for a system with ac driving in the y direction at $\alpha_m/\alpha_d = 1.0$. If the ac driving were applied in the x direction, this ratio of Magnus to damping terms would produce a constant skyrmion Hall angle of $\theta_{sk} = -45°$ with only Shapiro steps, as it was shown in Fig. 6.4. When the ac driving is in the y direction, however, a variety of locking regions appear that are associated with jumps both up and down in $\langle V_{\parallel} \rangle$ and $\langle V_{\perp} \rangle$. Jumps also occur in θ_{sk} among the values $\theta_{sk} = -45°, -38.65°, -36.87°, -33.6°$ and $-26.56°$. The corresponding velocity ratios are $\langle V_{\perp} \rangle / \langle V_{\parallel} \rangle = 1, 4/5, 4/3, 2/3$ and $1/2$ respectively. At higher drives, θ_{sk} decreases in magnitude to angles smaller than 45°. Meanwhile, for $F^D < 0.1$, in the low drive regime, there are several regions in which $\langle V_{\parallel} \rangle$ and $\langle V_{\perp} \rangle$ are both finite and positive, which produces a positive skyrmion Hall angle of $\theta_{sk} \approx 10°$.

Figure 6.14 - (a) The average velocities $\langle V_{\parallel} \rangle$ (black) and $\langle V_{\perp} \rangle$ (red) as a function of the applied dc force F^D under a finite ac driving force with amplitude $B = 0.5$. (b) The corresponding θ_{sk} curve as function of the applied dc drive F^D for a single skyrmion in the square obstacle array using $\alpha_m/\alpha_d = 1.0$ and $a_o = 0.65$ (From Vizarim *et. al.* [161], pg. 104413-8).

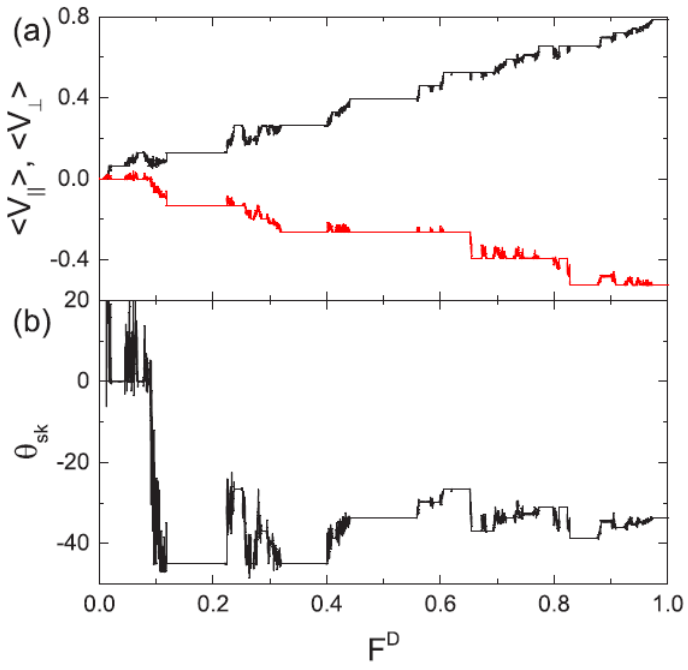

The motion in this regime is illustrated in Figs. 6.15 (a) and (b) at $F^D = 0.045$, where the motion is locked along x, and at $F^D = 0.065$, where the skyrmion is jumping intermittently in the positive y direction. Fig. 6.15 (c) shows the locking phase with $\theta_{sk} = -45°$ at $F^D = 0.2$, and in Fig. 6.15 (d) at $F^D = 0.55$, the skyrmion Hall angle is locked at $\theta_{sk} = -33.7°$. It is

possible that by varying other parameters such as the size of obstacles, clear regions of skyrmion Hall angle reversals may also appear, but the results here indicate that such reversal effects can arise for skyrmion under the influence of periodic obstacle arrays.

Figure 6.15 – The obstacles (open circles) and the skyrmion trajectory (black lines) for the system in Fig. 6.14 with $\alpha_m/\alpha_d = 1.0$, $a_0 = 0.65$ and ac driving in y direction $B = 0.5$. (a) $F^D = 0.045$ where the motion is locked in $\theta_{sk} = 0°$. (b) $F^D = 0.065$ the skyrmion moves with positive velocity component in y, resulting in a positive skyrmion Hall angle. (c) $F^D = 0.2$ the motion is locked to $\theta_{sk} = -45°$. (d) $F^D = 0.55$ where $\theta_{sk} = -33.7°$. (From Vizarim *et. al.* [161], pg. 104413-8).

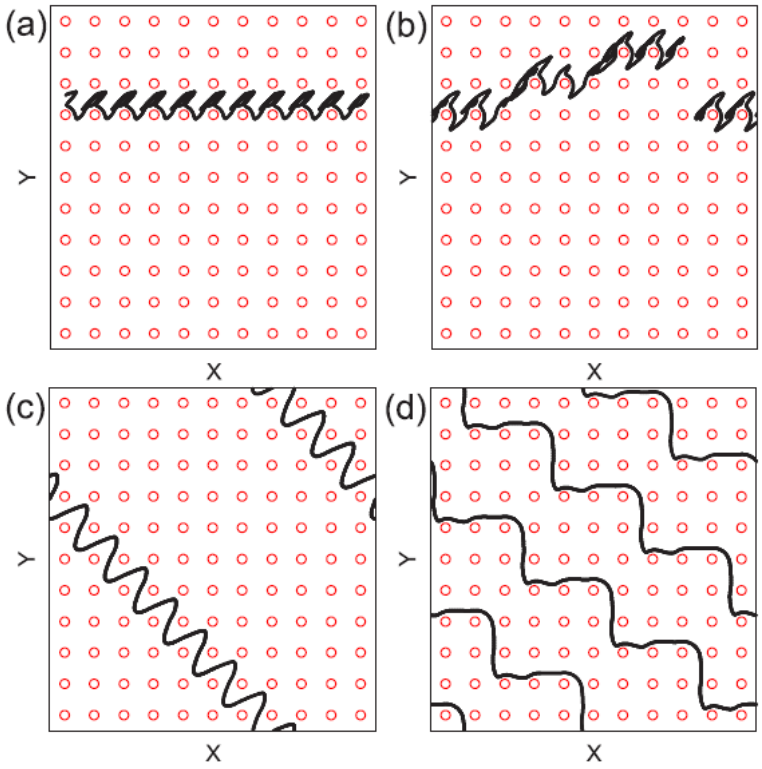

6.3.4 Influence of varying ac drive at a fixed dc drive

Now it is considered the case of a fixed dc drive of $F^D = 1.0$ and the ac drive in x direction with changing amplitude A using $\alpha_m/\alpha_d = 0.45$. In Fig. 6.16 (a) it is plotted the velocity components as a function of the external ac drive amplitude, A. In Fig. 6.16 (b) it is plotted the corresponding θ_{sk} curve. When $A = 0$, the skyrmion motion is locked in $\theta_{sk} = 0°$. As A increases, $\langle V_\parallel \rangle$ remains fairly constant due to the fixed value of F^D, but small cusps are present which are correlated to a series of increasing steps in $\langle V_\perp \rangle$. The steps in $\langle V_\perp \rangle$ produces a series of steps in the skyrmion Hall angle, since $\theta_{sk} = \arctan R = \arctan(\langle V_\perp \rangle / \langle V_\parallel \rangle)$. Some steps are observed for $R = 0,\ 1/10,\ 1/6,\ 1/5$ and a small step near $1/4$. There are also extended steps at $R = 1/3,\ 3/7$ and $1/2$. In general, it can be observed that the magnitude of the Hall angle increases with increasing A. In Fig. 6.17 (a) it is illustrated the skyrmion

trajectories for the systems of Figs. 6.16 (a) and (b) at $A = 0.2$ on the $R = 1/10$ $(-5.7°)$, where the skyrmion moves 10 lattice constants in x while moving one lattice constant in y. Fig. 6.17 (b) shows the same system on the $R = 1/3$ $(-18.43°)$ at $A = 1.0$.

Figure 6.16 - The average velocities $\langle V_{\parallel} \rangle$ (black) and $\langle V_{\perp} \rangle$ (red) and θ_{sk} as a function of the ac drive amplitude A (B) for a fixed dc driving force $F^D = 1.0$ in the x direction using $\alpha_m/\alpha_d = 0.45$. (a) and (b) for a ac drive applied in the x direction. (c) and (d) for ac driving in y (Adapted from Vizarim *et. al.* [161], pg. 104413-9).

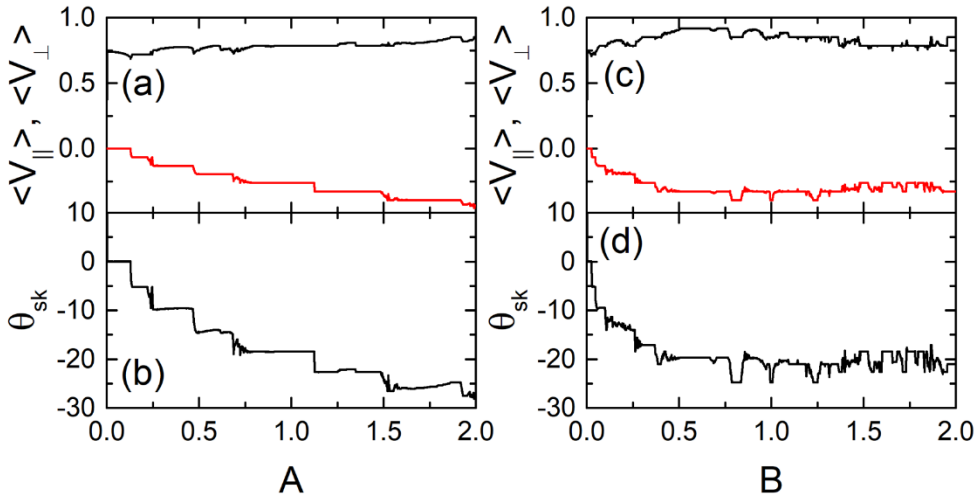

Figure 6.17 – The obstacles (open circles) and the skyrmion trajectory (black lines) for the system in Fig. 6.16 with $\alpha_m/\alpha_d = 1.0$ and fixed dc drive $F^D = 1.0$. (a) At $A = 0.2$ where the skyrmion moves 10 lattice constants in x and one lattice constant in y. (b) A $R = 1/3$ step at $A = 1.0$. (c) Skyrmion motion at $B = 0.34$ and (d) for $B = 1.0$. (From Vizarim *et. al.* [161], pg. 104413-9).

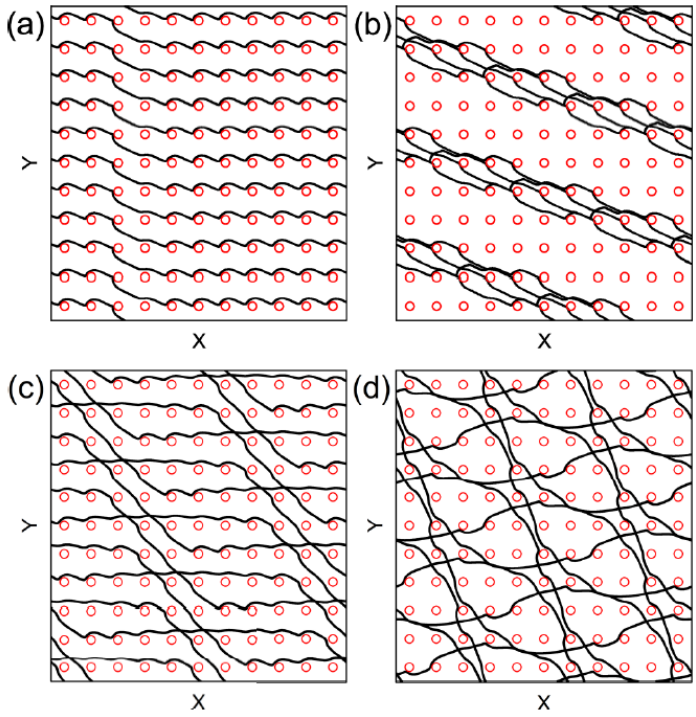

In Figs. 6.16 (c) and (d) it is plotted the velocities and θ_{sk} versus ac drive amplitude for the same system as in Figs. 6.16 (a) and (b) but for ac driving in the y direction, that is, $A = 0$ and B finite. In this case, the Hall angle is initially zero since the skyrmion motion is locked in the x direction. The velocities and skyrmion Hall angle increase and decrease in a series of jumps as B is varied. In Fig. 6.17 (c) it is illustrated the skyrmion trajectories for $B = 0.34$ along a step at which the skyrmion moves 11 lattice constants in x and 4 lattice constants in y. At $B = 1.0$ in Fig. 6.17 (d), there is a more complicated motion where the skyrmion flow 11 lattice constants in x and 5 lattice constants in y. These results indicate that it is possible to controle the skyrmion Hall angle using an ac drive an adjusting the amplitude of the ac drive.

6.3.5 Discussion and Summary

In this work we have numerically examined a skyrmion moving over a 2D periodic array of obstacles under a dc drive with additional ac drive applied either parallel or perpendicular to the dc drive. We find that the Magnus force induces new types of dynamical locking effects that are not observed for overdamped systems with 2D periodic substrates. When the ac and dc drive are parallel, the skyrmion exhibits Shapiro steps similar to those observed in overdamped systems as well as directional locking in which the skyrmion motion locks to different symmetry directions of the substrate. The locking is associated with steps or cusps in the velocities as well as changes in the skyrmion Hall angle. For certain ratios of Magnus force, we find that even though the skyrmion Hall angle is fixed in a particular direction of motion, Shapiro steps still appear in the velocity curves. At high drives, the skyrmion Hall angle gradually approaches the intrinsic value and show oscillations as a function of increasing drive.

In the locked phases, the skyrmion performs quantized motion along x and y directions. This suggests that ac drive could be used to control skyrmion motion in different types of devices [8]. Such controlled motion could be applied to more complex geometries such as rows of pinning or different tailored geometries. It is expected that similar results would appear for triangular array of obstacles, however the preferential directions of motion in this case would be 30° and 60°. A possible future area to address is the inclusion of temperature, where thermal effects could strongly affect the transition points or jumps between different locked states, and also could produce thermal creeps [172]. For high temperature it is expected that the locking effects would vanish. In section 5 it is shown that locking effects are more prominent in systems with obstacle arrays, but if pinning arrays were used instead, the locking effects would persist but should be smaller steps of directional locking and also smaller Shapiro steps.

The skyrmions are modelled as point-like particles, however, actual skyrmions often have additional internal modes of motion. These modes can be excited at much higher frequencies where they could induce additional locking frequencies. Such effects could be further explored in continuum-based simulations using LLG equations [173], which can also capture features like annihilation, or creation of skyrmions and possible distortions of the skyrmion structure due to interactions with the obstacles. Moreover, if multiple interacting skyrmions are present, additional locking effects could arise as a result of emergent soliton dynamics, which would most be pronounced just outside of rational filling fractions of $1/2$, or $1/1$ [40,174].

Although our results are predicted for skyrmions, similar effects could arise in systems with particles in effectively 2D systems where gyroscopic forces can arise, including active spinners [175–177] or charged particles in magnetic fields moving over periodic substrates [25,178,179].

7 Skyrmion Transverse Mobility and Biharmonic ac Drives

7.1 Skyrmions under biharmonic ac drives

Here we further investigate the single skyrmion dynamics under the influence of dc drive associated with an ac drive. However, we focus on the case where the ac drives are applied in both x and y directions, that is, biharmonical. There is also a quick analysis on the temperature effects on the system dynamics. This work was published on The European Physical Journal B [180]. Interestingly, this work had a kind of press release by Springer, and it appeared in some science divulgation websites [181–183].

In this work, we numerically examine the dynamics of a skyrmion interacting with a two-dimensional periodic substrate under dc and biharmonic ac drives. We show that the Magnus force of the skyrmion produces circular orbits that can resonate with the ac drive and the periodicity of the substrate to create quantized motion both parallel and perpendicular to the dc drive. The skyrmion Hall angle exhibits a series of increasing and/or decreasing steps along with strongly fluctuating regimes. In the phase locked regimes, the skyrmion Hall angle is constant and the skyrmion motion consists of periodic orbits encircling an integer number of obstacles per every or every other ac drive cycle. We also observe phases in which the skyrmion

moves at 90° with respect to the driving direction even in the presence of damping, a phenomenon called absolute transverse mobility that can exhibit reentrance as a function of dc drive. When the biharmonic ac drives have different amplitudes in the two directions, we find regimes in which the skyrmion Hall angle shows a sign reversal from positive to negative, as well as a reentrant pinning effect in which the skyrmion is mobile at low drives but becomes pinned at higher drives. These behaviors arise due to the combination of the Magnus force with the periodic motion of the skyrmions, which produce Shapiro steps, directional locking, and ratchet effects.

7.2 Model and Simulation details

This system is modelled exactly as shown in the previous section 6, we just focused here on the case where both ac drives are applied together. The dynamical properties of the skyrmion system interacting with the obstacle array were simulated using the particle model for skyrmions, shown in Eq. (6.1) from section 6, using Molecular Dynamics technique.

In this work case, the $\mathbf{F}^{ac}$ has the following form:

$$\mathbf{F}^{ac} = A\,\mathrm{sen}(\omega_1 t)\,\hat{\mathbf{x}} + B\cos(\omega_2 t)\,\hat{\mathbf{y}} \tag{7.1}$$

Where A and B are the ac drive amplitudes and $\omega_{1,2}$ are the ac drive frequencies. In the fisrt part of the work we fix $A = B$ and $\omega_1 = \omega_2$, and throughout the work we fix $\omega_1 = 2 \times 10^{-4}$ in inverse simulation steps. We measure the skyrmion velocity parallel, $\langle V_{\parallel}\rangle$, and perpendicular, $\langle V_{\perp}\rangle$, to the drive. When the skyrmion is flowing without obstacles in the overdamped limit $\alpha_m/\alpha_d = 0$, the skyrmion moves only in the direction of the drive. However, if there is a finite value for α_m/α_d , the skyrmion moves with a Hall angle, $\theta_{sk} = \arctan(\langle V_{\perp}\rangle/\langle V_{\parallel}\rangle) = \arctan(\alpha_m/\alpha_d)$. If one increases the quantity α_m/α_d, the angle θ_{sk} is increased respective to the drive. In order to quantify the direction of the skyrmion motion we measure $R = \langle V_{\perp}\rangle/\langle V_{\parallel}\rangle$. The external dc drive is increased in small steps of $\delta F^D = 0.001$ and wait 10^5 simulation time steps between increments to ensure steady state. We normalize the damping and magnus coefficients as $\alpha_d^2 + \alpha_m^2 = 1$.

7.3 Results

7.3.1 Dc and biharmonic ac drives

In this section we analyze the case where the skyrmion is subjected to both ac and dc drive, where the ac drive is fixed, $A = B = 0.5$ and the dc drive is increased slowly for $\alpha_m/\alpha_d = 0.577$, 1.732 and 9.962. In all cases in this section the obstacle radius is $a_0 = 0.65$ and $F_o = 1.0$. In Fig. 7.1 (a) it is plotted the velocity components $\langle V_\parallel \rangle$ and $\langle V_\perp \rangle$ versus F^D for the system with $\alpha_m/\alpha_d = 0.577$ while in Fig. 7.1 (b) it is plotted the corresponding skyrmion Hall angle curve. Both velocity components increase in a series of steps. The Hall angle, θ_{sk}, also increase with steps, but these steps show oscillatory jumps up and down, indicating that the skyrmion Hall angle can both increase and decrease as a function of increasing F^D. This is in contrast to the behavior in the absence of ac drive where the skyrmion Hall angle monotonically increases with F^D [39,137]. The intrinsic Hall angle in this case is $\theta_{sk}^{int} = -29.98°$, and the measured θ_{sk} gradually approaches the intrinsic value for high values of external dc driving. In Fig. 7.2 (a) – (c) it is shown a close up of $\langle V_\parallel \rangle$, $\langle V_\perp \rangle$ and θ_{sk} as a function of F^D over the range $0 < F^D < 1.0$ for the system in Fig. 7.1. There is an initial pinned phase for $F^D \leq 0.075$ where both velocity components are null. In Fig. 7.3 (a) it is illustrated the skyrmion trajectory in the pinned phase at $F^D = 0.028$, where the skyrmion moves in a circular orbit around a single obstacle. When $A = B = 0$, the ac driving is absent and there is no pinned phase since the range of obstacles is finite and the skyrmion can always move between obstacles. Under the presence of a finite ac drive, the effective dynamical radius of the skyrmion increases, causing the skyrmion to interact with a larger number of obstacles during each ac drive cycle and permitting it to become trapped even under a finite dc drive.

In Fig. 7.2, $\langle V_\parallel \rangle$ is finite but $\langle V_\perp \rangle = 0$ over the range of $0.075 < F^D < 0.15$, resulting in a skyrmion Hall angle of $\theta_{sk} = 0°$. In Fig. 7.3 (b) it is plotted the skyrmion trajectory at $F^D = 0.1$, where the skyrmion translates along the x direction by one obstacle per ac drive cycle. Within the range of dc forces for which the velocity is locked in the x direction, it is possible to have steps in $\langle V_\parallel \rangle$ on which the motion is similar to those found in Fig. 7.3 (b) but where the skyrmion encircles each obstacle twice per ac drive cycle befoe translating one lattice constant in the x direction. For the interval $0.15 \leq F^D < 0.2$, the skyrmion begins to move in the y direction as well, since $\langle V_\perp \rangle$ also becomes finite. However, the motion is chaotic, with no drive interval at which the motion is locked to a specific direction. For $0.2 \leq F^D < 0.4$, the skyrmion motion is periodic and the Hall angle is locked at $\theta_{sk} = -26.56°$. In this case, during each ac

drive cycle, the skyrmion translates by two lattice constants in the x direction and one in the y, giving $\theta_{sk} = \arctan(1/2) = -26.56°$. In Fig. 7.3 (c) it is illustrated a skyrmion trajectory in this regime at $F^D = 0.24$.

Figure 7.1 – (a) The average velocities $\langle V_{\parallel} \rangle$ (black) and $\langle V_{\perp} \rangle$ (red) as a function of the applied dc force F^D under a finite ac driving force with amplitudes $A = B = 0.5$, $\omega_1 = \omega_2$, $\alpha_m/\alpha_d = 0.577$ and $a_o = 0.65$. (b) The corresponding θ_{sk} curve. (From Vizarim *et. al.* [180], pg. 3).

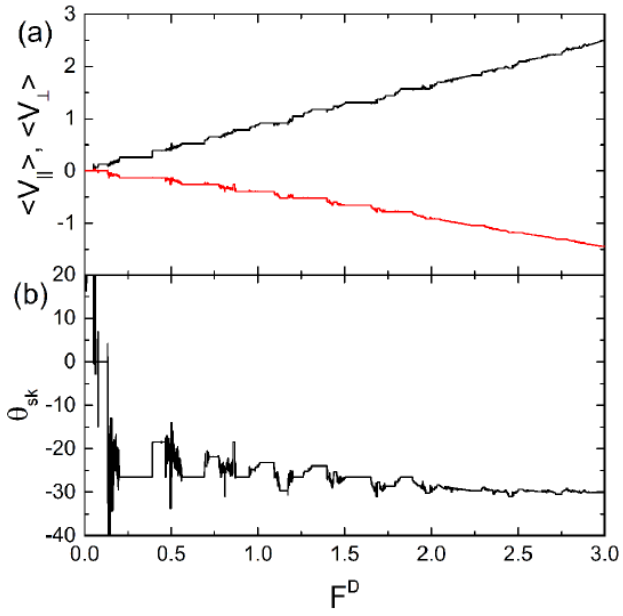

Figure 7.2 - The average velocities (a) $\langle V_{\parallel} \rangle$ (black) and (b) $\langle V_{\perp} \rangle$ (red) and (c) θ_{sk} as a function of the applied dc force F^D under a finite ac driving force with amplitudes $A = B = 0.5$ for the interval $0 < F^D < 1.0$ using $\alpha_m/\alpha_d = 0.577$, $a_o = 0.65$ and $\omega_1 = \omega_2$. (From Vizarim *et. al.* [180], pg. 4).

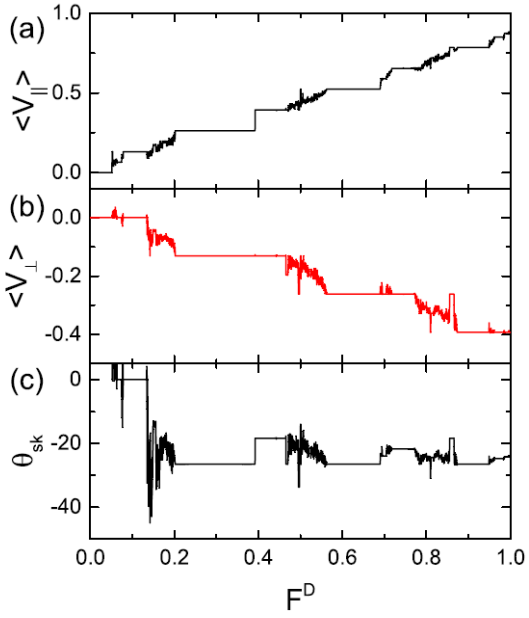

When $0.4 \leq F^D < 0.475$, the magnitude of the skyrmion Hall angle decreases and the locking angle is $\theta_{sk} = -18.43°$, where the skyrmion moves three lattice constants in x and one in y direction for each ac drive cycle, as shown in Fig. 7.3 (d) at $F^D = 0.425$. As F^D increases further, θ_{sk} jumps between the two main locking directions $\theta_{sk} = -26.56°$ and $\theta_{sk} = -18.43°$, and additional fractional locking steps appear in the velocities and the skyrmion Hall angle. There are also several regions of chaotic motion, denotated by noisy fluctuations in the velocity curves.

Figure 7.3 - The obstacles (open circles) and the skyrmion trajectory (black lines) for the system in Fig. 7.1 with $\alpha_m/\alpha_d = 0.577$ and ac drive amplitudes $A = B = 0.5$, $\omega_1 = \omega_2$ and $a_0 = 0.65$. (a) $F^D = 0.028$ in the pinned phase. (b) $F^D = 0.1$ where the skyrmion motion is locked in the x direction. (c) $F^D = 0.24$where locking occurs at $\theta_{sk} = -26.56°$. (d) $F^D = 0.425$, where locking occurs at $\theta_{sk} = -18.43°$. (From Vizarim *et. al.* [180], pg. 4).

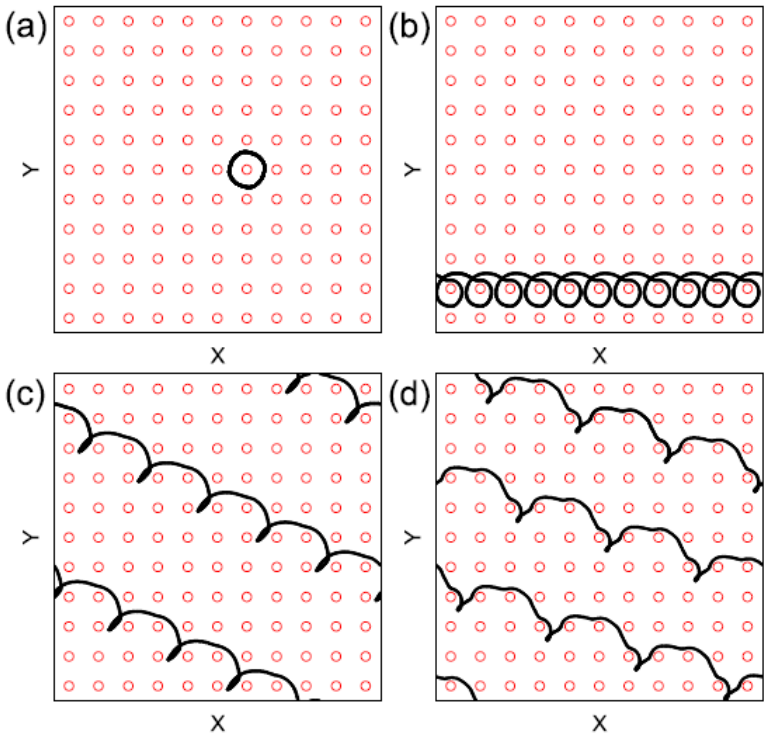

In Fig. 7.4 (a) it is plotted $\langle V_{\parallel} \rangle$ and $\langle V_{\perp} \rangle$ versus F^D for a system using $\alpha_m/\alpha_d = 1.732$ and $A = B = 0.5$, while in Fig. 7.4 (b) it is plotted the corresponding θ_{sk} curve. Here, the intrinsic Hall angle is $\theta_{sk}^{int} = -60°$. The number of locking steps is higher than for samples with lower intrinsic Hall angles, as it is possible to observe a series of jumps in θ_{sk} as a function of F^D. The jumps primarily appear for $F^D < 1.25$, while θ_{sk} has a more oscillating behavior for $F^D \geq 1.25$. The inset of Fig. 7.4 (b) shows θ_{sk} over the range $1.6 < F^D < 1.875$, highlighting the large number of locking steps that accompany a decrease in the magnitude of θ_{sk}. As F^D is increased further, θ_{sk} gradually approaches the intrinsic Hall angle value. In Fig. 7.5 (a) it is

plotted the skyrmion trajectory for the system of Fig. 7.4 at $F^D = 0.011$, where a pinned orbit occurs in which the skyrmion encircles two obstacles during each ac drive cycle. In Fig. 7.5 (b), at $F^D = 0.067$, $\langle V_\parallel \rangle = 0$ and $\langle V_\perp \rangle$ is finite, giving rise to a $\theta_{sk} = -90°$. This is an example of an absolute transverse mobility in which the skyrmion translation is strictly perpendicular to the dc drive. The interval of F^D over which the transverse mobility occurs is small, but it can be extended by varying other parameters as it will be demonstrated later. At $F^D = 0.13$ in Fig. 7.5 (c), the motion is locked to $\theta_{sk} = -45°$ and the skyrmion completes a loop around an obstacle during every ac drive cycle. In Fig. 7.6 (d) at $F^D = 0.47$, the trajectory is still locked to $\theta_{sk} = -45°$ but the shape of the orbit has changed. At $F^D = 0.62$, in Fig. 7.5 (e), the skyrmion Hall angle is $\theta_{sk} = -53.13°$. In Fig. 7.5 (f), at $F^D = 0.95$ is another example of the possibilities for the skyrmion to move in this system.

Figure 7.4 – (a) The average velocities $\langle V_\parallel \rangle$ (black) and $\langle V_\perp \rangle$ (red) as a function of the applied dc force F^D under a finite ac driving force with amplitudes $A = B = 0.5$, $\omega_1 = \omega_2$, $\alpha_m/\alpha_d = 1.732$ and $a_o = 0.65$. (b) The corresponding θ_{sk} curve. (From Vizarim *et. al*. [180], pg. 4).

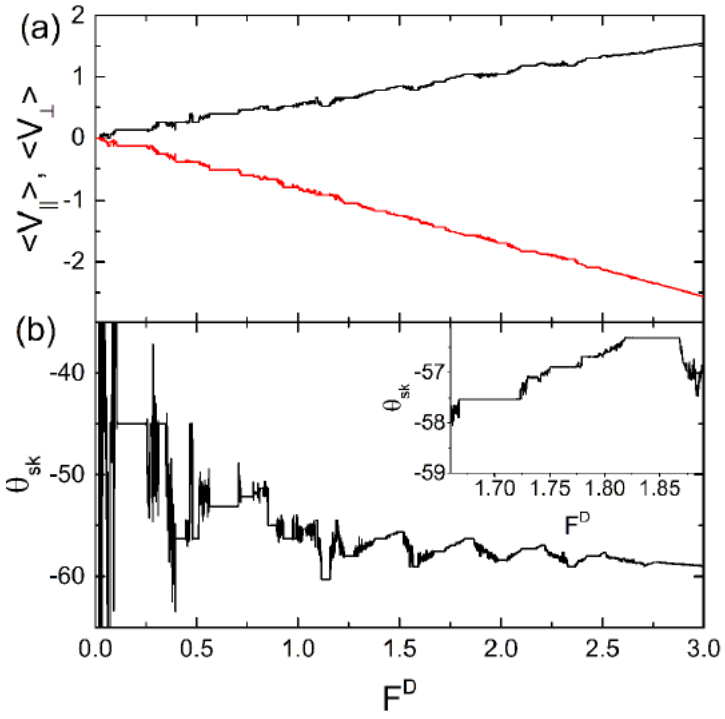

In general, the locking steps arise due to a combination of effects. One of them is the directional locking effect associated with the drive dependence of the skyrmion Hall angle that occurs in the presence of periodic and absence of ac driving [39,137]. Another effect is the Shapiro steps that appear due to locking of the ac drive frequency with periodicity of the velocity component induced by the skyrmion motion over the periodic substrate [31,162]. Here, since the skyrmion is moving in both x and y directions, there are two different velocity

frequencies that can resonate with the ac drive frequency in order to create Shapiro steps, providing additional possible ways in which phase locking can occur. The combined effect of the directional locking and the Shapiro steps accounts for the large number of phase locking steps that appear in velocity-force curves under combined dc and ac driving. Many of these different phase locking effects compete with one another, producing frustration effects where, certain driving conditions, the skyrmion can lock to multiple phase locked orbits for the same value of F^D, causing the skyrmion to jump between orbits creating chaotic regimes in the velocity force curves.

Figure 7.5 - The obstacles (open circles) and the skyrmion trajectory (black lines) for the system in Fig. 7.1 with $\alpha_m/\alpha_d = 1.732$ and ac drive amplitudes $A = B = 0.5$, $\omega_1 = \omega_2$ and $a_0 = 0.65$. (a) $F^D = 0.011$ in the pinned phase. (b) $F^D = 0.068$ the absolute transverse mobility where the skyrmion has net motion only in the y direction, with $\theta_{sk} = -90°$. (c) $F^D = 0.13$ where locking occurs at $\theta_{sk} = -45°$. (d) $F^D = 0.47$. (e) $F^D = 0.62$. (f) $F^D = 0.95$ (From Vizarim *et. al.* [180], pg. 5).

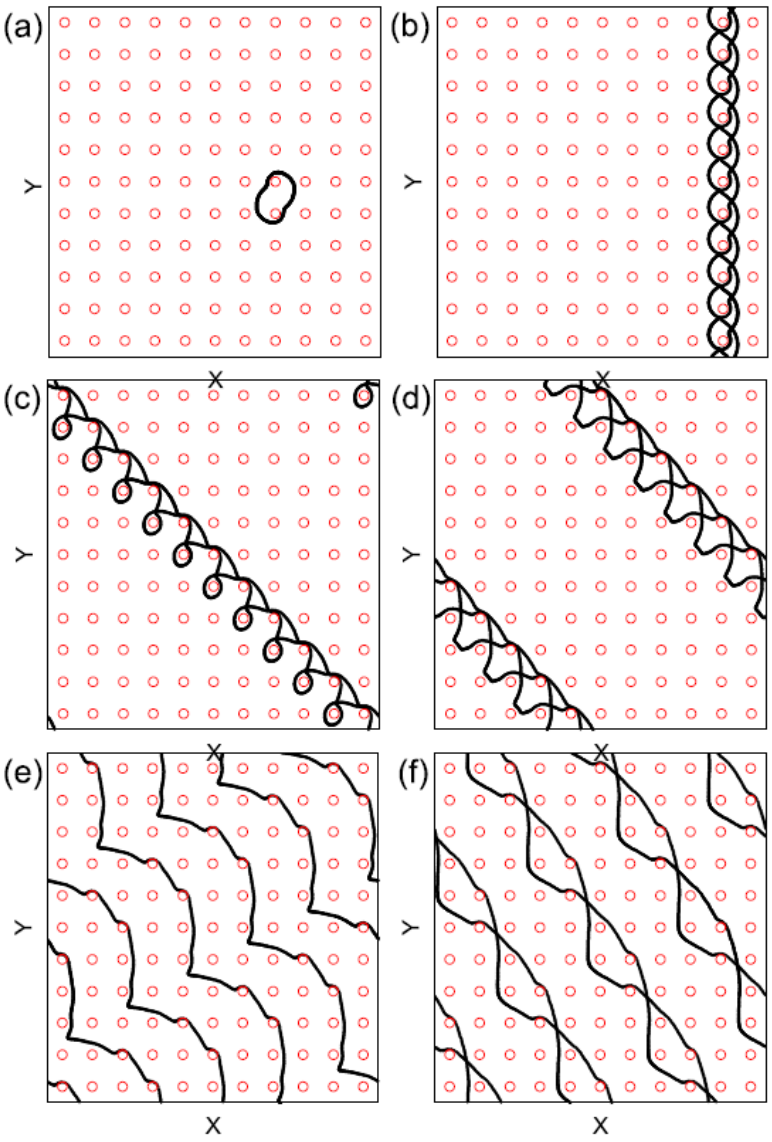

In Fig. 7.6 (a) it is plotted the velocity components versus the external dc driving force and in Fig. 7.6 (b) its corresponding skyrmion Hall angle curve for a system with $\alpha_m/\alpha_d = 9.962$ and $A = B = 0.5$, where the intrinsic Hall angle is $\theta_{sk}^{int} = -85.26°$. The windows of disordered motion are now larger, but there are still some steps in the velocity force curves corresponding to different locking steps. In Fig. 7.7 it is shown a blowup of the velocity force-curves from Fig. 7.6 over the range $0 < F^D < 0.15$. At low values of F^D, there is a pinned region with $\langle V_\parallel \rangle = \langle V_\perp \rangle = 0$. For higher values of dc external driving, it is possible to see a regime in which $\langle V_\parallel \rangle = 0$ while the magnitude of $\langle V_\perp \rangle$ is increasing with F^D, which is another example of transverse mobility. In Fig. 7.7 (b), the corresponding θ_{sk}vs. F^D curve shows that there is an interval over which the Hall angle is close to $\theta_{sk} = -90°$. In Fig. 7.8 (a) it is shown the skyrmion trajectories for the system of Fig. 7.7 at $F^D = 0.01$ in the pinned phase, where the skyrmion encircles four obstacles for every ac drive cycle. The radius of the pinned orbit increases with increasing Magnus force because the Magnus term effectively magnifies the ac driving amplitude. At $F^D = 0.11$ in Fig. 7.8 (b), the transverse mobility regime is illustrated, where the skyrmion moves in the $-y$ direction and encircles two obstacles every ac drive cycle. In Fig. 7.8 (c) at $F^D = 0.63$, the motion is locked to $\theta_{sk} = -78.6°$ and the skyrmion translates one lattice constant in the x direction and five lattice constants in the y direction, giving a $R = 5$. In Fig. 7.8 (d) it illustrated a chaotic regime at $F^D = 0.41$.

Figure 7.6 - (a) The average velocities $\langle V_\parallel \rangle$ (black) and $\langle V_\perp \rangle$ (red) as a function of the applied dc force F^D under a finite ac driving force with amplitudes $A = B = 0.5$, $\omega_1 = \omega_2$, $\alpha_m/\alpha_d = 9.962$ and $a_o = 0.65$. (b) The corresponding θ_{sk} curve. (From Vizarim *et. al*. [180], pg. 5).

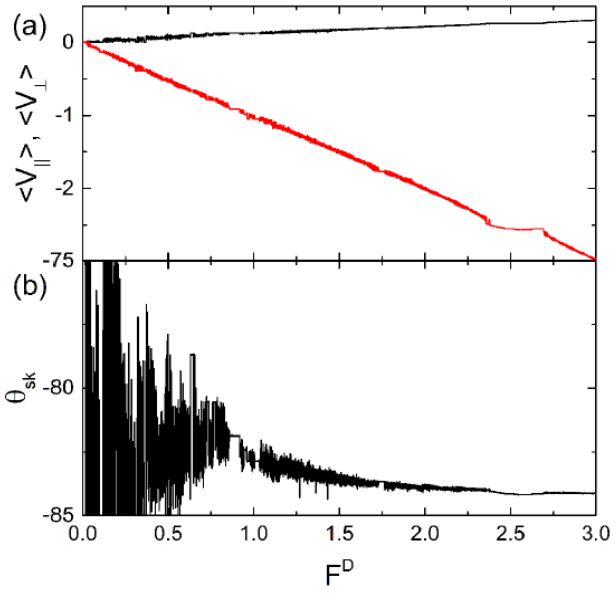

Figure 7.7 – Blowup of Fig. 7.7 for the interval $0 < F^D < 0.15$. (a) The average velocities $\langle V_\parallel \rangle$ (black) and $\langle V_\perp \rangle$ (red) as a function of the applied dc force F^D. (b) The corresponding θ_{sk} curve. (From Vizarim *et. al.* [180], pg. 6).

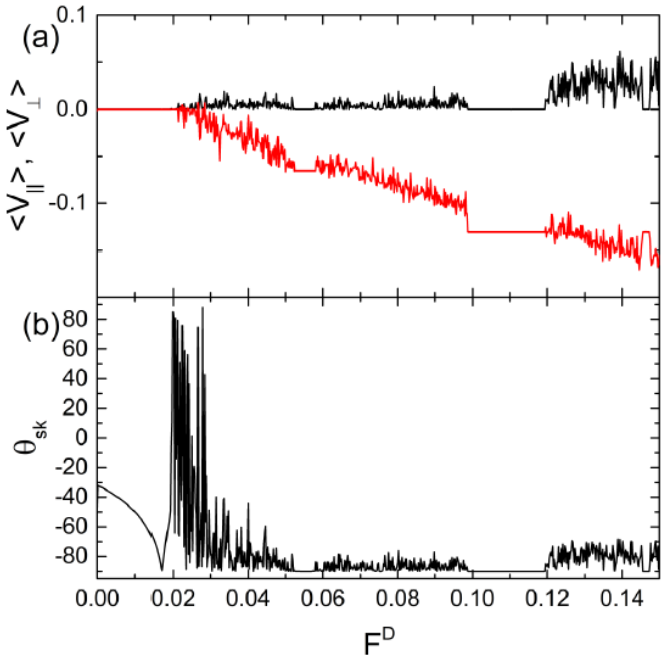

Figure 7.8 - The obstacles (open circles) and the skyrmion trajectory (black lines) for the system in Fig. 7.1 with $\alpha_m/\alpha_d = 9.962$ and ac drive amplitudes $A = B = 0.5$, $\omega_1 = \omega_2$ and $a_0 = 0.65$. (a) $F^D = 0.01$ in the pinned phase. (b) $F^D = 0.11$ the transverse mobility regime. (c) $F^D = 0.63$ where the skyrmion moves in both x and y directions. (d) $F^D = 0.41$, an example of chaotic motion. (From Vizarim *et. al.* [180], pg. 6).

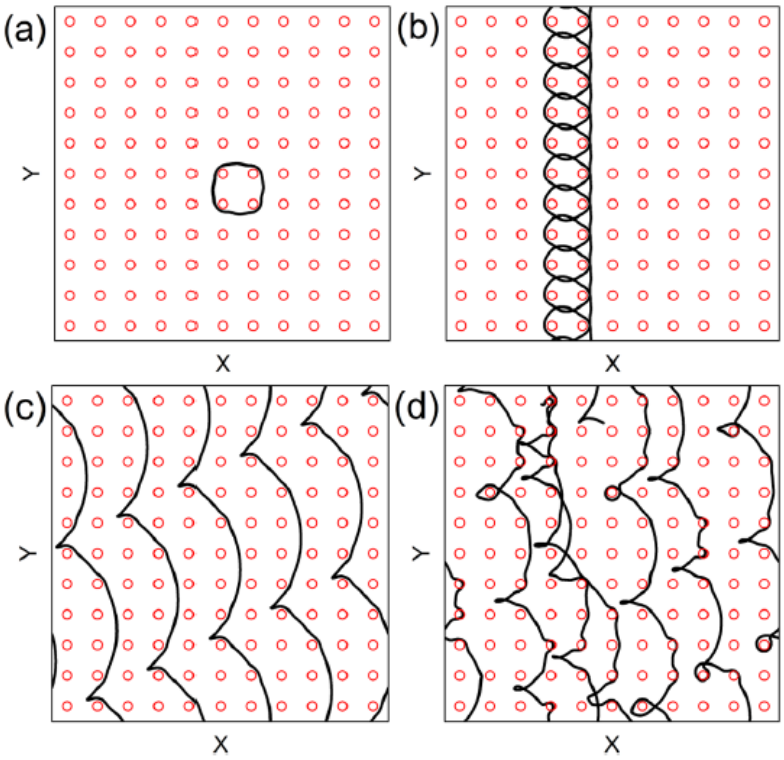

7.3.2 Varied ac drive amplitudes

In this section it is considered the effect on the velocity-force curves of varying the ac drive amplitude over a range of $A = 0$ to $A = 0.5$ for a fixed driving frequency. We summarize the results for only a few selected locking phases and disordered phases since there is a great number of different regimes as the amplitude A is varied. In Fig. 7.9 (a) it is plotted the dynamic phase diagram as a function of the dc drive F^D versus ac drive amplitude A for a system in Fig. 7.1 with $\alpha_m/\alpha_d = 0.577$, $A = B$ and $\omega_1 = \omega_2$. The highlighted phases are: the pinned phase, disordered phase, $\theta_{sk} = 0°$ locking, $\theta_{sk} = -26.6°$ locking, and $\theta_{sk} = -45°$ locking. When $A = 0$ the system is in the pinned phase for $F^D < 0.05$ and in the $\theta_{sk} = 0°$ for $0.05 < F^D < 0.5$. As F^D increases above $F^D = 0.5$, the system jumps to different locking phases that are not shown for better visualization of the highlighted phases. When A increases, the width of the pinned phases grows until it reaches a maximum near $A = 0.35$. The $\theta_{sk} = 0°$ phase is absent for $0.25 < A < 0.4$, which coincides with the window in which the $\theta_{sk} = -45°$ phase reaches its largest extend. Usually, disordered phases appear between the different locking phases. For $A < 0.35$, the skyrmion orbit is small enough so that the skyrmion is not able to encircle an obstacle, while for $A > 0.35$, the orbit becomes large enough to encircle an obstacle.

In Fig. 7.9 (b) it is plotted the dynamic phase diagram as a function of F^D versus A for the system in Figs. 7.6 and 7.7 with $\alpha_m/\alpha_d = 9.962$, $A = B$ and $\omega_1 = \omega_2$. The highlighted phases are only the pinned phase, disordered phase and the absolute transverse mobility phase with $\theta_{sk} = -90°$. The maximum extent for the pinned phase occurs for $A = 0.25$, which also corresponds to the ac drive at which the transverse mobility reaches its largest extent. There are two distinct windows of transverse mobility that are associated with two different types of skyrmion orbits. When $A < 0.1$, the skyrmion does not encircle any obstacles, while for larger amplitudes it encircles four obstacles. The reduction in the extent of the pinning and transverse mobility regions for A is the result of the larger orbit generated by the ac driving, with the skyrmion jumping to an orbit that encircles nine obstacles for values of $A > 0.5$.

These results indicate that the transverse mobility is most pronounced for higher values of α_m/α_d where the intrinsic Hall angle is the largest.

Figure 7.9 – Dynamic phase diagrams as a function of the dc drive, F^D, versus the ac driving amplitude, A in system with $A = B$ and $\omega_1 = \omega_2$. (a) The system of Fig. 9.1 where $\alpha_m/\alpha_d = 0.577$. (b) The system in Fig. 7.7 where $\alpha_m/\alpha_d = 9.962$. (From Vizarim *et. al.* [180], pg. 7).

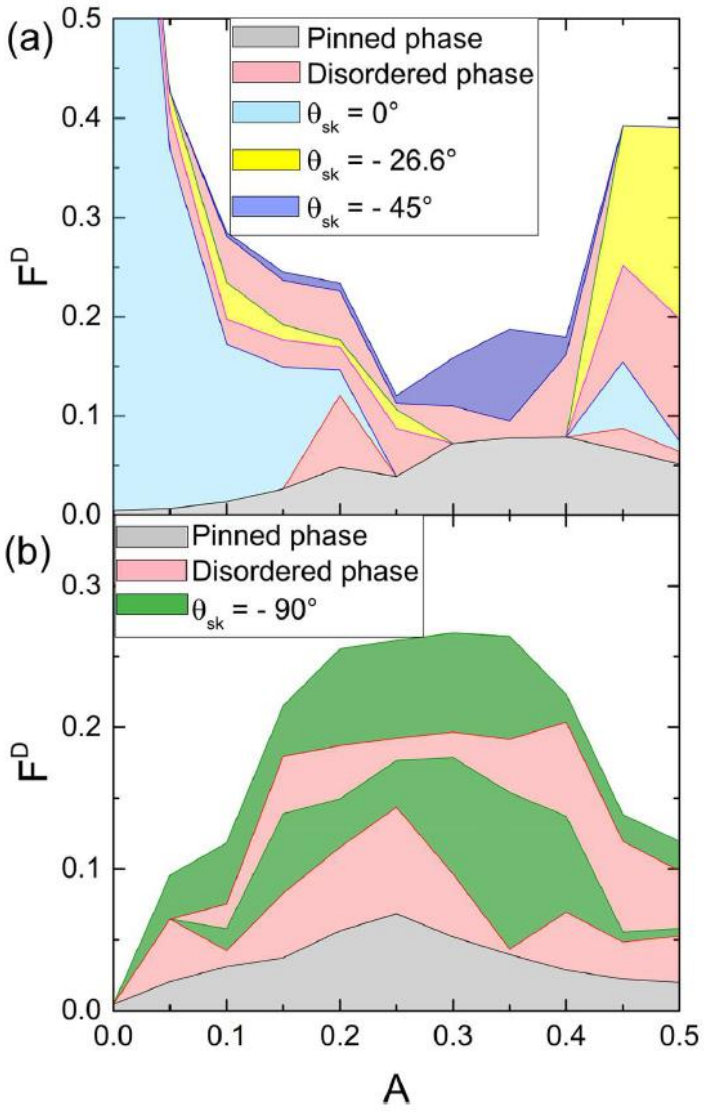

7.3.3 Two different ac drive amplitudes and skyrmion Hall angle reversal

Here it is considered the case where the ac drive amplitudes are different in the two directions, that is $A \neq B$. In Fig. 7.10 (a) it is plotted $\langle V_{\parallel} \rangle$ and $\langle V_{\perp} \rangle$ versus F^D for a system with $\alpha_m/\alpha_d = 0.577$, $A = 0.5$ and $B = 1.0$. In Fig. 7.11 (b) it is plotted the corresponding θ_{sk} versus F^D curve. Note that there is an extended region over which the system locks with $\theta_{sk} = -45°$ followed by a gradual decline to $\theta_{sk} = -30°$ for higher drives while a variety of locking steps and disordered regions appear. In Fig. 7.11 it is shown a zoomed version of Fig. 7.10 where $\langle V_{\parallel} \rangle$, $\langle V_{\perp} \rangle$ and θ_{sk} versus F^D appear for the interval $0 < F^D < 0.15$. At low values of F^D, there is an extended region where the skyrmion motion is locked in the x direction. The system has a reentrant pinned phase near $F^D = 0.09$ where both velocity components are null.

Figure 7.10 - (a) The average velocities $\langle V_{\parallel} \rangle$ (black) and $\langle V_{\perp} \rangle$ (red) as a function of the applied dc force F^D under a finite ac driving force with amplitudes $A = 0.5$ and $B = 1.0$, $\omega_1 = \omega_2$, $\alpha_m/\alpha_d = 0.577$ and $a_o = 0.65$. (b) The corresponding θ_{sk} curve. (From Vizarim *et. al.* [180], pg. 7).

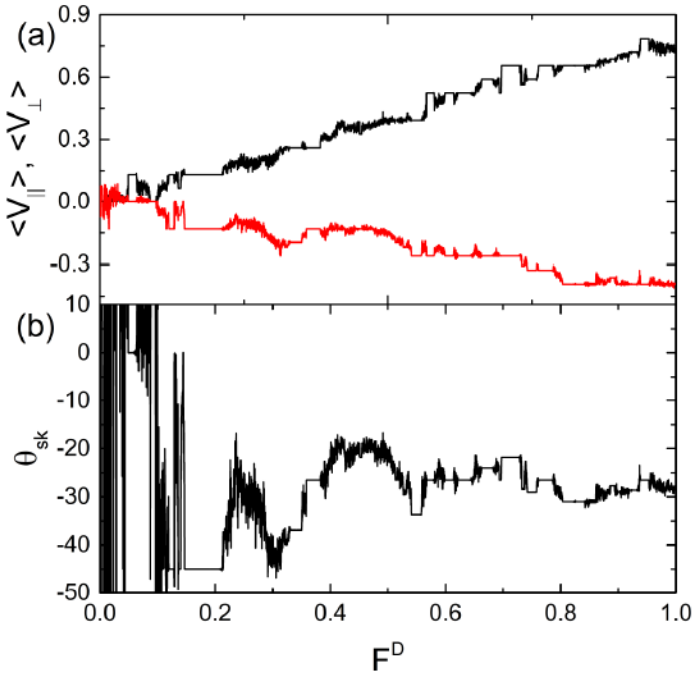

Figure 7.11 – Blowup of Fig. 9.10 for the interval $0 < F^D < 0.15$. (a) The average velocities $\langle V_{\parallel} \rangle$ (black) and $\langle V_{\perp} \rangle$ (red) as a function of the applied dc force F^D. (b) The corresponding θ_{sk} curve. (From Vizarim *et. al.* [180], pg. 7).

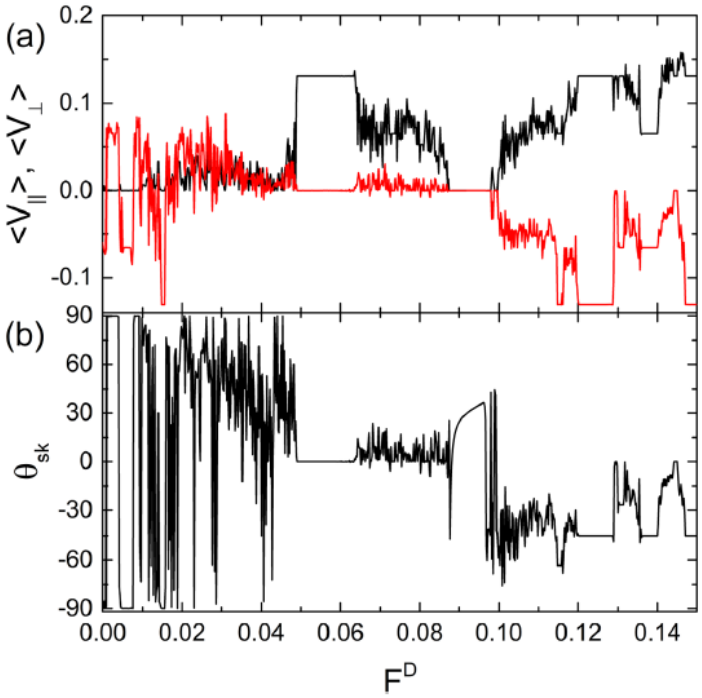

In Fig. 7.11 (b), for $F^D < 0.045$, the skyrmion Hall angle is oscillatory and undergoes repeated reversals from positive to negative values. The finite value of θ_{sk} in the pinned region near $F^D = 0.09$ results from the undefined θ_{sk} calculation that occurs when both the parallel

and perpendicular velocities are zero. In Fig. 7.12 (a) it is illustrated the skyrmion trajectories for the system in Fig. 7.11 at $F^D = 0.008$ where the transverse mobility occurs. The skyrmion is moving in the $+y$ direction, giving the Hall angle a positive value. In Fig. 7.12 (b) at $F^D = 0.055$, the motion is locked in the x direction and the skyrmion encircles two obstacles during the ac drive cycle. Figure 7.12 (c) shows the pinned orbit at $F^D = 0.093$, where the skyrmion encircles two obstacles but do not translate. In Fig. 7.12 (d) at $F^D = 0.2$, the motion is locked with $\theta_{sk} = -45°$.

Figure 7.12 - The obstacles (open circles) and the skyrmion trajectory (black lines) for the system in Fig. 7.10 with $\alpha_m/\alpha_d = 0.577$ and ac drive amplitudes $A = 0.5$ and $B = 1.0$, $\omega_1 = \omega_2$ and $a_0 = 0.65$. (a) $F^D = 0.008$ the transverse mobility phase. (b) $F^D = 0.055$ the skyrmion moving in the x direction. (c) $F^D = 0.093$ the reentrant pinned phase. (d) $F^D = 0.2$, where $\theta_{sk} = -45°$. (From Vizarim *et. al.* [180], pg. 8).

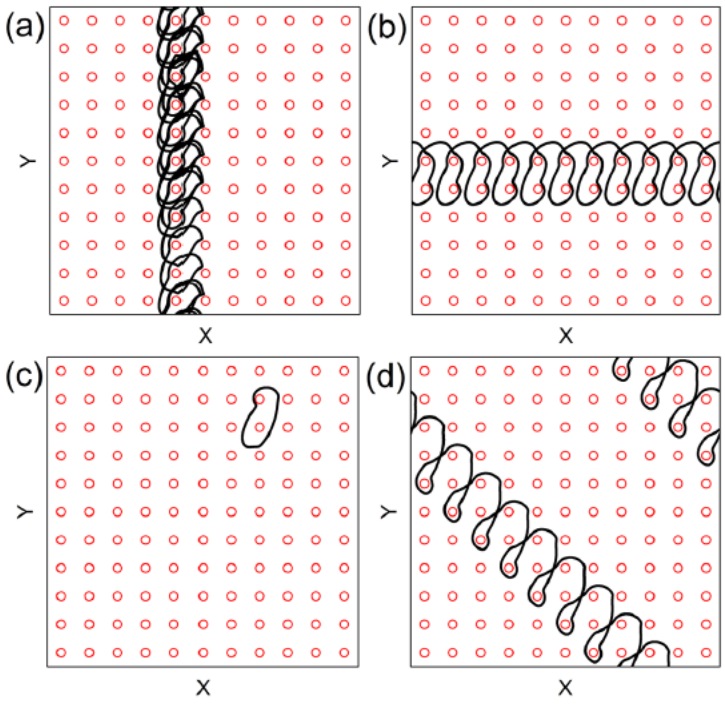

In Fig. 7.13 (a) it is shown a zoom of $\langle V_\parallel \rangle$ and $\langle V_\perp \rangle$ versus F^D for the system in Fig. 7.11 over the range $0 < F^D < 0.02$, and in Fig. 7.13 (b) the corresponding skyrmion Hall angle curve. The system passes through a series of locked phases that are associated with transverse mobility, but there are also repeated reversals of the Hall angle with increasing F^D. Another interesting feature is that at $F^D = 0$, the skyrmion has a finite velocity in the $-y$ direction. This motion, that occurs only where there is an ac drive and absent dc drive, represents a type of ratchet effect. In overdamped systems, similar ratchet effects can occurs for a particle on a periodic substrate that is subjected to biharmonic ac drives [184,185]. The ratchet effect occurs when enough symmetries are broken in a nonequilibrium system. Here, in the skyrmion system,

the Magnus force combined with dc and ac driving can produce asymmetric orbits as illustrated in Fig. 7.12 (c). In section 8 we will address the ratchet effects with skyrmions more carefully. In general, the ratchet effects are more prominent in systems without dc drive, or at least low values of F^D, whereas for high dc drives the Shapiro steps and directional locking are more prominent.

Figure 7.13 – Blowup of Fig. 7.10 for the interval $0 < F^D < 0.02$. (a) The average velocities $\langle V_\parallel \rangle$ (black) and $\langle V_\perp \rangle$ (red) as a function of the applied dc force F^D. (b) The corresponding θ_{sk} curve. (From Vizarim *et. al.* [180], pg. 8).

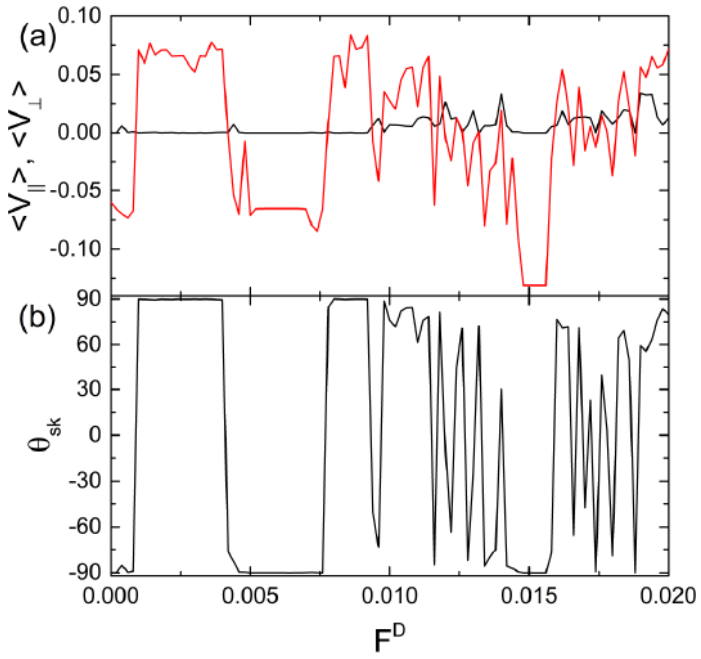

7.3.4 The ac drive frequency effect

Next it is considered the effect of holding the ac drive amplitudes fixed at $A = B$ but varying the ac drive frequencies so that $\omega_1 \neq \omega_2$. In Fig. 7.14 (a) it is plotted $\langle V_\parallel \rangle$ and $\langle V_\perp \rangle$ versus F^D for systems with $\alpha_m/\alpha_d = 0.45$, $A = B = 0.5$ using $\omega_1 = 2 \times 10^{-4}$ and $\omega_2 = 2\omega_1$, $3\omega_1$ and $4\omega_1$, while in Fig. 7.14 (b) it is shown the corresponding θ_{sk} curve. Some locking phases occurs for all three values of ω_2, however, the width of the locked phases varies with ω_2. When $\omega_2 = 2\omega_1$, the system locks to $\theta_{sk} = -45°$ at lower drives and then gradually approaches the intrinsic Hall angle value. In Fig. 7.15 (a) it is illustrated the skyrmion trajectory for the case of $\omega_2 = 2\omega_1$ at $F^D = 0.177$, where the motion is locked at $\theta_{sk} = -45°$. Fig. 7.15 (b) shows the skyrmion trajectory for $F^D = 0.3$, where the skyrmion moves with $\theta_{sk} = -26.56°$.

In Fig. 7.16 (a) it is plotted $\langle V_\parallel \rangle$ and $\langle V_\perp \rangle$ versus F^D for a system with $A = B = 0.5$ and $\alpha_m/\alpha_d = 1.732$. When $\omega_2 = 3\omega_1$ there is an initial pinned phase at low values of external dc driving. The system locks to $\theta_{sk} = -45°$ for several drive intervals, and there is also regions

where total transverse mobility occurs, as shown in Fig. 7.16 (b) in the corresponding θ_{sk} vs. F^D curve. When $\omega_2 = 2\omega_1$, the pinned phase extends out to higher values of dc driving and there is also regions where transverse mobility occurs. Although the systems with different frequencies exhibit lots of disordered phases, the results show that the transverse mobility can be induced by varying the ac drive frequencies.

Figure 7.14 - (a) The average velocities $\langle V_{\parallel} \rangle$ (black) and $\langle V_{\perp} \rangle$ (red) as a function of the applied dc force F^D under a finite ac driving force with amplitudes $A = B = 0.5$, $\alpha_m/\alpha_d = 0.45$ and $a_o = 0.65$ for varied values of ω_2/ω_1: $\omega_2 = 2\omega_1$ (black and red), $\omega_2 = 3\omega_1$ (green and blue), $\omega_2 = 4\omega_1$ (orange and yellow), (b) The corresponding θ_{sk} curve, $\omega_2 = 2\omega_1$ (black), $\omega_2 = 3\omega_1$ (red), $\omega_2 = 4\omega_1$ (blue), . (From Vizarim *et. al.* [180], pg. 9).

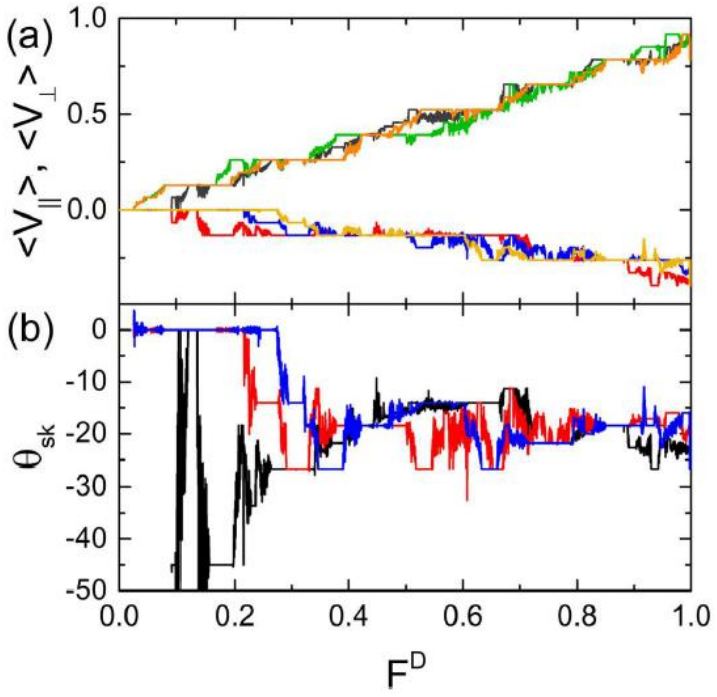

Figure 7.15 - The obstacles (open circles) and the skyrmion trajectory (black lines) for the system in Fig. 7.14 with $\alpha_m/\alpha_d = 0.45$ and ac drive amplitudes $A = B = 0.5$, $\omega_2 = 2\omega_1$ and $a_0 = 0.65$. (a) $F^D = 0.177$ the skyrmion moving with $\theta_{sk} = -45°$. (b) $F^D = 0.3$ where $\theta_{sk} = -26.56°$. (From Vizarim *et. al.* [180], pg. 9).

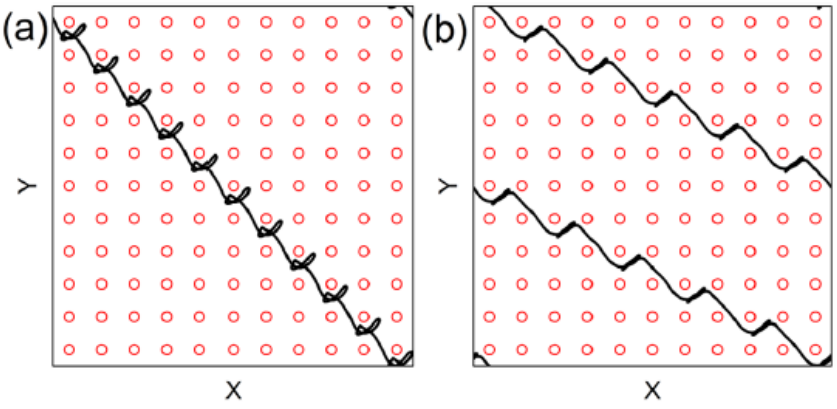

Figure 7.16 - (a) The average velocities $\langle V_{\parallel} \rangle$ (black) and $\langle V_{\perp} \rangle$ (red) as a function of the applied dc force F^D under a finite ac driving force with amplitudes $A = B = 0.5$, $\alpha_m/\alpha_d = 1.732$ and $a_o = 0.65$ for varied values of ω_2/ω_1: $\omega_2 = 2\omega_1$ (black and red), $\omega_2 = 3\omega_1$ (green and blue). (b) The corresponding θ_{sk} curve, $\omega_2 = 2\omega_1$ (black), $\omega_2 = 3\omega_1$ (red). (From Vizarim *et. al.* [180], pg. 9).

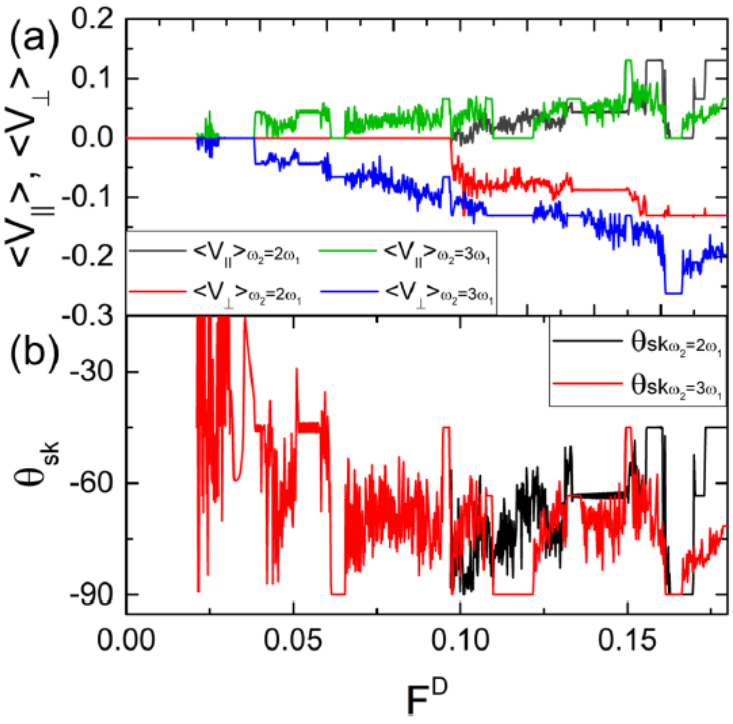

7.3.5 Discussion and Summary

In this work, the temperature effects were neglected. However, thermal effects can be important in certain skyrmion systems. Thermal fluctuations can wash out directional phase lockings, but in some cases they may also induce other type of phase lockings [186]. As an example, in Fig. 7.17 we illustrate the thermal effect in the system of Fig. 7.1, with $\alpha_m/\alpha_d = 0.577$, $A = B = 0.5$, and $\omega_1 = \omega_2$ at $F^D = 0.41$. At $T = 0$, the motion is locked to $\theta_{sk} = -18.43°$, but as the temperature grows, the magnitude of the skyrmion Hall angle gradually increases. A full exploration of thermal effects may be subject of a future work.

Experiments that could be performed in these systems include direct imaging of skyrmions and measurements of changes in the topological Hall effect. Another route for further exploitation would be to examine noise fluctuations [27] in order to observe the emergence of narrow band signals associated with phase locking. It has already been shown experimentally that such measurements are possible in skyrmion systems [187]. In the locked cases the skyrmion motion should be periodic and produce a large narrow band noise signal, while in disordered regions this signal should be reduced or lost. It would also be interesting to explore

the effect of the internal modes of skyrmions [131,132], which could induce additional oscillating signals that might produce different types of phase locking. We focused on the case of a single skyrmion, however, if lattices of skyrmions interact with 2D periodic substrates, we expect that additional collective effects would occur that would depend on the filling factor. Slightly away from commensurate fillings, at which the number of skyrmions is and integer multiple of the number of obstacles, soliton-like states can appear which could themselves exhibit Shapiro steps and other phase locking phenomena, similar to what has been observed in colloidal and superconducting vortices with periodic substrates. In actual physical realizations of skyrmions systems, such as, in chiral magnets or liquid crystals, skyrmion nucleation or destruction may occur. We assume that skyrmions are not created or destroyed within our simulation region, and it should not be difficult to reach such a regime experimentally by focusing on a portion of the sample that is not close to the boundaries.

Figure 7.17 - θ_{sk} vs. temperature T in the system of Fig. 7.1, with $\alpha_m/\alpha_d = 0.577$, $A = B$ and $\omega_1 = \omega_2$ at $F^D = 0.41$. At $T = 0$, the motion is ordered along $\theta_{sk} = -18.43°$. As the temperature rises, the magnitude of the skyrmion Hall angle increases (From Vizarim *et. al.* [180], pg. 10).

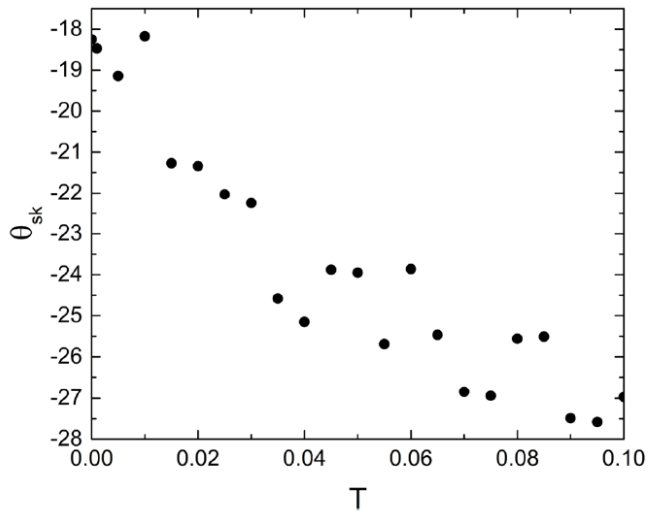

Our results here focus on the case where $\omega_1 = \omega_2$, or where the two frequencies are commensurate. If the driving frequencies are not commensurate, the skyrmion orbit can become asymmetric, which could lead to ratcheting behavior. We explore the ratching effect in further details in section 10.

We examined a skyrmion interacting with 2D periodic array of obstacles under applied dc drive and biharmonic ac drives, finding a rich variety of nonlinear dynamical effects due to the presence of the Magnus force and the velocity dependence of the skyrmion Hall angle. A biharmonic ac drive alone creates a circular skyrmion orbit in the absence of obstacles or a dc

drive. Under only dc driving and in the presence of the periodic obstacles, the skyrmion passes through a serial of directional locking phases due to the skyrmion Hall angle effect. When a finite biharmonic ac drive is included, we find that the velocity-force curves show a series of jumps and locking intervals in which the skyrmion motion locks to specific symmetry directions of the substrate. Within these locking phases, the skyrmion can encircle multiple obstacles during each ac drive cycle. We also observe regimes where the skyrmion motion is disordered and the motion is not locked to a specific direction. We find that the locking phases can be associated with both increases and decreases in the skyrmion Hall angle. Many of the locking phases are reentrant and recur repeatedly for increasing dc drive. In general, as the Magnus force increases, the skyrmion encircles a larger number of obstacles during each ac drive cycle, and for large Magnus forces, we observe a series of absolute transverse mobility phases in which the skyrmion moves at exactly 90° with respect to the dc driving direction. We find reentrance in both the transverse mobility and the pinning phase.

8 Skyrmion Pinball

8.1 Skyrmions in periodic pinning under the influence of ac drives only

In this work the main idea is to understand the skyrmion dynamics under the influence of just the ac drive, that is, there is no dc drive applied to the system. The work is inspired on a previous work concerning superconducting vortices under the influence of ac drive and a periodic obstacle array [188]. This work was recently published in Journal of Physics Communications [189].

We examine skyrmions interacting with a square array of obstacles under ac drives applied in one or two directions. For a single direction of ac driving, we find that the Magnus force in conjunction with the obstacle interactions can create elliptical skyrmion orbits of increasing size, leading to localized phases, chaotic phases, and translating or ratcheting orbits. Under two ac drives that are out of phase by 90° and applied in two directions, the skyrmions form localized commensurate orbits that encircle an integer number of obstacles, similar to the electron pinball effect observed for electrons in antidot lattices. As a function of ac amplitude, Magnus force strength, and obstacle size, we find that chaotic scattering regimes and directed motion can emerge even in the absence of asymmetry in the substrate. The directed motion

follows different symmetry axes of the periodic substrate, and we observe a variety of reversed ratchet effects. The Magnus force in the skyrmion system produces a significantly larger number of directed motion regimes than are exhibited by overdamped systems. We discuss how these results could be used to move skyrmions in a controlled way for possible applications.

8.2 Model and Simulation details

In this work we consider a two-dimensional skyrmion system with $L \times L$ with periodic boundary conditions on y and x directions. A single skyrmion is subjected to this obstacle landscape and ac drives are applied in the x and y direction, as illustrated in Fig. 8.1. The dynamical properties of the skyrmion system interacting with the obstacle array were simulated using the particle model for skyrmions, shown in Eq. (8.1), using Molecular Dynamics technique.

$$\alpha_d \mathbf{v_i} + \alpha_m \hat{z} \times \mathbf{v_i} = \mathbf{F}_i^o + \mathbf{F}^{ac} \tag{8.1}$$

In this equation, the first term on the left is the damping term, where α_d is the damping term. The second term on the left represents the Magnus force, where α_m is the Magnus term. We model the skyrmion-obstacle potential energy interaction in the Gaussian form $U_o = C_o e^{-(r_{io}/a_o)^2}$, where C_o is the strength of the obstacle potential, r_{io} is the distance between the skyrmion i and the obstacle o, and a_o is the obstacle radius. Thus, the force between the obstacles and the skyrmions take the form $\mathbf{F}_i^o = -\nabla U_o = -F_o r_{io} e^{-(r_{io}/a_o)^2} \hat{\mathbf{r}}_{io}$, where $F_o = 2U_o/a_o^2$. The obstacle density used in this work is $0.093/\xi^2$. The last term is the ac drive, $\mathbf{F}_x^{ac} = A \sin(2\pi\omega_1 t)\, \hat{\boldsymbol{x}}$ for longitudinal driving and $\mathbf{F}_y^{ac} = B \cos(2\pi\omega_2 t)\, \hat{\boldsymbol{y}}$ for transversal driving. We measure the skyrmion velocity in the $\langle V_\parallel \rangle = \langle \mathbf{v} \cdot \hat{\mathbf{x}} \rangle / (2\pi\omega_1 a)$, and the y component, $\langle V_\perp \rangle = \langle \mathbf{v} \cdot \hat{\mathbf{y}} \rangle / (2\pi\omega_1 a)$, where a is the substrate lattice constant. The velocities are averaged over 100 ac drive cycles. Under the normalization we use here, when $\langle V_\parallel \rangle = 1.0$ or $\langle V_\perp \rangle = 1.0$ indicated that the skyrmion is translating by one substrate lattice constant per ac drive cycle in the x or y direction, respectively. The external ac drive amplitude is increased in small steps of A (B) $= 0.002$ and wait 10^6 simulation time steps between increments to ensure steady state. We normalize the damping and Magnus coefficients as $\alpha_d^2 + \alpha_m^2 = 1$.

Figure 8.1 A schematic of the system, which consists of a square array of obstacles (red circles). The black lines correspond to the skyrmion trajectories under the influence of both damping, Magnus term, and ac drive. In (a) the ac drive is applied along the x direction and in (b) both x and y directions (From Vizarim *et. al.* [189], pg. 3)

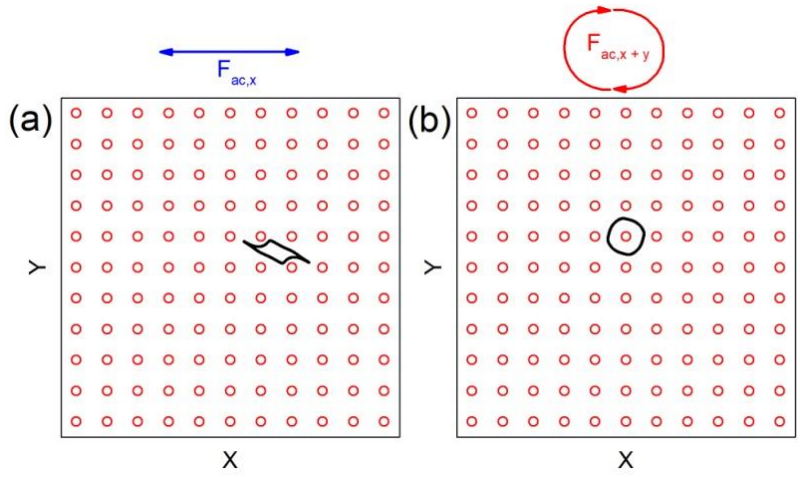

8.3 Results

8.3.1 AC drive just in x direction

In this section we consider the case of a skyrmion subjected to a linear ac drive applied along the x direction, that is, $B = 0$ and A is finite, as whon in Fig. 8.1 (a). In an overdamped system, a particle under the influence of such drive would remain localized and would simply follow a one-dimensional trajectory along the x direction between the obstacles. However, for the skyrmion case where there is a finite Magnus term, the skyrmion moves with 2D orbits, as illustrated in Fig. 8.2 for a system with $\alpha_m/\alpha_d = 0.577$ and $a_0 = 0.65$. At $A = 0.5$ in Fig. 8.2 (a), the orbiting motion is localized. For a larger ac drive amplitude of $A = 0.91$, in Fig. 8.2 (b), the orbit size becomes large enough so the skyrmion collides with multiple obstacles, resulting in a delocalization and diffusive chaotic motion but no net drift. In Fig. 8.2 (c) at $A = 1.22$, the skyrmion has relocalized with larger orbit. That is, the skyrmion has an orbit large enough to stabilize again and remain localized in the substrate lattice. The chaotic regime illustrated in Fig. 8.2 (b) occurs at the transition between a skyrmion orbit that spans one plaquette and the orbit that spans two plaquettes, as illustrated in Figs. 8.2 (a) and (c) respectively. In each case, the orbits are oriented at an angle to the linear drive due to the Magnus force. In the absence of a substrate, the skyrmion would move in a one-dimensional orbit at an angle of $\theta_{sk} = \arctan(\alpha_m/\alpha_d)$ to the x direction. As A increases above $A = 1.0$, the skyrmion remains locked in the localized state of Fig. 8.2 (c) until a transition occurs between localized motion spanning two plaquettes and the localized motion spanning three plaquettes, that is illustrated in Fig. 8.2 (e) at $A = 1.5$. A series of such localized phases occurs each time the skyrmion orbit spans an

integer number n of plaquettes, such as the $n = 4$ state shown in Fig. 8.2 (f) at $A = 2.0$. At the transition between different localized states, delocalized or chaotic motion appears. In some cases there can also be fractional localization, as shown in Fig. 8.2 (d) at $A = 1.22$, where the skyrmion repeatedly switches between localized orbits that spans two and three plaquettes.

Figure 8.2 - The obstacles (open circles) and the skyrmion trajectory (black lines) for the system with $\alpha_m/\alpha_d = 0.577$ and $a_0 = 0.65$ for linear ac driving along the x direction. (a) $A = 0.5$ the skyrmion is oscillating between obstacles, spanning one plaquette. (b) $A = 0.91$ the skyrmion motion is delocalized. (c) $A = 1.0$ the skyrmion motion is localized spanning two plaquettes. (d) $A = 1.22$, the skyrmion exhibits direct motion, where it moves one lattice constant in $-y$ direction for every two ac drive cycles. (e) $A = 1.5$, where the skyrmion orbit spans three plaquettes. (f) $A = 2.0$, where the skyrmion spans four plaquettes. (From Vizarim *et. al.* [189], pg. 4).

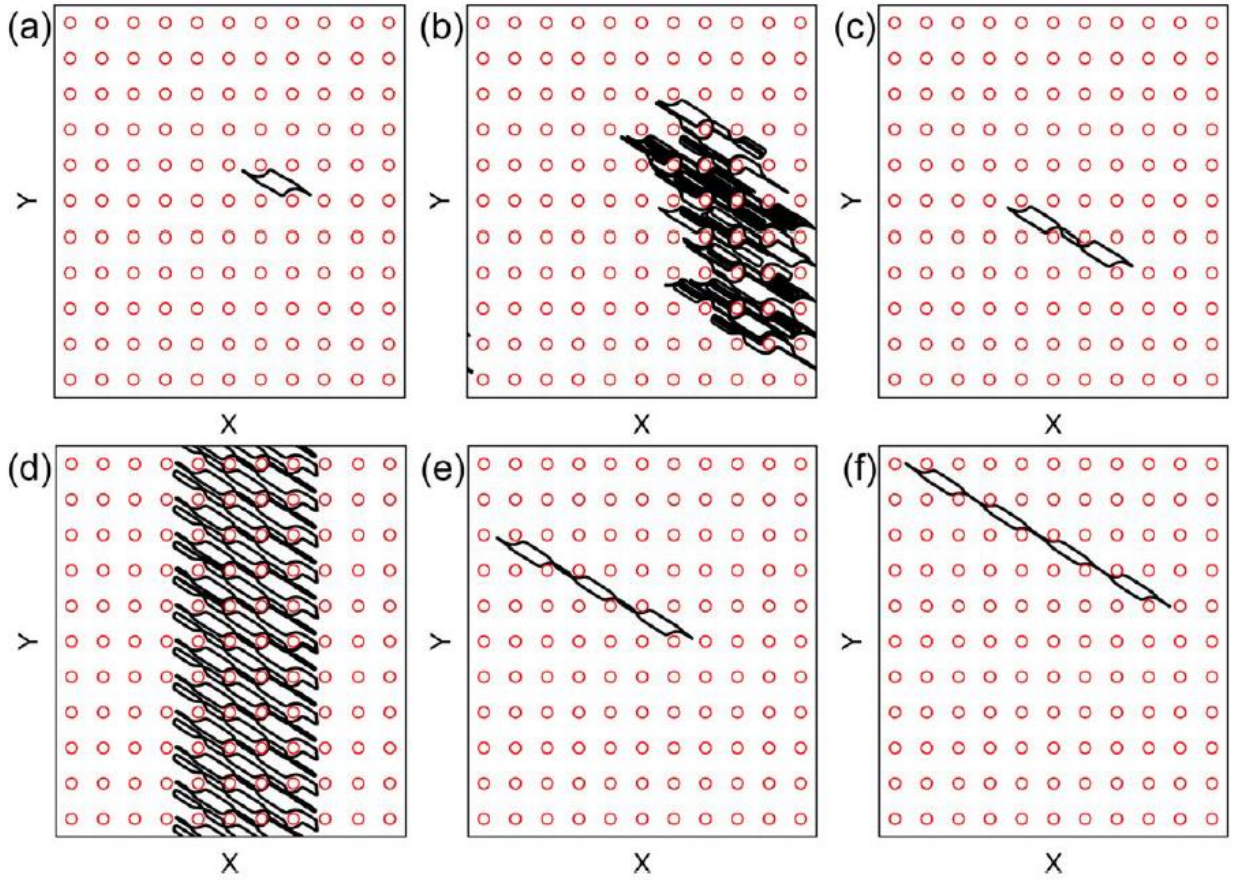

In the overdamped limit, particles on a 2D substrate under linear ac drive do exhibit any kind of directed motion or ratchet effect. However, if two perpendicular ac drives are applied, the orbits become two dimensional and direct motion can occur if the ac driving breaks symmetry [184,185,190–192]. In the skyrmion case, a linear ac drive in conjunction with skyrmion obstacle interactions produces a 2D orbit due to the Magnus force, as illustrated in Fig. 8.2 (a). Since the orbit is chiral, temporal symmetry is broken and a ratchet effect can occur. Under linear ac driving, only limited regimes of ratcheting were observed, but these results show

that even using simple linear ac driving is possible to induce ratchet effects on skyrmions in symmetric substrates.

In Fig. 8.3 it is plotted $\langle V_{\parallel} \rangle$ and $\langle V_{\perp} \rangle$ versus A for the system in Fig. 8.2 with linear ac driving along the x direction. In the localized states, $\langle V_{\parallel} \rangle = \langle V_{\perp} \rangle = 0$, while in the delocalized states, there are finite velocity fluctuations. Since the particle motion is diffusive, these fluctuations reduce in magnitude if the velocities are averaged over a long period of time. At $A = 1.22$, there is a direct skyrmion motion in the $-y$ direction and it is found that $\langle V_{\parallel} \rangle = 0$ and $\langle V_{\perp} \rangle = -0.5$, indicating that the skyrmion is translating one lattice constant every two ac drive cycles, as illustrated in Fig. 8.2 (d). The vertical dashed lines in Fig. 8.3 indicate the transition points where the skyrmion changes from a phase spanning n plaquettes to a $n + 1$ plaquettes. The transition between phases are characterized by disordered and chaotic phases or fractional localized states, where every two ac drive cycles the skyrmion is switching between a n plaquete state and a $n + 1$ plaquette state.

Figure 8.3 - The average velocities $\langle V_{\parallel} \rangle$ and $\langle V_{\perp} \rangle$ as a function of the ac drive amplitude A for a single skyrmion in the square obstacle array using $\alpha_m/\alpha_d = 0.577$, $a_o = 0.65$ and $B = 0$. Vertical dashed lines indicate the boundaries of the regions where the skyrmion orbits passes through $n = 1,2,3$ or 4 plaquettes, from left to right (From Vizarim *et. al.* [189], pg. 5).

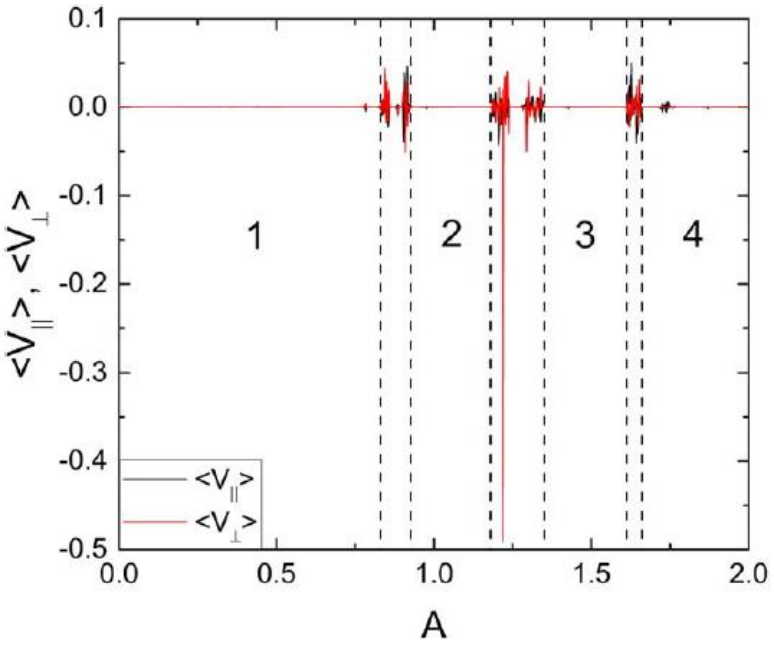

In Figs. 8.4 (a) – (f) it is plotted representative skyrmion trajectories for a system using larger Magnus component, $\alpha_m/\alpha_d = 1.732$. For $A = 0.5$ and $A = 0.934$ in Figs. 8.4 (a) and 8.4 (b), the orbit is localized at $n = 1$ and $n = 3$ plaquettes, respectively. The skyrmion motion remains entirely within the interstitial region between obstacles for $A = 0.5$, but when $A =$

0.934, the skyrmion encircles the obstacles. At $A = 1.05$ in Fig. 8.4 (c), there is a translating orbit in which the skyrmion moves one lattice constant in $+y$ direction per ac drive cycle. For $A = 1.136$, shown in Fig. 8.4 (d), the orbit is localized again but exhibits a more complex shape, encircling four obstacles that do not fall along a one-dimensional line. For $A = 1.29$ in Fig. 8.4 (e), there is a translating orbit where the skyrmion moves in the $-y$ and $+x$ directions at an angle of $-45°$, translating one lattice constant during every ac drive cycle. In Fig. 8.4 (f) at $A = 1.656$, there is a $n = 7$ localized orbit state that do not encircle any obstacle.

Figure 8.4 – The obstacles (open circles) and the skyrmion trajectory (black lines) for the system with $\alpha_m/\alpha_d = 1.732$ and $a_0 = 0.65$ for linear ac driving along the x direction. (a) $A = 0.5$ the skyrmion is oscillating between obstacles, spanning $n = 1$ plaquette. (b) $A = 0.934$ the skyrmion motion is localized in state $n = 3$ plaquettes. (c) $A = 1.05$ the skyrmion has direct motion in $+y$ direction. (d) Localized motion at $A = 1.136$. (e) At $A = 1.29$, the skyrmion translates along $-45°$ angle. (f) A $n = 7$ localized state at $A = 1.656$. (From Vizarim *et. al.* [189], pg. 6).

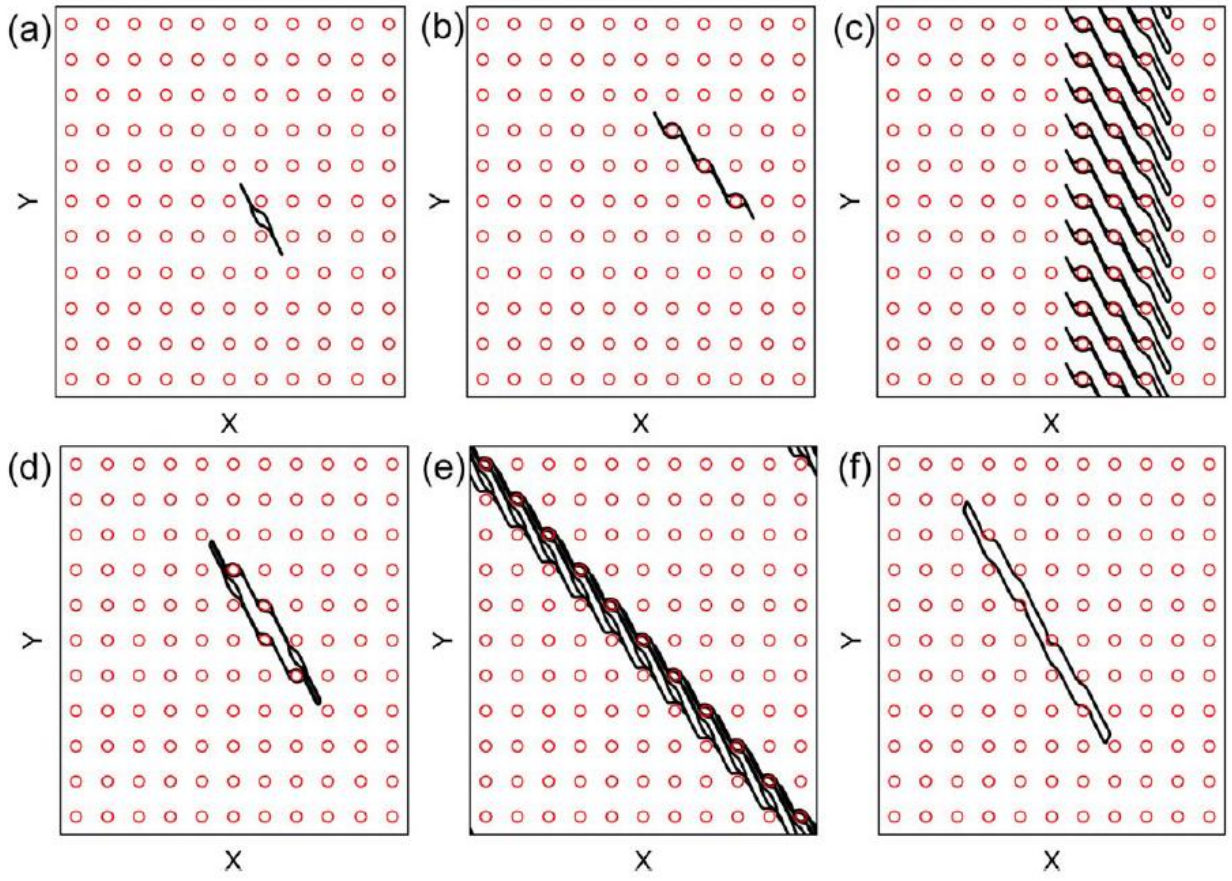

In Fig. 8.5 (a) it is plotted the velocity components as a function of the ac drive amplitude in the x direction for the system in Fig. 8.4 showing the different regions of localized and translating orbits. In Fig. 8.5 (b) is a blowup of Fig. 8.5 (a) over the range $0.9 < A < 1.35$. Localized orbits appear when $A < 0.96$, followed by a window of delocalized orbits for $0.96 \leq A < 1.03$. The translating orbit illustrated in Fig. 8.4 (c) corresponds to a plateau of positive

$\langle V_\perp \rangle$ extending from $A = 1.03$ to $A = 1.07$. As the amplitude increases, the system enters in another regime of chaotic motion. When $A = 1.26$, a translating state appears with motion along $-45°$. Here, the velocities plateau with $-\langle V_\parallel \rangle = \langle V_\perp \rangle$. This is followed by a small localized region, and then at $A = 1.28$ by a second regime of $-45°$ translation, where the skyrmion moves one lattice constant in $+y$ and $-x$ during every ac drive cycle. Note that this regime is distinct than the previous one, because in the previous one the motion occurred every two ac drive cycles. At $A = 1.29$ the $-45°$ state changes directionand the skyrmion moves one lattice constant in $+x$ and $-y$ direction for every ac drive cycle, as illustrated in Fig. 8.4 (e). The motion becomes localized again above $A = 1.3$ as shown in Fig. 8.4 (f). In general, as the Magnus term in increased, a greater and richer variety of distinct localized and translating orbits appear. The translating orbits are generally along the x or y directions or at a $45°$ angle, since these are the most prominent symmetry directions of the square obstacle lattice.

Figure 8.5 – (a) The average velocities $\langle V_\parallel \rangle$ and $\langle V_\perp \rangle$ as a function of the ac drive amplitude A for a single skyrmion in the square obstacle array using $\alpha_m/\alpha_d = 1.732$, $a_o = 0.65$ and $B = 0$. (b) A blowup of (a) for the range $0.9 < A < 1.35$. (From Vizarim *et. al.* [189], pg. 6).

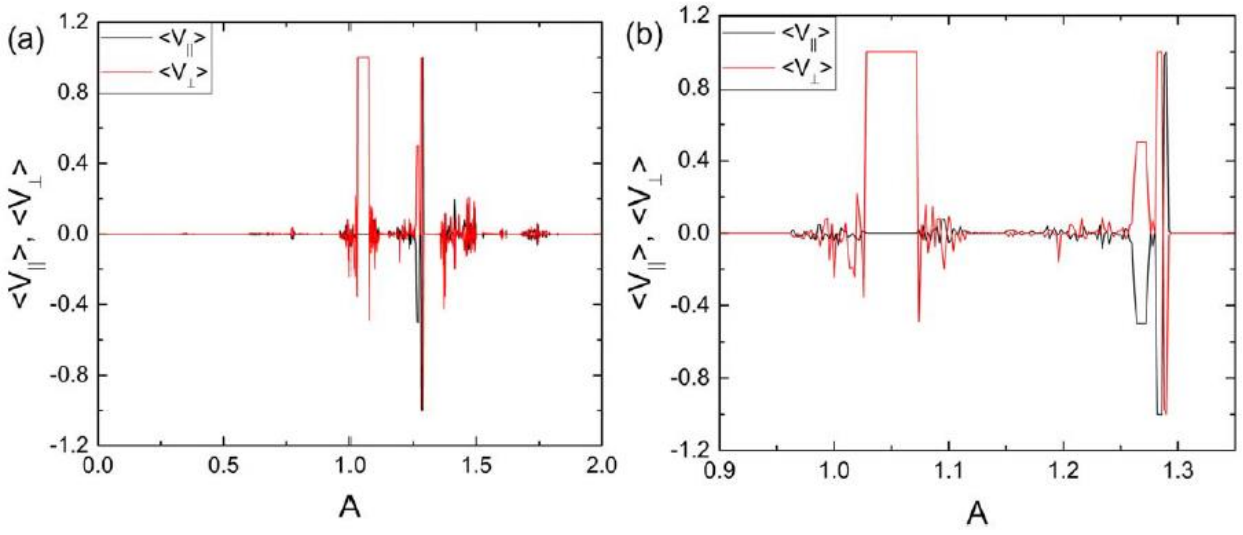

For higher values of α_m/α_d, it was found delocalized or chaotic motion that exhibit an average displacement. In Fig. 8.6 it is plotted some representative skyrmion trajectories for a system using $\alpha_m/\alpha_d = 9.962$. At $A = 0.5$ in Fig. 8.6 (a), there is a localized 1D orbited oriented at nearly 90° to the driving direction. For $A = 0.576$, the orbit is delocalized or chaotic but has a net drift in the $-y$ direction and a smaller net drift along $-x$ direction, as shown in Fig. 8.6 (b). When $A = 0.885$, as shown in Fig. 10.6 (c), the skyrmion performs a translating orbit with gradual motion by one lattice constant in $+y$ direction, where it can spend many ac drive cycles at each location before stepping to the next location. In Fig. 8.6 (d), at $A = 0.936$, a

localized orbit appears that encircles two obstacles at the top and bottom of the orbit. In Fig. 8.7 it is plotted $\langle V_{\parallel} \rangle$ and $\langle V_{\perp} \rangle$ versus A to illustrate the transitions between the different states. The motion is localized for $A < 0.55$ and $A > 1.7$, while in intermediate value of A, various fluctuating and localized regions occur.

Figure 8.6 – The obstacles (open circles) and the skyrmion trajectory (black lines) for the system with $\alpha_m/\alpha_d = 9.962$ and $a_0 = 0.65$ for linear ac driving along the x direction. (a) $A = 0.5$ the skyrmion is oscillating between obstacles, nearly along $90°$. (b) $A = 0.576$ a delocalized motion. (c) Translating along $+y$ at $A = 0.885$ (d) Localized motion at $A = 0.936$. (From Vizarim *et. al.* [189], pg. 7).

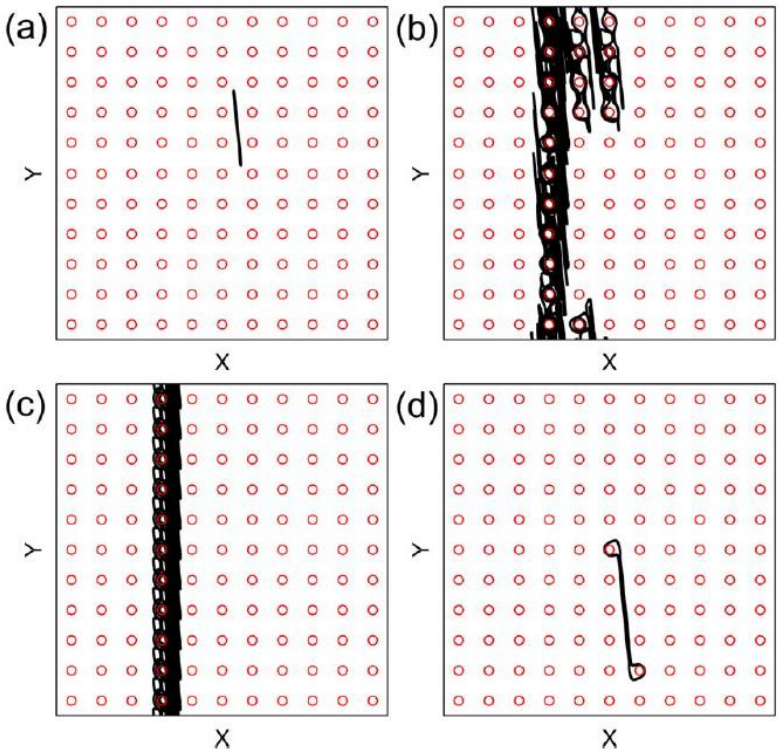

Figure 8.7 – The average velocities $\langle V_{\parallel} \rangle$ and $\langle V_{\perp} \rangle$ as a function of the ac drive amplitude A for a single skyrmion in the square obstacle array using $\alpha_m/\alpha_d = 9.962$, $a_o = 0.65$ and $B = 0$. (From Vizarim *et. al.* [189], pg. 8).

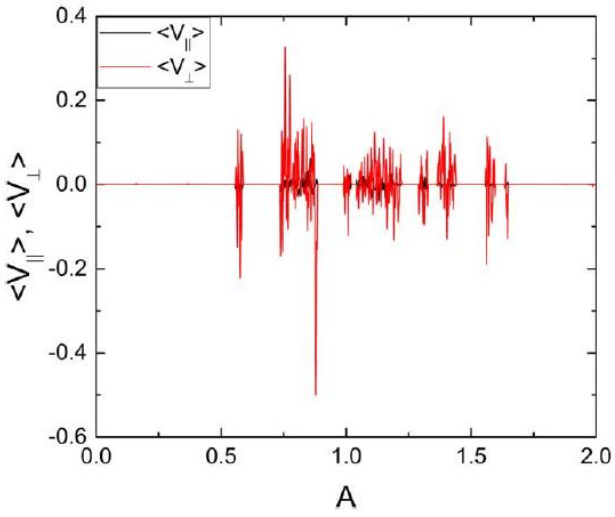

8.3.2 Circular ac drive with $A = B$

In this section it is considered the case of circular ac driving by applying two ac drives simultaneously that are perpendicular to each other and 90° out of phase. In the overdamped limit, a symmetric substrate does not produce any directed motion when the frequencies and amplitudes of the two ac drives are identical. However, if the amplitudes or frequencies are distinct, spatial symmetry can be broken, leading to a directed motion [184,185,190,191]. For $A = B$ and $\omega_1 = \omega_2$, if we set $\alpha_m/\alpha_d = 0$, no ratchet effect can be found and the dynamics are the same as those found in vortex pinball systems, with transitions between localized and delocalized orbits as the ac drive amplitude is increased [188].

In Fig. 8.8 it is shown the skyrmion trajectories in a system with circular ac driving at $\alpha_m/\alpha_d = 0.577$ for $A = B$ and $\omega_1 = \omega_2 = 2 \times 10^{-5}$. At $A = 0.25$, in Fig. 8.8 (a), the skyrmion forms a localized orbit that encircles one obstacle. In Fig. 8.8 (b) at $A = 0.375$, the skyrmion exhibits a translating orbit in which it spirals around two obstacles per ac drive cycle and moves in $-y$ direction. Fig. 8.8 (c) shows a localized orbit at $A = 0.5$ where the skyrmion encircles four obstacles, while the localized orbit at $A = 0.672$in Fig. 8.8 (d) has no net drift but exhibits diffusive motion over long-time scales. At $A = 0.978$ in Fig. 8.8 (e), there is a translating orbit in which the skyrmion moves one lattice constant in the $+x$ direction during every ac drive cycle, while at $A = 1.082$ in Fig. 8.8 (f), the skyrmion has a localized orbit encircling 21 obstacles. Similar orbit appears at higher ac drive amplitudes. The localized orbit of Fig. 8.8 (f) persists over the range$1.014 \leq A \leq 1.122$, while an orbit encircling 26 obstacles appears for $1.172 \leq A \leq 1.214$. At higher values of A additional localized orbits can be found, in which the skyrmion encircles 32, 45 or 69 obstacles. In general, stable localized orbits appear close to drives where the skyrmion can perfectly encircle n^2 obstacles. However, due to the square symmetry of the obstacle array, the orbits can deviate from purely circular states so that, for example, the stable orbit that encircles 26 obstacles rather than 25 obstacles.

In Fig. 8.9 it is plotted $\langle V_{\parallel} \rangle$ and $\langle V_{\perp} \rangle$ versus A for the system in Fig. 8.8, highlighting the locations of some of the localized phases where $n = 0,1,4,9,21,32,58$ and 69 obstacles are encircled. Several delocalized regions, inclusing translating or chaotic regimes appear between the localized states.

Figure 8.8 – The obstacles (open circles) and the skyrmion trajectory (black lines) for the system with $\alpha_m/\alpha_d = 0.577$ and $a_0 = 0.65$ for circular ac driving with $A = B$ and $\omega_1 = \omega_2 = 2 \times 10^{-5}$. (a) $A = 0.25$ the skyrmion is orbiting one obstacle. (b) $A = 0.375$ the skyrmion has direct motion in $+y$ direction. (c) $A = 0.5$ the skyrmion is encircling four obstacles. (d) A diffusive motion at $A = 0.672$. (e) At $A = 0.978$, a translating orbit. (f) A localized state where the skyrmion encircles 21 obstacles at $A = 1.082$. (From Vizarim *et. al.* [189], pg. 6).

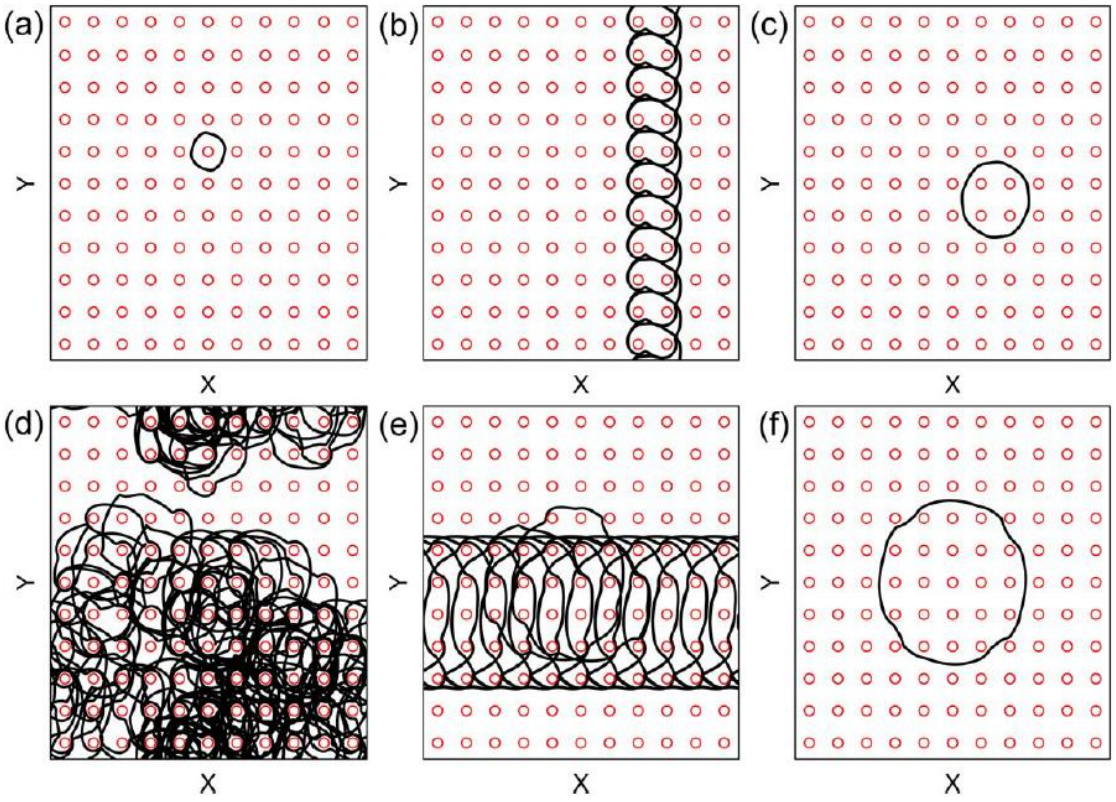

Figure 8.9 - The average velocities $\langle V_\parallel \rangle$ and $\langle V_\perp \rangle$ as a function of the ac drive amplitudes A and B, where $A = B$ for a single skyrmion in the square obstacle array using $\alpha_m/\alpha_d = 0.577$, $a_o = 0.65$. (From Vizarim *et. al.* [189], pg. 9).

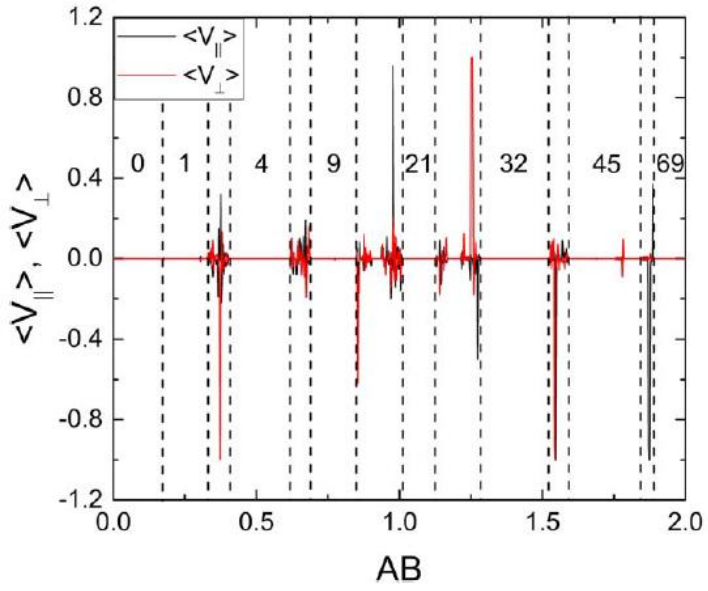

In Fig. 8.10 (a) – (d) it is plotted some skyrmion trajectories for a system with $\alpha_m/\alpha_d = 1.732$ and circular driving $A = B$ and $\omega_1 = \omega_2$. For $A = 0.215$ in Fig. 8.10 (a), the skyrmion forms a localized orbit encircling one obstacle, while at $A = 0.29$ in Fig. 8.10 (b), the motion is chaotic or diffusive. At $A = 0.712$, Fig. 8.10 (c) shows that there is a translating orbit that jumps between motion along $+45°$ and $-45°$. This orbit produces no net directed motion, but at short times the behavior is diffusive. In Fig. 8.10 (d) at $A = 0.836$, the skyrmion locks into an orbit that translates along the $+y$ direction. In Fig. 8.11 (a) it is plotted the velocity components versus the ac drive amplitudes for the system in Figs. 8.10 (a) – (d), where the vertical dashed lines indicate the regions where localized orbits encircles $n = 0,1,4,9,21,32,52,$ and 69 obstacles. In between $n = 9$ and $n = 21$ regimes, there are two regions of directed motion. Just above $n = 9$ regime, the skyrmion translates in $+x$ and $-y$ directions along $-45°$, while just below the $n = 21$ regime the skyrmion translates in $+y$ direction. There is also a smaller region between these two translating phases where the system forms a localized state encircling 16 obstacles.

Figure 8.10 – The obstacles (open circles) and the skyrmion trajectory (black lines) for the system with $a_0 = 0.65$ and circular ac driving with $A = B$ and $\omega_1 = \omega_2 = 2 \times 10^{-5}$. (a) – (d) Sample with $\alpha_m/\alpha_d = 1.732$. (a) $A = 0.215$ the skyrmion is orbiting one obstacle. (b) $A = 0.29$ has diffusive motion. (c) $A = 0.712$ the skyrmion has translating orbit jumping from $+45°$ and $-45°$ states. (d) A translating orbit in $+y$ direction at $A = 0.836$. (e) – (h) Sample with $\alpha_m/\alpha_d = 9.962$. (e) $A = 0.188$ the skyrmion is orbiting one obstacle. (f) $A = 0.25$ the skyrmion is encircling four obstacles. (g) $A = 0.596$ the skyrmion has diffusive motion. (h) A localized orbit encircling 16 obstacles at $A = 0.75$. (From Vizarim *et. al.* [189], pg. 9).

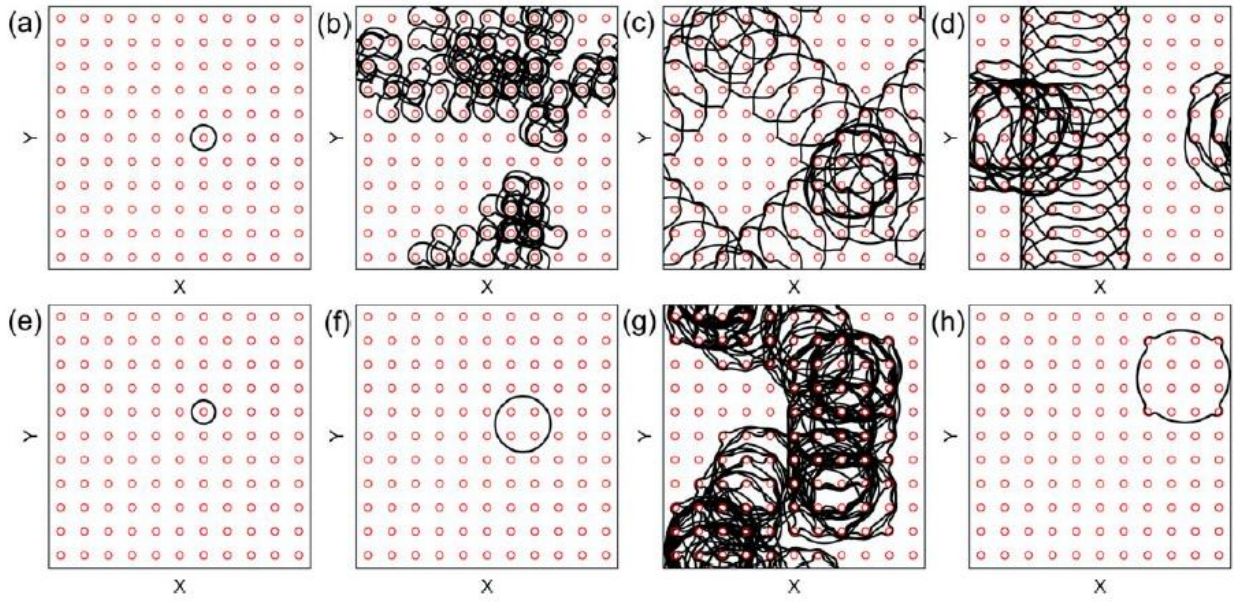

As the Magnus force is increased, there are fewer translating orbits and wider regions of delocalized orbits. In Figs. 8.10 (e) – (h) there are some skyrmion trajectories illustrated for a

system with $\alpha_m/\alpha_d = 9.962$. At $A = 0.188$, shown in Fig. 8.10 (e), the skyrmion is encircling a single obstacle, while in Fig. 8.10 (f) the skyrmion encircles four obstacles at $A = 0.25$. A delocalized and chaotic regime is shown in Fig. 8.10 (g) for $A = 0.596$, while in Fig. 8.10 (h) the skyrmion stabilizes in a localized orbit encircling 16 obstacles. In Fig. 8.11 (b) it is plotted $\langle V_\parallel \rangle$ and $\langle V_\perp \rangle$ versus A for the system in Figs. 8.10 (e) – (h), where the vertical dashed lines indicate the windows of localized phases in which the skyrmion encircles 0, 1, 4, 9, 16, 32, 52, or 69 obstacles. There are also several regions of chaotic flow in between the localized phases, and no direct motion.

Figure 8.11 - The average velocities $\langle V_\parallel \rangle$ and $\langle V_\perp \rangle$ as a function of the ac drive amplitudes A and B, where $A = B$ for a single skyrmion in the square obstacle array using (a) $\alpha_m/\alpha_d = 1.732$ and (b) $\alpha_m/\alpha_d = 9.962$, $a_o = 0.65$. (From Vizarim *et. al.* [189], pg. 10).

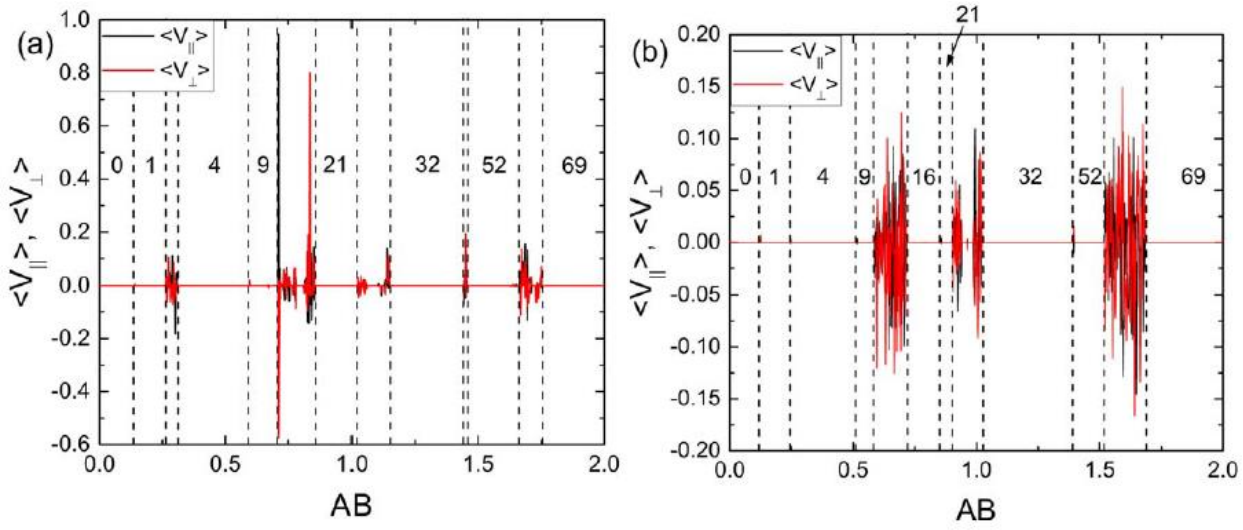

8.3.3 Ac drive with fixed B amplitude and varying A

In this section we also made calculations for the case where we have a fixed ac drive in one direction, while varying the ac drive in the other direction. That is, $B = 1.0$ is fixed and the values of A are varied. In Fig. 8.12 (a) it is plotted $\langle V_\parallel \rangle$ and $\langle V_\perp \rangle$ as a function of A using $\alpha_m/\alpha_d = 0.577$, $\omega_1 = \omega_2$ and $a_0 = 0.65$. In this case there are six regimes of skyrmion directed motion. Two of these regimes are illustrated in Fig. 8.12 (b), which is a zoomed version of Fig. 8.12 (a) for the range of $0 < A < 0.5$. The minima in $\langle V_\parallel \rangle$ correspond to a skyrmion motion in the $-x$ direction by one lattice constant for every ac drive cycle. Near $A = 0.8$, a fractional translation motion can be found, where the skyrmion moves one lattice constant in the $-x$ direction for every ac drive cycles, closely followed by a second fractional translation regime where the skyrmion moves one lattice constant in $+x$ every three ac drive cycles. For $A = 0.95$ there is also two regimes where the skyrmion moves one lattice constant in $+x$ and

$-y$ for every ac drive cycle. There are also several translation orbits for values close to $A = 1.25$.

Figure 8.12 – (a) The average velocities $\langle V_{\parallel} \rangle$ and $\langle V_{\perp} \rangle$ as a function of the ac drive amplitude A and fixed $B = 1.0$, for a single skyrmion in the square obstacle array using $\alpha_m/\alpha_d = 0.577$ and $a_o = 0.65$. (b) A blowup of (a) for the interval $0 < A < 0.5$ (From Vizarim *et. al.* [189], pg. 10).

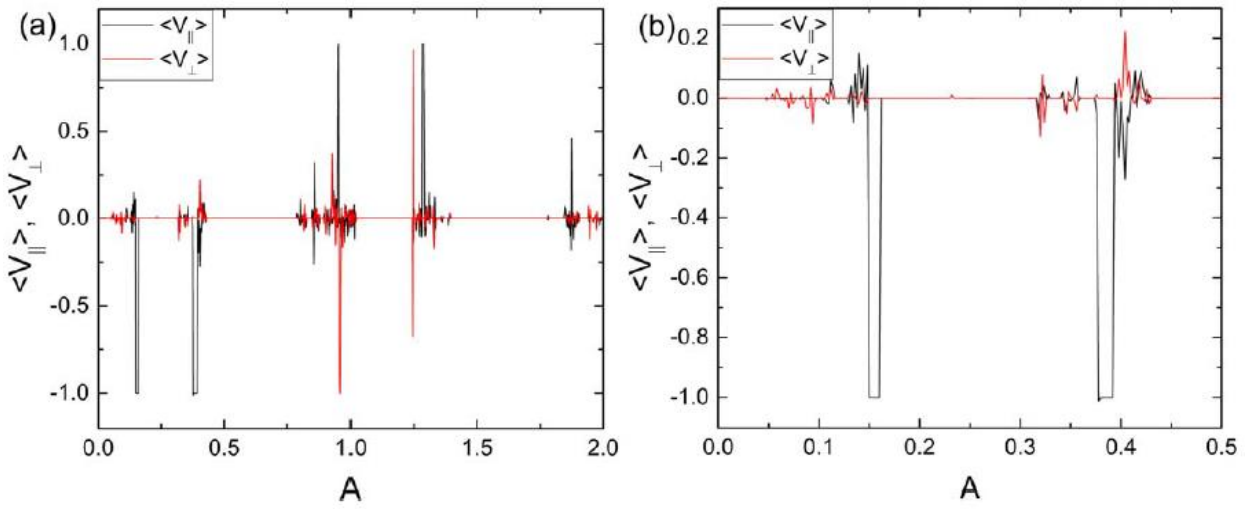

In Fig. 8.13 it is illustrated some representative skyrmion trajectories for the system of Fig. 8.12. In Fig. 8.13 (a) it is shown a localized skyrmion orbit, where it moves between four obstacles. At $A = 0.15$, in Fig. 8.13 (b), there is a translating orbit in which the skyrmion moves one lattice constant in $-x$ direction for every ac drive cycle. This phase corresponds to the first negative $\langle V_{\parallel} \rangle$ plateau illustrated in Fig. 8.12 (b). In Fig. 8.13 (c) it is shown another localized skyrmion orbit, which is asymmetric due to the ac drives profile and encircles six obstacles. In Fig. 8.13 (d) shows the second moving orbit from Fig. 8.12 (b) for $A = 0.384$, where it moves in $-x$ direction. At $A = 0.96$ in Fig. 8.13 (e), there is a translating orbit in which the skyrmion moves in $-y$ direction. In Fig. 8.13 (f) there is another localized orbit, but in this case it encircles 23 obstacles.

For increases values of α_m/α_d in this asymmetric system where $B = 1.0$ and A is varied, the number of translating phases increases. In Fig. 8.14 it is plotted the velocity components as a function of A for a system with $\alpha_m/\alpha_d = 1.732$ and $a_0 = 0.65$, where it is possible to see several translating phases where the skyrmion may move in x or y directions.

Figure 8.13 – The obstacles (open circles) and the skyrmion trajectory (black lines) for the system with $a_0 = 0.65$, ac drive with $B = 1.0$ and varied A and $\omega_1 = \omega_2 = 2 \times 10^{-5}$. (a) $A = 0.03$ the skyrmion performs a localized orbit. (b) $A = 0.15$ the skyrmion translates in $-x$ direction. (c) $A = 0.25$ a localized orbit. (d) A second translating orbit in $-x$ direction at $A = 0.384$. (e) $A = 0.96$ the skyrmion is translating along $-y$ direction. (f) $A = 0.25$ the skyrmion is encircling four obstacles. (g) $A = 0.596$ the skyrmion has diffusive motion. (h) A localized orbit encircling 23 obstacles at $A = 1.5$. (From Vizarim *et. al*. [189], pg. 11).

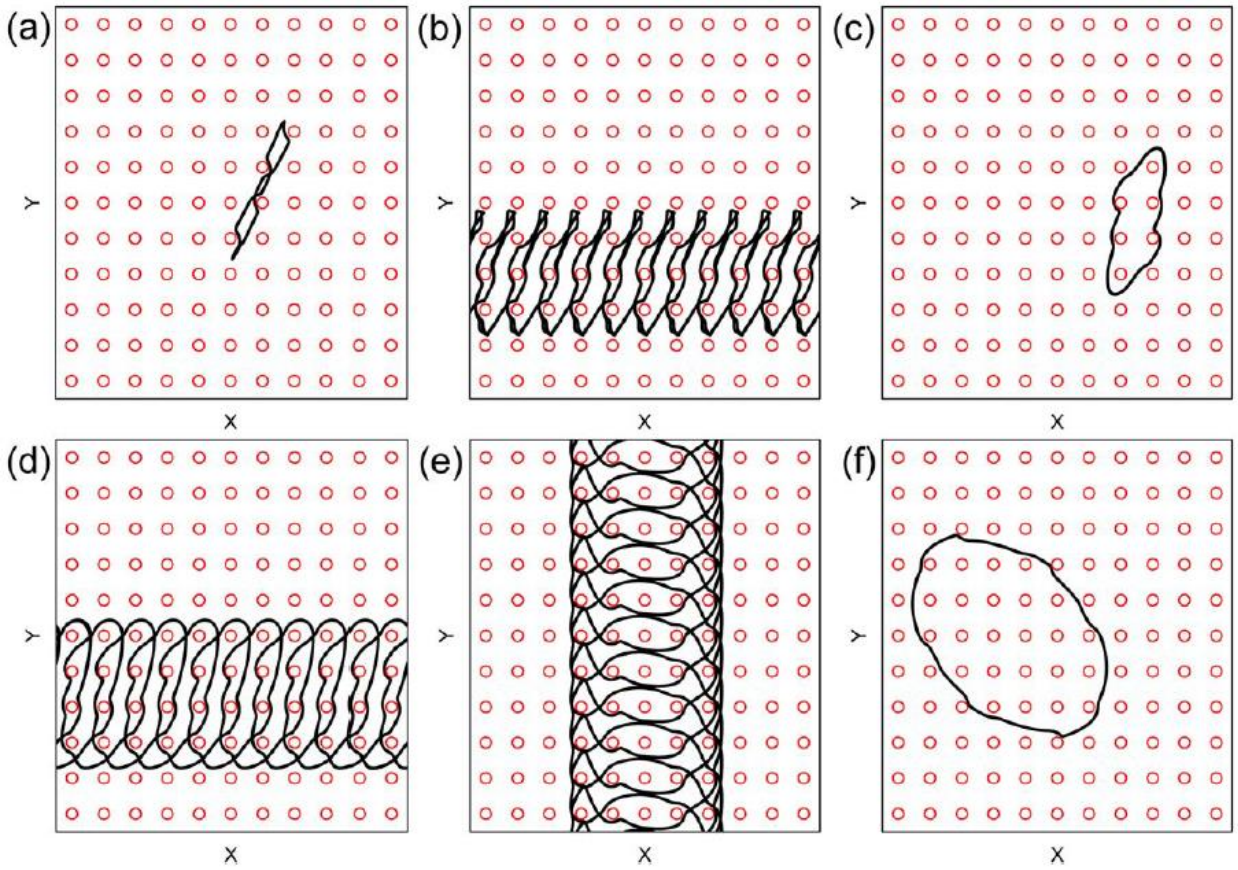

Figure 8.14 – The average velocities $\langle V_{\parallel} \rangle$ and $\langle V_{\perp} \rangle$ as a function of the ac drive amplitude A and fixed $B = 1.0$, using $\alpha_m/\alpha_d = 1.732$ and $a_o = 0.65$. (From Vizarim *et. al*. [189], pg. 12).

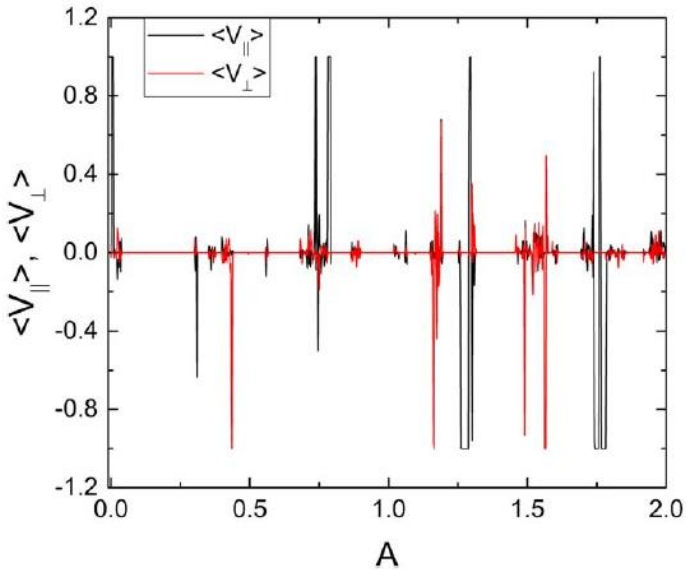

8.3.4 Obstacle size influence

In this section we investigate how the obstacle size influences on the skyrmion dynamics. As the obstacle size, a_0, is increased, the gaps between the obstacles are reduced, therefore restricting the skyrmion motion between obstacles. Initially, we look into the case of linear ac drive, that is, ac drive applied only in the x direction. In Fig. 8.15 (a) is plotted the velocity curves, $\langle V_{\parallel} \rangle$ and $\langle V_{\perp} \rangle$, as a function of the ac drive amplitude, A using $\alpha_m/\alpha_d = 0.577$ and $a_0 = 0.85$. Over the range $0 < A < 1.0$ all the skyrmion orbits are localized. For increased values of A there are two smaller regions where delocalized motion can occur. In Fig. 8.16 (a) it is illustrated the skyrmion trajectory for the system in Fig. 8.15 (a) for $A = 0.282$, where the skyrmion forms a localized orbit moving between two obstacles. As the amplitude is increased, the skyrmion passes through a series of localized elliptical orbits oriented along the x direction, as shown in Fig. 8.16 (b) for $A = 0.5$. In Fig. 8.16 (c) at $A = 1.048$, there is a translating orbit where the skyrmion moves one lattice constant in the $+y$ direction for every five ac drive cycles. In Fig. 8.16 (d) shows a localized orbit at $A = 1.5$ where the skyrmion moves between three plaquettes at an angle to the x axis. As the amplitude is further increased the localized orbits exhibit a structure similar to what is shown in Fig. 8.16 (d) but pass between an increasing number of obstacles.

Figure 8.15 – The average velocities $\langle V_{\parallel} \rangle$ and $\langle V_{\perp} \rangle$ as a function of the ac drive amplitude A for linear ac drive using $a_o = 0.85$.(a) A sample with $\alpha_m/\alpha_d = 0.577$. (b) A sample with $\alpha_m/\alpha_d = 1.732$. (c) A blowup of (b) for the interval $1.3 < A < 1.6$ (From Vizarim *et. al*. [189], pg. 10).

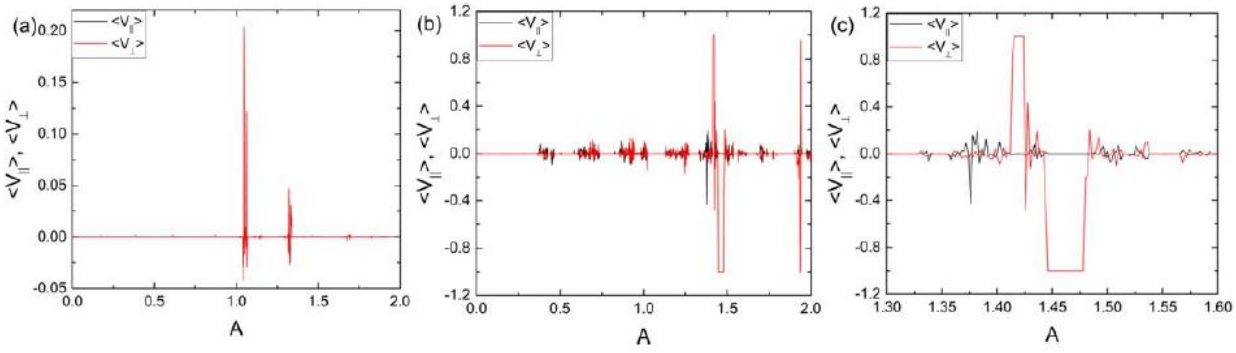

As the Magnus term in increased in samples with larger obstacles, there is an increased number of regions where delocalized and moving orbits appear. In Fig. 8.15 (b) it is plotted $\langle V_{\parallel} \rangle$ and $\langle V_{\perp} \rangle$ versus A for a sample with $a_0 = 0.85$, $\alpha_m/\alpha_d = 1.732$ and $B = 0$. As can be seen, there are several regions of chaotic or dissipative flow, several regions of moving orbits that are most likely to be found along the y direction and several reversals of moving orbit direction. In Fig. 8.16 (e) it is illustrated the skyrmion trajectories for $A = 0.5$, where the skyrmion moves

between two obstacles in a localized orbit. In Fig. 8.16 (f), at $A = 0.75$, the skyrmion encircles two obstacles and performs another type localized orbit. In Fig. 8.15 (c) there is a blowup of Fig. 8.15 (b) for the range of $1.3 < A < 1.6$. There is a small region near $A = 1.376$ where the skyrmion translates in the $-x$ direction by one lattice constant for every two ac drive cycles, as shown in Fig. 8.16 (g). This regime is followed by a delocalized chaotic motion. For the range of $1.415 < A < 1.42$, there is a translating orbit motion where the skyrmion moves one lattice constant in y direction for every ac drive cycle, as shown in Fig. 8.16 (h). After further increase in A, there is a reversal in the translation orbit direction of motion at the range of $1.425 < A < 1.48$.

Figure 8.16 – The obstacles (open circles) and the skyrmion trajectory (black lines) for the system with $a_0 = 0.85$ and linear ac driving where $B = 0$ and $\omega_1 = \omega_2 = 2 \times 10^{-5}$. (a) – (d) Sample with $\alpha_m/\alpha_d = 0.577$. (a) $A = 0.272$ a localized orbit. (b) $A = 0.5$ a more extended localized orbit. (c) $A = 1.047$ a moving orbit along $+y$ direction. (d) A localized orbit at $A = 1.5$. (e) – (h) Sample with $\alpha_m/\alpha_d = 1.732$. (e) $A = 0.5$ a localized orbit. (f) $A = 0.75$ another localized orbit. (g) $A = 1.376$ a translating orbit. (h) A translating orbit at $A = 0.75$. (From Vizarim *et. al.* [189], pg. 13).

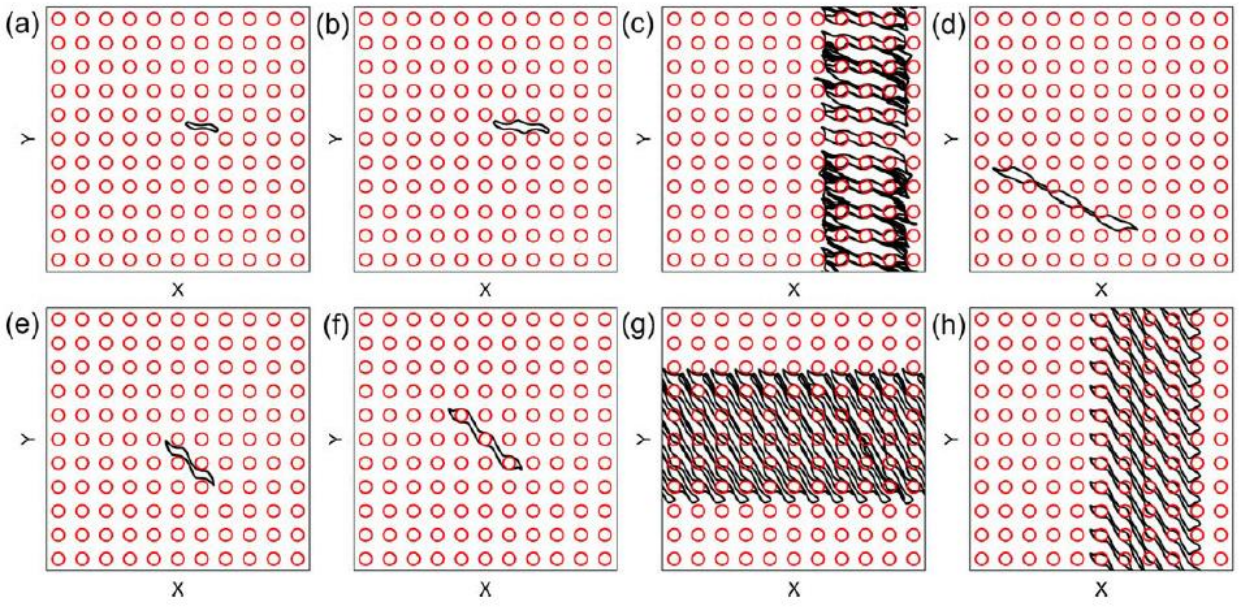

Now we look into the case of circular ac driving, where $A = B$. In Fig. 8.17 it is plotted $\langle V_{\parallel} \rangle$ and $\langle V_{\perp} \rangle$ versus A for a sample with $\alpha_m/\alpha_d = 0.577$ at $a_0 = 0.45$, 0.65 and 0.95. For small values of obstacle size, most orbits remain localized as A increases, while for larger obstacles more delocalized and direct motion phases can be observed. However, if the obstacles are too large, the number of delocalized orbits also reduces due to the reduced gap between obstacles that confines the skyrmion motion and restricts possible types of motion. After several simulations it was possible to plot a dynamical phase diagram as a function of A versus a_0, as

shown in Fig. 8.18. The locations of the delocalized, localized and moving orbits are indicated. The localized orbits are labelled according to the number of obstacles each phase encircles, that is, 0, 1, 4, 9 or 16 obstacles. Some localized orbits may also have different shapes although the number of obstacles encircled is the same, and therefore it is another phase.

Figure 8.17 – The average velocities $\langle V_{\parallel} \rangle$ and $\langle V_{\perp} \rangle$ as a function of the ac drive amplitude A where $A = B$, using $\alpha_m/\alpha_d = 0.577$ and $\omega_1 = \omega_2$ for $a_0 = 0.45$, 0.65 and 0.95. (From Vizarim *et. al.* [189], pg. 13).

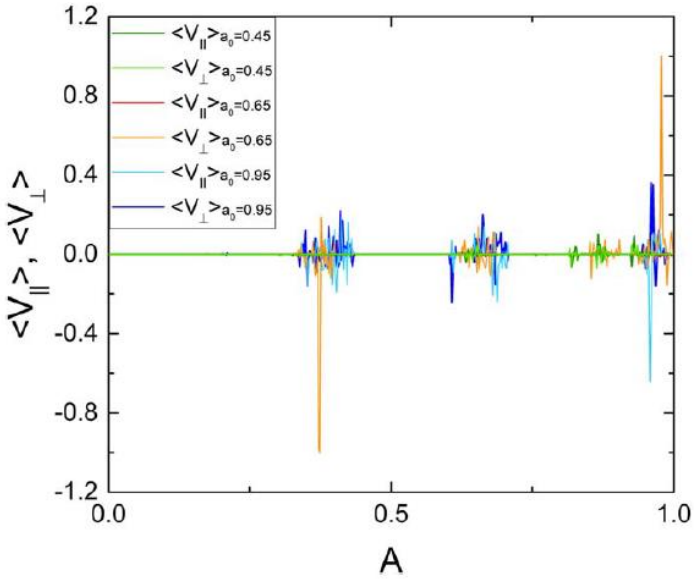

Figure 8.18 – Dynamic phase diagrams as a function of A versus a_0 with $A = B$, $\omega_1 = \omega_2$ and $\alpha_m/\alpha_d = 0.577$. Blue indicates the localized phases; red regions are delocalized orbits and green regions are direct motion phases. Phase 16_E is the skyrmion encircling 16 obstacles with elliptical shape, while 16_S has circular shape. (From Vizarim *et. al.* [189], pg. 14).

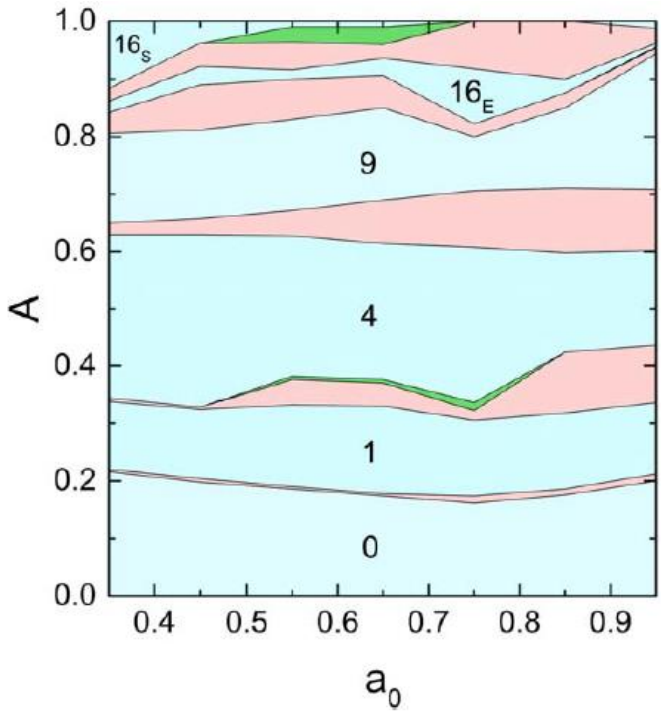

From Fig. 8.17 it is possible to see that for reduced obstacle sizes, the skyrmion motion is less influenced by the obstacles. This means that the skyrmion performs mainly orbits that increase in its radius. Note that there are few peaks in the velocity curves, indicating that the skyrmions does not disperse much through the sample, even when changing its orbit size. In Fig. 8.19 (a) we illustrate the skyrmion orbit for $A = 0.5$, where the orbit is very close to a perfect circle, due to the reduced effect of the obstacles. In Fig. 8.19 (b) it is shown the skyrmion dispersing when increasing its orbit. As can be seen, the dispersion is not throughout the sample, it is concentrated in a certain region, performing circular motions. For intermediate values of obstacle size, the skyrmion exhibits the most pronounced velocity peaks. This means that for this size of obstacle the skyrmion performs ordered motion. However, if the obstacle size is too large, the skyrmion orbit becomes more squared due to the reduced gaps between obstacles [See Fig. 8.19 (c)], and the transition between orbits may be chaotic [See Fig. 8.19 (d)]. The phase diagram of Fig. 8.18 also demonstrates that for larger values of a_0 the localized orbits become elliptical, such as the 16_E state which encircles 16 obstacles, while at smaller values of a_0 the orbits are more circular due to the reduced influence of obstacles, as can be seen for the case of 16_S case.

Figure 8.19 – The obstacles (open circles) and the skyrmion trajectory (black lines) for the system with $\alpha_m/\alpha_d = 0.577$ and circular ac driving where $A = B$ and $\omega_1 = \omega_2 = 2 \times 10^{-5}$. (a) and (b) Sample with $a_0 = 0.45$. (a) $A = 0.5$ a localized orbit. (b) $A = 0.652$ a chaotic regime. (c) and (d) Sample with $a_0 = 0.95$. (c) $A = 0.5$ a localized squared orbit. (d) $A = 0.608$ a delocalized orbit. (From Vizarim *et. al*. [189], pg. 14).

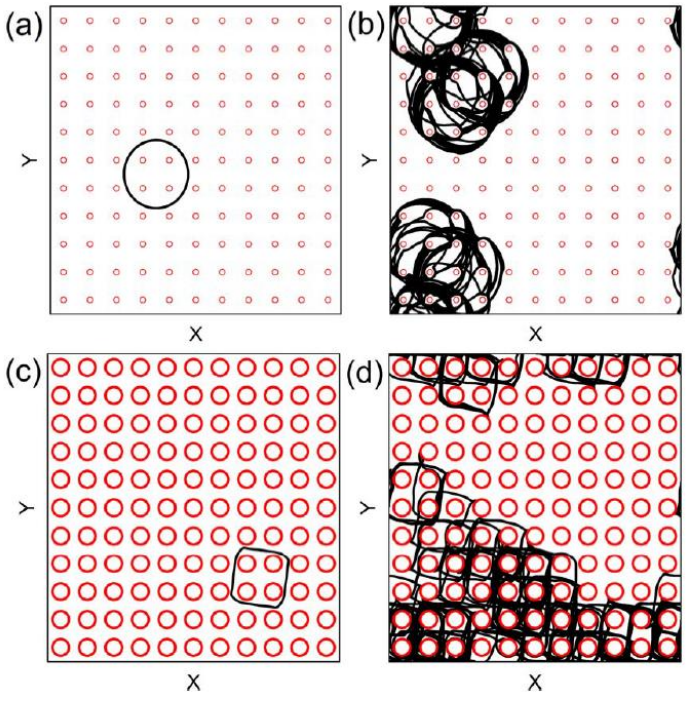

8.3.5 Frequency rate ω_2/ω_1 influence

In this section we investigate the influence of the oscillating frequency of the ac drives. If the frequencies are not equal, that is $\omega_1/\omega_2 \neq 1$, it is expected an asymmetry in the ac drives, which can enhance the ratchet effects in skyrmions. In Fig. 8.20 it is illustrated the skyrmion orbits in the absence of a substrate for a system with $A = B = 1.0$ and $\alpha_m/\alpha_d = 0.45$ at $\omega_2/\omega_1 = 0.5$, 1.0, 1.5, 2.0 and 3.0. As can be seen for $\omega_2/\omega_1 = 1.0$ the orbit is circular, but for the other values the orbit is asymmetric.

Figure 8.20 – The skyrmion trajectories for varied values of ω_2/ω_1 for a system without substrate, $A = B = 1.0$ and $\alpha_m/\alpha_d = 0.45$ (From Vizarim *et. al.* [189], pg. 15).

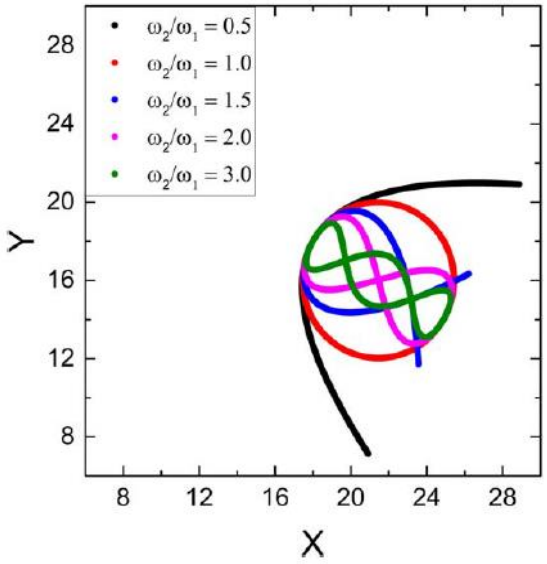

In Fig. 8.21 (a) it is plotted plotted $\langle V_{\parallel}\rangle$ and $\langle V_{\perp}\rangle$ versus A for a system with circular driving $A = B$ using $\alpha_m/\alpha_d = 0.577$, $a_0 = 0.65$ at $\omega_2/\omega_1 = 0.5$ and 1.0. For $\omega_2/\omega_1 = 0.5$ there are larger regions of moving orbits with several reversals in the direction of the moving orbit. In Fig. 8.21 (b) shows the same kind of plot but for $\omega_2/\omega_1 = 1.5$ and 2.0. When $\omega_2/\omega_1 = 1.5$ most of the translating orbit regions exhibit $\langle V_{\parallel}\rangle = 0.5$ or $\langle V_{\perp}\rangle = 0.5$, which means that the moving orbits translate one lattice constant for every two ac drives cycles. On the other hand, for $\omega_2/\omega_1 = 2.0$ most of the translating orbit has $\langle V_{\parallel}\rangle = 1.0$ or $\langle V_{\perp}\rangle = 1.0$, which means that the skyrmion moves one lattice constant for every ac drive cycle. That is, the direct motion is more efficient for $\omega_2/\omega_1 = 2.0$. In Fig. 8.22 it is illustrated some representative skyrmion trajectories for the system of Fig. 8.21. In Fig. 8.22 (a) at $A = 0.4$ and $\omega_2/\omega_1 = 0.5$ the skyrmion is translating in the $+x$ direction, while in (b) for $A = 0.58$ the skyrmion translates along 45°. In Fig. 8.22 (c) for $\omega_2/\omega_1 = 2.0$ at $A = 0.2$ the orbit translates in $-x$ direction, but it

is also disordered. In Fig. 8.22 (d) using the same ratio as (c) but for $A = 1.0$, the skyrmion translates in the $+y$ direction.

Figure 8.21 The velocities $\langle V_{\parallel} \rangle$ and $\langle V_{\perp} \rangle$ as a function of the ac drive amplitude, $A = B$, for a single skyrmion in the square obstacle array using $\alpha_m/\alpha_d = 0.577$ and obstacle sizes of $a_0 = 0.65$. In (a) curves for $\omega_2/\omega_1 = 0.5$ and 1.0, in (b) for $\omega_2/\omega_1 = 1.5$ and 2.0 (From Vizarim *et. al.* [189], pg. 16).

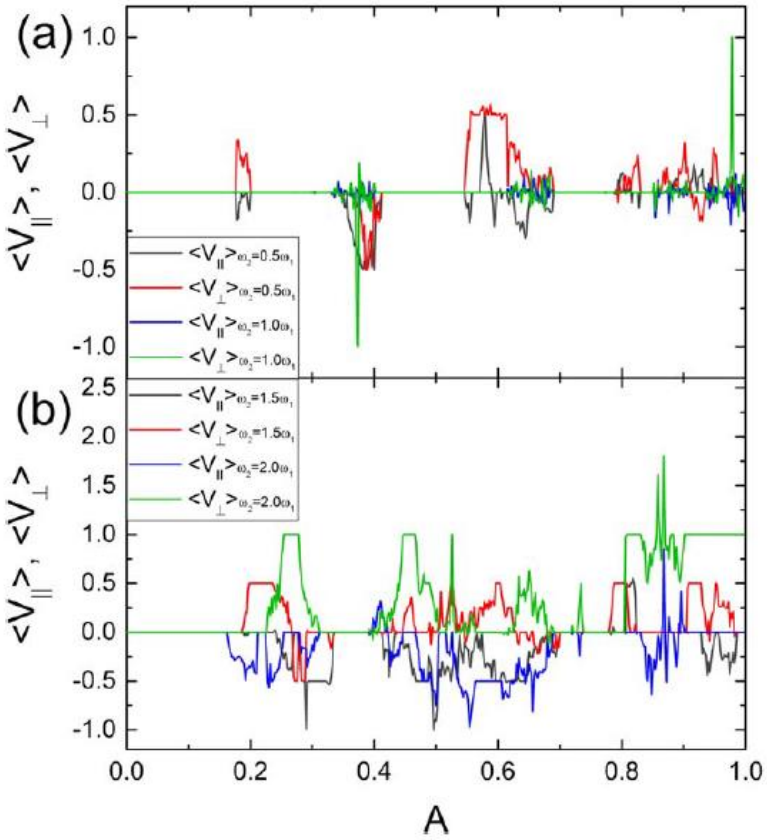

Figure 8.22 - The obstacles (open circles) and the skyrmion trajectory (black lines) for the system with $\alpha_m/\alpha_d = 0.577$ and circular ac driving where $A = B$ and $a_0 = 0.65$. (a) and (b) Sample with $\omega_2/\omega_1 = 0.5$. (a) $A = 0.4$ a translating orbit along $+x$ direction. (b) $A = 0.58$ a translating orbit along 45°. (c) and (d) Sample with $\omega_2/\omega_1 = 2.0$. (c) $A = 0.2$ a disordered translating orbit along $-x$ direction. (d) $A = 1.0$ a translating orbit along $+y$ direction. (From Vizarim *et. al.* [189], pg. 16).

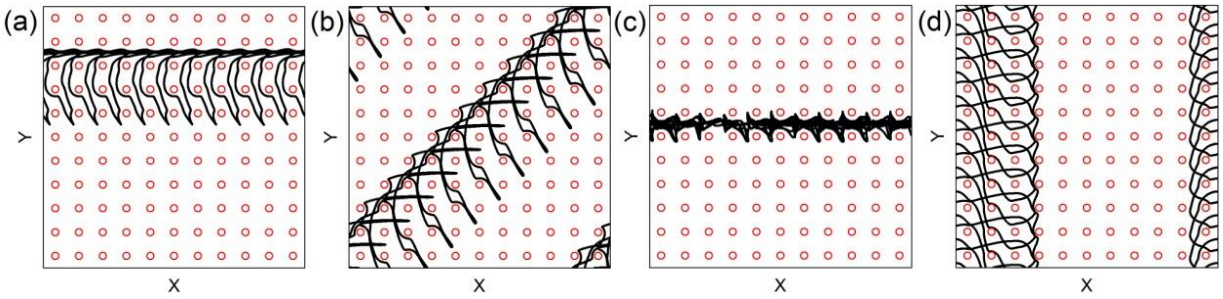

8.3.6 Discussion and Summary

Our results could be tested experimentally in a system containing a periodic array of antidots with one or two applied ac drives. The different orbits could be measured using direct imaging or through electrical detection. Another method for observing the orbits is to analyze the noise fluctuations, since the localized states or ordered translating orbits should produce low noise along with a narrow band signal at a specific frequency. In contrast, the delocalized phases would exhibit broadband noise signals or multiple frequencies due to the jumping of the skyrmion between different orbit shapes. It would also be interesting to consider a finite number of skyrmions instead of an individual skyrmion. At low densities where the skyrmions do not interact, we expect that the results would be similar to what is described above. However, for multiple interacting skyrmions, there could be an enhancement of the disordered regime or even new types of ordered phases. In our model, the skyrmions are treated as rigid particles; however, actual skyrmions can exhibit internal modes or shape distortions which could induce additional phases. This also suggests that another method for driving skyrmions in circular orbits would be to use oscillating fields, since continuum studies have shown that this technique can generate skyrmion motion even without a substrate [131]. In a sample where a dc drive is superimposed on an ac drive, various types of phase locking phenomena should appear in the velocity force curves as has been studied in previous work of section 7.

Our model neglects thermal effects, but we expect such effects would become important near the transition between two different localized orbits, and could induce a creep motion for certain translating orbits. Our results also suggest that by controlling the obstacle geometry and the ac driving, it should be possible to cause the skyrmion to translate at a designated skyrmion Hall angle over a specific number of lattice constants per ac drive cycle. The behavior should also depend on the type of skyrmion considered. For antiferromagnetic skyrmions [193,194] and liquid crystal skyrmions [195], where the Hall angle is absent, the dynamics would be similar to those found in the vortex pinball systems. In other skyrmion systems where internal modes are important, there could be complex trochoidal motion of the skyrmions [196].

9 Interface Guided Motion

9.1 Guiding skyrmions through interface between periodic obstacle arrays

The main idea of this work is to use designed asymmetric obstacle landscape to guide the skyrmion motion through the sample, following a designed path. The asymmetry in our case is an interface between different regions of obstacle landscape: one region where obstacles have reduced size, and another region where obstacles have a larger size. This difference in obstacle sizes create an asymmetric potential in the interface, which the idea is to lead the skyrmion motion. In order to induce their motion, it is applied a circular ac drive, and as the skyrmion increases its orbit with increasing ac drive amplitude, it may eventually reach the interface between the obstacle regions and finally be guided. Experimentally biharmonic ac drives could be achieved using a cross-shaped bridge of the type developed for superconducting vortex samples [12,197]. Our results show that the skyrmion flows through the interface, even turning sharp corners to follow the interface. This work has been recently published in Journal of Magnetism and Magnetic Materials [198].

9.2 Model and Simulation details

The simulation method is exactly the same as the skyrmion pinball work, in previous section 8. Only an ac drive is applied to a single skyrmion in a 2D periodic landscape. The main difference is the obstacle landscape that exhibits regions with different obstacles sizes. The region with smaller obstacles has the obstacle size $R_o^S = 0.45$, and the region with larger obstacles has $R_o^L = 0.85$ radii. The dynamical properties of the skyrmion system interacting with the obstacle array were simulated using the particle model for skyrmions, shown in Eq. (9.1), using Molecular Dynamics technique.

$$\alpha_d \mathbf{v_i} + \alpha_m \hat{z} \times \mathbf{v_i} = \mathbf{F}_i^o + \mathbf{F}^{ac} \tag{9.1}$$

The system has a size of $72\xi \times 72\xi$. In the center of the simulation box, we inserted a region where the obstacles are larger, and outside this central region the obstacles size are reduced (See Fig. 9.1). The obstacle density is the same in both regions, $0.093/\xi^2$. The last term is the ac drive, $\mathbf{F}_x^{ac} = A\sin(2\pi\omega_1 t)\,\hat{\boldsymbol{x}}$ for longitudinal driving and $\mathbf{F}_y^{ac} = B\cos(2\pi\omega_2 t)\,\hat{\boldsymbol{y}}$ for transversal driving. We measure the skyrmion velocity in the $\langle V_x\rangle = \langle \mathbf{v}\cdot\hat{\mathbf{x}}\rangle/(2\pi\omega_1 a)$, and the y

component, $\langle V_y \rangle = \langle \mathbf{v} \cdot \hat{\mathbf{y}} \rangle / (2\pi\omega_1 a)$, where a is the substrate lattice constant. The velocities are averaged over 100 ac drive cycles. Under the normalization used here, when $\langle V_{\parallel} \rangle = 1.0$ or $\langle V_{\perp} \rangle = 1.0$ indicates that the skyrmion is translating by one substrate lattice constant per ac drive cycle in the x or y direction, respectively. The external ac drive amplitude is increased in small steps of A $(B) = 0.002$ and wait 10^6 simulation time steps between increments to ensure steady state. We normalize the damping and Magnus coefficients as $\alpha_d^2 + \alpha_m^2 = 1$.

Figure 9.1 - A schematic of the system, which consists of regions of a square array of obstacles (red circles) with different sizes. The larger obstacles have $R_0^L = 0.85$ and the small ones $R_0^s = 0.45$. The black lines correspond to the skyrmion trajectories under the influence of both damping, Magnus term, and circular ac drive (From Vizarim *et. al.* [198], pg. 2)

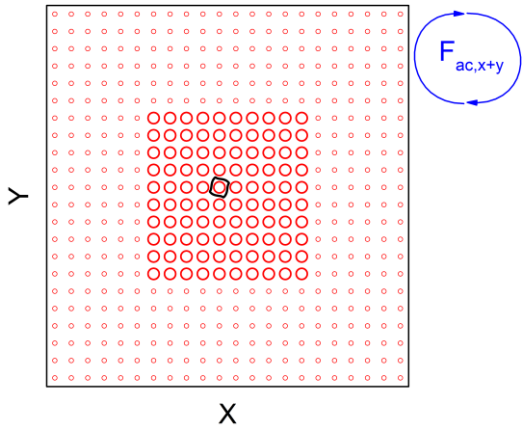

9.3 Results

9.3.1 Transport along central interface between superior and inferior obstacle arrays

As the main focus of this work is to understand how the skyrmion behave under the presence of an interface between two different pinning landscapes, first we consider the case of one-dimensional interface, where the upper part of the sample is composed of smaller obstacles, while the bottom part of larges obstacles. The skyrmion is initially placed between the two regions as it is used a system with $\alpha_m/\alpha_d = 0.45$ and $\omega = 1 \times 10^{-5}$. If the skyrmion interacts with homogeneous obstacles, that is, without any size differences, the skyrmion may exhibit localized orbits, chaotic or directed motion, as shown in details in section 10. However, for the case here where the obstacle lattice is not homogeneous, the interface between the obstacle produce an asymmetric potential for the skyrmion, which induces a ratchet motion. In Fig. 9.2 (a), for $A = 0.1$, the skyrmion is performing a localized orbit, encircling one obstacle. The result would be analogous if the skyrmion were placed on the other half of the sample with larger obstacles. When the drive amplitude is increased to $A = 0.4$, as in Fig. 9.2 (b), the skyrmion remains trapped in a localized orbit encircling four obstacles. Depending on the initial skyrmion position, there can be an initial transient of diffusive motion before settling into a stable and

localized orbit as demonstrated in this figure. It is also possible that due to the obstacle size difference, on one parte of the sample the skyrmion has a localized orbit and on the other side the motion can be chaotic, as demonstrated in section 8 on how the obstacle size affects the skyrmion dynamics under ac drive. In Fig. 9.2 (c) it is illustrated the formation of a translating orbit at $A = 0.5$, where the skyrmion moves a distance $2a$ in the $+x$ direction during every ac drive cycle, where a is the lattice constant. Note that the direction of motion can be better seen in Fig. 9.3, where the velocity curves are demonstrated. For $A = 0.5$, the skyrmion velocity is $\langle V_x \rangle = 2.0$ and $\langle V_y \rangle = 0$. In Fig. 9.2 (d) it is illustrated another type of moving orbit at $A = 0.77$, but now the skyrmion moves a in the $+x$ direction for every ac drive cycle.

Figure 9.3 - The obstacles (open circles) and the skyrmion trajectory (black lines) for the system with $\alpha_m/\alpha_d = 0.45$ and circular ac driving where $A = B$ and $\omega = 1 \times 10^{-5}$. (a) $A = 0.1$ a localized orbit encircling one obstacle. (b) $A = 0.4$ a localized orbit encircling four obstacles. (c) $A = 0.5$ a translating orbit moving $2a$ for every ac drive cycle in the $+x$ direction. (d) $A = 0.77$ a translating orbit along $+x$ direction, moving a for every ac drive cycle. (From Vizarim *et. al.* [198], pg. 3).

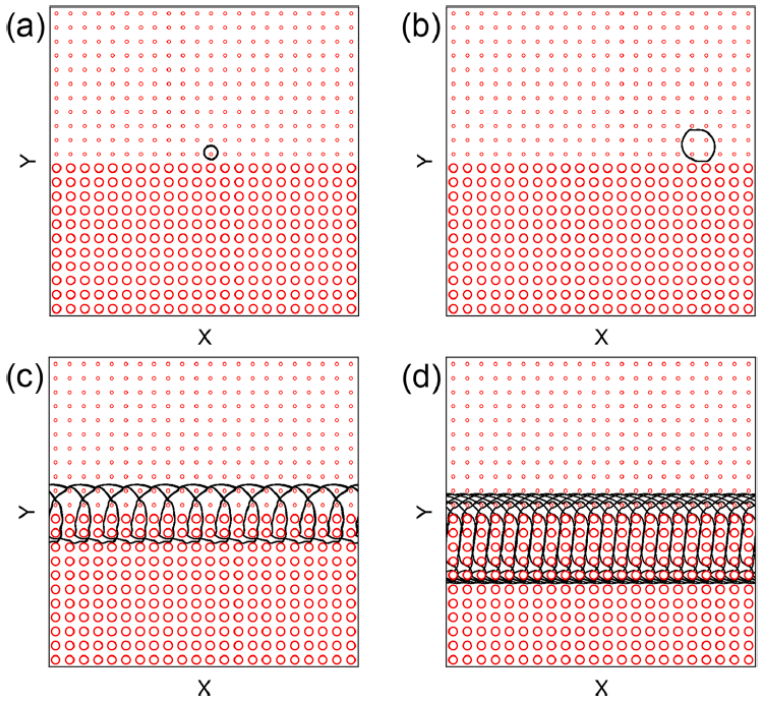

In Fig. 9.3 it is plotted the velocity components $\langle V_x \rangle$ and $\langle V_x \rangle$ as a function of A for the system in Fig. 9.2. Note that in this system the perpendicular velocity $\langle V_y \rangle \cong 0$ for all values of A since the transport motion can only occur along the x direction, which is parallel to the interface. The skyrmion can translate in both $+x$ or $-x$ since there is no preferable direction. For the interval $0.425 < A < 0.475$, the skyrmion moves along the interface a distance a in the $-x$ direction during each ac drive cycle, while for $0.475 < A < 0.51$, the skyrmion translates in the $+x$ direction by $2a$ for every ac drive cycle. As can be seen there is also several other

windows of motion along the interface where the skyrmion may move a or $2a$ during each ac drive cycle in both $+x$ or $-x$ direction, including sharp reversals of skyrmion motion. If the ac drive polarity is reversed, the same curves are obtained but with flipped y axis. The motion following the interface occurs due to a combination of broken time symmetry from the ac drive and the broken spatial symmetry from the interface, which produces a ratchet effect. Here, the ac drive cycle is spatially symmetric, but when a portion of the skyrmion orbit is on the other side of the interface, the orbit becomes asymmetric and the ratchet effect is more likely.

Figure 9.3 – The average velocities $\langle V_x \rangle$ and $\langle V_y \rangle$ as a function of the ac drive amplitude A for the system in Fig. 9.2 using $\alpha_m/\alpha_d = 0.45$. (From Vizarim *et. al.* [198], pg. 3).

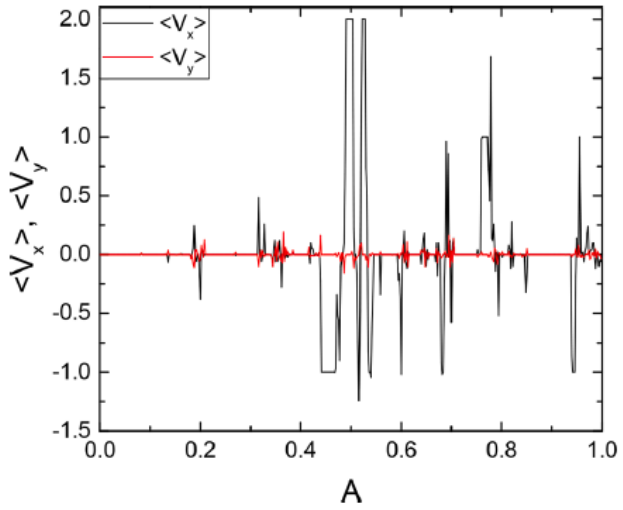

In Fig. 9.4 it is plotted $\langle V_x \rangle$ and $\langle V_y \rangle$ as a function of A for the same system as Fig. 9.3 but with stronger Magnus components of $\alpha_m/\alpha_d = 1.732$ [See Fig. 9.4 (a)] and $\alpha_m/\alpha_d = 9.962$ [See Fig. 9.4 (b)]. For the case of $\alpha_m/\alpha_d = 1.732$, there are small regions of directed motion, while for $\alpha_m/\alpha_d = 9.962$ the regions of directed motion are more extended. In Fig. 9.5 (a) it is shown the skyrmion trajectories for the system of Fig. 9.4 (a) at $A = 0.22$, where the skyrmion exhibits a short time transient motion in the small obstacle region before entering a diffusive motion in the larger obstacles region. In Fig. 9.5 (b) it is shown the trajectory at $A = 0.534$, where the skyrmion performs a moving orbit in the $+x$ direction, moving a distance a for every ac drive cycle. In Fig. 9.5 (c), for the system with $\alpha_m/\alpha_d = 9.962$, at $A = 0.382$ the skyrmion is performing a delocalized and chaotic orbit. In Fig. 9.5 (d) at $A = 0.6$ the skyrmion is performing a complex moving orbit at the edge of the interface that translates a during every ac drive cycle in the $+x$ direction. In general, as the Magnus force is increased, the delocalized orbits are more prominent than the localized ones.

Figure 9.4 – The average velocities $\langle V_x \rangle$ and $\langle V_y \rangle$ as a function of the ac drive amplitude A for the same system as Fig.9.2 but using (a) $\alpha_m/\alpha_d = 1.732$ and (b) $\alpha_m/\alpha_d = 9.962$. (From Vizarim *et. al.* [198], pg. 3).

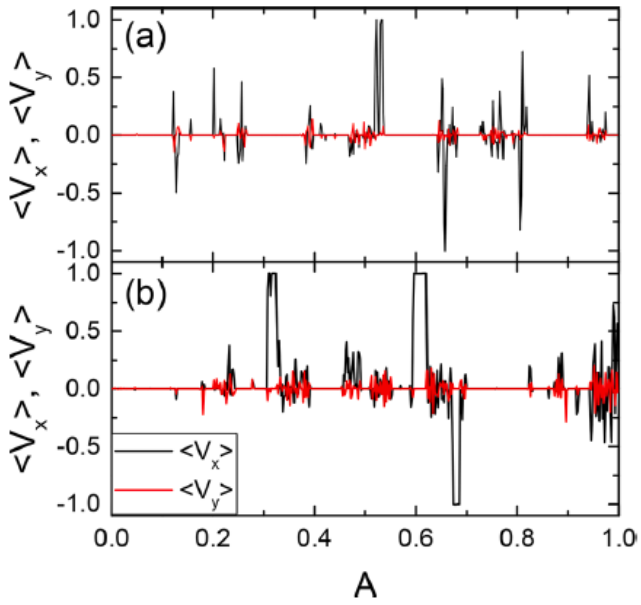

Figure 9.5 - The obstacles (open circles) and the skyrmion trajectory (black lines) for the system using circular ac driving where $A = B$ and $\omega = 1 \times 10^{-5}$. (a) and (b) samples with $\alpha_m/\alpha_d = 1.732$. (a) $A = 0.22$ a delocalized diffusive orbit. (b) $A = 0.534$ a translating orbit in the $+x$ direction. (c) and (d) samples with $\alpha_m/\alpha_d = 9.962$. (c) $A = 0.372$ a chaotic delocalized orbit. (d) $A = 0.6$ a complex translating orbit along $+x$ direction, moving a for every ac drive cycle. (From Vizarim *et. al.* [198], pg. 4).

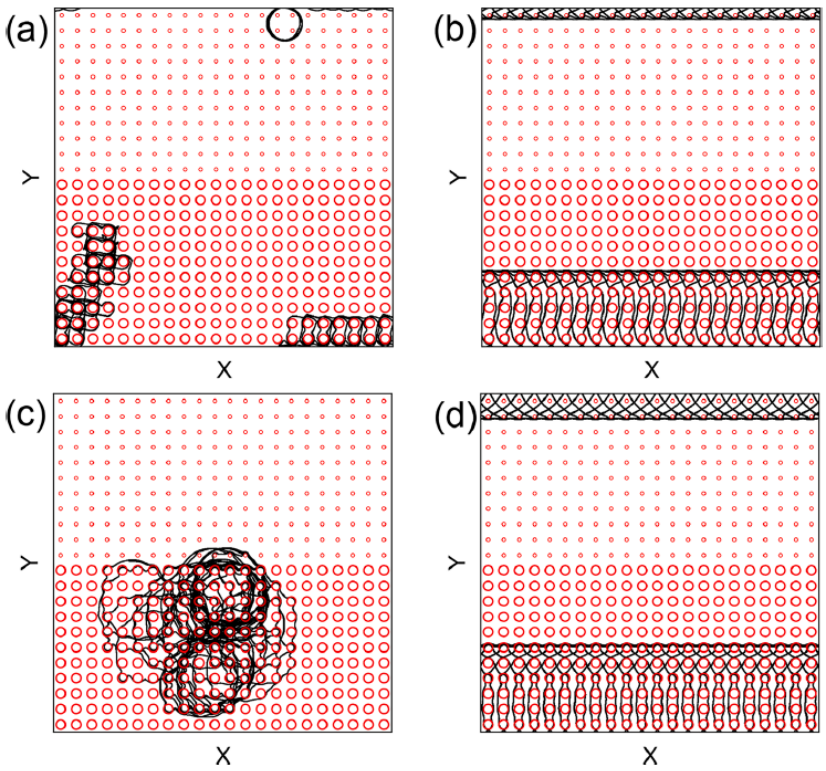

9.3.2 Guided transport along corners

Since skyrmions can be guided through an interface between different obstacle landscapes, now we consider the case where the interface is not straight, but may exhibit sharp corners. If the skyrmion can follow an interface with sharp corners, it would allow the creation of designed interfaces that could guide the skyrmion motion through the sample in order to achieve different types of devices. So, for a better understanding of this phenomena we considered the case illustrated in Fig. 9.1, where there is a central region with larger obstacles surrounded by a region with smaller obstacles. In Fig. 9.6 it is shown some representative skyrmion trajectories for the system illustrated in Fig. 9.1 using $\alpha_m/\alpha_d = 0.45$ and $\omega = 1 \times 10^{-5}$. In Figs. 9.6 (a) and (b) it is possible to see localized orbits at $A = 0.1$ and $A = 0.2$, respectively. For $A = 0.1$ the skyrmion is orbiting between obstacles and for $A = 0.2$ the skyrmion encircles one obstacle. In Fig. 9.6 (c), at $A = 0.4$, the skyrmion is performing a localized orbit encircling 12 obstacles in the small obstacle region. At $A = 0.47$, for the 1D interface case, the skyrmion was following the interface in a directed motion, similar to shown in Fig. 9.3. Here, the skyrmion also exhibits directed motion, even for a 2D interface, the skyrmion follows the interface turning all four corners in clockwise direction [See Fig. 9.6 (d)], where the skyrmion moves $2a$ for every ac drive cycle. Fig. 9.6 (e) shows a localized orbit where the skyrmion encircles 23 obstacles at $A = 0.66$. In Fig. 9.6 (f) at $A = 0.86$, the skyrmion performs another type of direct motion following the interface, which is wider than shown in Fig. 9.6 (d).

In Fig. 9.7 it is plotted $\langle V_x \rangle$ and $\langle V_y \rangle$ as a function of A for the system in Fig. 9.6. Differently from the 1D interface case, here there are finite velocity component values for both x and y directions. As the skyrmion changes direction following the interface, finite values of the velocity components may appear and they do not exhibit smooth steps as the 1D case. However, the regions where the translation occur is characterized by large fluctuations in $\langle V_x \rangle$ and $\langle V_y \rangle$. Note that there are several intervals in which the skyrmion moves along the interface. There are also some regions where the skyrmion follows the interface partially, then cannot turn corners and performs chaotic motion. This situation will be demonstrated later.

Figure 9.6 - The obstacles (open circles) and the skyrmion trajectory (black lines) for the system using $\alpha_m/\alpha_d = 0.45$, circular ac driving where $A = B$ and $\omega = 1 \times 10^{-5}$. (a) $A = 0.1$ a localized orbit between obstacles. (b) $A = 0.2$ a localized orbit encircling one obstacle. (c) $A = 0.4$ a localized orbit encircling 12 obstacles. (d) $A = 0.47$ a translating orbit that can turn all four corners of the interface in the clockwise direction. (e) $A = 0.66$ a localized orbit encircling 23 obstacles. (f) $A = 0.86$ another type of moving orbit following the interface, but wider than in (d). (Adapted from Vizarim *et. al*. [198], pg. 5).

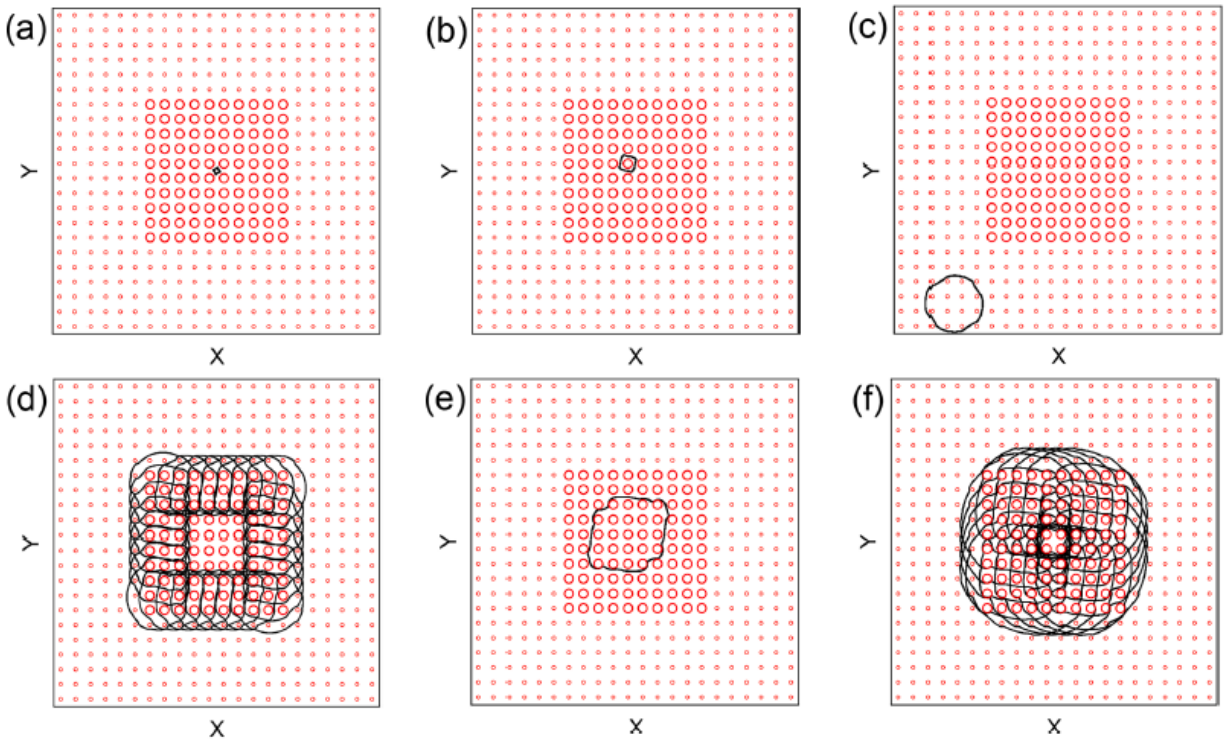

Figure 9.7 – The average velocities $\langle V_x \rangle$ and $\langle V_y \rangle$ as a function of the ac drive amplitude A for the system in Fig. 9.6 using $\alpha_m/\alpha_d = 0.45$. The regions with strong oscillations correspond to directed motion following the interface. (From Vizarim *et. al*. [198], pg. 6).

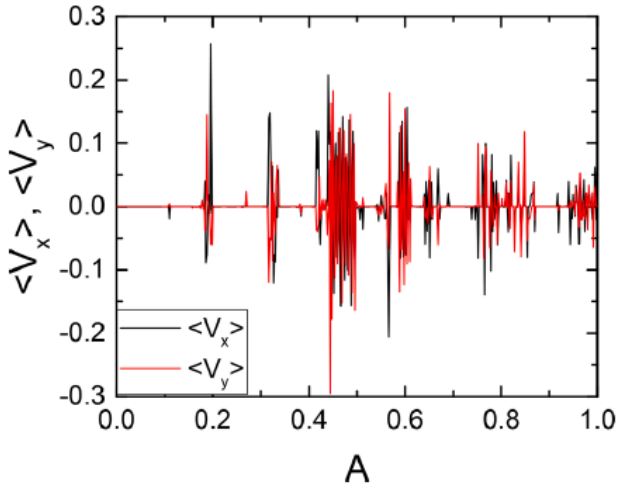

In general, the values of α_m/α_d and A that directed motion can occur is the same for 1D and 2D interfaces turning corners, however the intervals of A where direct motion occurs with

the skyrmion being able to turn corners to follow the interface is reduced when compared to the directed motion in 1D interface. In Fig. 9.8 (a) at $A = 0.886$ it is illustrated an example of a skyrmion following partially the interface. In this case, the skyrmion has chaotic motion before reaching the interface, when it reaches it follows the interface with directed motion. However, when it reaches the corner, it cannot turn and the skyrmion detaches from the interface and diffuses through the sample. This system is similar to the system of Fig. 9.6, but here the ac drive frequency is higher, $\omega = 2 \times 10^{-5}$. In Fig. 9.8 (b) it is illustrated the skyrmion trajectory for the same system but with $A = 0.894$ where the skyrmion can turn all four corners.

Figure 9.8 - The obstacles (open circles) and the skyrmion trajectory (black lines) for the system using $\alpha_m/\alpha_d = 0.45$, circular ac driving where $A = B$ and $\omega = 2 \times 10^{-5}$. (a) $A = 0.886$ a partially motion along the interface, where the skyrmion cannot turn corners. (b) $A = 0.894$ a translating orbit where the skyrmion follows the interface turning all four corners. (From Vizarim *et. al.* [198], pg. 6).

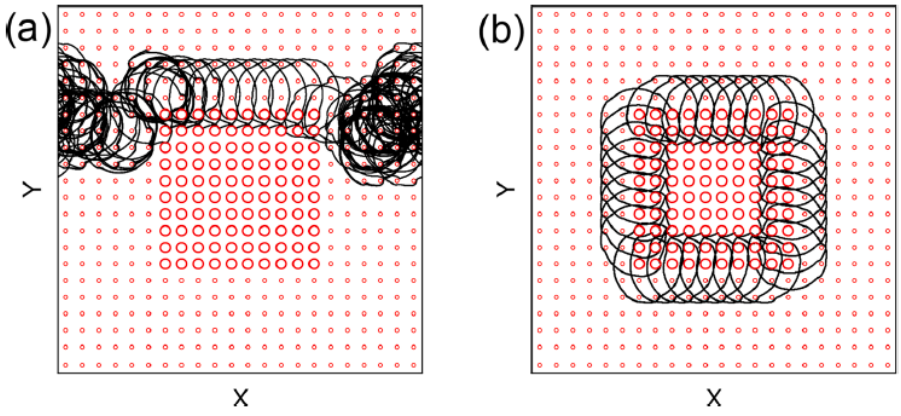

For fixed ac drive frequency, ω, and as α_m/α_d increases it is possible to observe a regime in which the skyrmion follows the interface turning all four corners but the motion has a partially stochastic component to its motion. In Fig. 9.9 it is illustrated some representative skyrmion trajectories for a system similar to 9.6, but using $\alpha_m/\alpha_d = 1.732$. In Fig. 9.9 (a) at $A = 0.06$ it is illustrated a skyrmion orbit oscillating between obstacles, while in Fig. 9.9 (b) at $A = 0.074$ shows the skyrmion undergoing diffusive motion through the large obstacle region. In Fig. 9.9 (c) at $A = 0.246$, the skyrmion performs directed motion along the interface, but there are intermittent windows of stochastic motion, reducing the efficiency of the motion to a distance much smaller than one lattice constant per ac drive cycle. In Fig. 9.9 (d) there is a localized orbit at $A = 0.33$ encircling 9 obstacles. Fig. 9.9 (e) at $A = 0.38$ shows another example of directed motion with reduced stochastic component than Fig. 9.9 (c). At $A = 0.532$ a translating orbit with no stochastic component. In Fig. 9.9 (g) a localized orbit encircling 52 obstacles at $A = 0.74$, while in Fig. 9.9 (h) a big translating orbit at $A = 0.838$.

Figure 9.9 - The obstacles (open circles) and the skyrmion trajectory (black lines) for the system using $\alpha_m/\alpha_d = 1.732$, circular ac driving where $A = B$ and $\omega = 1 \times 10^{-5}$. (a) $A = 0.06$ a localized orbit between obstacles. (b) $A = 0.074$ a diffusive motion in the bulk region. (c) $A = 0.246$ an interface motion with stochastic component. (d) $A = 0.33$ a localized orbit encircling nine obstacles. (e) $A = 0.38$ a clockwise edge transport. (f) $A = 0.532$ another type of moving orbit following the interface. (g) $A = 0.74$ a localized orbit encircling 52 obstacles. (h) $A = 0.838$ a big translating orbit through the interface. (Adapted from Vizarim *et. al.* [198], pg. 7).

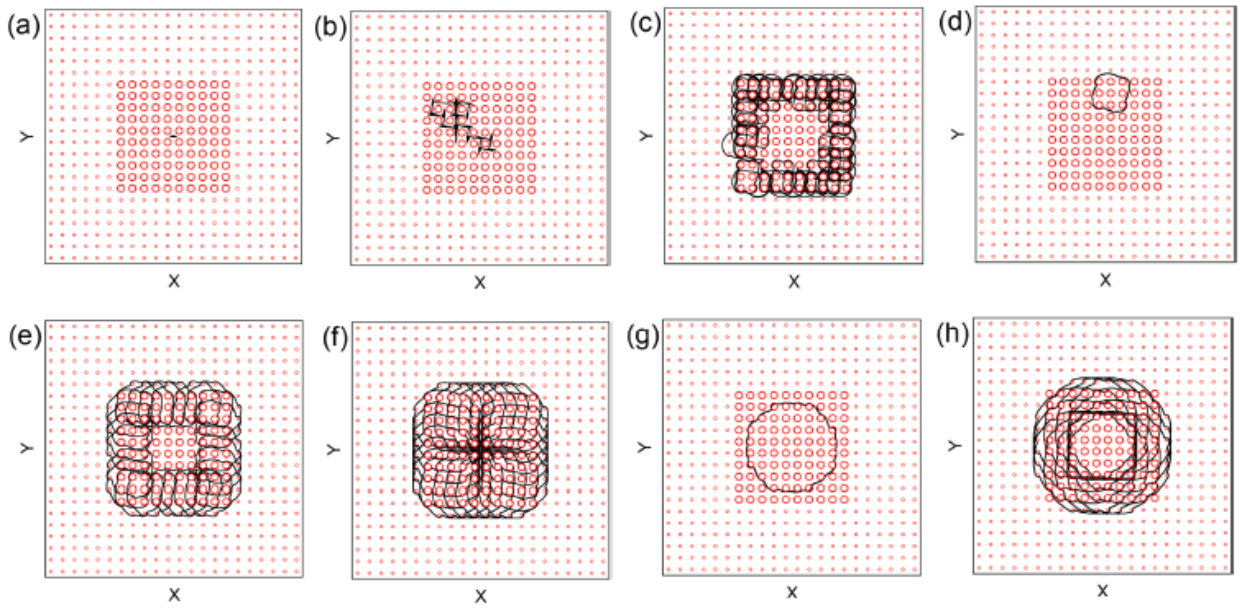

For even higher values of Magnus term, the skyrmion motion becomes more chaotic or localized, that is, regions of direct transport though the interface is significantly reduced. In Fig. 9.10 we show some skyrmion trajectories for a system similar to 9.9, but using $\alpha_m/\alpha_d = 9.962$. In Figs. 9.10 (a) and (b) the skyrmion is performing a localized orbits encircling four obstacles ($A = 0.03$) and nine obstacles ($A = 0.1$), respectively. In Fig. 9.10 (c) at $A = 0.324$ the skyrmion performs a very odd type of trajectory. It partially follows the interface turning two corners and then enters in the bulk, returning to a stochastic trajectory. For long times this pattern repeats itself. In Fig. 9.10 (d) at $A = 0.34$ the skyrmion performs a chaotic motion with no edge transport. In Fig. 9.11 it is plotted $\langle V_x \rangle$ and $\langle V_y \rangle$ as a function of A for the system in Fig. 9.10 showing some regions where strong oscillations in the velocity curves appear, corresponding to intermittent transport along the interface or ordered motion in the bulk. There are several regions where the velocity components are null, indicating several localized orbit regions.

Figure 9.10 - The obstacles (open circles) and the skyrmion trajectory (black lines) for the system using $\alpha_m/\alpha_d = 9.962$, circular ac driving where $A = B$ and $\omega = 1 \times 10^{-5}$. (a) $A = 0.03$ a localized orbit encircling four obstacles. (b) $A = 0.1$ a localized orbit encircling nine obstacles. (c) $A = 0.324$, the skyrmion jumps between clockwise motion trhough the interface and chaotic motion in the bulk. (d) $A = 0.34$ a chaotic motion. (From Vizarim *et. al.* [198], pg. 8).

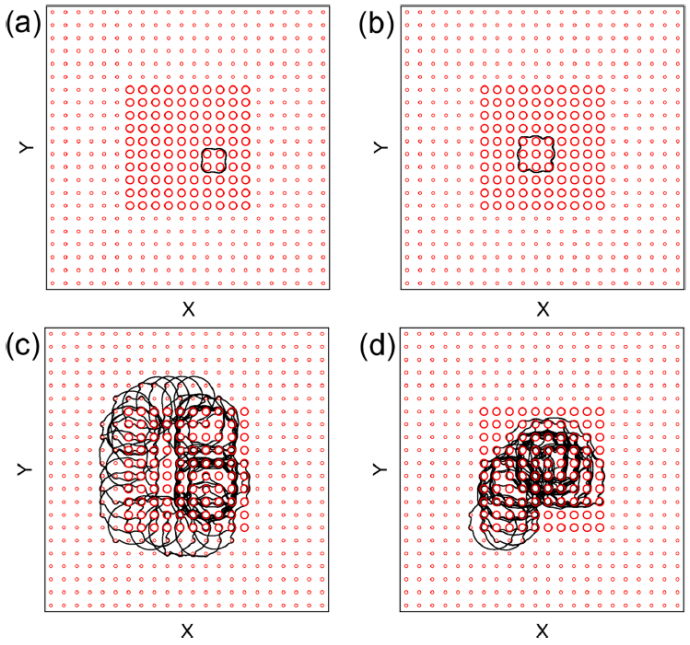

Figure 9.11 – The average velocities $\langle V_x \rangle$ and $\langle V_y \rangle$ as a function of the ac drive amplitude A for the system in Fig. 9.10 using $\alpha_m/\alpha_d = 9.962$. (From Vizarim *et. al.* [198], pg. 8).

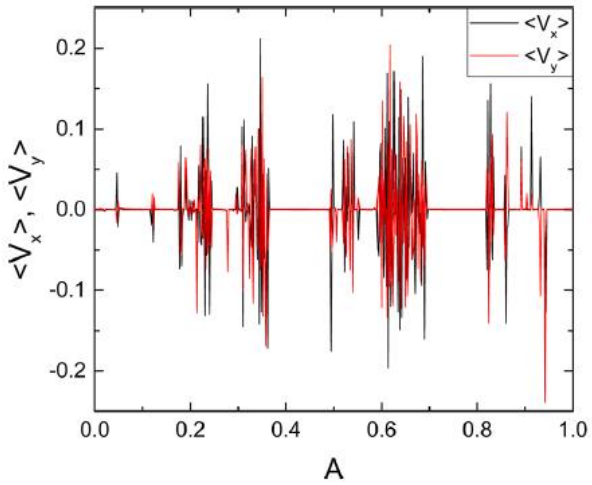

9.3.3 The influence of the bulk size

Now we consider the influence on changing the size of the central area where the larger obstacles are present. It is considered a smaller central area of 2×2 larger obstacles and another sample with 14×14 larger obstacles in the central area using $\alpha_m/\alpha_d = 0.45$ and $\omega = 1 \times 10^{-5}$. In Fig. 9.12 (a,b) it is plotted $\langle V_x \rangle$ and $\langle V_y \rangle$ as a function of A for these two systems.

For the 2×2 system, the results is very similar to what has been previously found in systems with homogeneous obstacle landscapes (see section 8). In this case the interface is too short for the skyrmion to follow, but as the ac drive amplitude increases, the skyrmion orbits tends to stabilize near the region with larger obstacles, as illustrated in Fig. 9.13 (a) with $A = 0.446$, and Fig. 9.13 (b) with $A = 0.578$.

Figure 9.12 – The average velocities $\langle V_x \rangle$ and $\langle V_y \rangle$ as a function of the ac drive amplitude A for a system using $\alpha_m/\alpha_d = 0.45$ and $\omega = 1 \times 10^{-5}$. (a) A system with 2×2 larger obstacles in the central area, (b) a system with 14×14 larger obstacles in the bulk. (From Vizarim *et. al.* [198], pg. 8).

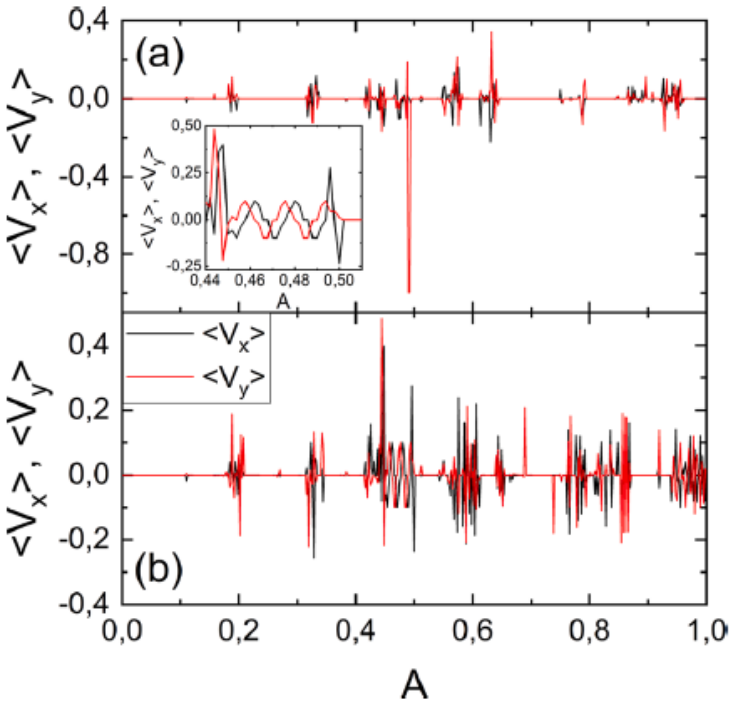

In the system with 14×14 larger obstacles in the central area, shown in Fig. 9.12 (b), it is possible to observe multiple regions with oscillations in $\langle V_x \rangle$ and $\langle V_y \rangle$, as highlighted in the blowup of the interval $0.44 \leq A \leq 0.51$ found in the inset of Fig. 9.12 (a). The skyrmion trajectory within this oscillatory region at $A = 0.47$ is illustrated in Fig. 9.13 (c). In this case, the skyrmion flows orderly following the interface in clockwise direction. For $A = 0.86$ it is also possible to observe another region where velocities are oscillating and the skyrmion is performing an edge transport, as shown in Fig. 9.13 (d). These results show that if the central area is further expanded, the window of A over which ordered edge transport occurs can be expanded, since there would be a greater amount of interface and also depth to accommodate the skyrmion orbits.

Figure 9.13 - The obstacles (open circles) and the skyrmion trajectory (black lines) for the system using $\alpha_m/\alpha_d = 0.45$, circular ac driving where $A = B$ and $\omega = 1 \times 10^{-5}$. (a) and (b) samples with 2×2 larger obstacles in central area. (a) and (b) the skyrmion encircling the central area with (a) $A = 0.446$ and (b) $A = 0.578$. (c) and (d) samples with 14×14 larger obstacles in central area (c) $A = 0.47$, the skyrmion flowing through the interface. (d) $A = 0.86$ edge transport with wider orbits. (From Vizarim *et. al*. [198], pg. 9).

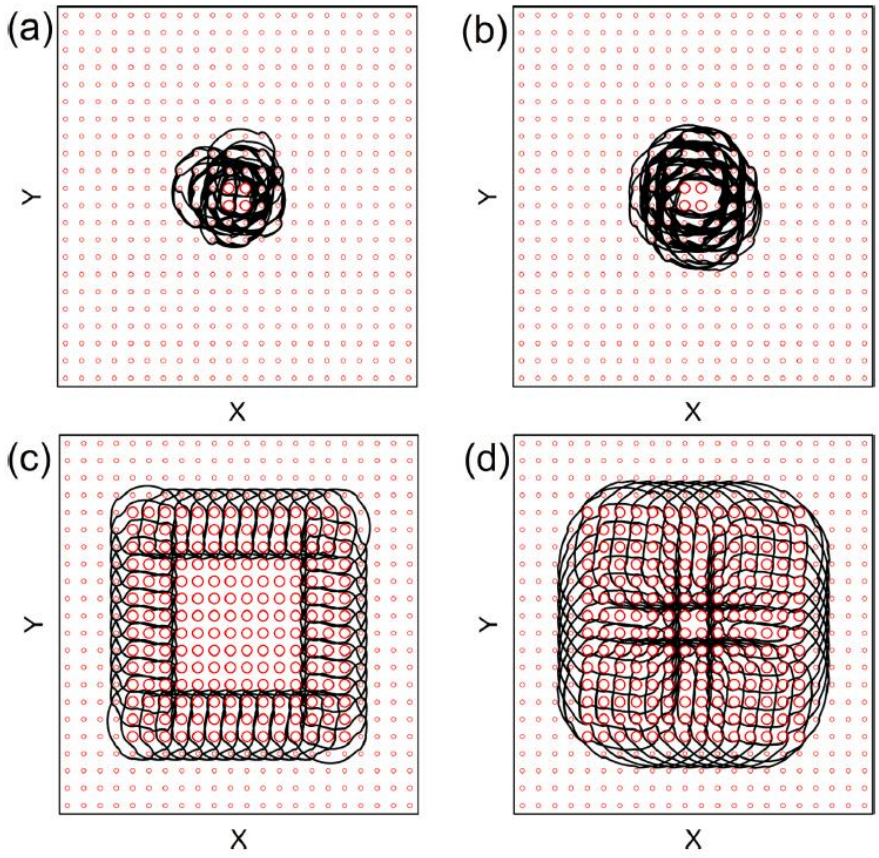

9.3.4 Discussion and Summary

Recently, it was published a study where particles exhibited directed motion while interacting with a periodic lattice substrate in what are called colloidal topological insulators [199]. In this work, a colloid driven in a circular or closed orbit can exhibit direct motion when interacting with an interface between two types of substrate lattices. Similarly, our results show that if a collective of skyrmions is interacting with an interface in a substrate, various types of edge transport modes can occur that would create a version of a skyrmion topological insulator in which skyrmion motion would not occur in the bulk but could appear in the edge. Concerning the collective effects, if the density of skyrmion is low enough, it is expected that the skyrmions behavior to be very similar to what has been presented in this section 9. On the other hand, if skyrmions are too close, it is possible that they could form a more complex orbit and move as a group through the edge.

In this work we only considered the regions with different obstacle sizes, but it would also be interesting to see how the system would behave if the obstacles array were different, such as a region with triangular lattice and another with square. Additionally, continuum-based simulation could also be interesting to see how the internal structure of the skyrmion would behave in a system like this. It is well-known that skyrmion internal modes can be excited and produce ratchet effects [131,132].

The closest experimental geometry to the system we studied here is skyrmion interacting with antidot lattices such as those fabricated by Saha *et. al*. [64]. Using this technique, it would be possible to create a sample with a fixed substrate lattice constant but different antidot sizes in different regions.

The most interesting feature of the guided interface motion is that a single applied ac drive can produce an arbitrary path of skyrmion trajectory following the interface in a desired design. If the obstacles were absent, it would be necessary to keep changing the driving direction in order to achieve the same designed path. Although both procedures produce the same result for a single skyrmion case, if multiple skyrmion were introduced, the interface guided motion could guide part of the skyrmion and keep the others in localized orbits. Moreover, skyrmion could be driven along diverse pathways, while external driving in absence of interface or obstacle would move all skyrmion in the same direction at the same time. Thus, guided motion can provide a form of parallel processing that is not possible using only dc drive and no interface.

10 The Influence of Obstacle Density on Skyrmion Dynamics

10.1 Directional Locking and Obstacle Density effects

In this work it is analyzed the effects of the obstacle density on the skyrmion dynamics. It is known from section 5 that the obstacle size can influence significantly the skyrmion dynamical behavior, and even can be used as a topological selector. Here, we investigate how the obstacle density affects the dynamics. The obstacle array has different symmetry, it is used triangular and honeycomb obstacle lattices. So, it is expected that the preferred angles for the skyrmion motion are $\phi = \arctan\left(\sqrt{3}p/(2q+1)\right)$, which are mainly 30° and 60°. The results show that the obstacle density can increase or reduce the number of possible dynamical regimes,

hence controlling the skyrmion motion. This work was published in Journal of Physics: Condensed Matter [200].

10.2 Model and Simulation details

The simulation method is exactly the same as the obstacle size analysis, in previous section 5. There is only a dc drive applied to a single skyrmion in a 2D periodic landscape. In this case it is analyzed samples using triangular and honeycomb lattices with varied obstacle densities, as illustrated in Fig. 10.1. The dynamical properties of the skyrmion system interacting with the obstacle array were simulated using the particle model for skyrmions, shown in Eq. (12.1), using Molecular Dynamics technique.

$$\alpha_d \mathbf{v_i} + \alpha_m \hat{z} \times \mathbf{v_i} = \mathbf{F}_i^o + \mathbf{F}^D \tag{10.1}$$

The system has a size of $L \times L$ with periodic boundary conditions in both x and y directions. Throughout this work we fixed $a_0 = 0.65$ and $F_0 = 1.0$. All distances are normalized by ξ and the obstacle densities by $1/\xi^2$. The velocities parallel, $\langle V_\parallel \rangle$, and perpendicular, $\langle V_\perp \rangle$, to the external dc drive are measured. The external dc drive is increased in small steps of $\delta F^D = 0.001$ and wait 10^5 simulation time steps between increments to ensure steady state. We normalize the damping and Magnus coefficients as $\alpha_d^2 + \alpha_m^2 = 1$.

Figure 10.1 – An illustration of the obstacle lattices used in this work. (a) Triangular obstacle array and (b) the honeycomb lattice. (From Vizarim *et. al*. [200], pg. 2)

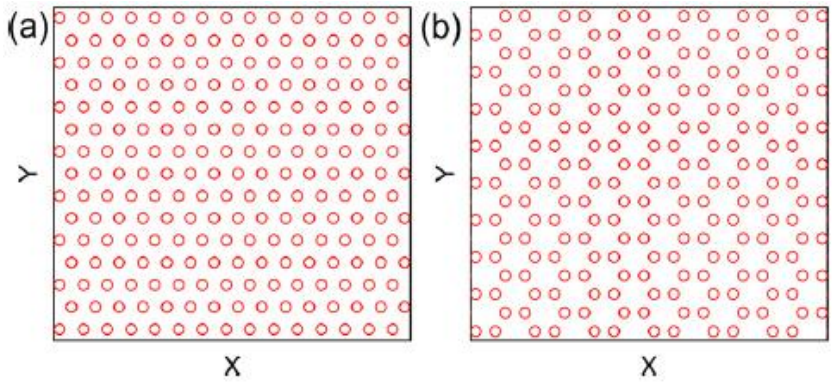

10.3 Results

10.3.1 Directional locking on honeycomb and triangular obstacle arrays

In Figs. 10.2 (a) and (b) it is plotted the $\langle V_\parallel \rangle$, $\langle V_\perp \rangle$ and θ_{sk} versus the external dc drive, F^D for a sample with triangular obstacle array where the obstacle density is $\rho_t = 0.128$ and

$\alpha_m/\alpha_d = 1.0$. In the case where the obstacles were absent, the skyrmion would flow in the direction of the intrinsic skyrmion Hall angle, $\theta_{sk}^{int} = -45°$. As shown in Fig. 10.2 (b), in the presend of obstacles the skyrmion motions exhibit a series of quantized locking steps up to $F^D = 1.7$, followed at higher drives by a continuous saturation of θ_{sk} to the intrinsic angle. For $F^D \leq 0.307$ the skyrmion is locked to $\theta_{sk} = 0°$, as shown in Fig. 10.3 (a). From Fig. 10.2 (a) it is also possible to see that $\langle V_\perp \rangle \cong 0$ and $\langle V_\parallel \rangle$ is increasing as a function of F^D for this range of forces, indicating the motion only in the x direction. For $0.307 < F^D \leq 1.041$ the skyrmion is strongly locked at $\theta_{sk} = -30°$, which is a preferable direction of motion due to the triangular obstacle array symmetry. In this case the skyrmion moves one lattice constant in x for every lattice constant in y, giving $\theta_{sk} = \arctan\left(\sqrt{3}p/(2q+1)\right) = \arctan\left(\sqrt{3}/3\right) = 30°$. This motion locked in $\theta_{sk} = -30°$ can be seen in Fig. 10.3 (b). In Fig. 10.3 (c) shows the skyrmion trajectory at $F^D = 1.1$, when $\theta_{sk} = -36.56°$. For $F^D = 1.5$, the skyrmion Hall angle is approaching the intrinsic value, and the skyrmion is locked to $\theta_{sk} = -40.8°$. For even higher values of appled external drive, the skyrmion continuously approaches the intrinsic value.

Figure 10.2 – (a) The average velocities $\langle V_\parallel \rangle$ (black) and $\langle V_\perp \rangle$ (red) as a function of the applied dc force F^D for a sample with triangular obstacle array with density $\rho_t = 0.128$ and $\alpha_m/\alpha_d = 1.0$. (b) The corresponding θ_{sk} curve. (From Vizarim *et. al.* [200], pg. 3).

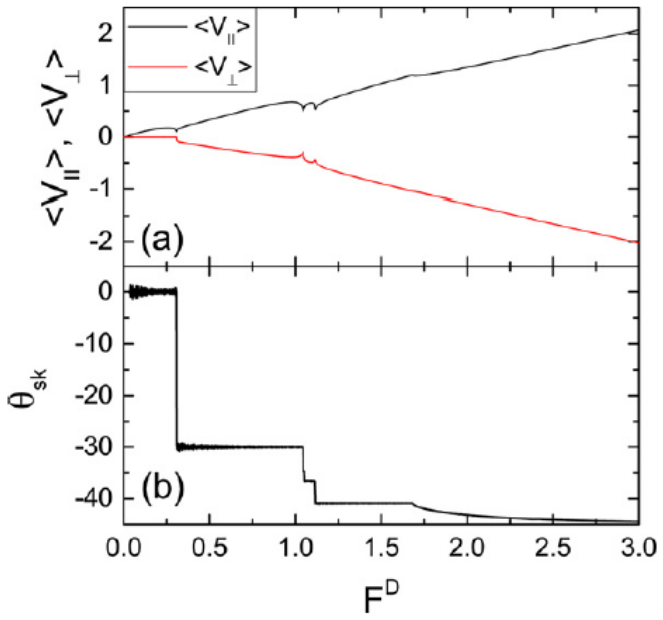

Figure 10.3 – The obstacles (open circles) and the skyrmion trajectory (black lines) for the system in Fig. 10.2 (a) with $\alpha_m/\alpha_d = 1.0$ and $\rho_t = 0.128$. (a) The $\theta_{sk} = 0°$ state at $F^D = 0.25$, (b) the $\theta_{sk} = -30°$ state at $F^D = 0.5$, (c) the $\theta_{sk} = -36.56°$ state at $F^D = 1.1$ and (d) $\theta_{sk} = -40.8°$ state at $F^D = 1.5$. (From Vizarim et. al. [200], pg. 4).

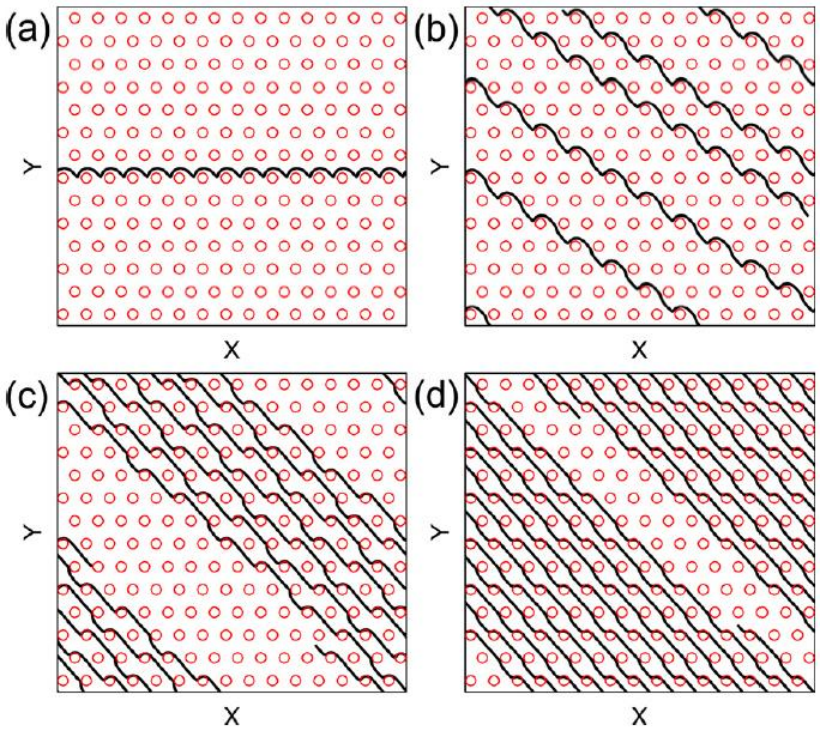

Another possible way to visualize the locking steps is locking into the time series of the skyrmion velocities. In Fig. 10.4 (a) it is shown the parallel and perpendicular skyrmion velocities at $F^D = 0.5$ when the system is directionally locked in $\theta_{sk} = -30°$, while in Fig. 10.4 (b) shows the skyrmion component velocities at $F^D = 2.5$, where the system is in a non-step region, as can be seen in Fig. 10.2. In the locked phase, the velocities are exactly periodic with the same signal appearing every cycle. However, in the non-step region, the patterns are no exactly the same, although there is still periodicity in the signal due to the periodic triangular obstacle array. The difference can be clearer when analyzing the Fourier transform $S(\omega)$ of the velocity signals for the x direction velocity component $V_{\parallel}$, as shown in Fig. 10.5. The peaks in $S(\omega)$ are more pronounced in the locking regime than in the non-step region. This suggests that if an ac driving is introduced, the regions with locking steps should exhibit strong Shapiro steps while in the non-step regions the Shapiro would be absent or very weak.

Figure 10.4 – Time series of the velocities $V_{\parallel}$ (black) and $V_{\perp}$ (red) for a sample with triangular obstacle array with density $\rho_t = 0.128$ and $\alpha_m/\alpha_d = 1.0$. (a) A locking regime at $F^D = 0.5$ and stable $\theta_{sk} = -30°$. (b) A nonlocking step regime at $F^D = 2.5$. In the locking regime the signals are exactly the same for every cycle, while in the non-locking regime the signals are not the same. (From Vizarim *et. al*. [200], pg. 4).

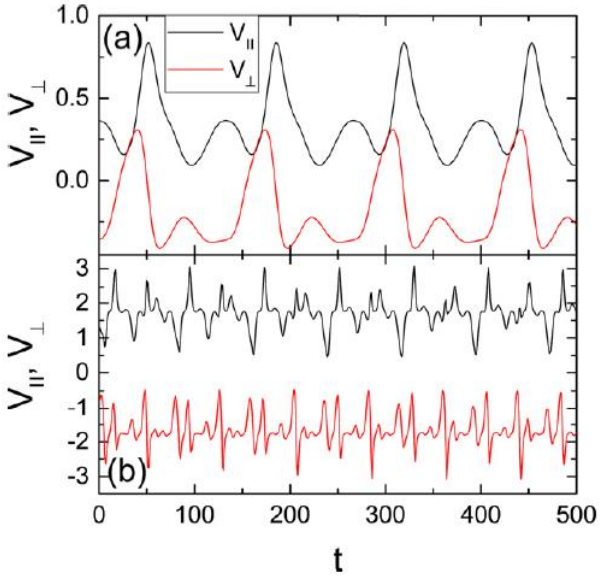

Figure 10.5 – The Fourier transform $S(\omega)$ of the $V_{\parallel}$ data exhibited in Fig. 12.4. for the triangular array with $\rho_t = 0.128$ and $\alpha_m/\alpha_d = 1.0$ in the locking regime (black) and the non-locking regime (red). The peaks are much stronger in the locking regime. (From Vizarim *et. al*. [200], pg. 4).

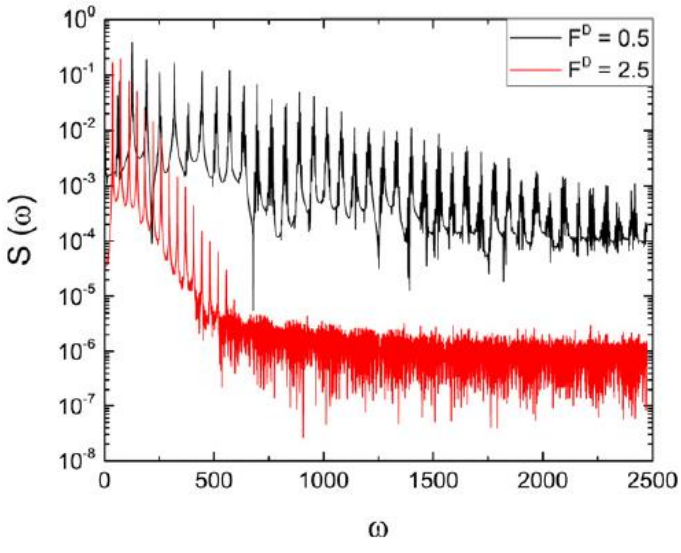

Now for the case of a honeycomb lattice, the system exhibits a strong difference. In Fig. 10.6 it is plotted $\langle V_{\parallel} \rangle$, $\langle V_{\perp} \rangle$ and θ_{sk} versus the external dc drive, F^D for a sample with honeycomb obstacle array where the obstacle density is $\rho_h = 0.123$ and $\alpha_m/\alpha_d = 1.0$. As can be seen, there is a pinned phase for $F^D \leq 0.076$ when the skyrmion is trapped between

obstacles. Differently from the triangular array, for the honeycomb there is no phase with motion $\theta_{sk} = 0°$. After the depinning, the skyrmion moves along $\theta_{sk} = -30°$ [See Fig. 10.7 (a)]. This happens due to the obstacle vacancy of the honeycomb lattice that pins the skyrmion for very low drives, and after the depinning enables the skyrmion to flow with a higher angle. For $F^D > 1.294$, there is a series of transitions in the skyrmion motion, which approaches the instrinsic angle value. As an example of such closely spaced short steps, in Fig. 10.7 (b) it is shown the trajectory at $F^D = 1.7$, where $\theta_{sk} = -40.8°$.

Figure 10.6 – (a) The average velocities $\langle V_{\parallel} \rangle$ (black) and $\langle V_{\perp} \rangle$ (red) as a function of the applied dc force F^D for a sample with honeycomb obstacle array with density $\rho_h = 0.123$ and $\alpha_m/\alpha_d = 1.0$. (b) The corresponding θ_{sk} curve. (From Vizarim *et. al.* [200], pg. 5).

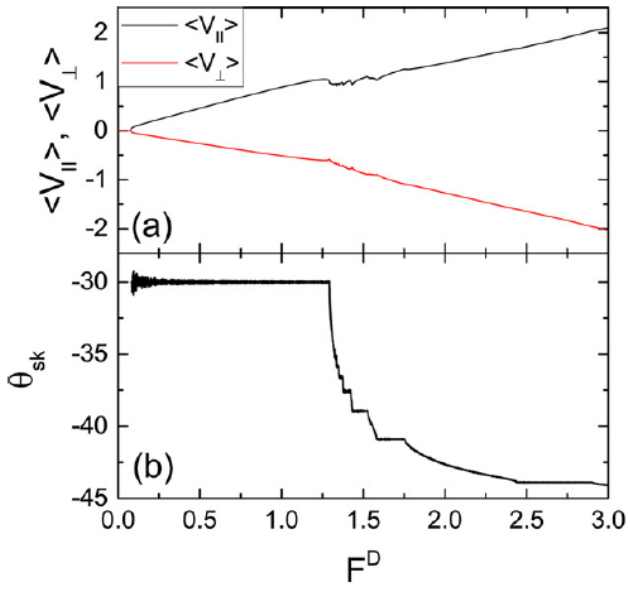

Figure 10.7 – The obstacles (open circles) and the skyrmion trajectory (black lines) for the system in Fig. 10.6 (a) with $\alpha_m/\alpha_d = 1.0$ and $\rho_h = 0.123$. (a) The $\theta_{sk} = -30°$ state at $F^D = 0.5$ and (b) the $\theta_{sk} = -40.8°$ state at $F^D = 1.7$. (From Vizarim *et. al.* [200], pg. 4).

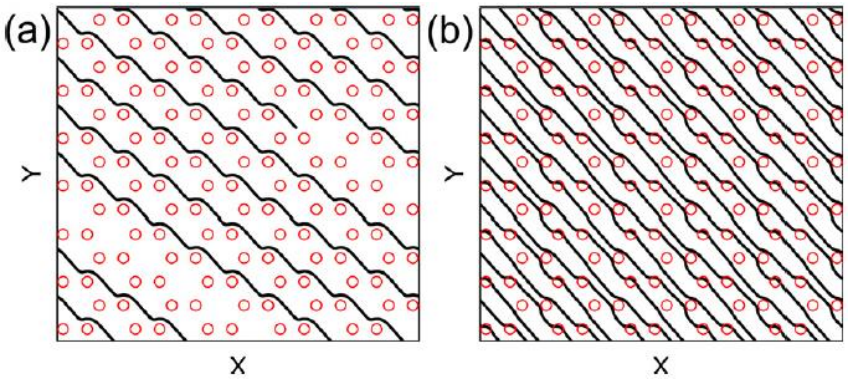

10.3.2 Varying the obstacle density and Magnus force

For the study of the effects of obstacle density we fix the Magnus force as $\alpha_m/\alpha_d = 1.0$ and consider five samples with varied obstacle densities for both triangular and honeycomb obstacle arrays. For each sample separately we then vary α_m/α_d in order to see how the Magnus force affect each sample. In Fig. 10.8 it is plotted the Hall angle, θ_{sk}, versus the external dc drive, F^D, for varied obstacle densities for the triangular and honeycomb arrays, showing a clear influence of the obstacle density on the dynamics. In Fig. 10.8 (a), at very low values of obstacle density, such as $\rho_t = 0.032$, the skyrmion motion is very close to the intrinsic Hall angle, which for $\alpha_m/\alpha_d = 1.0$ is $\theta_{sk} = -45°$. That is, the skyrmion is flowing with very reduced obstacle effects, since they are widely spaced in the sample. As more obstacles are added to the sample, the skyrmion dynamics becomes richer with more diversity of possible dynamic phases. For the triangular array there are three main locking steps: $0°$, $-30°$ and $-40.8°$. The phase where $\theta_{sk} = 0°$ occurs only when the obstacle density is higher, with $\rho_t > 0.128$, while the $-30°$ phase is present for all obstacle densities studied here, although its extent is very limited for $\rho_t = 0.032$, just between the interval $0 \leq F^D \leq 0.05$. The locking step with $\theta_{sk} = -40.8°$ is also present fr all obstacle densities studied here, but it is more robust for low values of obstacle density. In the honeycomb array there are only two main locking directions, $\theta_{sk} = -30°$ and $-40.8°$. The phase with $\theta_{sk} = -30°$ is very prominent for all obstacle densities, on the other hand the phase $\theta_{sk} = -40.8°$ is not very robust and becomes weak for high obstacle density values.

Using the results of Fig. 10.8 it is possible to construct a dynamic phase diagram of the main locking directions as a function of the obstacle density ρ_t or ρ_h versus F^D, as shown in Fig 10.9. In both cases, the pinned phase extends with increasing obstacle density. The pinned phase is even higher in the honeycomb lattice due to the pinning of skyrmions inside the lattice vacancy sites. For the triangular array in Fig. 10.9 (a), the phase where $\theta_{sk} = 0°$ is absent only occurs for very low values of obstacle density, and increases in width up to a maximum at $\rho_t = 0.288$. In contrast, the $\theta_{sk} = -40.8°$ phase is largest for low values of ρ_t. For the honeycomb lattice case, the $\theta_{sk} = -30°$ phase retains a nearly uniform width over all obstacle densities values studied in this work. However, note that the location of the step shifts to higher values of F^D with increasing ρ_h. The phase with $\theta_{sk} = -40.8°$ is considerably reduced when compared to triangular array case.

Figure 10.8 – The Hall angle, θ_{sk}, as a function of the applied dc force F^D for samples with varied values of obstacle density using $\alpha_m/\alpha_d = 1.0$. In (a) using triangular array and (b) honeycomb. (From Vizarim *et. al.* [200], pg. 6).

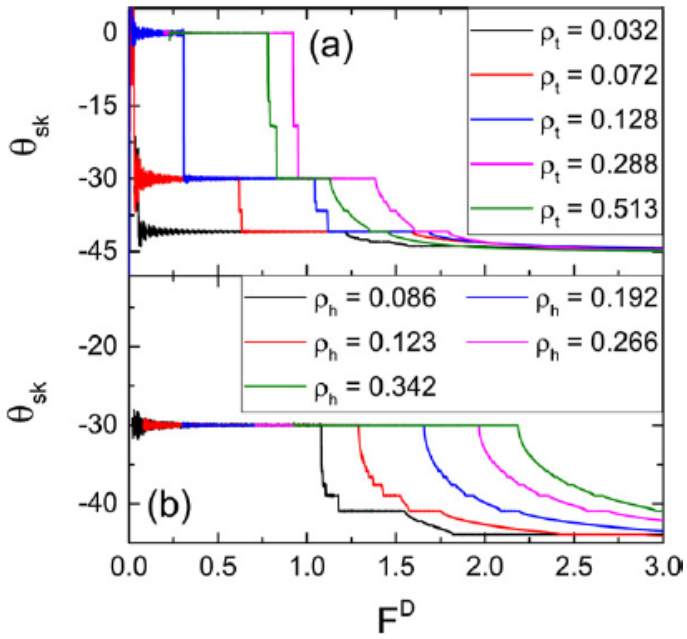

Figure 10.9 – Dynamic phase diagram as a function of obstacle density versus F^D for samples with $\alpha_m/\alpha_d = 1.0$. (a) The triangular obstacle array with obstacle density ρ_t. (b) The honeycomb array with density ρ_h. Colors indicate the selected main dynamic phases: pinned (yellow), $\theta_{sk} = 0°$ (dark grey), $\theta_{sk} = -30°$ (red), $\theta_{sk} = -40.8°$ (blue) and unlocked or minor phases in blank areas. (From Vizarim *et. al.* [200], pg. 6).

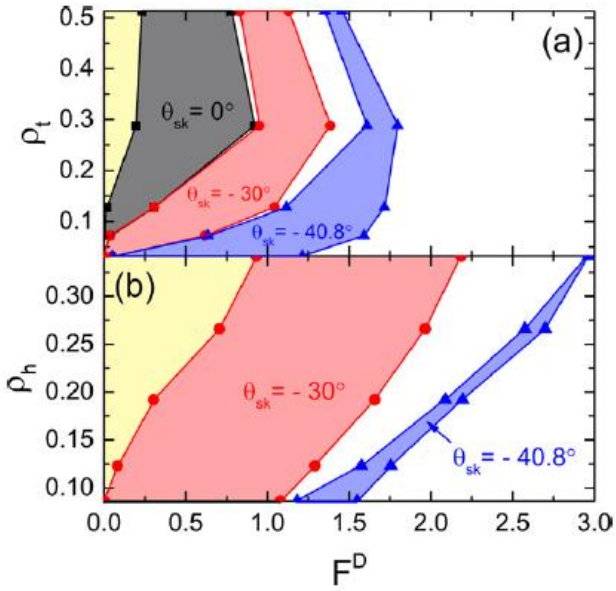

In Fig. 10.10 it is plotted the skyrmion Hall angle, θ_{sk}, as a function of F^D for different values of α_m/α_d at varied obstacle densities for both triangular and honeycomb arrays. Note that the case of $\alpha_m/\alpha_d = 1.0$ is already shown in Fig. 10.8.

From Fig. 10.10 it is possible to see that as α_m/α_d is modified, the locking angles changes strongly. For higher values of Magnus force, the intrinsic Hall angle is higher and enables more possibilities for the skyrmion to lock its motion. When $\alpha_m/\alpha_d = 0.5$, the intrinsic angle is $\theta_{sk}^{int} = -26.57°$. As a result, the skyrmion can strongly lock to the substrate symmetry direction of $\theta_{sk} = -30°$, even though $|\theta_{sk}| > |\theta_{sk}^{int}|$ for this particular case. The obstacle induced motion at an angle that is higher than the intrinsic Hall angle was observed in previous works [39], and also illustrated in this thesis in previous section 5 in detail, but here we show that it also depends on the obstacle density. As illustrated in Fig. 10.10 (a), the locking step $\theta_{sk} = -30°$ only exists for very low obstacle densities, such as $\rho_t < 0.072$, and disappears completely for higher obstacle densities. In Fig. 10.11 (a) it is illustrated the skyrmion trajectories for the $\theta_{sk} = -30°$ step at $F^D = 1.5$, $\rho_t = 0.072$ and $\alpha_m/\alpha_d = 0.5$. Also, from Fig. 10.10 (a), the number of dynamic phases seems to be related to the obstacle density. At $\rho_t = 0.128$, the system has a very rich set of dynamic phases, while for other densities the number of dynamic phases is reduced. For very low ρ_t the skyrmion motion is very close to the intrinsic Hall angle, so the number of dynamic phases is reduced. On the other hand, as ρ_t increases, there is a reduction in the gaps between the obstacles, which pinches off many possible skyrmion trajectories, therefore reducing the number of dynamic phases.

Interestingly, our results show that for a given value of F^D, varying the obstacle density may cause the skyrmion to move with different directions. For example, at $F^D = 0.75$, the skyrmion can move along $\theta_{sk} = 0°$ or $\theta_{sk} = -30°$ depending on the obstacle density. For $\rho_t \leq 0.072$, the skyrmion locks to $\theta_{sk} = -30°$, while for $\rho_t > 0.072$, it locks to $\theta_{sk} = 0°$. This feature opens the possibility of designing devices in which regions with distinct obstacle densities may coexist in order to force the skyrmion to follow a designed trajectory. The pinning geometry is very important, however some combinations of pinning landscape and α_m/α_d may produce strong symmetry locking directions that even for varied obstacle densities the skyrmion motion is always locked to a single direction of motion, regardless the obstacle density used, as can be seen from Fig. 12.10 (b), where the motion is always along $\theta_{sk} = -30°$.

Figure 10.10 – Plots of skyrmion Hall angle, θ_{sk}, as a function of the applied dc force F^D for samples with varied values of obstacle density using and varied values of α_m/α_d. In the left column results using a triangular array, in the right column results using a honeycomb array. In (a) triangular with $\alpha_m/\alpha_d = 0.5$, (b) honeycomb with $\alpha_m/\alpha_d = 0.5$, (c) triangular with $\alpha_m/\alpha_d = 2.0$, (d) honeycomb with $\alpha_m/\alpha_d = 2.0$, (e) triangular with $\alpha_m/\alpha_d = 3.0$ and (f) honeycomb with $\alpha_m/\alpha_d = 3.0$ (From Vizarim *et. al*. [200], pg. 7).

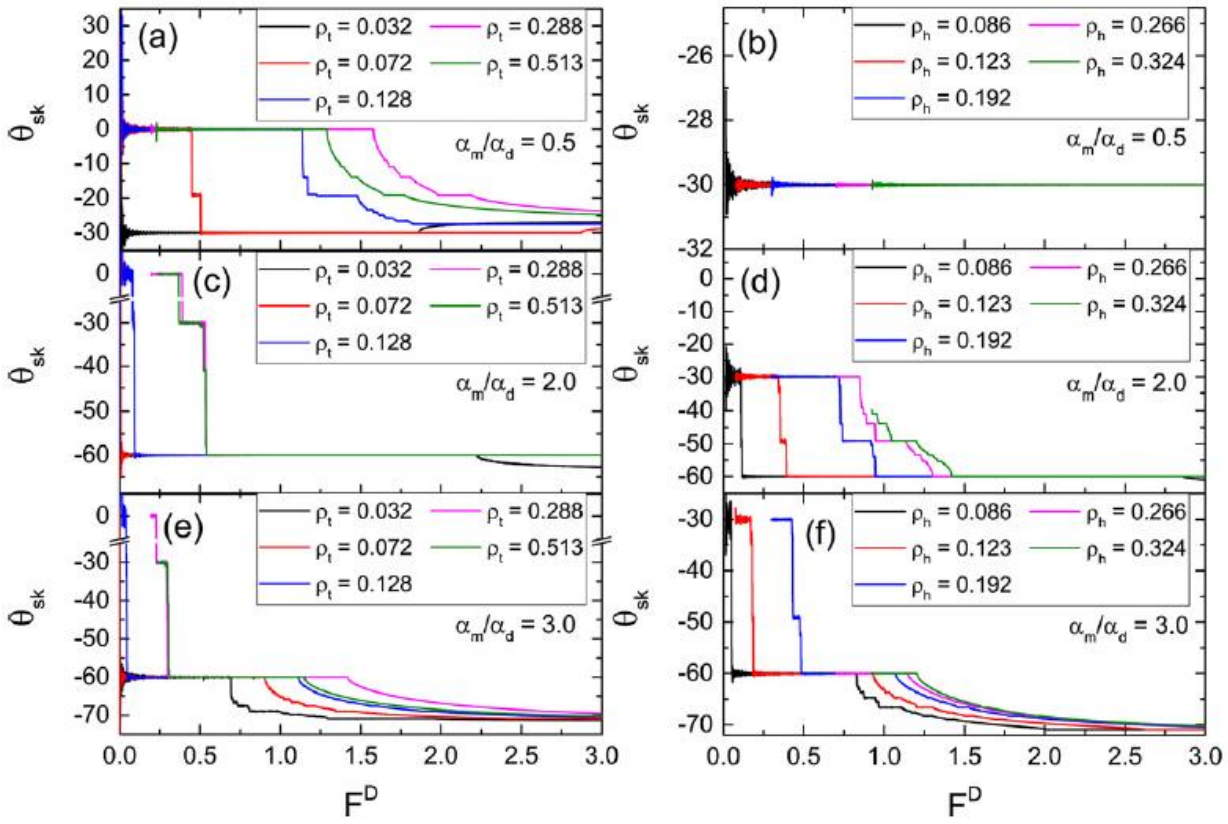

At $\alpha_m/\alpha_d = 2.0$, shown in Figs. 10.10 (c) and (d), the intrinsic Hall angle is $\theta_{sk}^{int} = -63.44°$. For the triangular array in Fig. 10.10 (c), for obstacle densities $\rho_t \leq 0.072$ the skyrmion depins and move along $\theta_{sk} = -60°$, as illustrated in Fig. 10.11 (b). Due to the symmetry of the triangular array, this is a very strong locking step angle. For higher values of obstacle density, such as, $\rho_t \geq 0.128$, additional locking steps emerge, such as $\theta_{sk} = 0°$ and $-30°$. For the honeycomb lattice, shown in Fig. 10.10 (d), when $\rho_h \leq 0.266$ the skyrmion depins into the $\theta_{sk} = -30°$ locking step. This is also a very strong locking direction due to the symmetry of the honeycomb lattice. However, at $\rho_h = 0.342$ the skyrmion depins and flow with a higher angle of $\theta_{sk} = -40.8°$, as shown in Fig. 10.11 (c). For the honeycomb case, the number of dynamic phases increases as the obstacle density increases. For example, the $\theta_{sk} = -49°$ step illustrated in Fig. 10.11 (d) is absent for $\rho_h \leq 0.123$. In Figs. 10.10 (e) and (f) it is illustrated the results for samples with $\alpha_m/\alpha_d = 3.0$, where the intrinsic Hall angle is $\theta_{sk}^{int} = -71.57°$. For each array, the locking steps in both $\theta_{sk} = -30°$ and $-60°$ are significantly reduced in size. For higher values of Magnus force, the intrinsic Hall angle forces the skyrmion

to move at higher angles, therefore reducing the robustness of the strong locking direction, due to the symmetry of the pinning landscape.

Figure 10.11 – The obstacles (open circles) and the skyrmion trajectory (black lines) for systems shwon in Fig. 10.10. (a) and (b) samples with triangular obstacle array with $\rho_t = 0.072$. (a) At $F^D = 1.5$ and $\alpha_m/\alpha_d = 0.5$ the skyrmion motion is locked at $\theta_{sk} = -30°$. (b) At $F^D = 1.0$ and $\alpha_m/\alpha_d = 2.0$ the skyrmion motion is locked at $\theta_{sk} = -60°$. (c) and (d) sample with honeycomb obstacle array with $\rho_h = 0.324$. (c) At $F^D = 0.95$ and $\alpha_m/\alpha_d = 2.0$ the motion is locked at $\theta_{sk} = -40.8°$. (d) At $F^D = 1.125$ and $\alpha_m/\alpha_d = 2.0$ the motion is locked at $\theta_{sk} = -49°$. (From Vizarim *et. al*. [200], pg. 7).

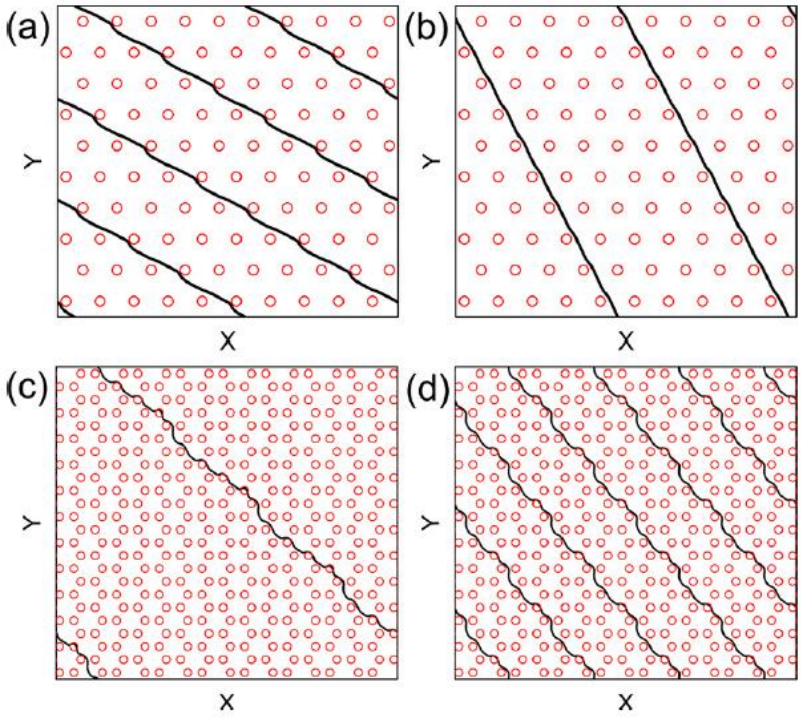

10.3.3 Stability of the directional locking as a function of α_m/α_d

As discussed previously, both triangular and honeycomb obstacle arrays should have preferred directions of motion along $\theta_{sk} = -30°$ and $-60°$ due to the symmetry of the pinning landscape. In this section we aim to quantify the robustness of these dynamics phases as a function of α_m/α_d for arbitrary obstacle densities. Also, the possibility of topological selection is discussed, since different species of skyrmion, with different Magnus terms, may coexist in a given sample [154,201,202]. Note that the results found here are considering the single skyrmion case, however, we expect that the result would remain reliable for a system with low density of skyrmions.

The obstacle densities are chosen arbitrarily and remain fixed for triangular ($\rho_t = 0.072$) and honeycomb ($\rho_h = 0.123$) obstacle arrays and vary the rate α_m/α_d to investigate how the locking steps $\theta_{sk} = -30°$ and $-60°$ behave. In Fig. 10.12 it is plotted a dynamic phase diagram

as a function of α_m/α_d versus F^D highlighting these selected locking steps. For the triangular array, shown in Fig. 10.12 (a), both steps have a range of α_m/α_d for which the step extends over nearly the entire window of F^D. This range is wider for the $\theta_{sk} = -60°$ step than for $\theta_{sk} = -30°$ step. This feature could be of interest for technological applications since the direction of motion remains unchanged on each step. Besides that, when $\alpha_m/\alpha_d \leq 1.2$, the skyrmion can only lock along $\theta_{sk} = -30°$, while for $\alpha_m/\alpha_d \geq 1.3$ it can only lock along $\theta_{sk} = -60°$. That is, the phases where $\theta_{sk} = -30°$ and $-60°$ can never coexist for a given value of α_m/α_d. This enables the possibility to create devices for topological selection, since skyrmions with stronger Magnus components would lock in a different direction than skyrmions with weaker Magnus components. In the honeycomb array, shown in Fig. 10.12 (b), the steps $\theta_{sk} = -30°$ and $-60°$ can coexist together over the range $1.5 \leq \alpha_m/\alpha_d \leq 5.0$. In this case, the skyrmions could be switched from $\theta_{sk} = -30°$ to $-60°$ by a fine adjustment in the external dc drive, F^D. For values of $\alpha_m/\alpha_d < 1.5$ the skyrmion can only lock to $\theta_{sk} = -30°$, and for $\alpha_m/\alpha_d > 5.0$ it can only lock to $\theta_{sk} = -60°$. As mentioned before, the obstacle density plays an important role on skyrmion dynamics, so it is expected that changing the obstacle density may result in different phase diagram than illustrated in Fig. 10.12.

Figure 10.12 – Dynamic phase diagram as a function of α_m/α_d versus F^D. (a) The triangular obstacle array with obstacle density $\rho_t = 0.072$. (b) The honeycomb array with density $\rho_h = 0.123$. Colors indicate the selected main dynamic phases: pinned (yellow), $\theta_{sk} = -30°$ (dark grey), $\theta_{sk} = -60°$ (red) and unlocked or minor phases in blank areas. (From Vizarim *et. al*. [200], pg. 8).

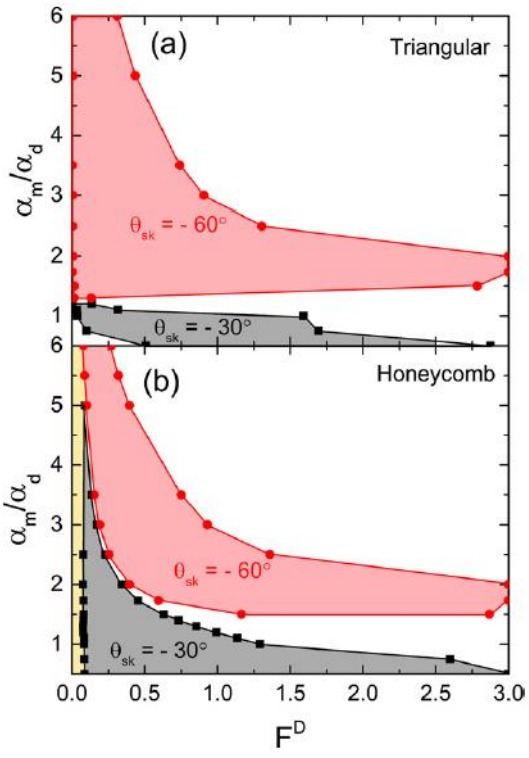

10.3.4 Discussion and Summary

The behavior of a single skyrmion interacting with triangular and honeycomb obstacle arrays with different obstacle densities has been investigated in this work. It is shown that the skyrmion exhibit a series of directional locking effects that can be quantized or continuous as a function of the dc external drive. For low obstacle densities, the depinning forces are weak and the skyrmion tends to move at an angle very close to the intrinsic one, reducing the number of possible dynamic phases. On the other hand, at higher densities, the depinning forces are larger and a richer variety of dynamic phases can be seen. The main difference between the honeycomb and the triangular lattice is that the locking step $\theta_{sk} = 0°$ is absent for the system with honeycomb lattice. The vacancies in the honeycomb lattice trap the skyrmions more effectively and prevent them from moving until the drive is too large to permit a motion along $\theta_{sk} = 0°$. For the triangular lattice, the step $\theta_{sk} = 0°$ is more prominent at higher obstacle densities and lower values of α_m/α_d. Both arrays show prominent locking steps at $\theta_{sk} = -30°$ and $-60°$ due to the obstacle array symmetry. These locking steps appear over a wide range of obstacle densities and values of α_m/α_d. It is also shown the robustness of these phases as a function of α_m/α_d and discussed the possibilities for topological sorting or switching the skyrmion motion between these two main locking steps.

For a given value of external dc drive, different obstacle densities can produce different directions of skyrmion motion. This interesting property can be used to build devices containing regions with distinct obstacle densities which can steer the skyrmion along a desired trajectory. We expect that similar behavior can occur for other periodic array geometries but that the angles of motion would be different, depending on the substrate symmetry. Our model is based on point-like skyrmions, however, actual skyrmions may be distorted in shape by the driving force or through interactions with the obstacles in the sample [29], especially in high-density obstacle samples. Such effects could be further explored in continuum-based simulations.

11 Soliton Motion in Skyrmion Chains

11.1 Stabilization and Guidance using nanoengineered pinning

In this work we search for alternatives to avoid the skyrmion Hall angle using a soliton of skyrmions. The soliton is formed when in a chain of skyrmions pinned to pinning centers there is an extra interstitial skyrmion or a vacancy (pinning center without a pinned skyrmion). We considered two types of samples: a quasi-one-dimensional (q1D) sample; where rigid walls confine a single chain of skyrmions, and a 2D sample; with no walls and multiple chains of skyrmions. We find that when an external current is applied, just above the depinning threshold, the soliton moves with a Hall angle equal to zero. For higher drives, the whole chain of skyrmions depin, and in the 2D sample, both the soliton and the chain of skyrmions flow with Hall angle of zero for low values of applied drive. Moreover, in a 2D system with a 1D interface that is placed at an angle respective to the applied drive, we found that can be a reversal in the skyrmion Hall angle signal, going from positive to negative. Our results suggest that skyrmion solitons could be used as information carriers in nanotracks that can avoid the drawbacks of the skyrmion Hall angle. Moreover, the soliton motion occurs for very low drives, prior to the skyrmion depinning as a chain, suggesting low energy cost devices using soliton motion in skyrmion chains. This work was published in Physical Review B [209].

11.2 Model and simulation details

The simulation considers the dynamical behavior of N_{sk} skyrmions interacting with N_p attractive pinning centers in a two-dimensional box with $L_x \times L_y$ dimensions using periodic boundary conditions in both x and y directions, as illustrated in Fig. 11.1. We define the skyrmion density as $n_{sk} = N_{sk}/L_x L_y$ and the pinning density as $n_p = N_p/L_x L_y$. The simulations are conducted just outside the commensuration ratio $N_{sk}/N_p = 1$. We say that the system is commensurate when the number of skyrmions is an integer or a rational fraction of the number of pinning sites. We start our simulations considering a simplest case of a q1D sample, where skyrmions are confined in a line of pinning sites and by repulsive barrier walls located at $y = 0$ and $y = L_y$, as shown in Fig. 11.1 (a). Then, we next consider a 2D sample with no barrier walls, but a weak line of pinning potentials embedded in a square lattice of stronge pinning potentials, as shown in Fig. 11.1 (b). The weak line of pinning centers is usually aligned with the external drive, along the x direction. However, we also consider a case where the weak

line is 45° respective to the drive. The skyrmion dynamics is governed by the equation of motion shown in Eq. (11.1).

$$\alpha_d \mathbf{v_i} + \alpha_m \hat{z} \times \mathbf{v_i} = \mathbf{F}_i^{SS} + \mathbf{F}_i^{W} + \mathbf{F}_i^{P} + \mathbf{F}^{D} \tag{11.1}$$

Figure 11.1 – Illustration of the samples used in this work. (a) The quasi-one-dimensional system, where skyrmions are confined in a line of weak pinning sites (red circles) and by repulsive barrier walls located at the edges of the sample in the *y* direction. (b) The 2D sample with a square array of pinning centers and no repulsive barriers. All pinning sitres are modelled using Gaussian pinning potentials. Red circles indicate stronger pinning potentials and blue circles indicate weak pinning. (From Vizarim *et. al.* [203], pg. 224409-3).

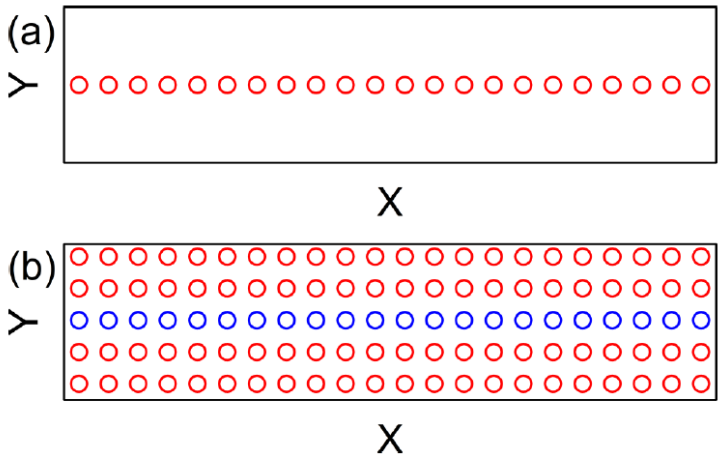

The first term on the right side is the skyrmion-skyrmion repulsion, the second term, $\mathbf{F}_i^{W}$, is the skyrmion-wall interaction. In the presence of wall barrier, the skyrmion behavior is similar to what is observed in quasi-1D potential well. We model the wall potential as $U_W = U_{W_0}\cos(\omega y)$, where $U_{W_0} = 12.0$ and $\omega = 2\pi/L_y$. The strength of the barrier wall was adjusted so that skyrmions cannot surpass the barrier even for high applied currents. The force exerted by the wall is then $\mathbf{F}_i^{W} = -\nabla U_W = -F_W \sin(\omega y)$, where $F_W = 2\pi U_{W_0}/L_y$. The applied drive is $\mathbf{F}^{D} = F^{D}\hat{\mathbf{x}}$, where F^{D} is the drive strength. F^{D} is increased in small steps of $\delta F^{D} = 0.01$ and spend 2×10^5 time steps at each drive increment to ensure steady state. We measure the skyrmion average velocities $\langle V_x \rangle = \langle \mathbf{v} \cdot \hat{\mathbf{x}} \rangle$ and $\langle V_y \rangle = \langle \mathbf{v} \cdot \hat{\mathbf{y}} \rangle$ and all distances are normalized by the screening length, ξ.

11.3 Results

11.3.1 The Quasi-one-dimensional system

We first consider the case of a quasi-one-dimensional (q1D) system as illustrated in Fig. 11.1 (a), where skyrmions interact with a line of attractive pinning centers and repulsive barrier walls. We add 23 skyrmions to interact with the present 22 pinning sites, resulting in a filling factor of $N_{sk}/N_p = 1.044$, which is just above the commensuration ratio. Fort this system we consider $L_x = 36\xi$ and $L_y = 6.546\xi$. The pinning density is set as $n_p = 0.093/\xi^2$. In Fig. 11.2 it is plotted the velocity curves, $\langle V_x \rangle$ and $\langle V_y \rangle$ as a function of the applied drive, F^D, for a system with $\alpha_m/\alpha_d = 0.5$. Just above the depinning at $F^D = 0.02$, there is a low velocity regime in which $\langle V_y \rangle$ is noisy and $\langle V_x \rangle$ increases slowly and monotonically with the applied drive. The behavior of $\langle V_x \rangle$ is highlighted in the inset of Fig. 11.2 (a). The motion is confined in the x direction due to the repulsive barrier walls placed in $y = 0$ and $y = L_y$ constricting the skyrmion motion. Over the range $0.02 < F^D < 0.43$, a soliton pulse is translating along the skyrmion chain. As the applied drive push skyrmions to move, the initial interstitial skyrmion shown in 11.3 (a), displaces its neighboring skyrmion from the pinning site. The previous neighboring skyrmion becomes the new interstitial skyrmion and the previous interstitial skyrmion is now pinned. The result is a propagation of the location of the interstial skyrmion along the chain in the $+x$ direction, as illustrated in Fig. 11.3 (b).

Figure 11.1 – The skyrmion average velocities (a) $\langle V_x \rangle$ and (b) $\langle V_y \rangle$ as a function of the applied drive, F^D, for the samnple illustrated in Fig. 11.1 (a) with $N_{sk}/N_p = 1.044$, $\alpha_m/\alpha_d = 0.5$ and $n_p = 0.093/\xi^2$. The inset shows a blowup of panel (a) over the range $0 < F^D < 0.5$. (From Vizarim *et. al.* [207], pg. 224409-3).

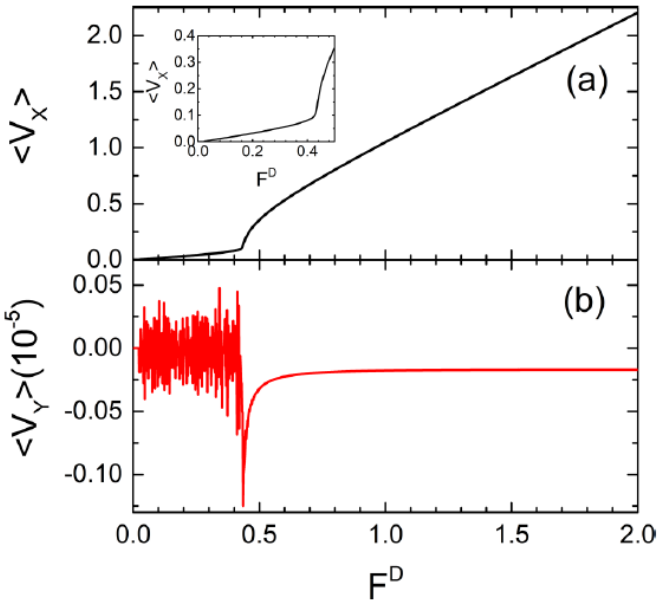

Figure 11.3 – In [(a), (b), (c)] the representation of the pinning site positions (red circles) and the skyrmion trajectories (black lines) for a sample with $N_{sk}/N_p = 1.044$, $\alpha_m/\alpha_d = 0.5$, $C_p = 0.15$ and $n_p = 0.093/\xi^2$. (a) At $F^D = 0.01$, the skyrmions are static in the pinned phase. The interstitial skyrmion is present due to the incommensuration between the skyrmion and the pinning site number. (b) For $F^D = 0.3$, the interstitial skyrmion moves as a soliton by hopping from site to sitewith slow average velocity. (c) At $F^D = 1.0$ all skyrmions flow simultaneously at higher velocities. [(d) and (e)] Skyrmion positions as a function of time. (d) For $F^D = 0.3$, as shown in panel (b), the soliton pulse propagates through the sample. (e) For $F^D = 1.0$, all skyrmions flow through the sample, as shown in panel (c). (From Vizarim *et. al.* [207], pg. 224409-4).

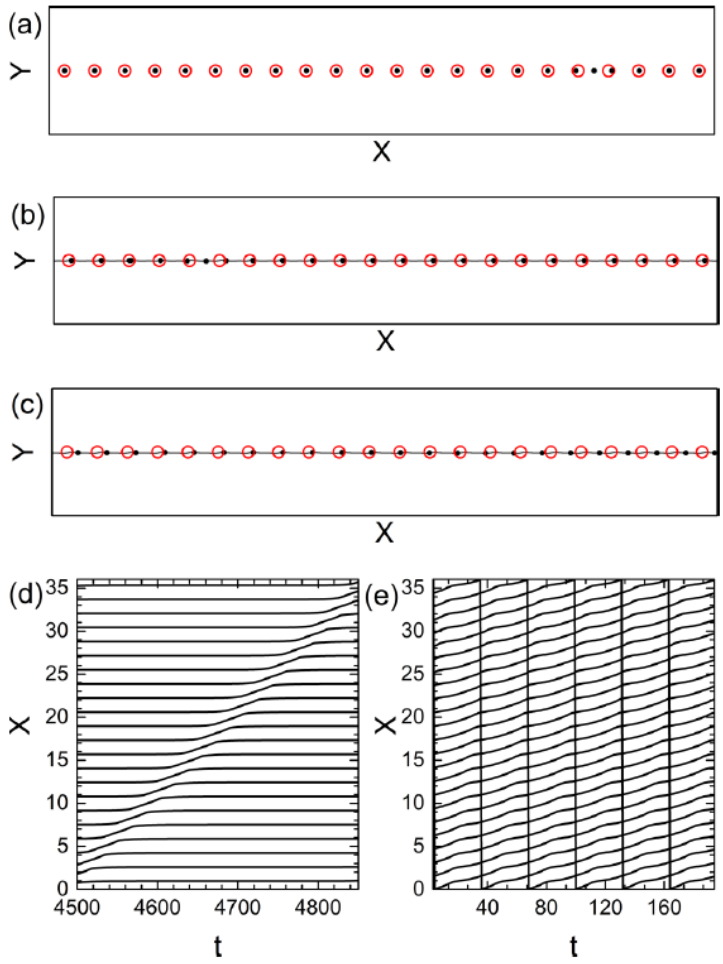

For $F^D > 0.43$, as skyrmions depin from their pinning sites and flow through the sample in unison, producing a spike in the velocity-force curve as shown in Fig. 11.2 (a). Due to the orderliness of the skyrmion motion, the y componente of the velocity vanishes. As the soliton is not associated with a single continuously moving particle, it does not have the same equation of motion as skyrmions, and in particular it does not exhibit the skyrmion Hall angle effect associated with a continuously moving skyrmion. Since the soliton can be pinned or put into motion, the soliton itself could be employed as an information carrier, but with the absence of a skyrmion Hall effect. Moreover, it would be interesting technologically, since the soliton motion

occurs for even lower applied transport currents, resulting in a very low energy cost type of information transport.

The differences in Fig. 11.3 (b) and (c) may be difficult to see just looking at the trajectories. Thus, in Fig. 11.3 (d) and (e) it is plotted the position of each skyrmion in x as a function of time. In Fig. 11.3 (d), the system from Fig. 11.3 (b), contains a clearly propagating soliton pulse in the $+x$ direction. In contrast, Fig. 11.3 (e) shows the system from Fig. 11.3 (c) at $F^D = 1.0$, where all skyrmion are moving coherently as a crystal and the soliton motion is absent.

Figure 11.4 – The skyrmion average velocities (a) $\langle V_x \rangle$ and (b) $\langle V_y \rangle$ as a function of the applied drive, F^D, for the sample illustrated in Fig. 11.1 (a) with $N_{sk}/N_p = 0.96$, $\alpha_m/\alpha_d = 0.5$ and $n_p = 0.093/\xi^2$. The inset shows a blowup of panel (a) over the range $0.35 < F^D < 0.6$. (From Vizarim *et. al.* [207], pg. 224409-4).

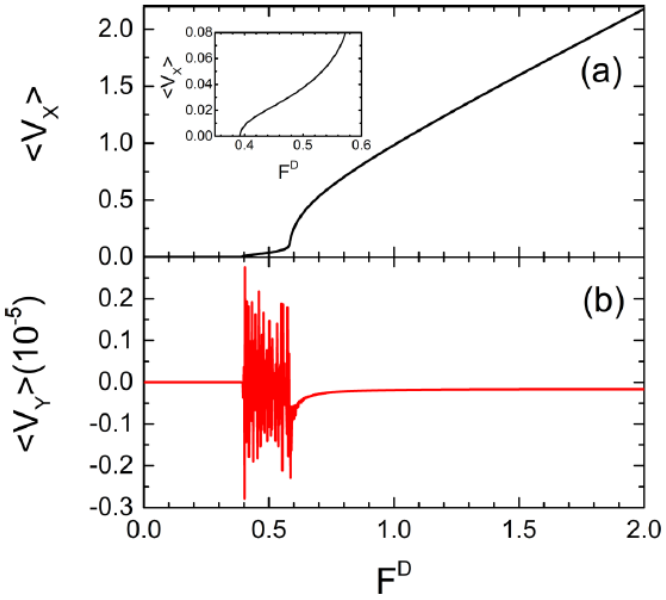

In Fig. 11.4 it is plotted the skyrmion average velocities, $\langle V_x \rangle$ and $\langle V_y \rangle$ as a function of the applied drive, F^D, for a system with $N_{sk}/N_p = 0.96$ and $\alpha_m/\alpha_d = 0.5$. Note that in this case, we have less skyrmions than pinning sites. The depinning threshold is $F^D = 0.39$ [See Fig. 11.4 (a)], which is higher than in the previous case since less skyrmions are stabilized in the sample. Just above the depinning, shown in Fig. 11.4 (a), it is also possible to observe a low velocity regime, very similar to the previous case. However, the dynamics here is very different. As shown in Fig. 11.5 (a), there is a vacancy due to the incommensurate ration between the skyrmion and the pinning site number. Here, the vacancy forms a soliton that can be viewed as a suppression of the local skyrmion density. The vacancy moves through the sample in the $-x$ direction as the neighboring pinned skyrmion depins and move to the previously vacant pinning

center, leaving its previous spot vacant. A repetition of this process occurs for the interval $0.39 < F^D < 0.58$, where $\langle V_y \rangle$ is noisy and $\langle V_x \rangle$ increases smoothly and monotonically with the increasing drive. This can be clearly seen in the inset of Fig. 11.4 (a). Experimentally, the soliton can be detected in the same way as skyrmions, by looking for variations in the skyrmion spacing. For $F^D > 0.58$, all skyrmions depin and flow coherently, where $\langle V_x \rangle$ increases and $\langle V_y \rangle = 0$. The plot of the skyrmion positions as a function of time can be seen in Fig. 11.5 (b) and (c), with $F^D = 0.45$ and $F^D = 1.0$, respectively. In Fig. 11.5 (b) it is clear the soliton pulse in the positions as a function of time, but note that in this case, the motion is along the $-x$ direction.

Figure 11.5 – In (a) the representation of the pinning site positions (red circles) and the skyrmion trajectories (black lines) for a sample with $N_{sk}/N_p = 0.96$, $\alpha_m/\alpha_d = 0.5$, $C_p = 0.15$ and $n_p = 0.093/\xi^2$. (a) At $F^D = 0.3$, the skyrmions are static in the pinned phase. The vacant pinning site is present due to the incommensuration between the skyrmion and the pinning site number. [(b) and (c)] Skyrmion positions as a function of time. (b) For $F^D = 0.45$ the soliton pulse propagates through the sample along $-x$ direction. (c) For $F^D = 1.0$, all skyrmions are flowing as a moving crystal. (From Vizarim *et. al*. [207], pg. 224409-5).

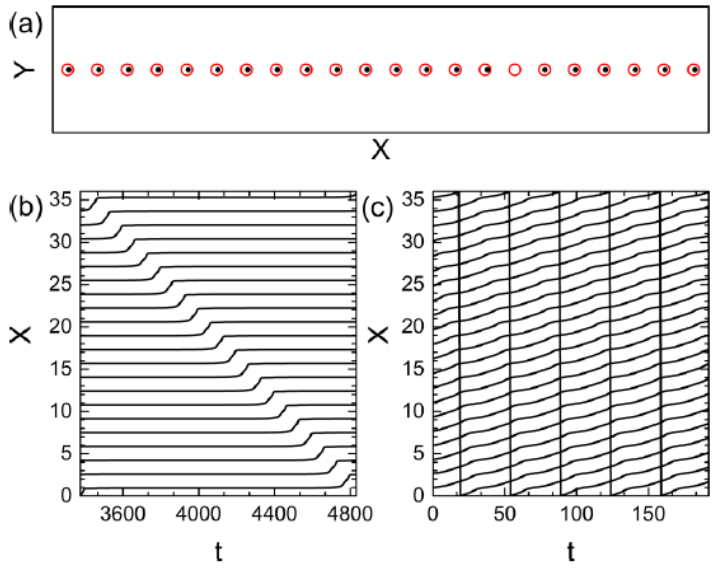

11.3.2 The 2D system

Now we consider a 2D system without the constraint of repulsive barrier walls, $F^W = 0$, and adding multiple rows of strong pinning sites next to the central row of pinning sites, forming a square array of pinning sites as shown in Fig. 11.1 (b). In this system we use 110 pinning sites, most of them interacting strongly with skyrmions with $C_p = 1.0$. The central line of pinning centers, that serves as a guide for the skyrmion motion, is weaker with $C_p = 0.15$. The pinning density we use is $n_p = 0.373/\xi^2$ and we set $L_x = 36\xi$ and $L_y = 8.2\xi$.

Figure 11.6 – The skyrmion average velocities (a) $\langle V_x \rangle$ and (b) $\langle V_y \rangle$ as a function of the applied drive, F^D, for the 2D sample illustrated in Fig. 14.1 (b) with $N_{sk}/N_p = 1.01$, $\alpha_m/\alpha_d = 1.0$ and $n_p = 0.373/\xi^2$. The inset shows a blowup of panel (a) over the range $0.1 < F^D < 0.45$. (From Vizarim *et. al.* [207], pg. 224409-5).

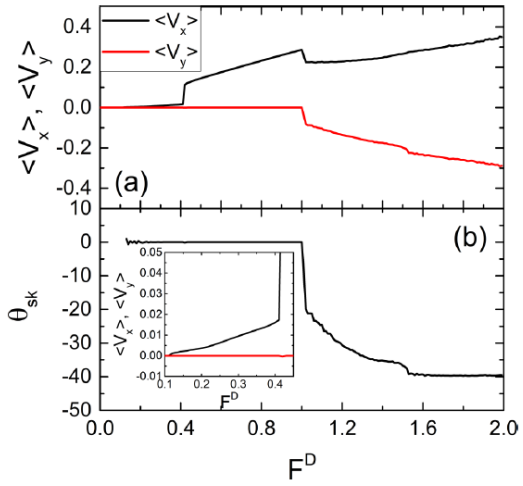

Figure 11.7 – In (a) the representation of the pinning site positions (red circles) and the skyrmion trajectories (black lines) for a sample with $N_{sk}/N_p = 1.01$, $\alpha_m/\alpha_d = 1.0$, weak pins $C_p = 0.15$, strong pins $C_p = 1.0$ and $n_p = 0.373/\xi^2$. (a) At $F^D = 0.0$, the ground state, where most skyrmions are pinned and there is one interstitial skyrmion. (b) The soliton phase at $F^D = 0.25$. (c) For $F^D = 0.5$ all skyrmions in the weak line of pinning sites depin and flow along the $+x$ direction due to the confinement of the pinned skyrmions in the strong pins. (d) For $F^D = 1.8$, all skyrmions are depinned and the resulting skyrmion Hall angle is $\theta_{sk} \approx -40°$. [(e) and (f)] The x position of skyrmions as a function of time. (e) For $F^D = 0.25$, as shown in panel (b), the soliton pulse propagates through the sample. (e) For $F^D = 0.5$, skyrmions flowing in a chain, as shown in panel (c). (From Vizarim *et. al.* [207], pg. 224409-6).

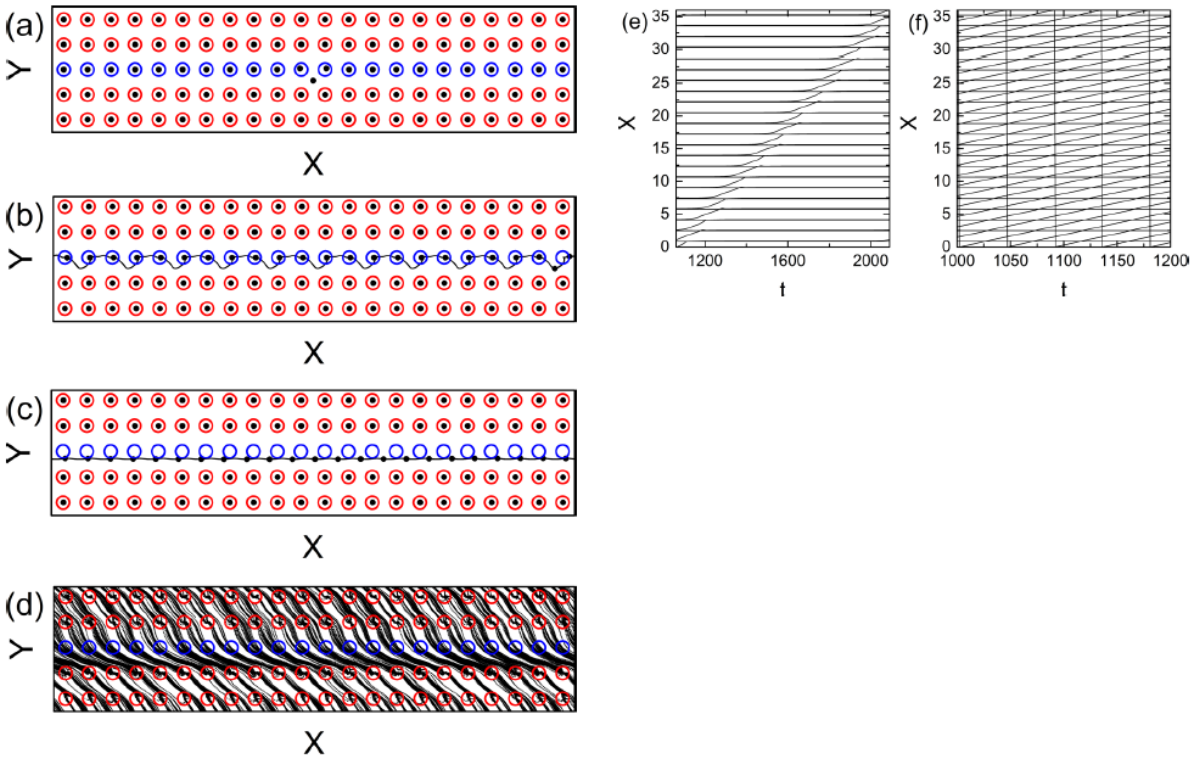

In Fig. 11.6 (a) it is plotted $\langle V_x \rangle$ and $\langle V_y \rangle$ as a function of the drive F^D for a system containing $N_{sk} = 111$ and $N_p = 110$, so that $N_{sk}/N_p = 1.01$, and $\alpha_m/\alpha_d = 1.0$, while in Fig. 11.6 (b) we show the skyrmion Hall angle, θ_{sk}, as a function of F^D. As can be seen in Fig. 11.6 (b), the dynamics is no longer locked in the x direction since there are no repulsive barrier walls in this case. For $F^D \leq 0.11$ the system is in the pinned phase, as can be seen in Fig. 11.7 (a). There is an interstitial skyrmion stabilized between four pinning centers, two of shich are strong and two are weak. The skyrmions pinned in the weak pinning sites exhibits greater displacement that skyrmion trapped in the stronger pinning sites due to the presence of the neighboring interstitial skyrmion. For $0.11 < F^D < 0.41$, there is a soliton phase very similar to the soliton phase saw in the q1D system. The interstitial skyrmion displaces a skyrmion form the weak pinning site, taking its place. Meanwhile, the previous pinned skyrmions becomes the new interstitial skyrmion. This process propagates through the chain as a soliton pulse along the $+x$ direction. The trajectories for the skyrmion motion can be seen in Fig. 11.7 (b), where oscillations in the y direction are present due to a combination of the skyrmion Hall angle effect and the swapping of interstitial and pinned skyrmions. For the interval $0.41 < F^D < 1.0$, all skyrmions previously trapped in the weak line of pinning sites depin and flow along the $+x$ direction, as can be seen in Fig. 11.7 (c). Note from Fig. 11.6 (b) that the skyrmion Hall angle is still zero due to the trapped skyrmions in the strong pinning sites serving as a barrier for the motion along y. For $F^D > 1.0$, skyrmions in the strong pinning sites also depin, destroying the quasi-1D motion and creating a 2D motion. This motion occurs in two steps as can be seen in Fig. 11.6. In the chaotic phase, from $1.0 < F^D < 1.53$, the skyrmion Hall angle increases irregularly in magnitude with increasing drive, while for $F^D > 1.53$, the skyrmion Hall angle stabilizes around $\theta_{sk} \approx -40°$. If the applied drive was increased further, we expect the skyrmion Hall angle to reach its intrinsic value of $\theta_{sk}^{int} = \arctan(\alpha_m/\alpha_d) = -45°$. The transition from q1D to 2D motion is also characterized by an increase in $\langle V_y \rangle$ and a decrease in $\langle V_x \rangle$. The average skyrmion motion is slower in the 2D motion since the skyrmions must travel through the region of strong pinning sites, which hinders the motion and reduces the velocity. In Fig. 11.7 (d) it is plotted the skyrmion trajectories for $F^D = 1.8$, where the skyrmion Hall angle is stabilized. As in the q1D system, the soliton pulse can be clearly seen in a plot of the skyrmion trajectories as a function of time. In Fig. 11.7 (e) it is shown the x position of skyrmions as a function of time for $F^D = 0.25$, where a soliton pulse propagates along the $+x$ direction. On the other hand, as shown in Fig. 11.7 (f) for $F^D = 0.5$, all skyrmions in the weak pinning sites depin and flow through the sample, destroying the soliton pulse.

Figure 11.8 – The skyrmion average velocities (a) $\langle V_x \rangle$ and (b) $\langle V_y \rangle$ as a function of the applied drive, F^D, for the 2D sample illustrated in Fig. 11.1 (b) with $N_{sk}/N_p = 0.99$, $\alpha_m/\alpha_d = 1.0$ and $n_p = 0.373/\xi^2$. The inset shows a blowup of panel (a) over the range $0.2 < F^D < 0.45$. (From Vizarim *et. al.* [207], pg. 224409-6).

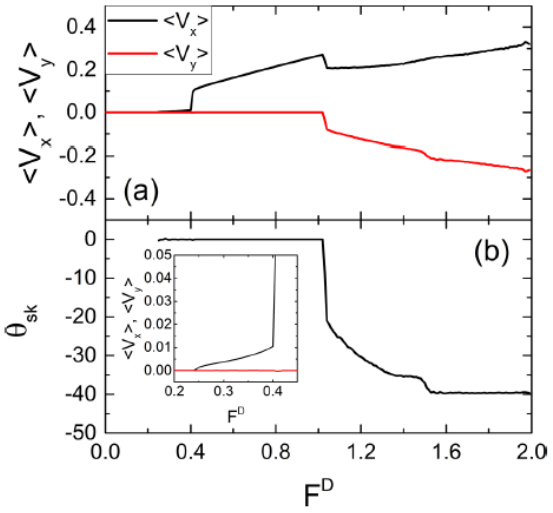

Figure 11.9 – In (a) the representation of the pinning site positions (red circles) and the skyrmion trajectories (black lines) for a sample with $N_{sk}/N_p = 0.99$, $\alpha_m/\alpha_d = 1.0$, weak pins $C_p = 0.15$, strong pins $C_p = 1.0$ and $n_p = 0.373/\xi^2$. (a) At $F^D = 0.0$, the ground state, where most skyrmions are pinned and a single vacancy is present. (b) The soliton phase at $F^D = 0.3$. (c) For $F^D = 0.5$ all skyrmions in the weak line of pinning sites depin and flow along the $+x$ direction. (d) For $F^D = 1.6$, all skyrmions are depinned and the resulting skyrmion Hall angle is $\theta_{sk} \approx -40°$. [(e) and (f)] The x position of skyrmions as a function of time. (e) For $F^D = 0.3$, as shown in panel (b), the soliton pulse propagates through the sample. (e) For $F^D = 0.5$, skyrmions flowing in a chain, as shown in panel (c). (From Vizarim *et. al.* [207], pg. 224409-7).

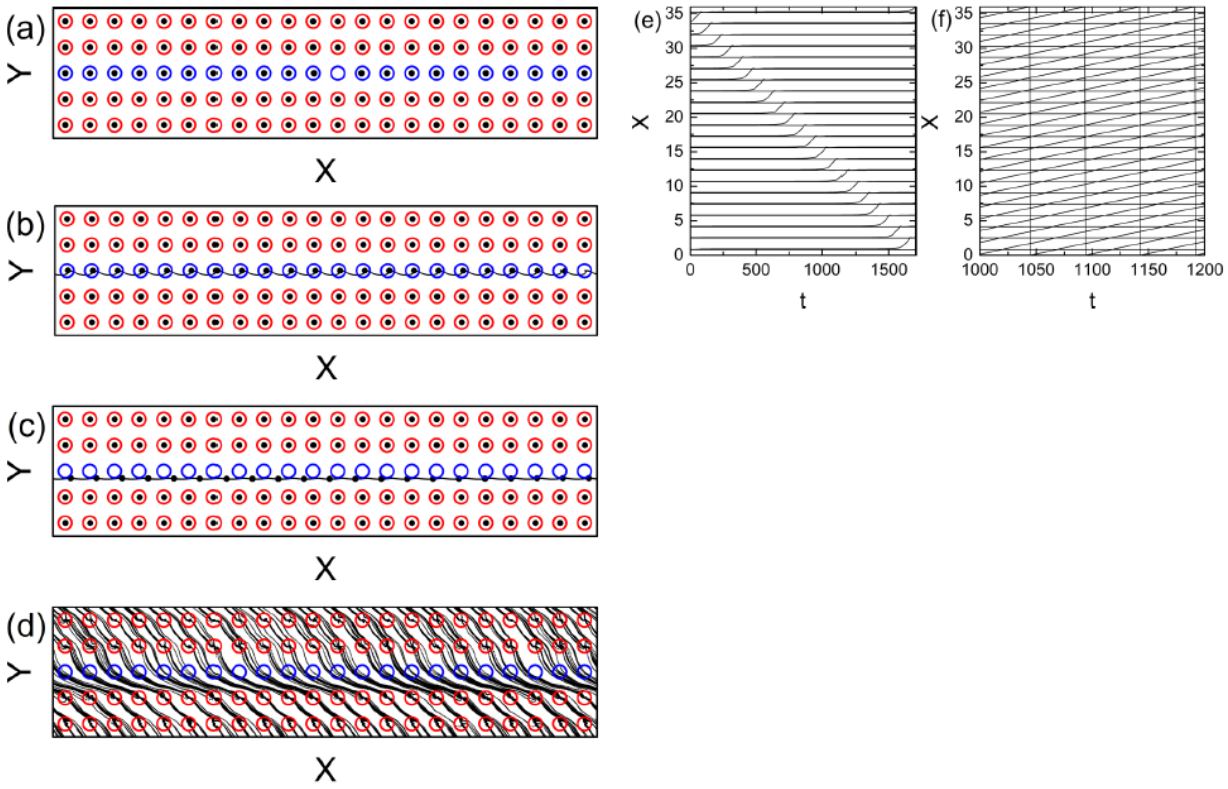

In Fig. 11.8 (a) it is plotted the skyrmion average velocities $\langle V_x \rangle$ and $\langle V_y \rangle$ as a function of the drive F^D for a system containing $N_{sk} = 109$ and $N_p = 110$, so that $N_{sk}/N_p = 0.99$, and $\alpha_m/\alpha_d = 1.0$, while in Fig. 11.8 (b) it is plotted the skyrmion Hall angle, θ_{sk}, as a function of F^D. For $F^D \leq 0.24$, the skyrmions are stabilized in the static phase as shown in Fig. 11.9 (a). In this case, there is vacant pinning center due to the incommensuration between the skyrmion and the pinning number. This incommensuration leads to a distortion in the skyrmion lattice, as can be seen in Fig. 11.9 (a). For $0.24 < F^D < 0.4$, the system enters in a soliton phase similar to what is shown in Fig. 11.4 and Fig. 11.5 (b) for the q1D case. The vacancy translates along the $-x$ direction due to the hopping of skyrmions along the $+x$ direction. The skyrmion trajectories for this regime can be seen in Fig. 11.9 (b). For $0.4 < F^D < 1.02$, the skyrmions in the strong pinning centers also depin. Similar to previous case of Fig. 11.6, in Fig. 11.8 there are also two dynamic regimes for $F^D > 1.02$:, one chaotic regime where the skyrmion Hall angle is varying continuously for $1.02 < F^D < 1.53$, and a regime where the skyrmion Hall angle is stabilized around $\theta_{sk} \approx -40°$ for $F^D > 1.53$. It is expected that the dynamics in both systems for high drives are similar, since the difference in the skyrmion density is very low and this difference becomes unimportant in the drive-dominant regime. However, the main differences can be seen in the soliton phase regime. To illustrate this difference, in Fig. 11.9 (e) we plot the skyrmion x positions as a function of time at $F^D = 0.3$, where the soliton pulse is clearly visible. For $F^D = 0.5$, the soliton motion is lost as shown in Fig. 11.9 (f).

The soliton phases for the interstitial or vacancy case are very similar in their dynamics, but exhibit a crucial difference in the soliton motion, since in the interstitial case the soliton moves along $+x$ direction and in the vacancy case it moves along the $-x$ direction. This controlled soliton motion could be exploited in devices with low energy cost and precise motion.

11.3.3 Soliton stabilization as a function of α_m/α_d

In this section we investigate how stable is the soliton phase varying the α_m/α_d parameter. When α_m/α_d increases, the skyrmion Hall angle also increases, so it is important to verify how stable is the soliton motion under these circunstances. Two samples are prepared with fixed values of $N_{sk}/N_p = 1.01$ and $N_{sk}/N_p = 0.99$, both using $n_p = 0.373/\xi^2$, and we perfom simulations for a range of values of α_m/α_d. Combining the resulted data, we plotted the dynamic phase diagram of F^D vs. α_m/α_d illustrated in Fig. 11.10, where the locations of the pinned phase, soliton phase, 1D motion and 2D motion are identified. The pinned phase is the

phase where all skyrmions are static so that $\langle V_x \rangle = \langle V_y \rangle = 0$. In the soliton phase, the localized lattice deformation propagates through the sample. The soliton can propagate along $+x$ or $-x$ depending on the type of soliton. The 1D motion is represented by the motion of all skyrmions trapped in the weak pinning sites moving along the $+x$ direction. The 2D motion is when all skyrmions in the sample are depinned and flowing through the sample with finite skyrmion Hall angle.

Figure 11.10 –Dynamic phase diagrams as a function of external dc drive F^D vs. α_m/α_d for the system in Fig. 11.1 (b) at $n_p = 0.373/\xi^2$ and (a) $N_{sk}/N_p = 1.01$ and (b) $N_{sk}/N_p = 0.99$. Pinned phase: Gray; soliton phase: Yellow; 1D motion: Red; 2D motion: Blue. (From Vizarim *et. al*. [207], pg. 224409-7).

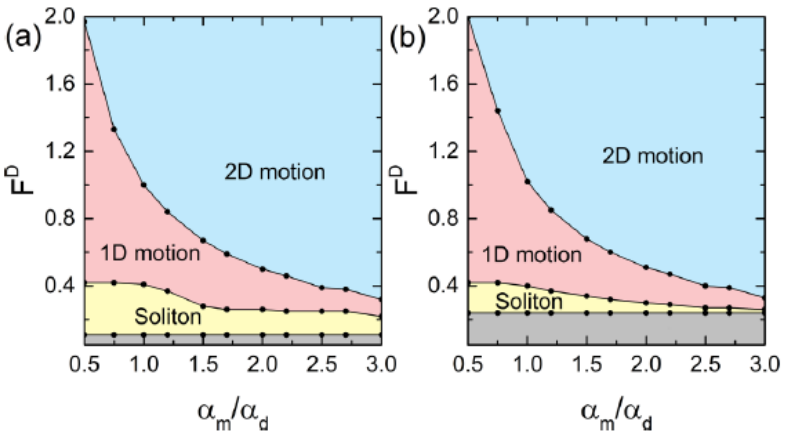

For the case of $N_{sk}/N_p = 1.01$, Fig. 11.10 (a) indicates that the depinning threshold is very low, resulting in a wider range of soliton motion when compared to Fig. 11.10 (b), with $N_{sk}/N_p = 0.99$. Interstitial skyrmions are more mobile than vacancies since the interstitial skyrmion is trapped only by the caged potential of the neighboring skyrmions and not directly by a pinning site. As a result, the depinning threshold lowers for these systems with interstitial skyrmions. Both systems exhibit the transition from the soliton phase to the 1D motion at roughly the same values of F^D, since these values of force are controlled by the strength of the weak pinning potentials. Analogously, the transition from 1D to 2D motion occurs for roughly the same values of F^D, but in this case the force values are controlled by the strength of the strong pinning potentials.

11.3.4 The pinning density effect

We next vary the pinning density, n_p, for samples with $N_{sk}/N_p = 1.01$ and $N_{sk}/N_p = 0.99$ while fixing $\alpha_m/\alpha_d = 0.5$. The pinning density is an important parameter since we expect that for low pinning density values the spacing between pinning sites increases, allowing skyrmions to flow between the pinning sites, destroying the soliton phase. In Fig. 11.11 (a) and

Fig. 11.11 (b) it is plotted the dynamic phase diagrams of F^D versus n_p for both systems. Here we observe the pinned phase, the soliton phase, 1D motion, 2D motion and an additional state that we term single skyrmion 1D motion (SK1D). In the SK1D phase, the interstitial skyrmion produced by the incommensuration between the number of skyrmions and pinning centers flows between the pinning centers without displacing any other pinned skyrmions. This behavior occurs only for low pinning densities of $n_p < 0.206$, when the gaps between pinning sites are sufficiently large, as shown in Fig. 11.11 (c). The SK1D phase is very similar to what has been previously illustrated in sections 5 and 10, where the motion of a single skyrmion interacting with an array of obstacles was investigated. As the pinning density increases, the SK1D phase vanishes and is replaced by the soliton motion. When the gap between pinning sites reduces, for increased values of n_p, it forbidden the skyrmions to flow between pinning sites, forcing the interstitial skyrmion to displace a previously pinned skyrmion, in a soliton-like fashion.

Figure 11.11 – [(a), (b)] Dynamic phase diagrams as a function of external dc drive F^D vs. n_p for the system in Fig. 11.1 (b) with $\alpha_m/\alpha_d = 0.5$ and (a) $N_{sk}/N_p = 1.01$ and (b) $N_{sk}/N_p = 0.99$. Pinned phase: Gray; soliton phase: Yellow; 1D motion: Red; 2D motion: Blue; single skyrmion 1D motion (SK1D): Green. (c) Pinning site positions (red circles: strong pins; blue circles: weak pins) and skyrmion trajectories (black lines) for $N_{sk}/N_p = 1.01$ sample at $F^D = 0.2$ and $n_p = 0.093\xi^2$ (From Vizarim *et. al.* [207], pg. 224409-8).

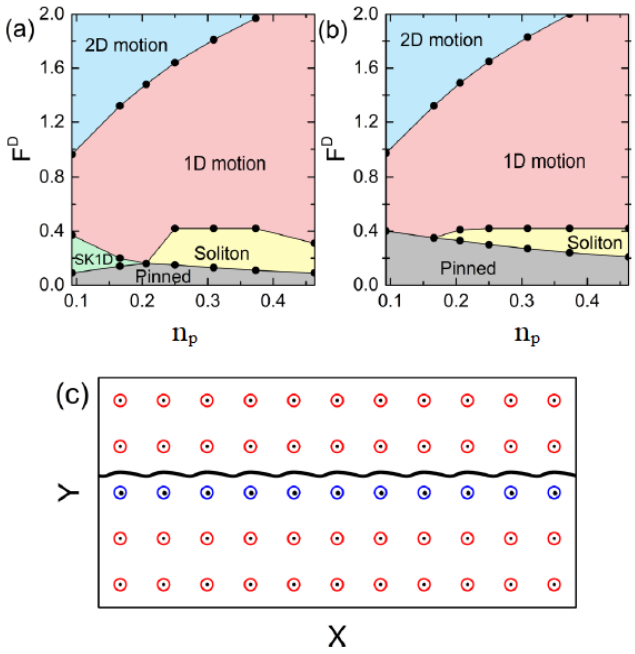

For the sample where the vacancy is present, $N_{sk}/N_p = 0.99$, there is a monotonic decrease of the depinning threshold as the pinning density increases, as shown in Fig. 11.11 (b). As n_p increases, the relative strength of the skyrmion-skyrmion interaction increases when compared to the skyrmion-pinning interactions, resulting in a suppression of the depinning threshold. Note that the soliton motion is completely lost for $n_p < 0.166$ due to the greater

distances between skyrmions and suppression of the collective behavior necessary for the soliton phase to exist. On the other hand, for $n_p > 0.166$, the extent of the soliton phase increases with n_p, primarily due to the decrease of the depinning threshold.

11.3.5 Guidance of Soliton Motion

In previous sections we have shown that the soliton motion through skyrmion chains can be enhanced depending on the choice of α_m/α_d and pinning density. The next fundamental question is: Can we guide the soliton motion along a specific direction? When we introduce a line of weak pinning potentials in the sample aligned with the applied drive, the soliton followed this line along $+x$ or $-x$ direction depending on the value of N_{sk}/N_p, even though this direction is not aligned with the intrinsic skyrmion Hall angle direction. That is, guiding the soliton motion to overcome the skyrmion Hall angle effect by using a line of weak pinning sites is possible. To further explore this effect, we change the pinning lattice so that the skyrmion Hall angle is perpendicular to the weak line of pinning potentials. As shown in Fig. 11.12, the weak line of pinning sites is placed along $\theta_p = +45°$ with respect to the driving direction along $+x$. Using $\alpha_m/\alpha_d = 1.0$, the intrinsic Hall angle is $\theta_{sk}^{int} = -45°$, so that, $\Delta\theta = \theta_p - \theta_{sk}^{int} = 90°$. For this section we use $L_x = L_y = 19.638\xi$.

Figure 11.12 – Pinning site positions (red circles: strong pins; blue circles: weak pins) for a sample with a diagonal line of weak pinning sites oriented at $+45°$ respective to the x direction. The weak pins have $C_p = 0.15$, strong pins $C_p = 1.0$ and we set $n_p = 0.373/\xi^2$. (From Vizarim *et. al.* [207], pg. 224409-8).

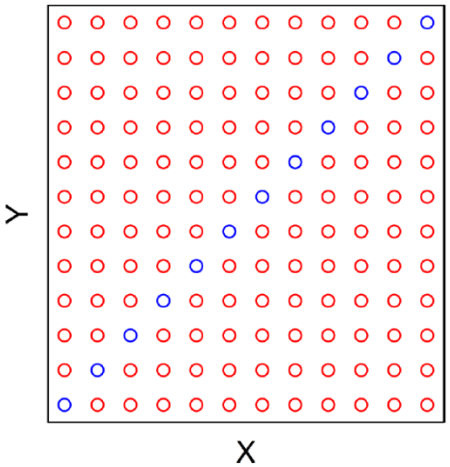

For a sample of $N_{sk}/N_p = 1.01$ it is plotted the skyrmion average velocities $\langle V_x \rangle$ and $\langle V_y \rangle$ versus F^D in Fig. 11.13 (a) and the corresponding skyrmion Hall angle, θ_{sk} versus F^D in Fig. 11.13 (b). When $F^D < 0.12$, skyrmions are in the pinned phase, marked by letter P in Fig. 11.13 (a). As the applied drive increases, we observe a small and continuous increase in both

velocity components, so that $\langle V_x \rangle = \langle V_y \rangle$. This means that the motion is locked at exactly $\theta_{sk} = +45°$ with respect to the driving direction, following the weak line of pinning potentials. The illustration of this motion can be seen in Fig. 11.14 (a). For $0.44 < F^D < 0.56$ the skyrmion velocity components remain equal and constant as the drive increases. In this regime, all skyrmions from the weak line of pinning potentials depin and flow following the weak line of pins, locked at $\theta_{sk} = +45°$, as shown in Fig. 11.14 (b). For $0.56 < F^D < 1.47$ there is a broad transient phase in which the skyrmion Hall angle is continuously changing from $\theta_{sk} = +45°$ to $\theta_{sk} = -45°$. Here, skyrmions in the strong pinning sites remain trapped, but skyrmions free from the weak pinning sites begin to escape from the weak pinning channel and instead start flowing in the region of strong pinning potentials. In Fig. 11.14 (c) there is an illustration of this regime, where skyrmions are flowing with $\theta_{sk} \approx -35°$ with $F^D = 1.0$. This motion is unstable, and θ_{sk} continue to increase as F^D increases. The collective motion of skyrmions only stabilizes for $F^D > 1.46$, where skyrmions flow in orderly fashion along $\theta_{sk} = -45°$, as shown in Fig. 11.14 (d). Here, some skyrmions that were previously pinned in the strong pinning sites depin to stabilize the flow. The depinning of the remained skyrmions occur only for higher drives not considered here. We expect that other Hall angle reversal may occur for different directions of weak line of pinning potentials or for different values of α_m/α_d.

11.3.6 Discussions and Summary

In this section, we showed that just outside commensurate states, skyrmions may exhibit a soliton phase for low drives that is of interstitial or vacancy type. We model the skyrmions as point-like rigid bodies that cannot deform or change size; however, in real materials, skyrmions may deform, change size, merge, or be annihilated. These features could be very interesting to explore further using continuum-based simulations. Thermal fluctuations were neglected here, but it could also modify the behavior, such as by introducing thermal creep in the low drive regimes. We expect that the soliton phase would remain stable for a certain range of temperatures. If different pinning landscapes are considered, we expect the soliton phase to occur, but the preferential directions of motion would be changed. For the square lattice we consider here, soliton motion is stabilized along 0° or 45° as shown in our results. For other geometries, such as a triangular pinning lattice, the soliton motion would occur along 0°, 30°, and 60°.

Figure 11.13 – (a) The skyrmion average velocities $\langle V_x \rangle$ and $\langle V_y \rangle$ as a function of the applied drive, F^D, for the 2D sample illustrated in Fig. 11.12 (b). In (b) the corresponding skyrmion Hall angle curve. This system uses $N_{sk}/N_p = 1.01$, $\alpha_m/\alpha_d = 1.0$ and $n_p = 0.373/\xi^2$. P indicates the pinned phase, Soliton is the soliton phase, $+45$ is the phase where skyrmion depinned from the weak pinning sites move with $\theta_{sk} = +45°$ respective to the drive. Transient is the phase where the skyrmion Hall angle is reversing. -45 is the phase where skyrmions are locked at $\theta_{sk} = -45°$. (From Vizarim *et. al.* [203], pg. 224409-9).

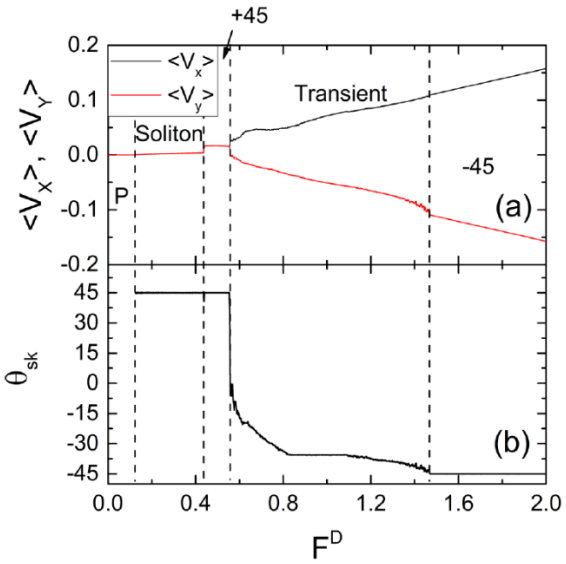

Figure 11.14 – Pinning site positions (red circles) and the skyrmion trajectories (black lines) for the sample of Fig. 11.13 with $N_{sk}/N_p = 1.01$, $\alpha_m/\alpha_d = 1.0$, weak pins $C_p = 0.15$, strong pins $C_p = 1.0$ and $n_p = 0.373/\xi^2$. (a) At $F^D = 0.25$ where the soliton flows following the weak line of pins, at $\theta_{sk} = +45°$. (b) At $F^D = 0.5$, the skyrmions trapped in the weak line of pins depin and flow along $\theta_{sk} = +45°$. (c) For $F^D = 1.0$ the transient phase, where θ_{sk} gradually reverses. In this case, $\theta_{sk} \approx -35°$. (d) For $F^D = 1.8$, the skyrmion Hall angle reversal is complete, the flow is locked at $\theta_{sk} = -45°$. (From Vizarim *et. al.* [203], pg. 224409-9).

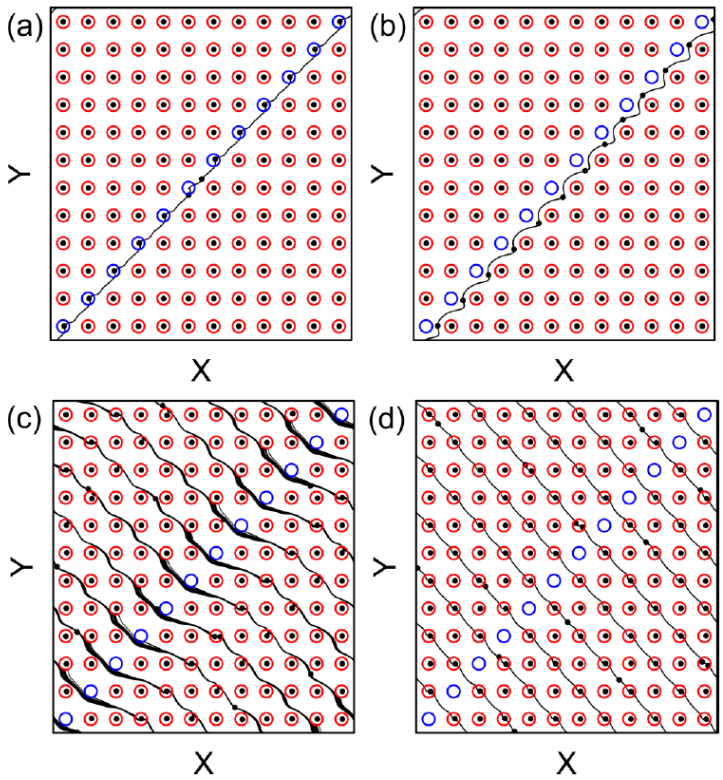

Part II

Skyrmions and Linear Defects

12 Skyrmion ratchet in funnel geometries

12.1 Skyrmion in funnel geometries

This work was developed by one of the students of our group, J. Bellezotti Souza, which is starting to study skyrmion dynamics under periodic and quasi-periodic substrates. Although J. Bellezotti is the main author, I have contributed to most part of the analysis and discussions in this work, and the results fit very well to the scope of this thesis. Using particle-model simulations, here the dynamical behavior of a single skyrmion under the influence of asymmetric funnel geometries and ac driving at zero temperature. Using the ratchet effect, the skyrmion motion can be controlled in the sample. Depending on the ac drive direction, the skyrmion can be moved in the easy or in the hard-axis. These results indicate that it is possible to achieve controlled skyrmion motion using funnel geometries, and possibly to perform data transfer operations. This work was published in Physical Review B [203].

12.2 Model and simulation details

The simulation consists of a single skyrmion in a two-dimensional box of dimensions $H \times L$ with periodic boundary conditions in the x direction, as illustrated in Fig. 12.1. The skyrmion interacts with an asymmetric funnel array aligned along the x direction, where N_F is the number of funnels, S is the length of each funnel, and O is the width of the funnel opening. The asymmetry in the funnel permits "easy" flow along the $+x$ direction and a "hard" flow along the $-x$ direction. The dynamical properties of the skyrmion system interacting with the funnel were simulated using the particle model for skyrmions, shown in Eq. (12.1), using Molecular Dynamics technique.

$$\alpha_d \mathbf{v_i} + \alpha_m \hat{z} \times \mathbf{v_i} = \mathbf{F}_i^W + \mathbf{F}^{ac} \tag{12.1}$$

The system has a size of $8\xi \times 20\xi$. The first term on the right side is the force exerted by the repulsive wall barrier, $\mathbf{F}_i^W$. The funnel is formed by two asymmetric sawtooth functions and the wall potential is given by a Gaussian form, $U(\mathbf{r}_{iw}) = U_0 e^{-(r_{iw}/a_0)^2}$, where $\mathbf{r}_{iw}$ is the shortest distance between the skyrmion and the barrier wall. U_0 is the potential strength and a_0 is the wall thickness. The resulting force is given by $\mathbf{F}_i^W = -\nabla U = -F_0 r_{iw} e^{-(r_{iw}/a_0)^2} \hat{\mathbf{r}}_i$, where $F_0 =$

$2U_0/a_o^2$. The last term is the ac drive, $\mathbf{F}_x^{ac} = A\sin(2\pi\omega_1 t)\,\hat{\boldsymbol{x}}$ for longitudinal driving and $\mathbf{F}_y^{ac} = B\cos(2\pi\omega_2 t)\,\hat{\boldsymbol{y}}$ for transversal driving. We measure the skyrmion velocity in the $\langle V_x\rangle = \langle \mathbf{v}\cdot\hat{\mathbf{x}}\rangle/(2\pi\omega_1 S)$, and the y component, $\langle V_y\rangle = \langle \mathbf{v}\cdot\hat{\mathbf{y}}\rangle/(2\pi\omega_1 S)$. The velocities are averaged over 100 ac drive cycles. Under the normalization used here, when $\langle V_\parallel\rangle = 1.0$ or $\langle V_\perp\rangle = 1.0$ indicates that the skyrmion is translating by one funnel length per ac drive cycle in the x direction, respectively. The external ac drive amplitude is increased in small steps of A $(B) = 0.005$ and wait 10^6 simulation time steps between increments to ensure steady state. We normalize the damping and Magnus coefficients as $\alpha_d^2 + \alpha_m^2 = 1$.

Figure 12.1 – Illustration of the funnel geometry used, where S is the length of each funnel and O is the width of the funnel opening. In this case $N_F = 4$ and $O = 1.0$, and the easy and hard-axis are labeled. (From Bellezotti Souza *et. al.* [203], pg. 2)

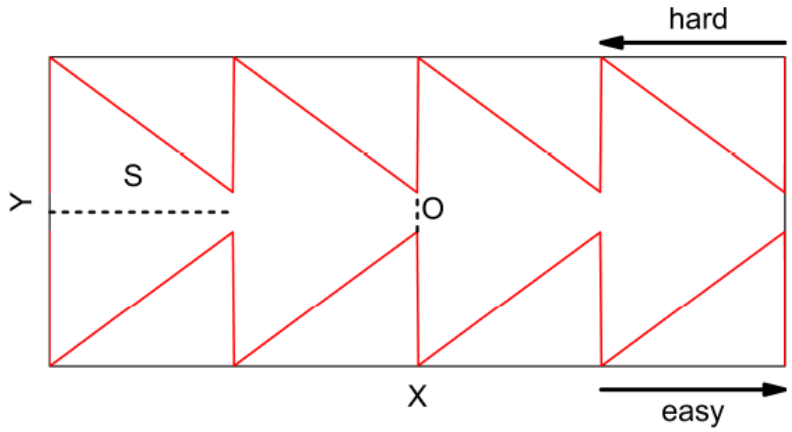

12.3 Results

12.3.1 Ac drive in the x or y direction

Initially we consider the case where the ac drive is applied along the x direction only, that is, $B = 0$ and $A \neq 0$. In Fig. 12.2 it is plotted $\langle V_x\rangle$ and $\langle V_y\rangle$ as a function of the ac drive amplitude A for a system with $\alpha_m/\alpha_d = 0.5$. The average velocity $\langle V_x\rangle$ exhibits a step-like behavior and also a monotonic increase with increasing A. As can be seen, the combination of the ac drive and the broken spatial symmetry of the funnel array generates a ratchet effect that results in a net dc motion of the skyrmion in the $+x$ direction. Although $\langle V_y\rangle$ is very close to zero, there are spikes of transversal motion at the edge of every step in $\langle V_x\rangle$.

Figure 12.2 – The average velocities (a) $\langle V_x \rangle$ and (b) $\langle V_y \rangle$ as a function of the ac drive amplitude A for the funnel system with $\alpha_m/\alpha_d = 0.5$, $N_F = 4$ and $O = 1.0$. The ac drive is applied only along the x direction. The inset in (a) shows a blowup of panel (a) for the range $0.92 < A < 1.05$ (From Bellizotti Souza *et. al.* [203], pg. 2).

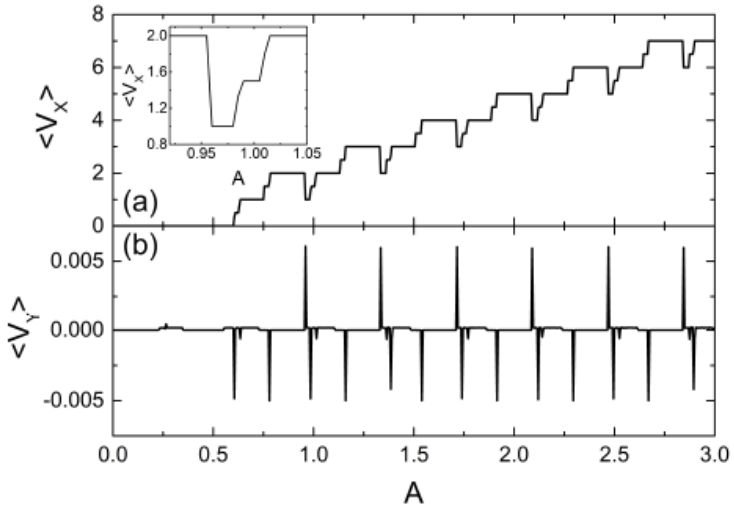

In Fig. 12.3 it is illustrated some representative skyrmion trajectories for the system of Fig. 12.2. At $A = 0.25$, Fig. 12.3 (a) shows that the ac drive amplitude is not large enough to produce a ratchet motion for the system, thus it forms a localized orbit inside one of the funnels. In Fig. 12.3 (b), at $A = 0.97$, the skyrmion performs a net dc motion along $+x$ direction in which the skyrmion translates by an average distance of $1.0S$ for every ac drive cycle, as can be seen in Fig. 12.2. The trajectory trace indicates that the skyrmion moves forward $2S$ during the positive ac drive cycle, and backwards $1S$ in the negative ac drive cycle. In Fig. 12.3 (c), at $A = 1.76$, the skyrmion translates an average distance of $3.5S$ for each ac drive cycle, while at $A = 2.4$ in Fig.12.3 (d), the skyrmion flows an average distance of $6S$, always in the $+x$ direction.

Now we consider the case where the ac drive is applied along the y direction, that is, $A = 0$ and $B \neq 0$. In Fig. 12.4 it is shown the results obtained from a system with $N_F = 4$, $O = 1.0$ and $\alpha_m/\alpha_d = 0.5$. For $B > 0.595$, a Magnus induces transverse ratchet occurs and the skyrmion flows along the $-x$ direction, as indicated in Fig. 12.4 (a). Interestingly, the motion has a steady average velocity of $\langle V_x \rangle = -1.0$ over a wide range of ac drive amplitudes, B. The stability in this motion can be of interest for technological applications since the translation speed remains constant for several values of B. In Fig. 12.4 (b) it is illustrated the skyrmion trajectory at $B = 0.5$, where the skyrmion remains trapped inside a single funnel. At $B = 1.0$, the ac drive amplitude is strong enough to produce the Magnus-induced transverse motion, and the skyrmion exhibits a dc net motion along the $-x$ direction.

Figure 12.3 – Funnel walls (red lines) and the skyrmion trajectory (black lines) for the system shown in Fig. 12.2. The blue arrows indicate the direction of the skyrmion motion. (a) $A = 0.25$ the skyrmion performs a localized orbit inside one funnel. (b) $A = 0.97$ the skyrmion translates along the $+x$ direction at a rate of $1S$ pr ac drive cycle. (c) $A = 1.76$ skyrmion translation along the $+x$ direction at a rate of $3.5S$ pr ac drive cycle. (d) $A = 2.4$ skyrmion translation along the $+x$ direction at a rate of $6S$ pr ac drive cycle. (From Bellizotti Souza *et. al.* [203], pg. 3).

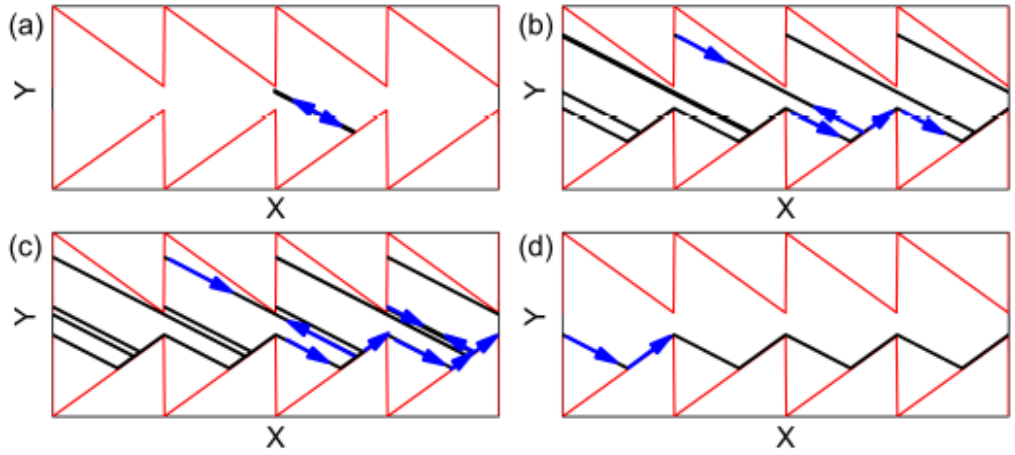

Figure 12.4 – (a) The average velocity $\langle V_x \rangle$ as a function of the ac drive amplitude B for the funnel system with $\alpha_m/\alpha_d = 0.5$, $N_F = 4$ and $O = 1.0$. The ac drive is applied only along the y direction. (b) and (c) Funnel walls (red lines) and the skyrmion trajectory (black lines) for the system shown in (a). The blue arrows indicate the direction of the skyrmion motion. (b) $A = 0.5$ the skyrmion performs a localized orbit inside one funnel. (c) $A = 1.0$ the skyrmion translates along the $-x$ direction at a rate of $1S$ per ac drive cycle. (From Bellizotti Souza *et. al.* [203], pg. 4).

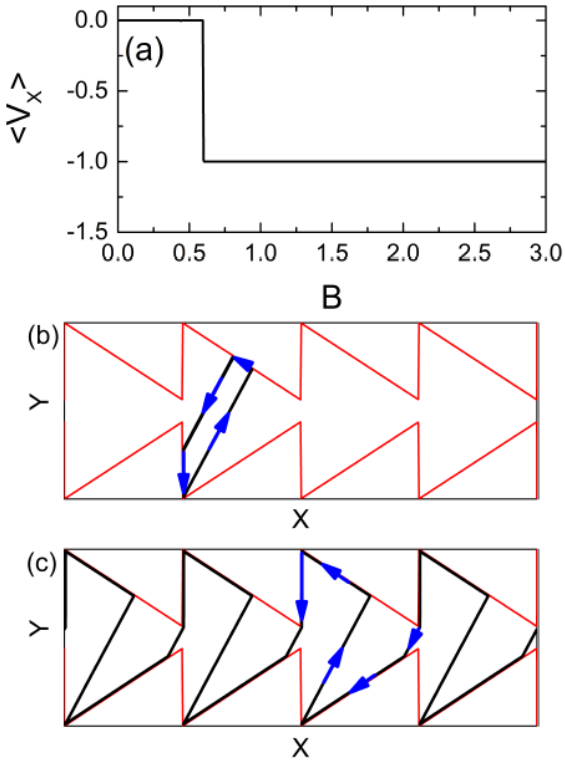

12.3.2 Guided motion using ac drives in funnel geometries

In the previous section it was shown that the skyrmion can be set into motion in the funnel array along the $+x$ or $-x$ direction according to the direction of the applied ac drive. That is, if the ac drive is applied parallel to the funnel axis, the skyrmion flows along the $+x$ direction, on the other hand, if the ac drive is applied perpendicular to the funnel axis, the skyrmion flows along the $-x$ direction. Now, it is considered a situation where a skyrmion must be guided from an initial funnel to another funnel and must return to its original position using only ac driving. This process is very relevant to spintronics devices in which a skyrmion acting as an information carrier is guided through the sample in order to transmit information. In Fig. 12.5 (a) it is illustrated the sample in which the skyrmion will move from the left funnel, labeled L, to the right funnel, labeled R and back again. In Fig. 12.6 (a) it is plotted the applied ac drive signals F_x^{AC} and F_y^{AC} used to produce this motion as a function of time, and in Fig. 12.6 (b) it is shown the corresponding instantaneous skyrmion velocities V_x and V_y.

Figure 12.5 – Funnel walls (red lines) and the skyrmion trajectory (black lines) for the system where the skyrmion starts in funnel L and must travel to R and return back to L. The blue arrows indicate the direction of the skyrmion motion. (a) skyrmion starting position in funnel L for $t = 0$. (b) First stage of operation with $A = 2.0$ and $B = 0$, where the skyrmion moves from L to R. (c) Second stage of operation with $A = 0$ and $B = 2.0$, where the skyrmion moves from R to L. (d) The complete trajectory, adding operations 1 and 2 together. (From Bellizotti Souza *et. al.* [203], pg. 8).

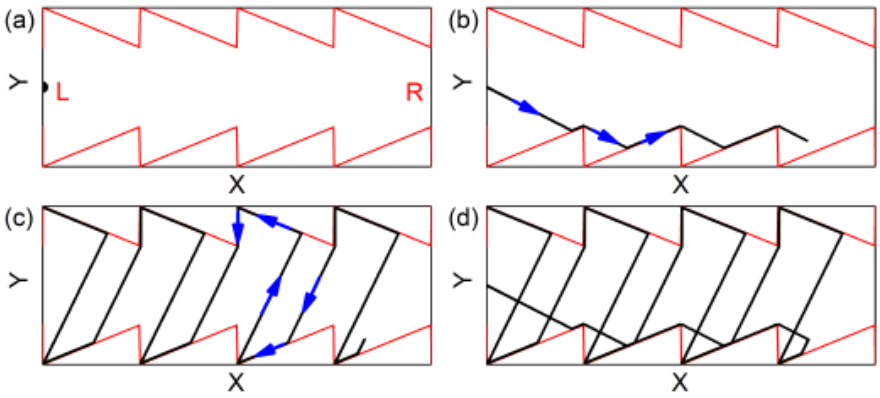

In order to guide the skyrmion along the easy direction, it is applied an ac drive along the x direction with $A = 2.0$ and $B = 0$ for 13500 time steps. The skyrmion trajectory for this interval is shown in Fig. 13.5 (b). As shown in Fig. 13.6 (a), only $1/4$ of ac drive cycle is enough to guide the skyrmion from funnel L to R due to the high efficiency of the motion in this direction. During this time interval, Fig. 13.6 (b) shows that the skyrmion velocity component V_x is always positive. Now that the skyrmion has reached the R funnel it is necessary to bring it back to funnel L using an ac drive applied perpendicular to the funnel axis, that is, $A = 0$ and

$B = 2.0$. This configuration produces a Magnus-induced transverse motion of the skyrmion along the $-x$ direction, as discussed in the previous section. The skyrmion trajectory for this time interval, which extends up to $t = 200{,}000$ time steps, is illustrated in Fig. 12.5 (c). The driving in this second stage must be applied for a much longer period of time due to the low efficiency of motion in the hard direction. This can also be seen in Fig. 12.6 (b) where the skyrmion velocity V_x drops to zero several times during the motion in the hard direction. Note that there are also some positive velocities along $+x$ that are compensated by stronge velocities along $-x$ direction.

Figure 12.6 – The applied ac drive forces F_x^{AC} (black) and F_y^{AC} (red), versus time t for the guided motion shown in Fig. 12.5. Note that the time axis is truncated at $t = 100{,}000$, but the same ac driving is applied at later times to achieve the results shown in Fig. 12.5. (b) The instantaneous skyrmion velocities V_x (black) and V_y (red) versus t under the driving shown in (a). The dashed vertical line indicates the transition at which the ac drive direction is switched. (From Bellizotti Souza *et. al*. [203], pg. 8).

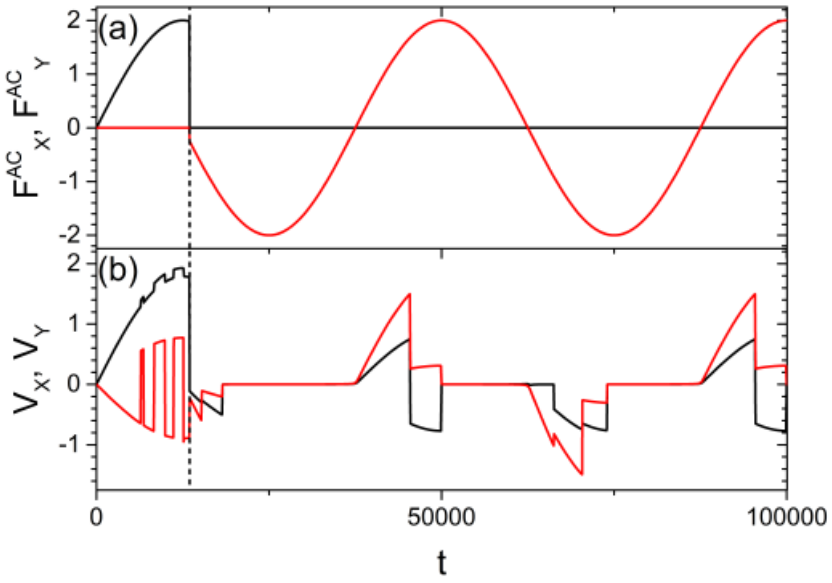

12.3.3 Discussion and Summary

The behavior of a single skyrmion under the influence of a funnel geometry with ac driving and zero temperature has been explored in this work. For ac driving applied either parallel or perpendicular to the funnel axis, the skyrmion can undergo net dc motion along either the easy or hard direction of the funnel. When the ac driving is applied parallel to the funnel axis, the skyrmion moves in the easy direction with quantized steps in the velocity that increases monotonically with increasing ac drive amplitude. On the other hand, when the ac drive is applied perpendicular to the funnel axis, the skyrmion flows in the hard direction at a constant average velocity due to the Magnus-induced transverse ratchet effect. Using a combination of ac drives, we showed that it is possible to guide the skyrmion inside the funnel array, where the

skyrmion can go from a starting funnel to another funnel and then return back, simulating a kind of data transfer process.

The ratchet motion in the easy direction of the funnel has been observed in a wide variety of systems with overdamped particles [24,129,204,205]. However, ratcheting motion along the hard axis is not very common. Previous works investigating ratchet reversals showed that type II superconducting vortices may exhibit a net dc motion along the hard axis when submitted to thermal noise and external drives [206,207]. However, the hard axis motion depends on the number of vortices per ratchet period. Here, in the skyrmion case, we show that even with a single skyrmion in the sample a ratchet motion along the hard axis can occur due to the Magnus effect. This feature could be exploited to build devices in which the skyrmion motion must be controlled precisely. Another important aspect to explore in the future is the temperature effects. It is well known that the temperature can change transition points and even vanish some dynamical effects [172]. Hence, it is possible that the motion in the hard direction may vanish by strong thermal fluctuations, since the motion is not very efficient. We expect that our results would not only be important to skyrmions, but also other magnetic textures exhibiting significant Magnus effects, such as merons [208].

Part III

Interaction Among Skyrmions: Micromagnetic approach

13 Interaction among skyrmions in conical backgrounds

13.1 Skyrmion in conical backgrounds

In addition to studying skyrmions interacting with a periodic substrate in ultrathin films to achieve control over their motion, we are also interested in understanding their behavior in a broader context, such as in thick films. In this preliminary work, we focus on analyzing the interaction between skyrmions, and in future studies, we plan to investigate their interaction with a substrate. Our analysis will be conducted from a microscopic perspective.

It is well-known that skyrmions are usually repulsive to each other in the ferromagnetic phase of chiral magnets. In fact, most of the work done in this thesis considers interacting skyrmions and defects in ultrathin ferromagnetic films. However, in thick films, the spins configurations may exhibit more phases. In Fig. 13.1 (a) it is shown an experimental observation of the phase diagram form a thin $Co_8Zn_{10}Mn_2$ plate. For low magnetic fields the system is stabilized in the helical phase, as illustrated in Fig. 13.1 (b). However, as the applied magnetic field in the *z* direction is applied, the helical phase transforms into the conical phase, with propagation direction along the applied field. An illustration of this phase can be seen in Fig. 13.1 (c). If the applied field is increased further, the system saturates into the ferromagnetic phase, where all spins are aligned with the field, as shown in Fig. 13.1 (d). When skyrmions are stabilized in the conical phase, regions of attractive interactions between skyrmions can be observed [210–212], where skyrmions are repulsive at long and short ranges, but attractive at intermediate ranges. This enable skyrmion lattices to form clusters in the sample, which is only possible in these peculiar systems. In this work we intend to investigate sample parameters that influences on this unusual skyrmion-skyrmion interaction in tridimensional systems. Thus, we perform a series of simulations investigating how the magnetic field and sample thickness affect the skyrmion-skyrmion interaction. This work is currently in development with collaborations from Rai M. Menezes under the supervision of Milorad V. Milošević.

13.2 Model and simulation details

In this section, in order to simulate skyrmions from the microscopical point of view, we use the micromagnetic model. As our focus shifts towards studying the interaction between skyrmions in three-dimensional thick films, the particle model described in section 2.3 is no longer applicable. Therefore, a more comprehensive and detailed analysis is necessary, leading us to utilize micromagnetic simulations provided by the MUMAX³ package [213]. The

micromagnetic simulations are very similar to the atomistic model described in section 2.2. The main difference is that the spin direction must change only a small angle from one lattice point to the other. The direction angles of spins can be approximated by a continuous function of position [214]. Thus, the state of a ferromagnet can be described by the continuous vector magnetization $\mathbf{M}(\mathbf{x})$. In a few words, instead of considering the dynamics of spins, as in the atomistic model, here it is considered the dynamics of a classical magnetization vector constituted by spins.

Figure 13.1 – (a) Phase diagram of the skyrmion density in the magnetic field (B) vs. temperature (T) plane deduced from LTEM observations for a $Co_8Zn_{10}Mn_2$ thin plate. (From Kim *et. al.* [212], pg. 5548). [(b), (c), (d)] Simulation results for spin configurations at a transversal section of a thin plate in the xz plane for varied applied magnetic field values in the z direction. (b) The spin configuration in the absence of field, the Helical phase. (c) For intermediate fields, the Conical phase. (d) For high fields, the saturated ferromagnetic phase, where all spins align with the applied field (Figs. (b), (c) and (d) are elaborated by the author).

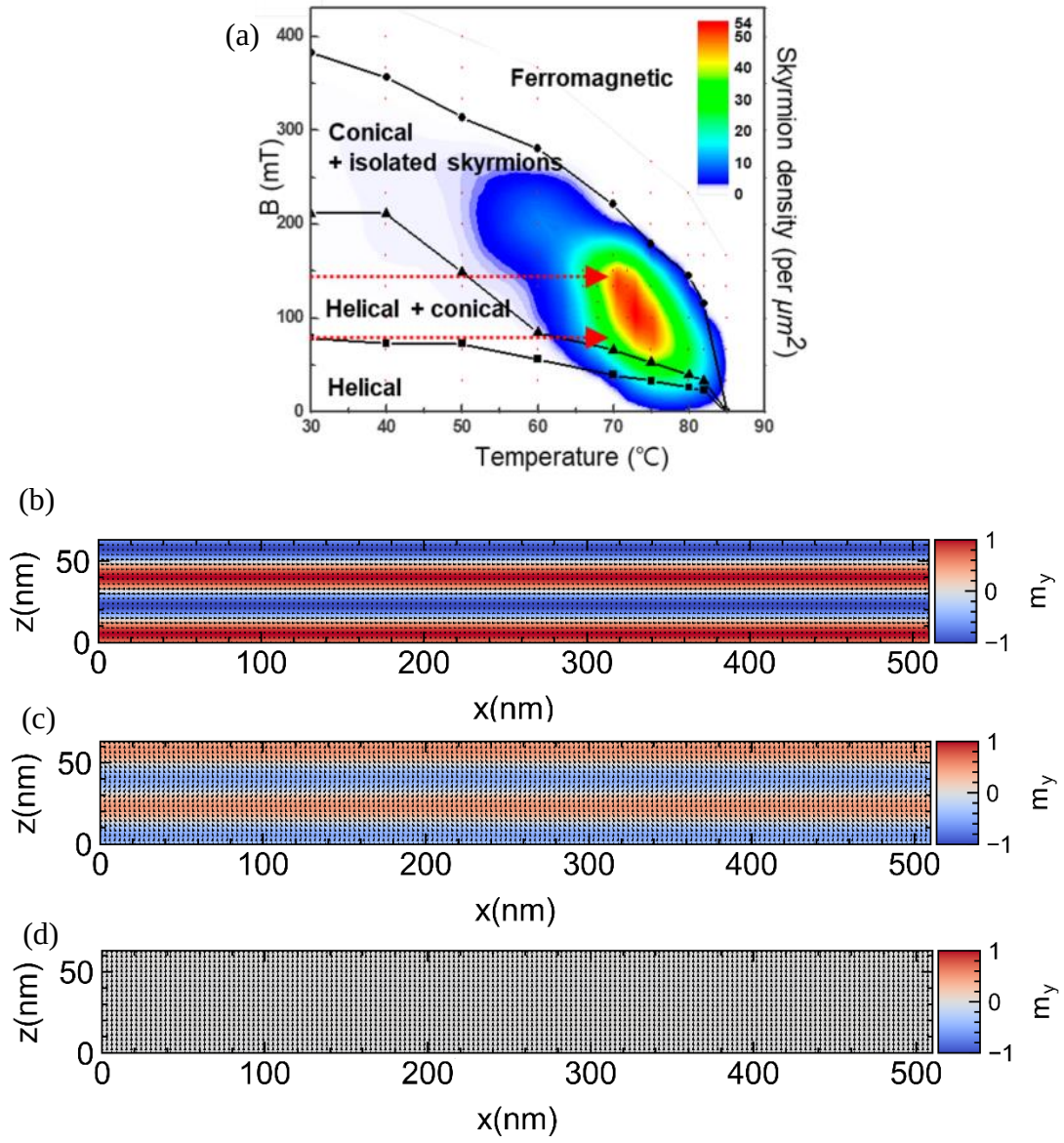

Here we consider a multi-layer film of FeGe which can host Bloch-type skyrmions at $T = 0$ K. The ferromagnetic sample has fixed dimensions of 1024 nm in the x direction and 256 nm in the y direction. The thickness of the film, d, is varied throughout the calculations. We add periodic boundary conditions along the x and y directions to simulate an infinite film in xy plane, and no boundary conditions are applied in z, in order to consider the finite dimension of the film in the z direction. We model the magnetic states using the energy density functional described in Eq. (13.1).

$$E = E_{ex} + E_{DM} + E_{Zeeman} = \frac{A_{ex}}{M_s}(\nabla \mathbf{m})^2 + \frac{D}{M_s}\mathbf{m} \cdot (\nabla \times \mathbf{m}) - \frac{\mu_0}{M_s}\mathbf{m} \cdot \mathbf{H} \qquad (13.1)$$

Here, E_{ex} is the exchange energy, E_{DM} is the Dzyaloshinskii-Moriya coupling energy, E_{Zeeman} is the Zeeman energy and $\mathbf{m} = (m_x, m_y, m_z)$ is the spin vector. We model the material using the FeGe parameters, where $M_s = 3.84 \times 10^5$ A/m is the saturation magnetization, $A_{ex} = 4.75 \times 10^{-12}$J/m is the exchange stiffness, $D = 0.853 \times 10^{-3}$J/m^2 is the Dzyaloshinskii-Moriya coupling constant, μ_0 is the permeability in vacuum and **H** is the applied magnetic field. The external field is only applied perpendicular to the film, $\mathbf{H} = (0,0,H)$. A conical state is achieved in the film for certain values of H where L_D is the helix period, where the helical state repeats itself. For example, in Fig. 13.1 (b), the film thickness is $d = 2L_D$. We use a cubic distribution of spin sites with distance between neighboring spins as $a = 2$ nm. The helix period stabilized in our simulations is $L_D = 32a$.

13.3 Results

13.3.1 Mapping the topological spin textures

First, we begin investigating the topological phases present in the sample as we vary the applied magnetic field, H and the sample thickness, d. As a result, a phase diagram of H/H_D vs. d/L_D is illustrated in Fig. 13.2. The magnetic field values are normalized by the saturation field, $H_D \approx 210$ mT, where all spins align with the applied external magnetic field. As H_D varies as a function of the sample thickness, we choose to calculate H_D for the bulk case as a threshold, where the sample is also infinite in the z direction. As can be seen in Fig. 13.2, the regions are separated in tons of blue, where the dark blue is the helical phase, the light blue is the conical phase and the white is the ferromagnetic. Moreover, we attempted to stabilize skyrmions in the square points in all regions of the phase diagram. Skyrmions were introduced on the sample arbitrarily and then the energy was minimized to verify if skyrmions could be stabilized. In cases where skyrmions were successfully stabilized, we used solid squares to indicate the

presence of skyrmions, and open squares to indicate that skyrmions were not stable. This step is crucial in verifying the stability of skyrmions in the conical phase. It will allow us to progress to the subsequent sections where we can investigate the behavior of skyrmions as we vary the applied magnetic field and sample thickness.

Figure 13.2 – Phase diagram of H/H_D vs. d/L_D for the sample FeGe simulated in this work. The different topological states can be identified by shades of blue. Dark blue corresponds to the helical phase, light blue to the conical phase and white to ferromagnetic phase. The black squares correspond to attempts to stabilize skyrmions in the sample: squares with solid interior are values where skyrmions were stabilized and squares with blank interior are values were skyrmions were unable to stabilize (Elaborated by the author).

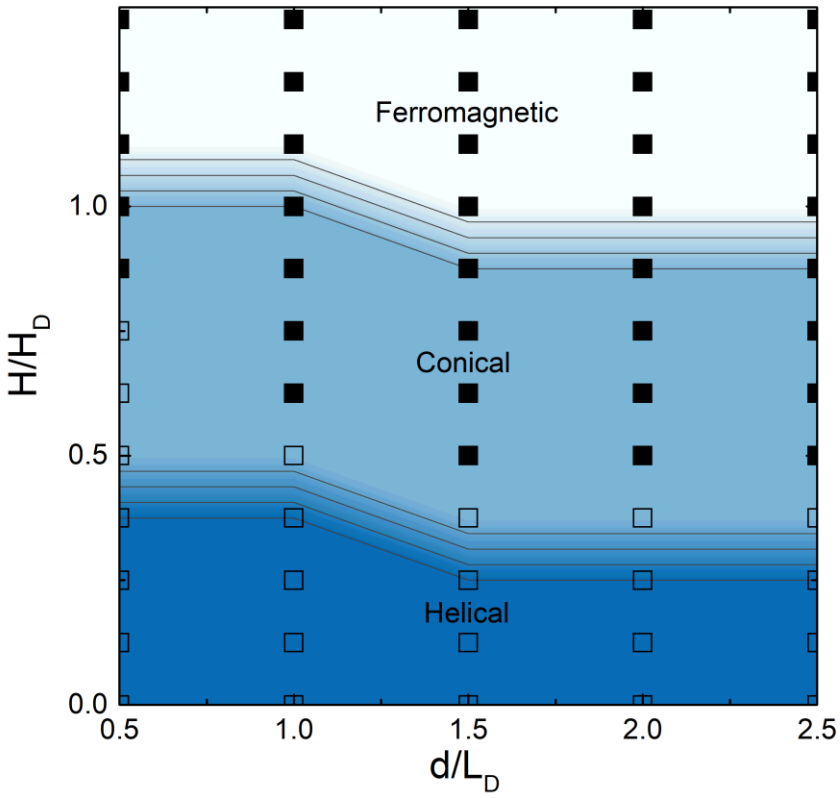

13.3.2 Skyrmion-Skyrmion interaction in multilayer films

In previous section we established the regions where skyrmions can be stabilized in the sample. Now, we look towards the skyrmion-skyrmion interaction shape for different backgrounds. As our diagram in Fig. 13.2 illustrated, skyrmions can only be stabilized with a conical background or a ferromagnetic one. Starting with the simplest case of skyrmion-skyrmion interaction with ferromagnetic background, we set $d/L_D = 1.0$ and simulated the skyrmion-skyrmion interaction for $H/H_D = 1.1$. The skyrmion-skyrmion interaction is simulated following the procedure: one skyrmion is fixed in the center of the sample, while the other is located at a distance r from the fixed skyrmion. The distance r measures the distance between the center of the skyrmions, as illustrated in Fig. 13.3 (c). Both skyrmions have frozen

spins in their center in order to maintain their stability. The frozen spins correspond to a tube of radius $3a$ and height d. Initially, skyrmions are set apart at a distance $r = 6.25L_D = 400$ nm and we slowly approach them, minimize the energy and plot the total energy as a function of the distance.

Figure 13.3 – The energy of the system E normalized by the respective background E_{ferr} or E_{cone} vs. the distance between the center of skyrmions, r/L_D, for samples with $d = 1.0L_D$ and (a) $H/H_D = 1.1$ and (b) $H/H_D = 0.9$. In (a) for stronger magnetic field the background state is ferromagnetic and the skyrmion-skyrmion interaction is monotically repulsive. In (b) for weaker applied field the background state is conical and the skyrmion-skyrmion interaction is similar to a Lennard-Jones potential. The inset of (b) shows in greater detail the attractive part of the interaction where R_{sk} is the optimal distance and ΔE is the attractive potential well depth. (c) 3D illustration of two interacting skyrmions in the FeGe sample. Skyrmions are separated at a distance r and the sample thickness is d. The colors indicate the spins orientation in the z direction, where red is in $+z$ and blue is along $-z$. ((a) and (b) elaborated by the author, (c) elaborated by the collaborator Rai M. Menezes).

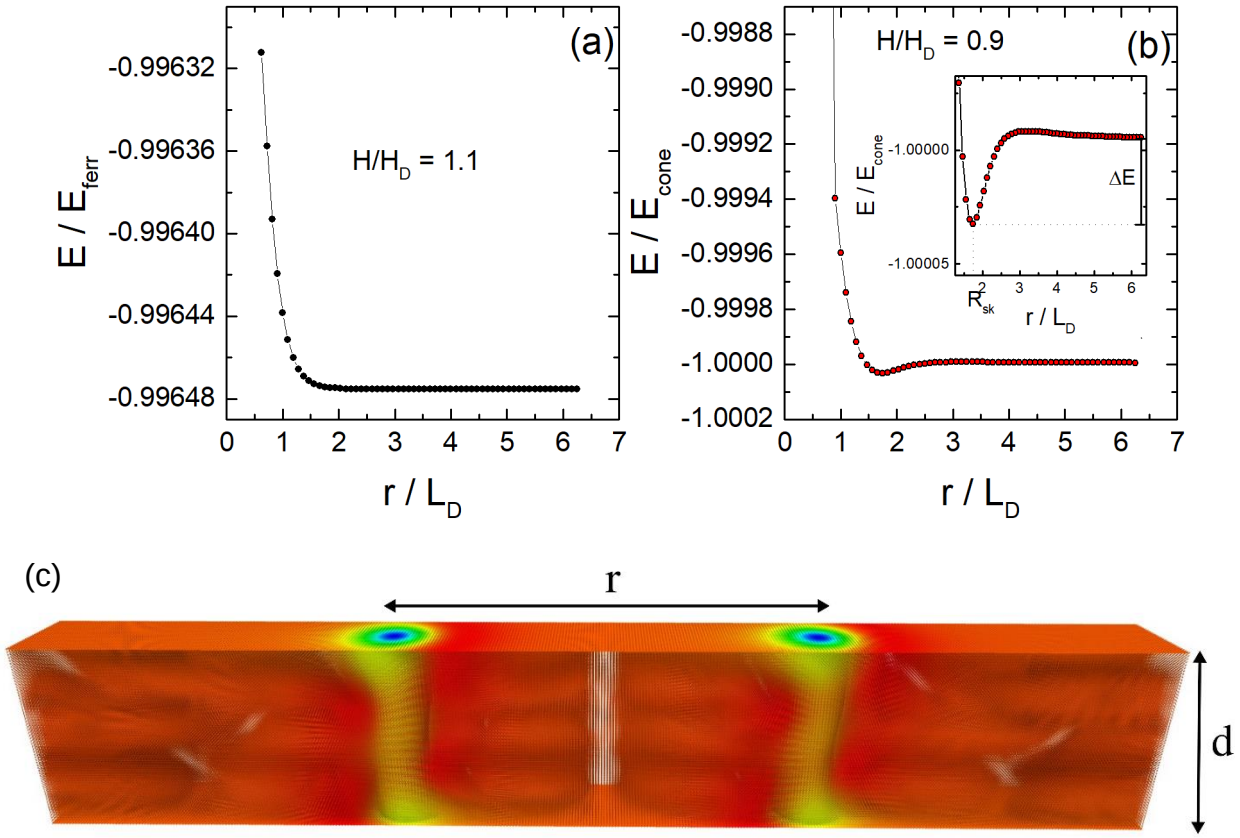

In Fig. 13.3 (a,b) it is plotted the total energy, E normalized by the corresponding background energy, the ferromagnetic E_{ferr} in Fig. 13.3 (a) and conical E_{cone} in (b). The energy profile seen in Fig. 13.3 (a) is very similar to the ordinary skyrmion-skyrmion repulsion observed in other works, where the interaction is monotonically repulsive [73,215,216]. However, In Fig. 13.3 (b) the skyrmion-skyrmion interaction exhibits a non-monotonic

behavior, similar to a Lennard-Jonnes potential [217]. In Fig. 13.3 (b) there is a horizontal dashed line that clarifies the attractive region of the potential. Moreover, it is possible to characterize an optimal skyrmion distance $R_{sk} = 1.75L_D$ that reduces the energy, favoring the formation of skyrmion clusters. This attractive interaction region among skyrmions was previously demonstrated both theoretically [211] and observed experimentally [210]. In our work, we intend to investigate further how can the applied magnetic field and sample thickness affect the skyrmion behavior.

13.3.3 Varying the applied magnetic field

Here we focus on this non-monotonic skyrmion-skyrmion interaction varying some conditions of the sample. First, we look into the influence of the applied magnetic field while keeping the sample thickness constant, $d = 1.0L_D$. In Fig. 13.4 (a), it is shown how the optimal distance, R_{sk}/L_D, varies as a function of the applied magnetic field, H/H_D. The optimal distance exhibits two types of behaviors: (i) For low applied magnetic fields, $H/H_D < 0.92$, R_{sk}/L_D increases linearly with increasing H/H_D. (ii) For stronger fields, $H/H_D > 0.92$, R_{sk}/L_D increases faster with applied magnetic field, as an exponential towards infinite. This happens since the magnet background is changing from conical do ferromagnetic. In the conical phase, the skyrmion interaction exhibits the non-monotonical behavior and the attractive region for skyrmions. However, as the backgrounds becomes saturated in the ferromagnetic state, the skyrmions become repulsive for all distances, resulting in a $R_{sk} \to \infty$ with increasing field.

Figure 13.4 – Results for a sample with fixed thickness, $d = 1.0L_D$. (a) The optimal distance R_{sk}/L_D vs. H/H_D and (b) the attractive potential depth $\Delta E/E_{cone}$ vs. H/H_D. The dashed regions correspond to magnetic fields where the background is no longer conical, but ferromagnetic.

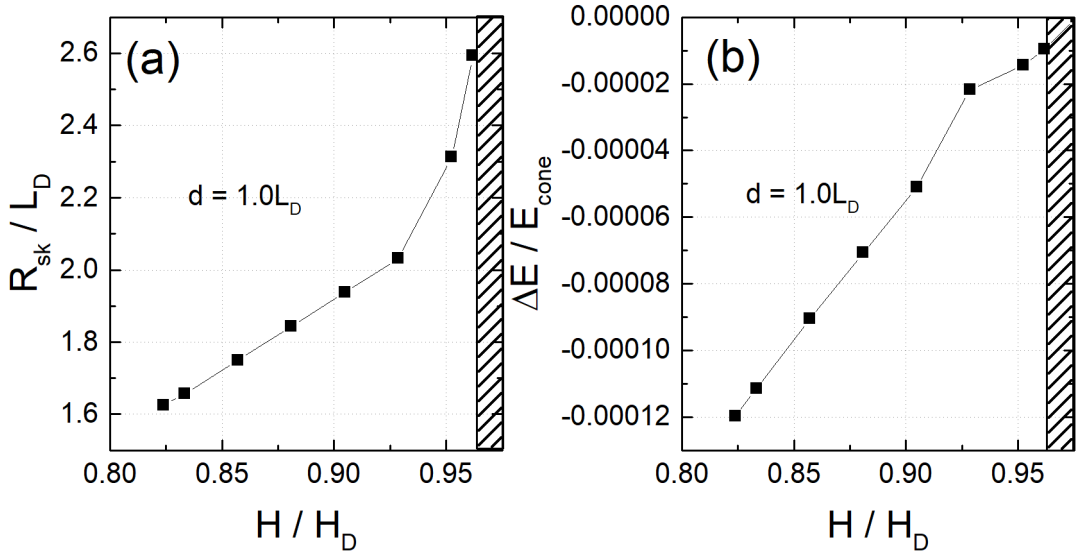

In Fig. 13.4 (b) it is shown how the attractive depth, $\Delta E/E_{cone}$, changes as a function of the applied field. There is an almost linear decrease in magnitude of $\Delta E/E_{cone}$ as H/H_D increases, and for $H/H_D > 1.0$, where the background reaches the ferromagnetic state, $\Delta E = 0$, indicating that the skyrmion-skyrmion interaction changes from non-monotonic to monotonic, as shown in Fig. 13.3. Note that for $0.9 < H/H_D < 0.96$, the linear behavior of $\Delta E/E_{cone}$ is lost. This occurs exactly at the transition region between the conical and the ferromagnetic background. Thus, we plot the energy contributions of $\Delta E = \Delta E_{ex} + \Delta E_{DMI} + \Delta E_{Zeeman}$ in Fig. 13.5. As can be seen, in the region $0.9 < H/H_D < 0.96$ the energies change dramatically, resulting in the total energy variations observed in Fig. 13.4 (b).

Figure 13.5 – Results for a sample with fixed thickness, $d = 1.0L_D$. The attractive potential depth of the energy contributions ΔE_{ex}, ΔE_{DMI}, ΔE_{Zeeman} as a function of H/H_D, where ΔE is the sum of all energy contributions. The dashed regions correspond to magnetic fields where the background is ferromagnetic. The horizontal dashed line separates the positive and negative energy contributions.

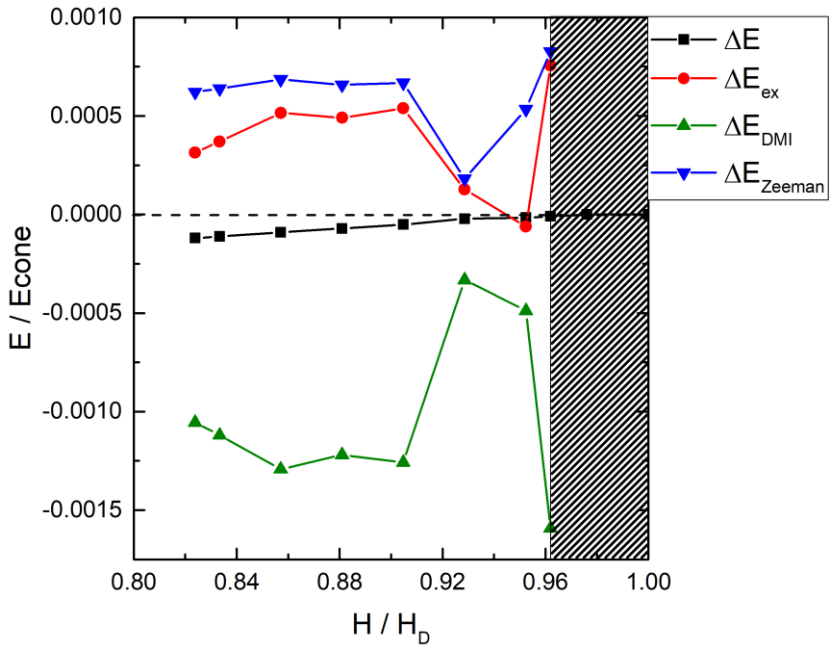

13.3.4 Discussions and Summary

In this study, we investigated the interaction between a pair of skyrmions in 3D thick FeGe films by varying the applied magnetic field. Our findings revealed that skyrmions can be stabilized for various values of the applied magnetic field and sample thickness. While we observed the absence of skyrmion stabilization with a helical background, we did find the presence of skyrmions in conical and ferromagnetic backgrounds. Specifically, in the saturated ferromagnetic phase, skyrmions exhibited the expected repulsive behavior, consistent with previous studies. However, in the conical phase, we observed a distinct interaction pattern:

repulsion at both short and long distances, but attraction in intermediate regions. This interaction energy can be compared to the well-known Lennard-Jones potential, with an optimal distance between skyrmions. As we varied the applied magnetic field for a fixed film thickness, we noted that the optimal distance increased linearly for low fields. However, as the applied field approached saturation, the optimal distance increased exponentially. Regarding the attractive energy depth between skyrmions in conical backgrounds, we found that it weakened almost linearly with increasing field. Nevertheless, close to the transition between conical and ferromagnetic backgrounds, the linear relationship is lost. Additionally, we observed strong energy contribution variations near this transition point. The implications of these results are not yet fully understood, and further data analysis is required to ascertain if a phase transition is occurring within this system. We are conducting extensive simulations, which were time-consuming due to the large size of the system ($1024 \times 512 \times 72$ nm). The energy minimization process for each system and skyrmion distance, r, required significant computational resources. We are also conducting simulations with varying sample thickness, but these cases involve even larger systems for thicker films. We anticipate that upon completion of these analyses, our work will contribute to a better understanding of interacting skyrmions in conical backgrounds.

14 General conclusions

It has been shown in this thesis that skyrmions under the influence of periodic substrates exhibit a rich variety of dynamical features that can be exploited for future technological devices. Concerning obstacle arrays, we showed here that the obstacle size can be used to control the skyrmion motion, where small obstacles allow the skyrmion to flow closer to the intrinsic Hall angle, with lower possible dynamic phases, while larger obstacles enrich the number of dynamic phases. Moreover, a periodic array of obstacles can be used as a topological sorting for skyrmions, where skyrmions from different species, with different Magnus force intensities, can be driven to locked to different angles in the sample, therefore sorting them. This sorting process can be very useful for applications, since skyrmions from the same species can be easier to control in a given sample.

Besides the obstacle size, another way to control skyrmions is using the obstacle density. Here, we show that skyrmions may exhibit different dynamical behavior under samples with different obstacle densities. In samples with low obstacle density, the skyrmion flows closer to the intrinsic Hall angle, with reduced number of possible locking directions, while for higher

densities the skyrmion dynamics is much richer, with more possibilities for locking directions. Another interesting feature is that for a given value of external dc driving, the skyrmion may move at different angles depending on the obstacle density. This opens the possibility to create a sample where regions with different obstacle densities may coexist in order to steer the skyrmion into a predefined trajectory, which can certainly be helpful for spintronics.

For the case of skyrmions under periodic substrates and ac driving only, we showed that besides the expected localized orbits, that also occurs for overdamped particles, in the skyrmion case it can also exhibit directed motion. As the ac drive amplitude is increased, the skyrmion orbit increases and can go from localized to delocalized orbits. Part of these delocalized orbits may exhibit directed motion due to ratchet effects that arise from the Magnus term. Using the ratchet effects, we also showed that in a given sample within regions with same obstacle array, but different obstacle sizes can be used to guide the skyrmion. The interface between these regions with different obstacle size create an asymmetry that under ac driving can induce a skyrmion transport through the edge. Our results show that the skyrmion can follow a straight interface, and if corners are added, the skyrmion can turn them and follow the interface, enabling the possibility for designed interfaces to work as a guide for the skyrmion.

When dc and ac drive are applied together in periodic substrates, skyrmions can exhibit Shapiro steps and even more different locking directions. Interestingly, we observed for the first time a skyrmion Hall angle reversal, where due to the periodic substrate, dc and ac drives, in certain circumstances the skyrmion can exhibit a positive skyrmion Hall angle, and then a reversal to negative Hall angle. Also, a total transverse motion can occur, where the dc drive is applied in one direction and the skyrmion flows perpendicularly to the applied dc drive direction. These results open novel possibilities to control the skyrmion motion in periodic substrates.

For the case of another type of periodic substrate, such as funnel geometries, skyrmion can exhibit very distinct dynamic behavior due to the asymmetric shape of funnels. Using only ac drives, we showed here that a skyrmion can be set into motion along the easy or hard direction of the funnel array, depending on the direction of the ac drive. For ac drive parallel to the funnel axis the skyrmion flows in the easy direction, while for ac drive perpendicular to the funnel axis it flows in the hard direction. This opens possibility for a kind of data transfer using skyrmions, which we simulated here. Using only ac drive the skyrmion was able to flow from an initial funnel to another and then travel back to the initial funnel.

The results presented in this work aim to contribute in the skyrmion dynamics area and also in transport phenomena of similar particles that exhibit significant Magnus effects. Here we report several different ways to obtain a controlled skyrmion motion using only dc drives, only ac drives, combination of dc and ac drives and also some temperature effects. We hope these results may help to develop new devices using skyrmions in spintronics and serve as inspiration for future investigations.

15 Scientific production

Papers published:

- **N. P. Vizarim**, C. Reichhardt, C. J. O. Reichhardt, and P. A. Venegas: "*Skyrmion Dynamics and Topological Sorting on Periodic Obstacle Arrays*" New Journal of Physics **22**, 053025 (2020).
- **N. P. Vizarim**, C. J. O. Reichhardt, P. A. Venegas, and C. Reichhardt: "*Skyrmion Dynamics and Transverse Mobility: Skyrmion Hall angle reversal on 2D periodic substrates with dc and biharmonic ac drives*" European Physics Journal B **93**, 112 (2020).
- **N. P. Vizarim**, C. J. O. Reichhardt, P. A. Venegas, and C. Reichhardt: "*Skyrmion Pinball and Directed Motion on Obstacle Arrays*" Journal of Physics Communications **4**, 085001 (2020).
- **N. P. Vizarim**, C. Reichhardt, P. A. Venegas, and C. J. O. Reichhardt: "*Shapiro Steps and Nonlinear Skyrmion Hall Angles For dc and ac Driven Skyrmions on a Two Dimensional Periodic Substrate*" Physical Review B **102**, 104413 (2020).
- **N. P. Vizarim**, J. C. B. Souza, C. Reichhardt, C. J. O. Reichhardt, and P. A. Venegas, *Directional Locking and the Influence of Obstacle Density on Skyrmion Dynamics in Triangular and Honeycomb Arrays*, Journal of Physics: Condensed Matter **33**, 305801 (2021).
- **N. P. Vizarim**, C. Reichhardt, P. A. Venegas, and C. J. O. Reichhardt, *Guided Skyrmion Motion along Pinning Array Interfaces*, Journal of Magnetism and Magnetic Materials **528**, 167710 (2021).
- J. C. B. Souza, **N. P. Vizarim**, C. J. O. Reichhardt, C. Reichhardt, and P. A. Venegas, *Skyrmion Ratchet in Funnel Geometries*, Physical Review B **104**, 054434 (2021).

- **N. P. Vizarim**, J. C. B. Souza, C. J. O. Reichhardt, C. Reichhardt, M. V. Milošević and P. A. Venegas, *Soliton motion in skyrmion chains: Stabilization and guidance by nanoengineered pinning*, Physical Review B **105**, 224409 (2022).
- J. C. B. Souza, **N. P. Vizarim**, C. J. O. Reichhardt, C. Reichhardt, and P. A. Venegas, *Magnus induced diode effect for skyrmions in channels with periodic potentials*, Journal of Physics: Condensed Matter **35**, 015804 (2022).
- J. C. B. Souza, **N. P. Vizarim**, C. J. O. Reichhardt, C. Reichhardt, and P. A. Venegas, *Clogging, diode and collective effects of skyrmions in funnel geometries*, New Journal of Physics **24**, 103030 (2022).
- J. C. B. Souza, **N. P. Vizarim**, C. J. O. Reichhardt, C. Reichhardt, and P. A. Venegas, *Spontaneous skyrmion conformal lattice and transverse motion during dc and ac compression*, New Journal of Physics **25**, 053020 (2023).

References

[1] Intel, *Moore's Law and Intel Innovation*, https://www.intel.com/content/www/us/en/history/museum-gordon-moore-law.html.

[2] N. S. Kim, T. Austin, D. Baauw, T. Mudge, K. Flautner, J. S. Hu, M. J. Irwin, M. Kandemir, and V. Narayanan, *Leakage Current: Moore's Law Meets Static Power*, Computer **36**, 68 (2003).

[3] M. Lundstrom, *Moore's Law Forever?*, Science **299**, 210 (2003).

[4] W. Kang, Y. Zhang, Z. Wang, J.-O. Klein, C. Chappert, D. Ravelosona, G. Wang, Y. Zhang, and W. Zhao, *Spintronics: Emerging Ultra-Low-Power Circuits and Systems beyond MOS Technology*, ACM J. Emerg. Technol. Comput. Syst. **12**, 16:1 (2015).

[5] C. Chappert, A. Fert, and F. N. Van Dau, *The Emergence of Spin Electronics in Data Storage*, in *Nanoscience and Technology* (Co-Published with Macmillan Publishers Ltd, UK, 2009), pp. 147–157.

[6] P. Khalili and K. L. Wang, *The Computer Chip That Never Forgets*, IEEE Spectr. **52**, 30 (2015).

[7] S. Mühlbauer, B. Binz, F. Jonietz, C. Pfleiderer, A. Rosch, A. Neubauer, R. Georgii, and P. Böni, *Skyrmion Lattice in a Chiral Magnet*, Science **323**, 915 (2009).

[8] A. Fert, N. Reyren, and V. Cros, *Magnetic Skyrmions: Advances in Physics and Potential Applications*, Nat. Rev. Mater. **2**, 17031 (2017).

[9] A. Fert, V. Cros, and J. Sampaio, *Skyrmions on the Track*, Nat. Nanotechnol. **8**, 152 (2013).

[10] F. Jonietz et al., *Spin Transfer Torques in MnSi at Ultralow Current Densities*, Science **330**, 1648 (2010).

[11] N. Nagaosa and Y. Tokura, *Topological Properties and Dynamics of Magnetic Skyrmions*, Nat. Nanotechnol. **8**, 12 (2013).

[12] J. E. Villegas, E. M. Gonzalez, M. I. Montero, I. K. Schuller, and J. L. Vicent, *Directional Vortex Motion Guided by Artificially Induced Mesoscopic Potentials*, Phys. Rev. B **68**, 224504 (2003).

[13] C. Reichhardt and C. J. Olson Reichhardt, *Directional Locking Effects and Dynamics for Particles Driven through a Colloidal Lattice*, Phys. Rev. E **69**, 041405 (2004).

[14] M. Balvin, E. Sohn, T. Iracki, G. Drazer, and J. Frechette, *Directional Locking and the Role of Irreversible Interactions in Deterministic Hydrodynamics Separations in Microfluidic Devices*, Phys. Rev. Lett. **103**, 078301 (2009).

[15] C. Reichhardt and C. J. Olson Reichhardt, *Dynamical Ordering and Directional Locking for Particles Moving over Quasicrystalline Substrates*, Phys. Rev. Lett. **106**, 060603 (2011).

[16] A. B. Kolton, D. Domínguez, C. J. Olson, and N. Grønbech-Jensen, *Driven Vortices in Three-Dimensional Layered Superconductors: Dynamical Ordering along the \textit{c} Axis*, Phys. Rev. B **62**, R14657 (2000).

[17] R. Ait-Haddou and W. Herzog, *Brownian Ratchet Models of Molecular Motors*, Cell Biochem. Biophys. **38**, 191 (2003).

[18] R. D. Astumian and M. Bier, *Fluctuation Driven Ratchets: Molecular Motors*, Phys. Rev. Lett. **72**, 1766 (1994).

[19] C. C. de Souza Silva, J. Van de Vondel, M. Morelle, and V. V. Moshchalkov, *Controlled Multiple Reversals of a Ratchet Effect*, Nature **440**, 7084 (2006).

[20] C.-S. Lee, B. Jankó, I. Derényi, and A.-L. Barabási, *Reducing Vortex Density in Superconductors Using the 'Ratchet Effect,'* Nature **400**, 6742 (1999).

[21] R. D. Leonardo, L. Angelani, D. Dell'Arciprete, G. Ruocco, V. Iebba, S. Schippa, M. P. Conte, F. Mecarini, F. D. Angelis, and E. D. Fabrizio, *Bacterial Ratchet Motors*, Proc. Natl. Acad. Sci. **107**, 9541 (2010).
[22] C. Reichhardt and C. J. O. Reichhardt, *Active Matter Ratchets with an External Drift*, Phys. Rev. E **88**, 062310 (2013).
[23] R. Wördenweber, P. Dymashevski, and V. R. Misko, *Guidance of Vortices and the Vortex Ratchet Effect in High-${T}_{c}$ Superconducting Thin Films Obtained by Arrangement of Antidots*, Phys. Rev. B **69**, 184504 (2004).
[24] J. E. Villegas, E. M. Gonzalez, M. P. Gonzalez, J. V. Anguita, and J. L. Vicent, *Experimental Ratchet Effect in Superconducting Films with Periodic Arrays of Asymmetric Potentials*, Phys. Rev. B **71**, 024519 (2005).
[25] D. Weiss, M. L. Roukes, A. Menschig, P. Grambow, K. von Klitzing, and G. Weimann, *Electron Pinball and Commensurate Orbits in a Periodic Array of Scatterers*, Phys. Rev. Lett. **66**, 2790 (1991).
[26] C. Reichhardt, D. Ray, and C. J. O. Reichhardt, *Collective Transport Properties of Driven Skyrmions with Random Disorder*, Phys. Rev. Lett. **114**, 217202 (2015).
[27] S. A. Díaz, C. J. O. Reichhardt, D. P. Arovas, A. Saxena, and C. Reichhardt, *Fluctuations and Noise Signatures of Driven Magnetic Skyrmions*, Phys. Rev. B **96**, 085106 (2017).
[28] C. Reichhardt and C. J. O. Reichhardt, *Noise Fluctuations and Drive Dependence of the Skyrmion Hall Effect in Disordered Systems*, New J. Phys. **18**, 095005 (2016).
[29] J. Iwasaki, M. Mochizuki, and N. Nagaosa, *Universal Current-Velocity Relation of Skyrmion Motion in Chiral Magnets*, Nat. Commun. **4**, ncomms2442 (2013).
[30] J.-V. Kim and M.-W. Yoo, *Current-Driven Skyrmion Dynamics in Disordered Films*, Appl. Phys. Lett. **110**, 132404 (2017).
[31] C. Reichhardt and C. J. O. Reichhardt, *Shapiro Steps for Skyrmion Motion on a Washboard Potential with Longitudinal and Transverse Ac Drives*, Phys. Rev. B **92**, 224432 (2015).
[32] C. Reichhardt, D. Ray, and C. J. O. Reichhardt, *Magnus-Induced Ratchet Effects for Skyrmions Interacting with Asymmetric Substrates*, New J. Phys. **17**, 073034 (2015).
[33] C. Reichhardt and C. J. O. Reichhardt, *Magnus-Induced Dynamics of Driven Skyrmions on a Quasi-One-Dimensional Periodic Substrate*, Phys. Rev. B **94**, 094413 (2016).
[34] C. Reichhardt and C. J. O. Reichhardt, *Shapiro Spikes and Negative Mobility for Skyrmion Motion on Quasi-One-Dimensional Periodic Substrates*, Phys. Rev. B **95**, 014412 (2017).
[35] I. Purnama, W. L. Gan, D. W. Wong, and W. S. Lew, *Guided Current-Induced Skyrmion Motion in 1D Potential Well*, Sci. Rep. **5**, 10620 (2015).
[36] D. Toscano, J. P. A. Mendonça, A. L. S. Miranda, C. I. L. de Araujo, F. Sato, P. Z. Coura, and S. A. Leonel, *Suppression of the Skyrmion Hall Effect in Planar Nanomagnets by the Magnetic Properties Engineering: Skyrmion Transport on Nanotracks with Magnetic Strips*, J. Magn. Magn. Mater. **504**, 166655 (2020).
[37] X. Chen, W. Kang, D. Zhu, X. Zhang, N. Lei, Y. Zhang, Y. Zhou, and W. Zhao, *Skyrmion Dynamics in Width-Varying Nanotracks and Implications for Skyrmionic Applications*, Appl. Phys. Lett. **111**, 202406 (2017).
[38] X. Zhang, Y. Zhou, M. Ezawa, G. P. Zhao, and W. Zhao, *Magnetic Skyrmion Transistor: Skyrmion Motion in a Voltage-Gated Nanotrack*, Sci. Rep. **5**, 1 (2015).
[39] C. Reichhardt, D. Ray, and C. J. O. Reichhardt, *Quantized Transport for a Skyrmion Moving on a Two-Dimensional Periodic Substrate*, Phys. Rev. B **91**, 104426 (2015).
[40] C. Reichhardt, D. Ray, and C. J. O. Reichhardt, *Nonequilibrium Phases and Segregation for Skyrmions on Periodic Pinning Arrays*, Phys. Rev. B **98**, 134418 (2018).
[41] T. H. R. Skyrme, *A Non-Linear Field Theory*, Proc R Soc Lond A **260**, 127 (1961).
[42] T. H. R. Skyrme, *A Unified Field Theory of Mesons and Baryons*, Nucl. Phys. **31**, 556 (1962).

[43] S. L. Sondhi, A. Karlhede, S. A. Kivelson, and E. H. Rezayi, *Skyrmions and the Crossover from the Integer to Fractional Quantum Hall Effect at Small Zeeman Energies*, Phys. Rev. B **47**, 16419 (1993).
[44] M. Abolfath, J. J. Palacios, H. A. Fertig, S. M. Girvin, and A. H. MacDonald, *Critical Comparison of Classical Field Theory and Microscopic Wave Functions for Skyrmions in Quantum Hall Ferromagnets*, Phys. Rev. B **56**, 6795 (1997).
[45] S. Heinze, K. von Bergmann, M. Menzel, J. Brede, A. Kubetzka, R. Wiesendanger, G. Bihlmayer, and S. Blügel, *Spontaneous Atomic-Scale Magnetic Skyrmion Lattice in Two Dimensions*, Nat. Phys. **7**, 713 (2011).
[46] A. O. Leonov, I. E. Dragunov, U. K. Rößler, and A. N. Bogdanov, *Theory of Skyrmion States in Liquid Crystals*, Phys. Rev. E **90**, 042502 (2014).
[47] J. Fukuda and S. Žumer, *Quasi-Two-Dimensional Skyrmion Lattices in a Chiral Nematic Liquid Crystal*, Nat. Commun. **2**, 246 (2011).
[48] L. S. Leslie, A. Hansen, K. C. Wright, B. M. Deutsch, and N. P. Bigelow, *Creation and Detection of Skyrmions in a Bose-Einstein Condensate*, Phys. Rev. Lett. **103**, 250401 (2009).
[49] J. Choi, W. J. Kwon, and Y. Shin, *Observation of Topologically Stable 2D Skyrmions in an Antiferromagnetic Spinor Bose-Einstein Condensate*, Phys. Rev. Lett. **108**, 035301 (2012).
[50] A. N. Bogdanov and D. A. Yablonskii, *Thermodynamically Stable "Vortices" in Magnetically Ordered Crystals. The Mixed State of Magnets*, Sov. Phys. JETP **68**, 101 (1988).
[51] A. Bogdanov and A. Hubert, *Thermodynamically Stable Magnetic Vortex States in Magnetic Crystals*, J. Magn. Magn. Mater. **138**, 255 (1994).
[52] U. K. Rößler, A. N. Bogdanov, and C. Pfleiderer, *Spontaneous Skyrmion Ground States in Magnetic Metals*, Nature **442**, 797 (2006).
[53] X. Z. Yu, Y. Onose, N. Kanazawa, J. H. Park, J. H. Han, Y. Matsui, N. Nagaosa, and Y. Tokura, *Real-Space Observation of a Two-Dimensional Skyrmion Crystal*, Nature **465**, 901 (2010).
[54] S. Seki and M. Mochizuki, *Skyrmions in Magnetic Materials*, 1st ed. 2016 edition (Springer, Cham, 2015).
[55] Y. Ishikawa, K. Tajima, D. Bloch, and M. Roth, *Helical Spin Structure in Manganese Silicide MnSi*, Solid State Commun. **19**, 525 (1976).
[56] J. Beille, J. Voiron, and M. Roth, *Long Period Helimagnetism in the Cubic B20 FexCo1−xSi and CoxMn1−x Si Alloys*, Solid State Commun. **47**, 399 (1983).
[57] B. Lebech, J. Bernhard, and T. Freltoft, *Magnetic Structures of Cubic FeGe Studied by Small-Angle Neutron Scattering*, J. Phys. Condens. Matter **1**, 6105 (1989).
[58] J. Jena, R. Stinshoff, R. Saha, A. K. Srivastava, T. Ma, H. Deniz, P. Werner, C. Felser, and S. S. P. Parkin, *Observation of Magnetic Antiskyrmions in the Low Magnetization Ferrimagnet Mn2Rh0.95Ir0.05Sn*, Nano Lett. **20**, 59 (2020).
[59] L. Peng et al., *Real-Space Observation of Nonvolatile Zero-Field Biskyrmion Lattice Generation in MnNiGa Magnet*, Nano Lett. **17**, 7075 (2017).
[60] S. Zhang, F. Kronast, G. van der Laan, and T. Hesjedal, *Real-Space Observation of Skyrmionium in a Ferromagnet-Magnetic Topological Insulator Heterostructure*, Nano Lett. **18**, 1057 (2018).
[61] K. Everschor-Sitte, J. Masell, R. M. Reeve, and M. Kläui, *Perspective: Magnetic Skyrmions—Overview of Recent Progress in an Active Research Field*, J. Appl. Phys. **124**, 240901 (2018).
[62] N. S. Kiselev, A. N. Bogdanov, R. Schäfer, and U. K. Rößler, *Chiral Skyrmions in Thin Magnetic Films: New Objects for Magnetic Storage Technologies?*, J. Phys. Appl. Phys. **44**, 392001 (2011).

[63] J. Hagemeister, N. Romming, K. von Bergmann, E. Y. Vedmedenko, and R. Wiesendanger, *Stability of Single Skyrmionic Bits*, Nat. Commun. **6**, 8455 (2015).
[64] S. Saha et al., *Formation of N\'eel-Type Skyrmions in an Antidot Lattice with Perpendicular Magnetic Anisotropy*, Phys. Rev. B **100**, 144435 (2019).
[65] X. Yu et al., *Current-Induced Nucleation and Annihilation of Magnetic Skyrmions at Room Temperature in a Chiral Magnet*, Adv. Mater. **29**, 1606178 (2017).
[66] X. Zhang, M. Ezawa, D. Xiao, G. P. Zhao, Y. Liu, and Y. Zhou, *All-Magnetic Control of Skyrmions in Nanowires by a Spin Wave*, Nanotechnology **26**, 225701 (2015).
[67] T. Schulz, R. Ritz, A. Bauer, M. Halder, M. Wagner, C. Franz, C. Pfleiderer, K. Everschor, M. Garst, and A. Rosch, *Emergent Electrodynamics of Skyrmions in a Chiral Magnet*, Nat. Phys. **8**, 301 (2012).
[68] X. Z. Yu, N. Kanazawa, W. Z. Zhang, T. Nagai, T. Hara, K. Kimoto, Y. Matsui, Y. Onose, and Y. Tokura, *Skyrmion Flow near Room Temperature in an Ultralow Current Density*, Nat. Commun. **3**, ncomms1990 (2012).
[69] T. L. Gilbert, *A Lagrangian Formulation of the Gyromagnetic Equation of the Magnetic Field*, Phys. Rev. **100**, (1955).
[70] T. L. Gilbert, *A Phenomenological Theory of Damping in Ferromagnetic Materials*, IEEE Trans. Magn. **40**, 3443 (2004).
[71] J. Iwasaki, M. Mochizuki, and N. Nagaosa, *Current-Induced Skyrmion Dynamics in Constricted Geometries*, Nat. Nanotechnol. **8**, 742 (2013).
[72] A. A. Thiele, *Steady-State Motion of Magnetic Domains*, Phys. Rev. Lett. **30**, 230 (1973).
[73] S.-Z. Lin, C. Reichhardt, C. D. Batista, and A. Saxena, *Particle Model for Skyrmions in Metallic Chiral Magnets: Dynamics, Pinning, and Creep*, Phys. Rev. B **87**, 214419 (2013).
[74] C. Reichhardt, C. J. O. Reichhardt, and M. V. Milošević, *Statics and Dynamics of Skyrmions Interacting with Disorder and Nanostructures*, Rev. Mod. Phys. **94**, 035005 (2022).
[75] S.-Z. Lin, C. Reichhardt, C. D. Batista, and A. Saxena, *Driven Skyrmions and Dynamical Transitions in Chiral Magnets*, Phys. Rev. Lett. **110**, 207202 (2013).
[76] Y.-H. Liu and Y.-Q. Li, *A Mechanism to Pin Skyrmions in Chiral Magnets*, J. Phys. Condens. Matter **25**, 076005 (2013).
[77] J. Müller and A. Rosch, *Capturing of a Magnetic Skyrmion with a Hole*, Phys. Rev. B **91**, 054410 (2015).
[78] J. M. D. Coey, *Magnetism and Magnetic Materials*, 1 edition (Cambridge University Press, Cambridge, 2010).
[79] Cohen-Tannoudji, B. Diu, and F. Laloë, *Quantum Mechanics, Vol. 1 1st*, Vol. 1 (Wiley, 2001).
[80] N. Mermin and N. Ashcroft, *Solid State Physics*, 1ª edição (Cengage Learning, Inc, New York, 1976).
[81] I. Dzyaloshinsky, *A Thermodynamic Theory of "Weak" Ferromagnetism of Antiferromagnetics*, J. Phys. Chem. Solids **4**, 241 (1958).
[82] T. Moriya, *Anisotropic Superexchange Interaction and Weak Ferromagnetism*, Phys. Rev. **120**, 91 (1960).
[83] D. Bloch, J. Voiron, V. Jaccarino, and J. H. Wernick, *The High Field-High Pressure Magnetic Properties of MnSi*, Phys. Lett. A **51**, 259 (1975).
[84] H. Yasuoka, V. Jaccarino, R. C. Sherwood, and J. H. Wernick, *NMR and Susceptibility Studies of MnSi above Tc*, J. Phys. Soc. Jpn. **44**, 842 (1978).
[85] Y. Ishikawa, G. Shirane, J. A. Tarvin, and M. Kohgi, *Magnetic Excitations in the Weak Itinerant Ferromagnet MnSi*, Phys. Rev. B **16**, 4956 (1977).
[86] O. Nakanishi, A. Yanase, A. Hasegawa, and M. Kataoka, *The Origin of the Helical Spin Density Wave in MnSi*, Solid State Commun. **35**, 995 (1980).

[87] T. Y. Ou-Yang, G. J. Shu, J.-Y. Lin, C. D. Hu, and F. C. Chou, *Mn Vacancy Defects, Grain Boundaries, AndA-Phase Stability of Helimagnet MnSi*, J. Phys. Condens. Matter **28**, 026004 (2015).
[88] A. R. Fert, *Magnetic and Transport Properties of Metallic Multilayers*, https://doi.org/10.4028/www.scientific.net/MSF.59-60.439.
[89] A. Fert and P. M. Levy, *Role of Anisotropic Exchange Interactions in Determining the Properties of Spin-Glasses*, Phys. Rev. Lett. **44**, 1538 (1980).
[90] L. D. Landau and E. Lifshitz, *On the Theory of Dispersion of Magnetic Permeability in Ferromagnetic Bodies*, Phys. Z. Sowjetunion **8**, 153 (1935).
[91] B. Hillebrands and K. Ounadjela, editors , *Spin Dynamics in Confined Magnetic Structures I*, 2002nd edition (Springer, Berlin ; New York, 2001).
[92] P. Ehrenfest, *Bemerkung Über Die Angenäherte Gültigkeit Der Klassischen Mechanik Innerhalb Der Quantenmechanik*, Z. Für Phys. **45**, 455 (1927).
[93] M. Lakshmanan, *The Fascinating World of the Landau–Lifshitz–Gilbert Equation: An Overview*, Philos. Trans. R. Soc. Math. Phys. Eng. Sci. **369**, 1280 (2011).
[94] T. L. Gilbert and J. M. Kelly, *Anomalous Rotational Damping in Ferromagnetic Sheets*, Conf Magn. Magn. Mater. 253 (1955).
[95] J. H. Han, *Skyrmions in Condensed Matter*, 1st ed. 2017 edition (Springer, New York, NY, 2017).
[96] M. V. Berry, *Quantal Phase Factors Accompanying Adiabatic Changes*, Proc. R. Soc. Lond. Math. Phys. Sci. **392**, 45 (1984).
[97] Ya. B. Bazaliy, B. A. Jones, and S.-C. Zhang, *Modification of the Landau-Lifshitz Equation in the Presence of a Spin-Polarized Current in Colossal- and Giant-Magnetoresistive Materials*, Phys. Rev. B **57**, R3213 (1998).
[98] J. Zang, M. Mostovoy, J. H. Han, and N. Nagaosa, *Dynamics of Skyrmion Crystals in Metallic Thin Films*, Phys. Rev. Lett. **107**, 136804 (2011).
[99] G. Tatara, H. Kohno, and J. Shibata, *Microscopic Approach to Current-Driven Domain Wall Dynamics*, Phys. Rep. **468**, 213 (2008).
[100] J. P. Liu, Z. Zhang, and G. Zhao, editors , *Skyrmions: Topological Structures, Properties, and Applications*, Illustrated edição (CRC Press, Boca Raton, FL, 2016).
[101] J. Sampaio, V. Cros, S. Rohart, A. Thiaville, and A. Fert, *Nucleation, Stability and Current-Induced Motion of Isolated Magnetic Skyrmions in Nanostructures*, Nat. Nanotechnol. **8**, 11 (2013).
[102] W. Jiang et al., *Direct Observation of the Skyrmion Hall Effect*, Nat. Phys. **13**, 162 (2017).
[103] G. Tatara, T. Takayama, H. Kohno, J. Shibata, Y. Nakatani, and H. Fukuyama, *Threshold Current of Domain Wall Motion under Extrinsic Pinning, β-Term and Non-Adiabaticity*, J. Phys. Soc. Jpn. **75**, 064708 (2006).
[104] L. Kong and J. Zang, *Dynamics of an Insulating Skyrmion under a Temperature Gradient*, Phys. Rev. Lett. **111**, 067203 (2013).
[105] M. Mochizuki, X. Z. Yu, S. Seki, N. Kanazawa, W. Koshibae, J. Zang, M. Mostovoy, Y. Tokura, and N. Nagaosa, *Thermally Driven Ratchet Motion of a Skyrmion Microcrystal and Topological Magnon Hall Effect*, Nat. Mater. **13**, 241 (2014).
[106] Z. Wang et al., *Thermal Generation, Manipulation and Thermoelectric Detection of Skyrmions*, Nat. Electron. **3**, 672 (2020).
[107] R. Yanes, F. Garcia-Sanchez, R. F. Luis, E. Martinez, V. Raposo, L. Torres, and L. Lopez-Diaz, *Skyrmion Motion Induced by Voltage-Controlled in-Plane Strain Gradients*, Appl. Phys. Lett. **115**, 132401 (2019).

[108] S. L. Zhang, W. W. Wang, D. M. Burn, H. Peng, H. Berger, A. Bauer, C. Pfleiderer, G. van der Laan, and T. Hesjedal, *Manipulation of Skyrmion Motion by Magnetic Field Gradients*, Nat. Commun. **9**, 1 (2018).
[109] K. Everschor, M. Garst, B. Binz, F. Jonietz, S. Mühlbauer, C. Pfleiderer, and A. Rosch, *Rotating Skyrmion Lattices by Spin Torques and Field or Temperature Gradients*, Phys. Rev. B **86**, 054432 (2012).
[110] R. M. Menezes, J. F. S. Neto, C. C. de S. Silva, and M. V. Milošević, *Manipulation of Magnetic Skyrmions by Superconducting Vortices in Ferromagnet-Superconductor Heterostructures*, Phys. Rev. B **100**, 014431 (2019).
[111] B. Göbel and I. Mertig, *Skyrmion Ratchet Propagation: Utilizing the Skyrmion Hall Effect in AC Racetrack Storage Devices*, Sci. Rep. **11**, 1 (2021).
[112] X. Ma, C. J. O. Reichhardt, and C. Reichhardt, *Reversible Vector Ratchets for Skyrmion Systems*, Phys. Rev. B **95**, 104401 (2017).
[113] I. Lima Fernandes, J. Bouaziz, S. Blügel, and S. Lounis, *Universality of Defect-Skyrmion Interaction Profiles*, Nat. Commun. **9**, 4395 (2018).
[114] J. Feilhauer, S. Saha, J. Tobik, M. Zelent, L. J. Heyderman, and M. Mruczkiewicz, *Controlled Motion of Skyrmions in a Magnetic Antidot Lattice*, ArXiv191007388 Cond-Mat (2019).
[115] T. Bohlein and C. Bechinger, *Experimental Observation of Directional Locking and Dynamical Ordering of Colloidal Monolayers Driven across Quasiperiodic Substrates*, Phys. Rev. Lett. **109**, 058301 (2012).
[116] C. Reichhardt, C. J. Olson, and F. Nori, *Dynamic Phases of Vortices in Superconductors with Periodic Pinning*, Phys. Rev. Lett. **78**, 2648 (1997).
[117] K. Harada, O. Kamimura, H. Kasai, T. Matsuda, A. Tonomura, and V. V. Moshchalkov, *Direct Observation of Vortex Dynamics in Superconducting Films with Regular Arrays of Defects*, Science **274**, 1167 (1996).
[118] A. N. Grigorenko et al., *Direct Imaging of Commensurate Vortex Structures in Ordered Antidot Arrays*, Phys. Rev. B **63**, 052504 (2001).
[119] S. B. Field, S. S. James, J. Barentine, V. Metlushko, G. Crabtree, H. Shtrikman, B. Ilic, and S. R. J. Brueck, *Vortex Configurations, Matching, and Domain Structure in Large Arrays of Artificial Pinning Centers*, Phys. Rev. Lett. **88**, 067003 (2002).
[120] K. Matsumoto and P. Mele, *Artificial Pinning Center Technology to Enhance Vortex Pinning in YBCO Coated Conductors*, Supercond. Sci. Technol. **23**, 014001 (2010).
[121] T. Schulz, R. Ritz, A. Bauer, M. Halder, M. Wagner, C. Franz, C. Pfleiderer, K. Everschor, M. Garst, and A. Rosch, *Emergent Electrodynamics of Skyrmions in a Chiral Magnet*, Nat. Phys. **8**, 301 (2012).
[122] C. J. Olson, C. Reichhardt, and F. Nori, *Nonequilibrium Dynamic Phase Diagram for Vortex Lattices*, Phys. Rev. Lett. **81**, 3757 (1998).
[123] S. A. Montoya, R. Tolley, I. Gilbert, S.-G. Je, M.-Y. Im, and E. E. Fullerton, *Spin-Orbit Torque Induced Dipole Skyrmion Motion at Room Temperature*, Phys. Rev. B **98**, 104432 (2018).
[124] T. Matsuda, K. Harada, H. Kasai, O. Kamimura, and A. Tonomura, *Observation of Dynamic Interaction of Vortices with Pinning Centers by Lorentz Microscopy*, Science **271**, 1393 (1996).
[125] J. Feilhauer, S. Saha, J. Tobik, M. Zelent, L. J. Heyderman, and M. Mruczkiewicz, *Controlled Motion of Skyrmions in a Magnetic Antidot Lattice*, Phys. Rev. B **102**, 184425 (2020).
[126] W. Koshibae and N. Nagaosa, *Theory of Current-Driven Skyrmions in Disordered Magnets*, Sci. Rep. **8**, 6328 (2018).

[127] P. Reimann, *Brownian Motors: Noisy Transport Far from Equilibrium*, Phys. Rep. **361**, 57 (2002).
[128] W. Hwang and M. Karplus, *Structural Basis for Power Stroke vs. Brownian Ratchet Mechanisms of Motor Proteins*, Proc. Natl. Acad. Sci. **116**, 19777 (2019).
[129] A. Libál, C. Reichhardt, B. Jankó, and C. J. O. Reichhardt, *Dynamics, Rectification, and Fractionation for Colloids on Flashing Substrates*, Phys. Rev. Lett. **96**, 188301 (2006).
[130] W. Gillijns, A. V. Silhanek, V. V. Moshchalkov, C. J. O. Reichhardt, and C. Reichhardt, *Origin of Reversed Vortex Ratchet Motion*, Phys. Rev. Lett. **99**, 247002 (2007).
[131] W. Chen, L. Liu, Y. Ji, and Y. Zheng, *Skyrmion Ratchet Effect Driven by a Biharmonic Force*, Phys. Rev. B **99**, 064431 (2019).
[132] W. Chen, L. Liu, and Y. Zheng, *Ultrafast Ratchet Dynamics of Skyrmion by Defect Engineering under Gigahertz Magnetic Fields*, ArXiv200208865 Cond-Mat (2020).
[133] W. Wang, M. Beg, B. Zhang, W. Kuch, and H. Fangohr, *Driving Magnetic Skyrmions with Microwave Fields*, Phys. Rev. B **92**, 020403 (2015).
[134] B. L. Brown, U. C. Täuber, and M. Pleimling, *Effect of the Magnus Force on Skyrmion Relaxation Dynamics*, Phys. Rev. B **97**, 020405 (2018).
[135] *Stochastic Dynamics and Irreversibility*, 2015 edition (Springer, 2014).
[136] C. J. Olson, C. Reichhardt, and V. M. Vinokur, *Hysteretic Depinning and Dynamical Melting for Magnetically Interacting Vortices in Disordered Layered Superconductors*, Phys. Rev. B **64**, 140502 (2001).
[137] N. P. Vizarim, C. Reichhardt, C. J. O. Reichhardt, and P. A. Venegas, *Skyrmion Dynamics and Topological Sorting on Periodic Obstacle Arrays*, New J. Phys. **22**, 053025 (2020).
[138] C. Tsallis and D. A. Stariolo, *Generalized Simulated Annealing*, Phys. Stat. Mech. Its Appl. **233**, 395 (1996).
[139] S. Kirkpatrick, C. D. Gelatt, and M. P. Vecchi, *Optimization by Simulated Annealing*, Science **220**, 671 (1983).
[140] H. Szu and R. Hartley, *Fast Simulated Annealing*, Phys. Lett. A **122**, 157 (1987).
[141] N. Metropolis, A. W. Rosenbluth, M. N. Rosenbluth, A. H. Teller, and E. Teller, *Equation of State Calculations by Fast Computing Machines*, J. Chem. Phys. **21**, 1087 (1953).
[142] S. Geman and D. Geman, *Stochastic Relaxation, Gibbs Distributions, and the Bayesian Restoration of Images*, IEEE Trans. Pattern Anal. Mach. Intell. **PAMI-6**, 721 (1984).
[143] A. Dall'Igna Júnior, R. S. Silva, K. C. Mundim, and L. E. Dardenne, *Performance and Parameterization of the Algorithm Simplified Generalized Simulated Annealing*, Genet. Mol. Biol. **27**, 616 (2004).
[144] F. P. Agostini, D. D. O. Soares-Pinto, M. A. Moret, C. Osthoff, and P. G. Pascutti, *Generalized Simulated Annealing Applied to Protein Folding Studies*, J. Comput. Chem. **27**, 1142 (2006).
[145] R. C. Bernardi, M. C. R. Melo, and K. Schulten, *Enhanced Sampling Techniques in Molecular Dynamics Simulations of Biological Systems*, Biochim. Biophys. Acta BBA - Gen. Subj. **1850**, 872 (2015).
[146] A. Boulle and A. Debelle, *Strain-Profile Determination in Ion-Implanted Single Crystals Using Generalized Simulated Annealing*, J. Appl. Crystallogr. **43**, ARRAY(0xa98e544) (2010).
[147] Y. Xiang and X. G. Gong, *Efficiency of Generalized Simulated Annealing*, Phys. Rev. E **62**, 4473 (2000).
[148] N. P. Vizarim, M. Carlone, L. G. Verga, and P. A. Venegas, *Commensurability Effects in the Critical Forces of a Superconducting Film with Kagomé Pinning Array at Submatching Fields*, Eur. Phys. J. B **90**, 169 (2017).

[149] N. P. Vizarim, M. Carlone, L. G. Verga, P. A. Venegas, N. P. Vizarim, M. Carlone, L. G. Verga, and P. A. Venegas, *Critical Forces at Fractional Matching Fields in Superconducting Thin Films with Triangular Pinning Lattice*, Mater. Res. **20**, 899 (2017).
[150] L. G. Verga, N. P. Vizarim, M. Carlone, and P. A. Venegas, *Vortex Dynamic Phases in Type II Superconducting Strips with Regular and Flattened Triangular Pinning Arrays*, J. Supercond. Nov. Magn. (2018).
[151] N. P. Vizarim, M. Carlone, L. G. Verga, and P. A. Venegas, *Surface Effects on the Dynamic Behavior of Vortices in Type II Superconducting Strips with Periodic and Conformal Pinning Arrays*, J. Supercond. Nov. Magn. **31**, 1981 (2018).
[152] N. Grønbech-Jensen, *Summation of Logarithmic Interactions in Nonrectangular Periodic Media*, Comput. Phys. Commun. **119**, 115 (1999).
[153] M. P. Allen, D. J. Tildesley, and L. Allen, *Computer Simulation of Liquids*, Edição: Revised ed. (Oxford University Press, USA, Oxford, 1989).
[154] W. Legrand, D. Maccariello, N. Reyren, K. Garcia, C. Moutafis, C. Moreau-Luchaire, S. Collin, K. Bouzehouane, V. Cros, and A. Fert, *Room-Temperature Current-Induced Generation and Motion of Sub-100 Nm Skyrmions*, Nano Lett. **17**, 2703 (2017).
[155] K. Zeissler et al., *Diameter-Independent Skyrmion Hall Angle Observed in Chiral Magnetic Multilayers*, Nat. Commun. **11**, 1 (2020).
[156] K. Litzius et al., *Skyrmion Hall Effect Revealed by Direct Time-Resolved X-Ray Microscopy*, Nat. Phys. **13**, 2 (2017).
[157] M. P. MacDonald, G. C. Spalding, and K. Dholakia, *Microfluidic Sorting in an Optical Lattice*, Nature **426**, 6965 (2003).
[158] A. M. Lacasta, J. M. Sancho, A. H. Romero, and K. Lindenberg, *Sorting on Periodic Surfaces*, Phys. Rev. Lett. **94**, 160601 (2005).
[159] K. Ladavac, K. Kasza, and D. G. Grier, *Sorting Mesoscopic Objects with Periodic Potential Landscapes: Optical Fractionation*, Phys. Rev. E **70**, 010901 (2004).
[160] J. Herrmann, M. Karweit, and G. Drazer, *Separation of Suspended Particles in Microfluidic Systems by Directional Locking in Periodic Fields*, Phys. Rev. E **79**, 061404 (2009).
[161] N. P. Vizarim, C. Reichhardt, P. A. Venegas, and C. J. O. Reichhardt, *Shapiro Steps and Nonlinear Skyrmion Hall Angles for Dc and Ac Driven Skyrmions on a Two-Dimensional Periodic Substrate*, Phys. Rev. B **102**, 104413 (2020).
[162] S. Shapiro, *Josephson Currents in Superconducting Tunneling: The Effect of Microwaves and Other Observations*, Phys. Rev. Lett. **11**, 80 (1963).
[163] O. V. Dobrovolskiy, *AC Quantum Interference Effects in Nanopatterned Nb Microstrips*, J. Supercond. Nov. Magn. **28**, 469 (2015).
[164] P. Martinoli, O. Daldini, C. Leemann, and E. Stocker, *A.C. Quantum Interference in Superconducting Films with Periodically Modulated Thickness*, Solid State Commun. **17**, 205 (1975).
[165] M. P. N. Juniper, A. V. Straube, R. Besseling, D. G. A. L. Aarts, and R. P. A. Dullens, *Microscopic Dynamics of Synchronization in Driven Colloids*, Nat. Commun. **6**, 7187 (2015).
[166] J. L. Abbott, A. V. Straube, D. G. A. L. Aarts, and R. P. A. Dullens, *Transport of a Colloidal Particle Driven across a Temporally Oscillating Optical Potential Energy Landscape*, New J. Phys. **21**, 083027 (2019).
[167] C. Reichhardt and C. J. O. Reichhardt, *Structural Transitions and Dynamical Regimes for Directional Locking of Vortices and Colloids Driven over Periodic Substrates*, J. Phys. Condens. Matter **24**, 225702 (2012).
[168] C. Reichhardt and F. Nori, *Phase Locking, Devil's Staircases, Farey Trees, and Arnold Tongues in Driven Vortex Lattices with Periodic Pinning*, Phys. Rev. Lett. **82**, 414 (1999).

[169] P. T. Korda, M. B. Taylor, and D. G. Grier, *Kinetically Locked-In Colloidal Transport in an Array of Optical Tweezers*, Phys. Rev. Lett. **89**, 128301 (2002).
[170] R. L. Stoop, A. V. Straube, T. H. Johansen, and P. Tierno, *Collective Directional Locking of Colloidal Monolayers on a Periodic Substrate*, Phys. Rev. Lett. **124**, 058002 (2020).
[171] X. Cao, E. Panizon, A. Vanossi, N. Manini, and C. Bechinger, *Orientational and Directional Locking of Colloidal Clusters Driven across Periodic Surfaces*, Nat. Phys. **15**, 776 (2019).
[172] C. Reichhardt and C. J. O. Reichhardt, *Thermal Creep and the Skyrmion Hall Angle in Driven Skyrmion Crystals*, J. Phys. Condens. Matter **31**, 07LT01 (2018).
[173] J. Leliaert, P. Gypens, M. V. Milošević, B. V. Waeyenberge, and J. Mulkers, *Coupling of the Skyrmion Velocity to Its Breathing Mode in Periodically Notched Nanotracks*, J. Phys. D: Appl. Phys. **52**, 024003 (2018).
[174] C. Reichhardt and C. J. O. Reichhardt, *Depinning and Nonequilibrium Dynamic Phases of Particle Assemblies Driven over Random and Ordered Substrates: A Review*, Rep. Prog. Phys. **80**, 026501 (2016).
[175] B. C. van Zuiden, J. Paulose, W. T. M. Irvine, D. Bartolo, and V. Vitelli, *Spatiotemporal Order and Emergent Edge Currents in Active Spinner Materials*, Proc. Natl. Acad. Sci. **113**, 12919 (2016).
[176] M. Han, J. Yan, S. Granick, and E. Luijten, *Effective Temperature Concept Evaluated in an Active Colloid Mixture*, Proc. Natl. Acad. Sci. **114**, 7513 (2017).
[177] C. Reichhardt and C. J. O. Reichhardt, *Reversibility, Pattern Formation, and Edge Transport in Active Chiral and Passive Disk Mixtures*, J. Chem. Phys. **150**, 064905 (2019).
[178] J. Wiersig and K.-H. Ahn, *Devil's Staircase in the Magnetoresistance of a Periodic Array of Scatterers*, Phys. Rev. Lett. **87**, 026803 (2001).
[179] S. R. Power, M. R. Thomsen, A.-P. Jauho, and T. G. Pedersen, *Electron Trajectories and Magnetotransport in Nanopatterned Graphene under Commensurability Conditions*, Phys. Rev. B **96**, 075425 (2017).
[180] N. P. Vizarim, C. J. O. Reichhardt, P. A. Venegas, and C. Reichhardt, *Skyrmion Dynamics and Transverse Mobility: Skyrmion Hall Angle Reversal on 2D Periodic Substrates with Dc and Biharmonic Ac Drives*, Eur. Phys. J. B **93**, 112 (2020).
[181] *Skyrmion Dynamics and Traverse Mobility*, https://www.sciencedaily.com/releases/2020/06/200619115709.htm.
[182] *Skyrmion Dynamics and Traverse Mobility*, https://phys.org/news/2020-06-skyrmion-dynamics-traversemobility.html.
[183] *Skyrmion Dynamics and Traverse Mobility*, https://www.eurekalert.org/pub_releases/2020-06/s-sda061920.php.
[184] D. Speer, R. Eichhorn, and P. Reimann, *Directing Brownian Motion on a Periodic Surface*, Phys. Rev. Lett. **102**, 124101 (2009).
[185] C. Reichhardt and C. J. Olson Reichhardt, *Absolute Transverse Mobility and Ratchet Effect on Periodic Two-Dimensional Symmetric Substrates*, Phys. Rev. E **68**, 046102 (2003).
[186] P. Mali, A. Šakota, J. Tekić, S. Radošević, M. Pantić, and M. Pavkov-Hrvojević, *Complexity of Shapiro Steps*, Phys. Rev. E **101**, 032203 (2020).
[187] T. Sato, W. Koshibae, A. Kikkawa, T. Yokouchi, H. Oike, Y. Taguchi, N. Nagaosa, Y. Tokura, and F. Kagawa, *Slow Steady Flow of a Skyrmion Lattice in a Confined Geometry Probed by Narrow-Band Resistance Noise*, Phys. Rev. B **100**, 094410 (2019).
[188] C. Reichhardt and C. J. Olson, *Vortex Pinball under Crossed Ac Drives in Superconductors with Periodic Pinning Arrays*, Phys. Rev. B **65**, 100501 (2002).

[189] N. P. Vizarim, C. J. O. Reichhardt, P. A. Venegas, and C. Reichhardt, *Skyrmion Pinball and Directed Motion on Obstacle Arrays*, J. Phys. Commun. **4**, 085001 (2020).
[190] P. Tierno, T. H. Johansen, and T. M. Fischer, *Localized and Delocalized Motion of Colloidal Particles on a Magnetic Bubble Lattice*, Phys. Rev. Lett. **99**, 038303 (2007).
[191] J. Loehr, M. Loenne, A. Ernst, D. de las Heras, and T. M. Fischer, *Topological Protection of Multiparticle Dissipative Transport*, Nat. Commun. **7**, 11745 (2016).
[192] S. Platonov, B. Kästner, H. W. Schumacher, S. Kohler, and S. Ludwig, *Lissajous Rocking Ratchet: Realization in a Semiconductor Quantum Dot*, Phys. Rev. Lett. **115**, 106801 (2015).
[193] J. Barker and O. A. Tretiakov, *Static and Dynamical Properties of Antiferromagnetic Skyrmions in the Presence of Applied Current and Temperature*, Phys. Rev. Lett. **116**, 147203 (2016).
[194] W. Legrand, D. Maccariello, F. Ajejas, S. Collin, A. Vecchiola, K. Bouzehouane, N. Reyren, V. Cros, and A. Fert, *Room-Temperature Stabilization of Antiferromagnetic Skyrmions in Synthetic Antiferromagnets*, Nat. Mater. **19**, 1 (2020).
[195] A. Duzgun, C. Nisoli, C. J. O. Reichhardt, and C. Reichhardt, *Commensurate States and Pattern Switching via Liquid Crystal Skyrmions Trapped in a Square Lattice*, Soft Matter **16**, 3338 (2020).
[196] U. Ritzmann, S. von Malottki, J.-V. Kim, S. Heinze, J. Sinova, and B. Dupé, *Trochoidal Motion and Pair Generation in Skyrmion and Antiskyrmion Dynamics under Spin–Orbit Torques*, Nat. Electron. **1**, 8 (2018).
[197] A. V. Silhanek, L. Van Look, S. Raedts, R. Jonckheere, and V. V. Moshchalkov, *Guided Vortex Motion in Superconductors with a Square Antidot Array*, Phys. Rev. B **68**, 214504 (2003).
[198] N. P. Vizarim, C. Reichhardt, P. A. Venegas, and C. J. O. Reichhardt, *Guided Skyrmion Motion along Pinning Array Interfaces*, J. Magn. Magn. Mater. **528**, 167710 (2021).
[199] J. Loehr et al., *Colloidal Topological Insulators*, Commun. Phys. **1**, 1 (2018).
[200] N. P. Vizarim, J. C. B. Souza, C. Reichhardt, C. J. O. Reichhardt, and P. A. Venegas, *Directional Locking and the Influence of Obstacle Density on Skyrmion Dynamics in Triangular and Honeycomb Arrays*, J. Phys. Condens. Matter **33**, 305801 (2021).
[201] W. Jiang et al., *Blowing Magnetic Skyrmion Bubbles*, Science **349**, 283 (2015).
[202] K. Karube et al., *Disordered Skyrmion Phase Stabilized by Magnetic Frustration in a Chiral Magnet*, Sci. Adv. **4**, eaar7043 (2018).
[203] J. C. B. Souza, N. P. Vizarim, C. J. O. Reichhardt, C. Reichhardt, and P. A. Venegas, *Skyrmion Ratchet in Funnel Geometries*, Phys. Rev. B **104**, 054434 (2021).
[204] H. Wang and G. Oster, *Ratchets, Power Strokes, and Molecular Motors*, Appl. Phys. A **75**, 315 (2002).
[205] S.-H. Lee, K. Ladavac, M. Polin, and D. G. Grier, *Observation of Flux Reversal in a Symmetric Optical Thermal Ratchet*, Phys. Rev. Lett. **94**, 110601 (2005).
[206] C. C. de Souza Silva, J. Van de Vondel, M. Morelle, and V. V. Moshchalkov, *Controlled Multiple Reversals of a Ratchet Effect*, Nature **440**, 7084 (2006).
[207] D. Perez de Lara, M. Erekhinsky, E. M. Gonzalez, Y. J. Rosen, I. K. Schuller, and J. L. Vicent, *Vortex Ratchet Reversal: Role of Interstitial Vortices*, Phys. Rev. B **83**, 174507 (2011).
[208] B. Göbel, I. Mertig, and O. A. Tretiakov, *Beyond Skyrmions: Review and Perspectives of Alternative Magnetic Quasiparticles*, Phys. Rep. **895**, 1 (2021).
[209] N. P. Vizarim, J. C. B. Souza, C. J. O. Reichhardt, C. Reichhardt, M. V. Milošević, and P. A. Venegas, *Soliton Motion in Skyrmion Chains: Stabilization and Guidance by Nanoengineered Pinning*, Phys. Rev. B **105**, 224409 (2022).

[210] T.-H. Kim, H. Zhao, B. Xu, B. A. Jensen, A. H. King, M. J. Kramer, C. Nan, L. Ke, and L. Zhou, *Mechanisms of Skyrmion and Skyrmion Crystal Formation from the Conical Phase*, Nano Lett. **20**, 4731 (2020).
[211] A. O. Leonov, T. L. Monchesky, J. C. Loudon, and A. N. Bogdanov, *Three-Dimensional Chiral Skyrmions with Attractive Interparticle Interactions*, J. Phys. Condens. Matter **28**, 35LT01 (2016).
[212] T.-H. Kim, H. Zhao, P.-V. Ong, B. A. Jensen, B. Cui, A. H. King, L. Ke, and L. Zhou, *Kinetics of Magnetic Skyrmion Crystal Formation from the Conical Phase*, Nano Lett. **21**, 5547 (2021).
[213] A. Vansteenkiste and B. Van de Wiele, *MuMax: A New High-Performance Micromagnetic Simulation Tool*, J. Magn. Magn. Mater. **323**, 2585 (2011).
[214] W. F. Brown, *Micromagnetics* (John Wiley & Sons Inc, 1963).
[215] R. Brearton, G. van der Laan, and T. Hesjedal, *Magnetic Skyrmion Interactions in the Micromagnetic Framework*, Phys. Rev. B **101**, 134422 (2020).
[216] D. Capic, D. A. Garanin, and E. M. Chudnovsky, *Skyrmion–Skyrmion Interaction in a Magnetic Film*, J. Phys. Condens. Matter **32**, 415803 (2020).
[217] J. E. Lennard-Jones, *Cohesion*, Proc. Phys. Soc. **43**, 461 (1931).